Metrology of High Harmonics Seeded Soft X-ray Laser Based on Solid-Plasma Amplifier

Lu Li

l'École Polytechnique

T H È S E

Présentée par

M. Lu LI

soutenue le

21 Novembre 2014

en vue de l'obtention du titre de

DOCTEUR de l'ÉCOLE POLYTECHNIQUE

Spécialité : Physique

Arrêté du 17 Septembre 2011

Sujet de thèse :

Metrology of High Harmonics Seeded Soft X-ray Laser Based on Solid-Plasma Amplifier

MEMBRES du JURY :

M. Hamed MERDJI	Chercheur	CEA	(***Rapporteur***)
M. Gregory J. TALLENTS	Professeur	University of York	(***Rapporteur***)
Mlle Sameh DABOUSSI	Maître-assistant	Universite de Sousse	
M. Victor MALKA	Professeur	Ecole Polytechnique	
M. Jorge J. ROCCA	Professeur	Colorado State University	
M. David ROS	Maître de Conférences	LASERIX / LPGP	
M. Philippe ZEITOUN	Directeur de Recherche	LOA	(***Directeur de thèse***)

Colleagues & Collaborators

Laboratoire d'Optique Appliquée (LOA), France
Philippe Zeitoun (*Supervisor*), Stéphane Sebban, Benoît Mahieu, Hugo Dacasa, Julien Gautier, Guillaume Lambert, Fabien Tissandier, Boris Vodungbo, Victor Ceban, Magali Lozano, Jean-Loup Charles

Colorado State University (CSU), US
Jorge J. Rocca, Yong Wang, Shoujun Wang, Liang Yin, Mark Berrill

Laboratoire de Physique des Gaz et des Plasmas (LPGP), France
David Ros, Gilles Maynard, Eduardo Oliva, T.T. Thuy Le, Olivier Guilbaud, Moana Pittman, Olivier Delmas, Julien Demailly, Sophie Kazamias,

Instituto Superior Tecnico (IST), Portugal
Marta Fajardo, Gareth Williams, Swen Künzel

GSI, Darmstadt, Germany
Thomas Kuehl, Boris Ecker

Lawrence Livermore National Laboratory (LLNL), US
Jim Dunn

Imagine Optic, France
Guillaume Dovillaire

School of nuclear science and technology, Lanzhou University, China
Bitao Hu

University of Bern, Switzerland
Davide Bleiner, Mabel Ruiz-Lopez

INFLPR, Romania
Daniel Ursescu

Lund University (UL), Sweden
Bastian Aurand

Abbreviations

1D	One dimensional
2D	Two dimensional
3D	Three dimensional
ASE	Amplified spontaneous emission
ATI	Above-threshold ionization
BBO	Barium borate
BW	Bandwidth
CCD	Charge-coupled device
CDI	Coherent diffraction imaging
CPA	Chirped pulse amplification
DGRIP	Double-pulse grazing incident pumping
EUV/XUV	Extreme ultraviolet
EXAFS	Extended x-ray absorption fine structure
FEL	Free-electron lasers
FWHM	Full width at half maximum
GRIP	Grazing incident pumping
HH	High order harmonics
ICF	Inertial confinement fusion
ICXRL	International conference on x-ray lasers
IR	Infrared
LTE	Local thermodynamic equilibrium
NEXAFS	Near-edge x-ray absorption fine structure
OAP	Off-axis parabolic
OFI	Optical-field-ionization
PES	Photo-emission spectrometer
PV	Peak-to-valley
QE	Quantum efficiency
QSS	Quasi-steady-state
RMS	Root-mean-square
ROI	Region of interest
SSXRL	Seeded soft x-ray laser
SXRL	Soft x-ray laser
TCE	Transient collisional excitation
TGRIP	Triple-pulse grazing incident pumping
TW	Travelling wave
XES	X-ray emission spectroscopy
XFEL	X-ray free-electron lasers

Résumé:
Les lasers émettant des rayons X-mous sous forme d'impulsions cohérentes ultracourtes (SXRL pour soft X-ray laser en anglais) sont des outils appropriés à l'étude de la dynamique ultrarapide des atomes, molécules, surfaces et matériaux. Le présent manuscrit expose des travaux numériques et expérimentaux sur l'injection par harmonique élevée d'un amplificateur SXRL compact.

Des essais sur l'installation LASERIX montrèrent une amplification limitée dans un plasma d'ions néonoïdes du titane ($32.6\ nm$), due à la réfraction du faisceau harmonique injecté. Le front d'onde d'un SXRL à $18.9\ nm$ fut ensuite mesuré au Colorado State University (CSU), en fonction de différents paramètres d'amplification. L'étude numérique d'un plasma à grande section efficace démontra la génération d'impulsion SXRL de plusieurs dizaines de μJ et d'une durée $80\ fs$. Une modélisation plus poussée du processus d'amplification a révélé une déplétion rapide ($< 300\ fs$) du gain suivie par une reprise après environ $1.5\ ps$, vérifiée expérimentalement durant une expérience pompe-sonde (rayons X / rayons X) effectuée au CSU. Ceci a inspiré le concept d'amplification à dérive de fréquence dans les rayons X. Une modélisation complète annonce une émission SXRL totalement cohérente de l'ordre du GW ($200\ fs$, plusieurs mJ).

Metrology of High Harmonics Seeded Soft X-ray Laser Based on Solid-Plasma Amplifier

Abstract:
Ultrashort coherent soft x-ray lasers (SXRL) are adequate to capture dynamics in atoms, molecules, surfaces and materials at the ultrashort time-scales. In current dissertation, we numerically and experimentally studied on a table-top fully coherent SXRL source. The main idea is to seed high harmonic pulse into laser-induced plasma achieving significant energy amplification.

The first attempt was tested using neon-like titanium plasma ($32.6\ nm$) at LASERIX facility. Then wave front of this seeded SXRL beam ($18.9\ nm$) was measured approaching diffraction-limited ($\lambda/14$) using Hartmann wave front sensor at Colorado State University. Numerical studying on short plasma with large cross-sectional area demonstrated $10's$ of μJ and $\sim 80\ fs$ SXRL pulse. Further modelling of the amplification process revealed a rapid depletion ($< 300\ fs$) of the gain followed by a full recovery after about $1.5\ ps$. A novel x-ray pump/x-ray probe experiment was successfully conducted to verify it. This inspired the X-ray chirped pulse amplification (CPA) concept. It promises GW fully coherent SXRL (several mJ) with a capability of reaching Fourier-limited beam ($\sim 100\ fs$).

Key Words: soft X-ray laser; plasma amplifier; Hartmann sensor; wave front; high harmonics; seeding; gain recovery; population inversion ...

Contents

CHAPTER 1

Introduction

Many of the important scientific challenges facing humanity are being addressed by advances that demand improved understanding and control of the matter. The understanding of matter was revolutionized by Röntgen's discovery of x-rays in 1895 [1]. Since that, four invaluable and well-known uses of x-rays have emerged – medical imaging [1], x-ray diffraction [2, 3], x-ray absorption and emission spectroscopy [4], and photo-electron spectroscopy [5, 6, 7, 8]. These innovations expected by the construction and operation of enhanced x-ray sources open the way to understand and ultimately control matter at the level of atoms, electrons, and spins, as illustrated in *Fig*. 1.1. The exploration of the atomic or nanoscopic

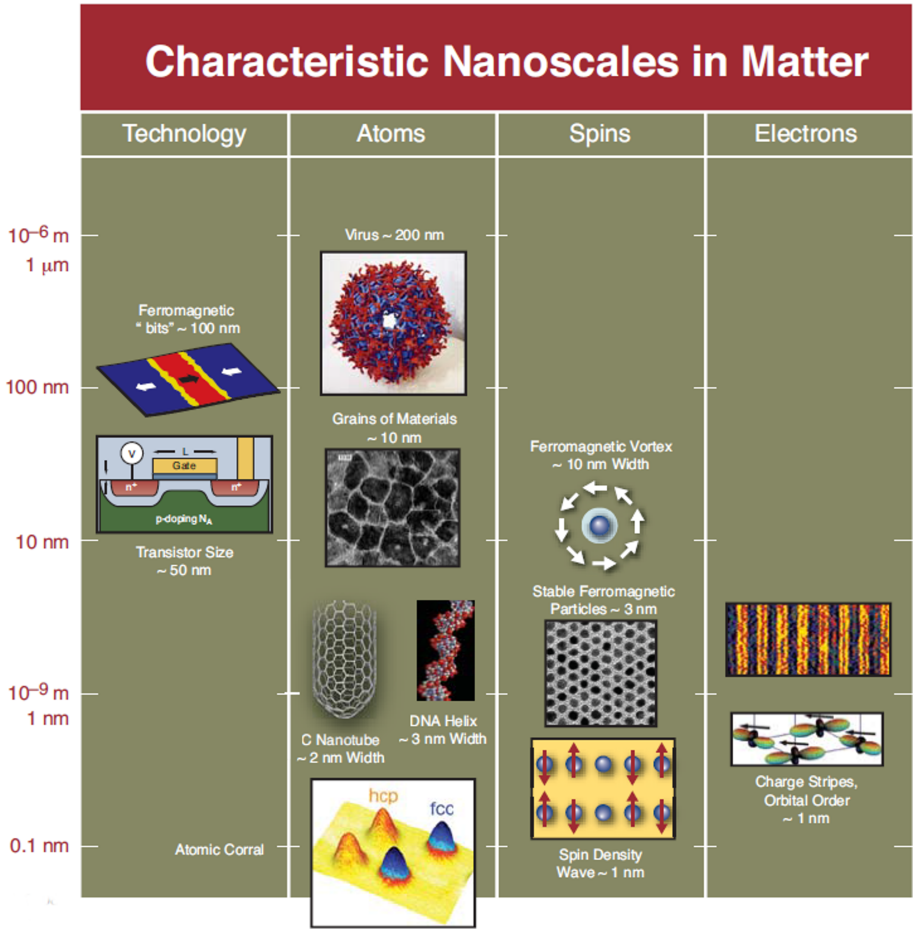

Figure 1.1: Illustration of characteristic features on the level of atoms, electrons, and spins in nanoworld in comparison with typycal lateral length scales in present advanced technological devices. from [9]

scales on the "natural" time scale and on the operational" time scale determinations are the key in the

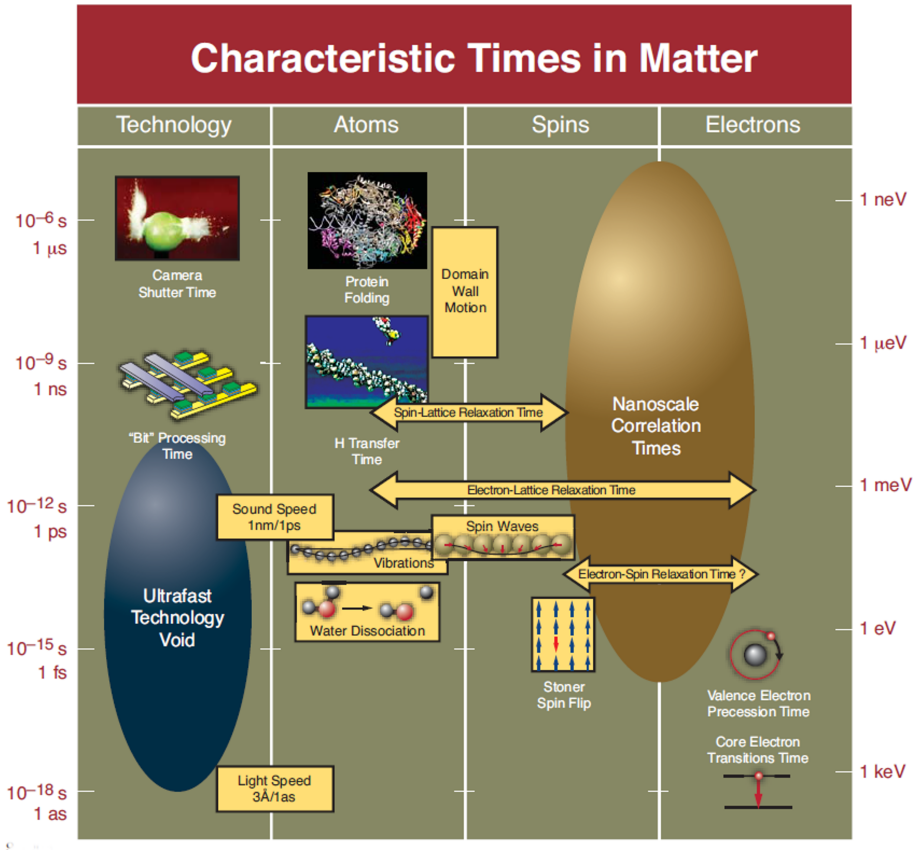

Figure 1.2: Illustration of typical times involved in the interactions of atoms, electrons, and spins. On the right, it is indicated the corresponding quantum mechanical interaction energies as estimated from the energy-time correlation $\Delta E \cdot \Delta t = h \sim 4\ fs \cdot eV$. from [9]

technological applications. $Fig.\ 1.2$ is the illustration of our present knowledge about the typical time scales of motions in atoms (about $100\ fs$), spin evolution (down to about $1\ fs$), or changes in electronic structure (down to attoseconds). All these scientific challenges are calling for more powerful, ultrashort and fully coherent x-ray sources that could extend our reach into regions of higher energy, temporal and spatial resolution.

X-rays are often divided into two major types $-$ hard x-rays and soft x-rays, which are depending on their wavelength, photon energy, and penetrating power, so that the type of experiments to each is the most suited. Hard x-rays ($\geq 10\ keV$) are able to determine the atomic structure of matter by yielding the relative positions of atoms in materials. The reconstruction of x-ray diffraction patterns has been used to give the real-space atomic structure of matter. Nowadays, most of the new macromolecular structures are determined using synchrotron radiation. With the advantage of the coherent x-ray scattering, it is possible today to determine the three-dimensional (3D) atomic structure of nano-objects [10, 11]. Furthermore, the tunability of the photon energy has led to the widespread use of x-ray absorption, which is so called extended x-ray absorption fine structure (EXAFS). A key component of future studies of matter with hard x-rays is the combination of the atomic resolution with temporal resolution on the sub-picosecond time scale of atomic motion.

Longer wavelengths with lower energy, soft x-rays ($30\ eV - 1\ keV$) enable the investigation of the electronic structure of matter. Soft x-ray spectroscopy, including near-edge x-ray absorption fine structure (NEXAFS), x-ray emission spectroscopy (XES) and photo-emission spectroscopy (PES), are providing information on how atoms are bound together by yielding information on the electron distribution in occupied and empty orbitals in molecules and the electronic energy bands. Recently, the coherent diffraction imaging (CDI) methods with x-ray free-electron lasers (FEL) are approaching temporal resolution of fs and spatial resolution of $1\ angstrom$ [12]. Key future developments are their extension to the multi-dimensional phase space of length scales down to nanometres and time scales down to femtoseconds, or even attoseconds. In this dissertation, we focus our attention on the so called soft x-ray laser (SXRL) sources.

Soft x-ray coherent imaging has shown impressive spatial and temporal resolution. Variety of techniques, based on the table-top coherent soft x-ray sources, have been demonstrated in laboratories all over the world. Depending on the excellent beam properties similar to the driven laser [13], high harmonics x-ray sources [14, 15] have attracted much attentions for the phase imaging applications, such as holography [16], diffraction imaging [17] and phase contrast imaging for the nano-structure detection [18]. However, owing to the pulse energy limits, most of the phase imaging are averaging over several to a lot of SXRL pulses, which will reduce the spatial and temporal resolutions due to intrinsic instabilities (such as vibrations, jitter, sample hysteresis or degradation by the pump or by the x-rays etc.). Moreover, some samples are too fragile and too complex to produce, or too expensive to allow for averaging imaging techniques. Consequently, in order to achieve high spatial (in nanometre) and temporal resolution (in femtosecond) of single-shot imaging, the soft x-ray pulse should reach an energy of about $1\ \mu J$ level and ultra-short pulse duration, as well as good wave front. There have been some successful soft x-ray single-shot imaging applications demonstrated so far. Several techniques have been employed such as femtosecond holography [19, 16, 20], CDI [21], scanning microscopy [12], crystallography [22, 23], tomography and psychology [24] and so on.

Attractive phase imaging of coherent soft x-rays encouraged the development of powerful, fully coherent and ultra-fast table-top SXRL sources. So far, there are several typical types of table-top SXRL sources haven been discovered. First large amplification on SXRL was observed in 1985 [25, 26] and was soon pushed to saturated amplification [27], where the amplified output signals are so called amplified spontaneous emission (ASE). The transient collisional excitation pumping scheme [28, 29] was then demonstrated with long pre-pulse (nanosecond class) coupled with short pump pulse (picosecond class) driven infrared (IR) lasers leading a substantially reduced cost but higher efficient x-ray plasma pumping approach. Unfortunately, after several decades of efforts [30, 31], the emitted x-ray pulse is limited to picoseconds duration and its poor spatial coherence is hard to be overcame. Simultaneously, the high order harmonics (HH) generation x-ray source was proposed [14, 15], and soon was proved to exhibit full temporal and spatial coherence [13]. Interestingly, this beam keeps similar beam properties as the input driven laser beam [32, 33], that gives a bright perspective of this source in multitude of applications [16, 17, 18, 34]. But the poor pulse energy is not satisfying considering single-shot imaging. An independent and compact capillary discharged SXRL laser was demonstrated in early of $1990's$ [35], and subsequently was optimized to reach milli-joule pulse energy with high degree of spatial coherence [36]. However, saturation level was obtained only at a wavelength of $46.9\ nm$ with long pulse duration (nanosecond level).

A breakthrough on table-top SXRL came in 1995 [37] by seeding coherent HH pulse into x-ray plasma amplifier, and the first successful amplification of the HH seed beam with this concept was

arriving ten years later [38]. The French group demonstrated full-polarized, excellent spatial coherence and narrow spectral bandwidth of SXRL by injecting HH seed into a gas-based plasma amplifier. And it is confirmed as diffraction limited beam after the wave front measurement [39]. This inspired people to work out with this novel technique. Several years later, similar result was obtained in the HH-injection seeded SXRL (SSXRL) experiment with solid-based plasma amplifier [40, 41] shown in $Fig.\ 1.3$. It revealed a bright prospect of this coherent seeding technique. The solid based-plasma amplifiers have the potential to reach higher plasma density than with the gas-plasma, which could lead bandwidth widening [42], subsequently open the way to shorter pulse duration. The study in this dissertation is actually based on this novel SXRL source from solid-plasma amplifier. With the aim of producing pulses with higher energy, we studied multi-stage amplifiers. More recently, we presented a concept of an x-ray laser based on the principle of chirped pulse amplification (CPA) which could produce high energy pulses of $100's\ fs$ pulse duration [43]. Sequentially, we proposed and participated at a practical experiment to verify the validity of SXRL CPA system [44].

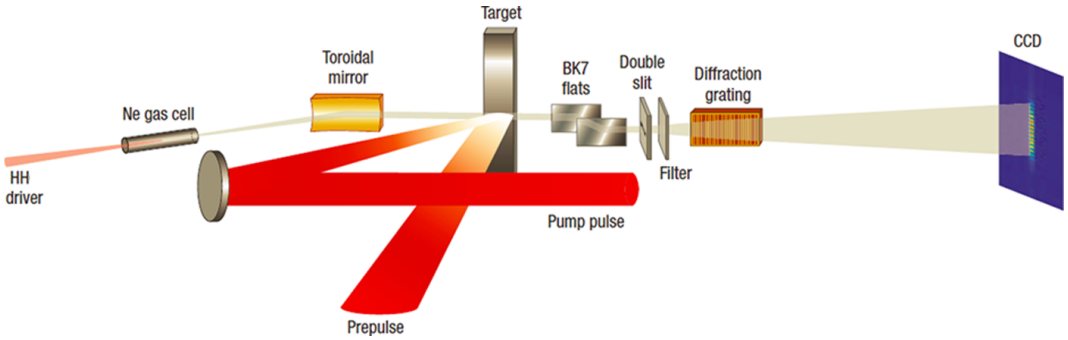

Figure 1.3: Schematically drawing of experimental setup on high harmonics injection seeded soft x-ray laser with solid-plasma amplifier. The main optical laser pulse exciting the amplifier impinges at 23° grazing incidence onto the target. A neon gas cell is used to generate the high harmonic seed. from [41]

In addition, with the purpose of high resolution phase contrast and diffraction imaging, wave front of the SXRL beam must be excellent. Indeed, diffraction or holographic imaging of a sample with a coherent source having an aberrant wave front will reduce the resolution and may even distort the image. Wave front characterization is also related to the radiation intensity of the beam spot with micrometer dimension, as explained in the relation with Strehl ratio [45]. Moreover, a good wave front of the beam source is contributed to match the subsequent spectral compensation, such as the previously proposed SXRL compressor [43]. Previous work on wave front of the HH source [32] and gas-plasma-based SSXRL source [39] showed near-diffraction limited characteristics. However, the wave front of HH-seeded SXRL from solid-based plasma amplifier have not been studied prior to this work. Despite its crucial role in the applications, we therefore performed an experiment [46] to measure the wave front of SSXRL based on solid-plasma amplifier as one of the major works in this study.

This dissertation is constructed as follow: i) the basic physics and brief evolution of SXRL population inversion mechanism are firstly presented; ii) the detailed optical properties on SSXRL are studied in the Chapter 3, which includes ASE self-seeding with oscillator-amplifier configuration, near field characteristics of HH-seeded SXRL source and the wave front measurement on solid-plasma-based HH-seeded SXRL; iii) in Chapter 4, technical and simulation details of SXRL CPA system coupled with some preliminary experiment results are discussed; iv) the gain dynamics of SXRL plasma amplifier is

theoretically and experimentally investigated in Chapter 5; v) finally, a brief summary and outlook of this work are given at the end.

Bibliography

[1] Stanton, Arthur, "Wilhelm Conrad Röntgen On a New Kind of Rays: translation of a paper read before the Würzburg Physical and Medical Society, 1895". Nature (Subscription-only access) 53 (1369): 274–6 (1895).

[2] W. Friedrich, P. Knipping,M. Von Laue, *"Interferenz-Erscheinungen bei Röntgenstrahlen"*, Sitzungsberichte der Mathematisch-Physikalischen Classe der Königlich-Bayerisch Akademie der Wissenschaften zu München, **303** (1912).

[3] W. L. Bragg, *"The Structure of Some Crystals as Indicated by their Diffraction of X-rays"*, Proc. R. Soc. Lond. A89 (610): 248–277 (JSTOR 93488) (1913).

[4] C. G. Barkla, *X-rays and the theory of radiation* (1918).

[5] K. Siegbahn, *Electron Spectroscopy for Chemical Analysis* (1973).

[6] I. Lindau and W.E. Spicer, Journal of Electron Spectroscopy and Related Phenomena **3**, 409-413 (1974).

[7] D. W. Turne, *Molecular photoelectron spectroscopy* (1970).

[8] H.C. Siegmann, Physics Report **17**, 37-76 (1975).

[9] *Scientific needs for future x-ray sources in the U.S.*, SLAC-R910, LBNL-1090E (2008).

[10] M. A. Pfeifer, G. J. Williams, I. A. Vartanyants, R. Harder and I. K. Robinson, Nature **442**, 63–66 (2006).

[11] Y. Nishino, Y. Takahashi, N. Imamoto, T. Ishikawa, and K. Maeshima, Phys. Rev. Lett.**102**, 018101 (2009).

[12] H. N. Chapman and K. A. Nugent, Nature Photonics **4**, 833-839 (2010).

[13] A. L'Huillier, K. J. Schafer and K. C. Kulander, J. Phys. B: At. Mol. Opt. Phys. **24**, 3315-3341 (1991).

[14] A. McPherson, G. Gibson, H. Jara, U. Johann, T. S. Luk, I. A. McIntyre, K. Boyer and C. K. Rhodes, J. Opt. Soc. Am. B **4**, 595 (1987).

[15] M. Ferray, A. L'Huillier, X. F. Li, L. A. Lompre, G. Mainfray and C. Manus, J. Phys. B: At. Mol. Opt. Phys. **21**, L31 (1988).

[16] A. Morlens, J. Gautier, G. Rey, Ph. Zeitoun, J. Caumes, M. Kos-Rosset, H. Merdji, S. Kazamias, K. Cassou and M. Fajardo, Optics Lett. **31**, 3095 (2006).

[17] A. Ravasio, D. Gauthier, F. R. N. C. Maia, M. Billon, J-P. Caumes, D. Garzella, M. Géléoc, O. Gobert, J-F. Hergott, A-M. Pena, H. Perez, B. Carré, E. Bourhis, J. Gierak, A. Madouri, D. Mailly, B. Schiedt, M. Fajardo, J. Gautier, Ph. Zeitoun, P. H. Bucksbaum, J. Hajdu, and H. Merdji, Phys. Rev. Lett. **103**, 028104 (2009).

[18] B. Vodungbo, J. Gautier, G. Lambert, A. B. Sardinha, M. Lozano, S. Sebban, M. Ducousso, W. Boutu, K. Li, B. Tudu, M. Tortarolo, R. Hawaldar, R. Delaunay, V. López-Flores, J. Arabski, C. Boeglin, H. Merdji, Ph. Zeitoun and J. Lüning, Nature Communication **3**, 999(2012).

[19] J. Trebes, S. B. Brown, E. M. Campbell, D. L. Matthews, D. G. Nilson, G. F. Stone and D. A. Whelan, *Proc. SPIE 0913*, High Intensity Laser-Matter Interactions, 88 (1988).

[20] H. N. Chapman, S. P. Hau-Riege, M.I J. Bogan, S. Bajt, A. Barty, S. Boutet, S. Marchesini, M. Frank, B. W. Woods, W. H.y Benner, R.A. London, U. Rohner, A. Szöke, E. Spiller, T. Moller, C. Bostedt, D. A. Shapiro, M. Kuhlmann, R. Treusch, E. Plönjes, F. Burmeister, M. Bergh, C. Caleman, G. Huldt, M. M. Seibert and J. Hajdu, Nature **448**, 676 (2007).

[21] A. Barty, C. Caleman, A. Aquila, N. Timneanu, L. Lomb, T. A. White, J. Andreasson, D. Arnlund, S. Bajt, T. R. M. Barends, M. Barthelmess, M. J. Bogan, C. Bostedt, J. D. Bozek, R. Coffee, N. Coppola, J. Davidsson, D. P. DePonte, R. B. Doak, T. Ekeberg, V. Elser, S. W. Epp, B. Erk, H. Fleckenstein, L. Foucar, P. Fromme, H. Graafsma, L. Gumprecht, J. Hajdu, C. Y. Hampton, R. Hartmann, A. Hartmann, G. Hauser, H. Hirsemann, P. Holl, M. S. Hunter, L. Johansson, S. Kassemeyer, N. Kimmel, R. A. Kirian, M. Liang, F. R. N. C. Maia, E. Malmerberg, S. Marchesini, A.V. Martin, K. Nass, R. Neutze, C. Reich, D. Rolles, B. Rudek, A. Rudenko, H. Scott, I. Schlichting, J. Schulz, M. M. Seibert, R. L. Shoeman, R. G. Sierra, H. Soltau, J. C. H. Spence, F. Stellato, S. Stern, L. Strüder, J. Ullrich, X. Wang, G. Weidenspointner, U.Weierstall, C. B. Wunderer and H. N. Chapman, Nature Photonics **2**, 415 (2008).

[22] H. N. Chapman, P.Fromme, A. Barty, T. A. White, R. A. Kirian, A. Aquila, M. S. Hunter, J. Schulz, D. P. DePonte, U. Weierstall, R. Bruce Doak, F. R. N. C. Maia, A. V. Martin, I. Schlichting, L. Lomb, N. Coppola, R. L. Shoeman, S. W. Epp, R. Hartmann, D. Rolles, A. Rudenko, L. Foucar, N. Kimmel, G. Weidenspointner, P. Holl, M. Liang, M. Barthelmess, C. Caleman, S. Boutet, M. J. Bogan, J. Krzywinski, C. Bostedt, S. Bajt, L. Gumprecht, B. Rudek, B. Erk, C. Schmidt, A. Hömke, C. Reich, D. Pietschner, L. Strüder, G. Hauser, H. Gorke, J. Ullrich, S. Herrmann, G. Schaller, F. Schopper, H. Soltau, K. Kühnel, M. Messerschmidt, J. D. Bozek, S. P. Hau-Riege, M. Frank, C. Y. Hampton, R. G. Sierra, D. Starodub, G. J. Williams, J. Hajdu, N. Timneanu, M. M. Seibert, J. Andreasson, A. Rocker, O. Jönsson, M. Svenda, S. Stern, K. Nass, R. Andritschke, C. Schröter, F. Krasniqi, M. Bott, K. E. Schmidt, X. Wang, I. Grotjohann, J. M. Holton, T. R. M. Barends, R. Neutze, S. Marchesini, R. Fromme, S. Schorb, D. Rupp, M. Adolph, T. Gorkhover, I. Andersson, H. Hirsemann, G. Potdevin, H. Graafsma, B. Nilsson and J. C. H. Spence, Nature **470**, 73(2011).

[23] S. Boutet, L. Lomb, G. J. Williams, T. R. M. Barends, A. Aquila, R. B. Doak, U. Weierstall, D. P. DePonte, J. Steinbrener, R. L. Shoeman, M. Messerschmidt, A. Barty, T. A. White, S. Kassemeyer, R. A. Kirian, M. M. Seibert, P. A. Montanez, C. Kenney, R. Herbst, P. Hart, J. Pines, G. Haller, S. M. Gruner, H. T. Philipp, M. W. Tate, M. Hromalik, L. J. Koerner, N. van Bakel, J. Morse, W. Ghonsalves, D. Arnlund, M. J. Bogan, C. Caleman, R. Fromme, C. Y. Hampton, M. S. Hunter, L. C. Johansson, G. Katona, C. Kupitz, M. Liang, A. V. Martin, K. Nass, L. Redecke, F. Stellato, N.r Timneanu, D. Wang, N. A. Zatsepin, D. Schafer, J. Defever, R. Neutze, P. Fromme, J. C. H. Spence, H. N. Chapman and I. Schlichting, Science **337**, 362 (2012).

[24] M. Dierolf, A. Menzel, P. Thibault, P. Schneider, C. M. Kewish, R. Wepf, O. Bunk and F. Pfeiffer, Nature **467**, 436–439 (2010).

[25] D. L. Matthews, P. L. Hagelstein, M. D. Rosen, M. J. Eckart, N. M. Ceglio, A. U. Hazi, H. Medecki, B. J. MacGowan, J. E. Trebes, B. L. Whitten, E. M. Campbell, C. W. Hatcher, A. M. Hawryluk, R. L. Kauffman, L. D. Pleasance, G. Rambach, J. H. Scofield, G. Stone, and T. A. Weaver, Phys. Rev. Lett. **54**,110 (1985).

[26] S. Suckewer, C. H. Skinner, . Milchberg, C. Keane, and D. Voorhees, Phys. Rev. Lett. **55**, 1753 (1985).

[27] A. Carillon, H. Z. Chen, P. Dhez, L. Dwivedi, J. Jacoby, P. Jaegle, G. Jamelot, J. Zhang, M. H. Key, A. Kidd, A. Klisnick, R. Kodama, J. Krishnan, C. L. S. Lewis, D. Neely, P. Norreys, D. O'Neill, G. J. Pert, S. A. Ramsden, J. P. Raucourt, G. J. Tallents, and J. Uhomoibhi, Phys. Rev. Lett. **68**, 2917 (1992).

[28] P. V. Nickles, M. Schnuer, M. R. Kalashnikov, I. Will and W. Sandner, Proc. SPIE **2520**, 373 (1995).

[29] P. V. Nickles, V. N. Shlyaptsev, M. Kalachnikov, M. Schnürer,I. Will, and W. Sandner, Phys. Rev. Lett. **78**, 2748-2751 (1997).

[30] J. Zhang, P. J. Warwick, E. Wolfrum, M. H. Key, C. Danson, A. Demir, S. Healy, D. H. Kalantar, N. S. Kim, C. L. S. Lewis, J. Lin, A. G. MacPhee, D. Neely, J. Nilsen, G. J. Pert, R. Smith, G. J. Tallents, and J. S. Wark, Phys. Rev. A **54**, R4653(1996).

[31] D. Zimmer, B. Zielbauer, V. Bagnoud, U. Eisenbarth, D. Javorkova and T. Kuehl, Optics Exp. **16**, 10398-10403 (2008).

[32] J. Gautier, Ph. Zeitoun, C. Hauri, A.-S. Morlens, G. Rey, C. Valentin, E. Papalarazou, J.-P. Goddet, S. Sebban, F. Burgy, P. Mercère, M. Idir, G. Dovillaire, X. Levecq, S. Bucourt, M. Fajardo, H. Merdji and J.-P. Caumes, Eur. Phys. J. D **48**, 459–463 (2008).

[33] G. Lambert, F. Tissandier, J. Gautier, C. P. Hauri, P. Zeitoun, C. Valentin, T. Marchenko, J. P. Goddet, M. Ribiere, A. Sardinha, M. Fajardo, F. Hamouda, G. Maynard, G. Rey, and S. Sebban, Eur. Phys. Lett., **89**, 24001 (2010).

[34] Tenio Popmintchev, Ming-Chang Chen, Paul Arpin, Margaret M. Murnane and Henry C. Kapteyn, Nature Photonics **4**, 822-832 (2010).

[35] J. J. Rocca, V. Shlyaptsev, F.G. Tomasel, O. D. Cortazar, D. Hartshorn, and J. L. A. Chilla, Phy. Rev. Lett. **73**, 2192 (1994).

[36] C. D. Macchietto, B. R. Benware, and J. J. Rocca, Opt. Lett. **24**, 1115 (1999)

[37] T. Ditmire, M. H. R. Hutchinson, M. H. Key, C. L. S. Lewis, A. MacPhee, I. Mercer, D. Neely, M. D. Perry, R. A. Smith, J. S. Wark and M. Zepf, Phys. Rev. A **51**, R4337 (1995).

[38] Ph. Zeitoun, G. Faivre, S. Sebban, T. Mocek, A. Hallou, M. Fajardo, D. Aubert, P. Balcou, F. Burgy, D. Douillet, S. Kazamias, G. De Lacheze-Murel, T. Lefrou, S. Le Pape, P. Mercere, H. Merdji, A. S. Morlens, J. P. Rousseau, and C. Valentin, Nature **431**, 426 (2004).

[39] J. P. Goddet, S. Sebban, J. Gautier, P. Zeitoun, C. Valentin, F. Tissandier, T. Marchenko, G. Lambert, M. Ribieres, D. Douillet, T. Lefrou, G. Iaquaniello, F. Burgy, G. Maynard, B. Cros, B. Robillard, T. Mocek, J. Nejdl, M. Kozlova, and K. Jakubczak, Opt. Lett. **34**, 2438 (2009).

[40] Y. Wang, E. Granados, M. A. Larotonda, M. Berrill, B. M. Luther, D. Patel, C. S. Menoni, and J. J. Rocca, Phys. Rev. Lett. **97**, 123901 (2006).

[41] Y. Wang, E. Granados, F. Pedaci, D. Alessi, B. Luther, M. Berrill, and J. J. Rocca, Nat. Photonics **2**, 94 (2008).

[42] Y. Wang, M. Berrill, F. Pedaci, M. M. Shakya, S. Gilbertson, Zenghu Chang, E. Granados, B. M. Luther, M. A. Larotonda, and J. J. Rocca, Phys. Rev. A **79**, 023810 (2009).

[43] E. Oliva, M. Fajardo, L. Li, M. Pittman, T. T. T. Le, J. Gautier, G. Lambert, P. Velarde, D. Ros, S. Sebban, and P. Zeitoun, Nat. Photonics **6**, 764 (2012).

[44] Y. Wang, S.Wang, E. Oliva, L. Li, M. Berrill, L. Yin, J. Nejdl, B. M. Luther, C. Proux, T. T. T. Le, J. Dunn, D. Ros, Ph. Zeitoun and J. J. Rocca, Nature Photonics **8**, 381-384 (2014).

[45] M. Born and E. Wolf, *Principles of Optics*(Cambridge University, 1999), PP..

[46] L. Li, Y. Wang, S. Wang, E. Oliva, L. Yin, T. T. T. Le, S. Daboussi, D. Ros, G. Maynard, S. Sebban, B. Hu, J. J. Rocca, and Ph. Zeitoun, Optics Lett. **38**, 4011-4014 (2013).

CHAPTER 2

Population Inversion Mechanism in SXRL

In the past decades after the first demonstration of a ruby laser at wavelength of $694.3\ nm$ in $1960's$ [1], the optical community immediately began seeking for lasers with shorter and shorter wavelength. As the energy of a laser transition increases, the excited state lifetime decreases, and the pump energy required to generate the population inversion increases. Therefore, pump energy must be concentrated in a pump pulse that can be deposited rapidly in the laser material. Further challenge is the lack of materials for reflecting or transmitting light efficiently in the short wavelength (extreme ultraviolet), which makes conventional mirror windows impractical. However, researchers shifted their approach to fix these problems. After some attempts of making a laser oscillator[2], they sought to highly excite cylindrical plasmas which were proved to generate intense x-ray pulses by amplifying stimulated emission along their length. The obvious way to excite the plasma was by firing intense optical laser pulse onto a target, and fortunately, x-ray lasing were becoming to be reality. Various SXRL population inversion mechanisms based on laser-induced plasma and the evolution of the different SXRL plasma pumping schemes will be discussed in this Chapter.

2.1 Basic physics of SXRL plasma

Gudzenko and Shelepin in 1965 [3], firstly proposed the lasing in recombining plasmas. They pointed out that the short wavelength lasers in SXRL region would need large energy gap to be realized in highly ionized ions. As a result high power IR lasers, providing fast energy delivery (pumping), are generally employed to create and heat the plasma, although in some cases fast electrical discharges [4] are employed. Population inversion, in which there are more electrons in the upper excited energy level than in the lower energy level, is generally accomplished through selective depopulation, rather than selective population. High gain lasing are observed in some preferred electron configurations: hydrogen-like, neon-like and nickel-like ions, which tend to have a large fraction of plasma ions in a desired ionization state.

There are three basic processes in the atom quantized evolution: absorption, spontaneous emission and stimulated emission, as described in $Fig.\ 2.1$. Lasing involves the amplified spontaneous emission (ASE) and stimulated emission. For the spontaneous emission process, the atom is initially excited as shown in $Fig.\ 2.1(b)$ and electrons are perturbed and oscillating between the upper and lower energy states. Due to the natural stochastic, this emission was turned out as incoherent light. For the stimulated emission, which occurs when incident photons with resonant frequency ω encounter an atom already in the upper excited state (see$Fig.\ 2.1(c)$). In this case, the emitted radiation is not only at the same frequency, but is phase coherent and with the same polarization.

Considering the lasing from plasma column illustrated in $Fig.\ 2.2$, which consists of free electrons and highly-charged ions. The emission is associated with spontaneous emission and stimulated emission. Early in the process, spontaneous emission dominates, which is phase incoherent as the initiation of the emission processes in different atoms is random and uncorrelated. However, as time processes,

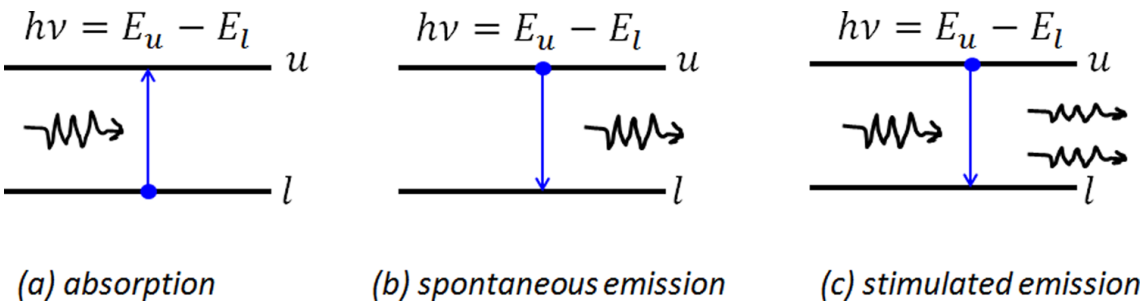

Figure 2.1: The processes of (a) absorption, (b) spontaneous emission and (c) stimulated emission.

the situation changes. Due to the consistence in frequency, there is a little chance the spontaneous emitted photons leading to the stimulated emission and thus achieve the substantial amplification. The stimulated emission from each unity is fully phase coherent, while the different unities (excited atom or ion) are not polarized between each others, the final output turning out as weakly coherent beam.

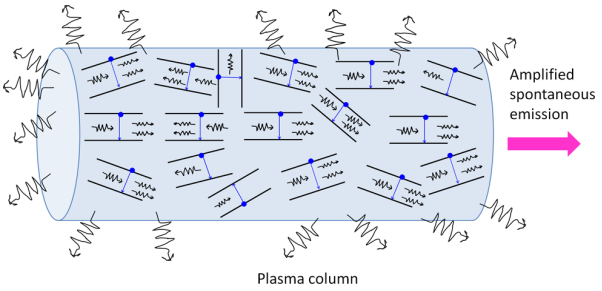

Figure 2.2: Emissions from x-ray amplifying plasma column.

The first idea to achieve phase coherent lasing is using long plasma column (seed $Fig.\ 2.3$), the radiation emitted along the long axial path, there is a much increased probability of interacting with excited atoms leading to stimulated phase coherent emission in a cascading. This is the process of amplified spontaneous emission. However, to achieve the phase fully coherent beam, a rather long plasma column is fundamentally required (tens of cm). This long size plasma with highly-ionized state is extremely difficult to create with the laser nowadays. The only fully coherent output within this concept was demonstrated using capillary discharge technique [4] (see $Fig.\ 2.3$).

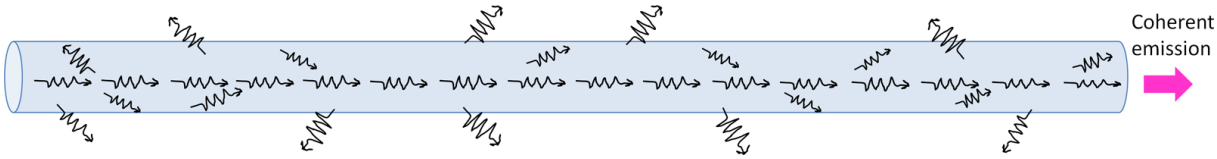

Figure 2.3: Emissions from a long-narrow x-ray amplifying plasma column.

Another possibility is to use mode control, which involves phase space, bandwidth and polarization limitations imposed by geometry and cavity optics. However, in the soft x-ray short wavelength region, to find high efficient mirror remains very challenging. A novel solution was reported ten years ago [5], which demonstrated that fully phase coherent and highly-polarized SXRL beam can be obtained by seeding

plasma with coherent high order harmonics (HH) seed beam. This idea was soon extended to seeding with solid-plasma amplifier [6], and similar results were observed. This behaviour was then explained using an one dimensional (1D) Maxwell-Bloch code [7]. As schematically described in $Fig.\ 2.4$, when the coherent seed field arrives in the plasma, plasma is strongly polarized. The various stimulating emissions are associated with phase fully coherent beam. And the coherent seed beam is significantly amplified. It is also the main topic of this dissertation.

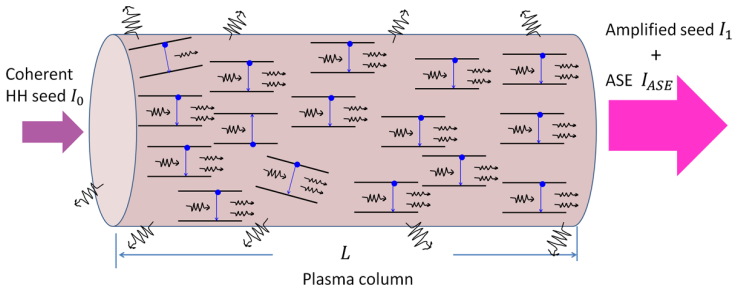

Figure 2.4: X-ray plasma amplifier with coherent HH seeding.

In order to work with the x-ray plasma amplifier, we subsequently start to study with the gain properties. A stimulated emission requires a population density inversion. We therefore, define the electron densities in the upper and lower state as n_u and n_l, respectively. Conceptual geometry of seeding is displayed in $Fig.\ 2.4$. For an homogeneous plasma amplifier of length L, the output intensity I_{out} is given by the incoherent sum of the amplified seed I_1 and the ASE I_{ASE}:

$$I_{out} = I_{ASE} + I_1 = I_{seed} e^{G(\nu,t)L} + j(\nu,t)/G(\nu,t) e^{G(\nu,t)L}, \tag{2.1}$$

where $G(\nu,t)$ is the temporal frequency-dependent gain coefficient, and $j(\nu,t)$ is the emissivity (parameter characterising self-emission level). The gain is often expressed in terms of atomic cross-sections for stimulated emission σ_{stim} and absorption σ_{abs} : [8]

$$G = n_u \sigma_{stim} - n_l \sigma_{abs}, \tag{2.2}$$

coupled with the density inversion factor

$$F \equiv 1 - \frac{n_l \sigma_{abs}}{n_u \sigma_{stim}} = 1 - \frac{n_l g_u}{n_u g_l}, \tag{2.3}$$

then the gain can be written as

$$G \equiv n_u \sigma_{stim} F. \tag{2.4}$$

In above, g_u and g_l are the statistical weights of upper lasing level and lower lasing level, respectively. Moreover, the gain G is given explicitly as [8]

$$G = \frac{\lambda^3 n_u F A_{ul}}{8\pi c(\Delta\lambda/\lambda)}, \tag{2.5}$$

where, A_{ul} is the spontaneous decay rate from upper level u to lower level l. The Quantum mechanical Einstein coefficient A can be expressed in terms of the oscillator strength f_{lu} as

$$A_{ul} = \frac{e^2 \omega^2}{2\pi \varepsilon_0 m c^3} \left(\frac{g_l}{g_u}\right) f_{lu}, \tag{2.6}$$

where ω is the lasing photon frequency. Then, the cross-section for stimulated emission can be written as

$$\sigma_{stim} = \frac{\pi\lambda r_e}{\Delta\lambda/}(\frac{g_l}{g_u})f_{lu}, \tag{2.7}$$

here classical electron radius $r_e = e^2/4\pi\varepsilon_0 mc^2 = 2.82\times10^{-13}\ cm$.

For SXRL, the observed linewidth is dominated by Doppler broadening n the hot plasma. The resultant spectral bandwidth is given by

$$\left.\frac{\Delta\lambda}{\lambda}\right|_{FWHM} = \frac{v_i}{c} = \frac{2\sqrt{2ln2}}{c}\sqrt{\frac{\kappa T_i}{M}}, \tag{2.8}$$

where v_i is the root-mean-square (RMS) ion thermal velocity, κT_i is the ion temperature in eV and M is the ion mass. FWHM is the full width at half maximum.

It is worth noting that we may also try to increase the saturation fluence by reducing the stimulated emission cross-section. To take into account the saturation of the population inversion, the gain G is given by the formula:

$$G = \frac{G_0}{1+I/I_s}. \tag{2.9}$$

The key parameter of x-ray plasma amplifier is the saturation intensity I_s, which is given by the following formula [9]

$$I_s = \frac{\hbar\omega}{\sigma_{stim}\tau_r}. \tag{2.10}$$

Here, τ_r is the recovery time of the population inversion which will be discussed in Chapter 4 and Chapter 5.

In general, optimizing the plasma conditions may lead to significant enhancement of the lasing spectral width. This conclusion is particularly important since achievement of short pulses goes also through the production of SXRL with spectral width as large as possible. This assumption has been often verified with visible or IR lasers. Gas lasers due to very narrow spectral width are known to have much lower saturation influence than solid lasers and also they support amplification of pulses with much longer duration than solid lasers. Therefore, our search will be mainly oriented towards the use and optimization of x-ray amplifiers created from interaction of intense pump laser with solid target.

2.2 Hydrogen-like ion recombination scheme

Hydrogen-like ions, for which accurate transitions rates and energy level data are available, provide the simplest atomic system to investigate the production of population inversion by plasma recombination. In $1970's$, Irons and Peacock [10], Dewhurst *et al.* [11] succeeded to observe the population inversion in hydrogen-like carbon ions. The lasing is so called $Balmer-\alpha$ line ($n=3-2$ transition, where n is the principal quantum number), as illustrated in $Fig.\ 2.5$ [12]. During the plasma rapid expansion cooling appears, the fully stripped ions go into the recombination phase, then strong three-body recombination occurs. Electrons are preferentially trapped in the highly excited states following cascade decay to the lower energy level ($n=2$) and the ground state ($n=$). As the collisional electron de-excitation is inversely proportional to the square root of the energy difference between the levels [13], this electronic

cascade reaches a level at which electron de-excitation is no longer dominate over radiative decay. Then the population inversion occurs between the specific energy levels. For plasmas of large volume re-absorption (photon trapping) of the $2-1$ decay radiation can reduce the population inversion. This behaviour was soon explained with a recombination-laser theoretical model developed by Pert [14].

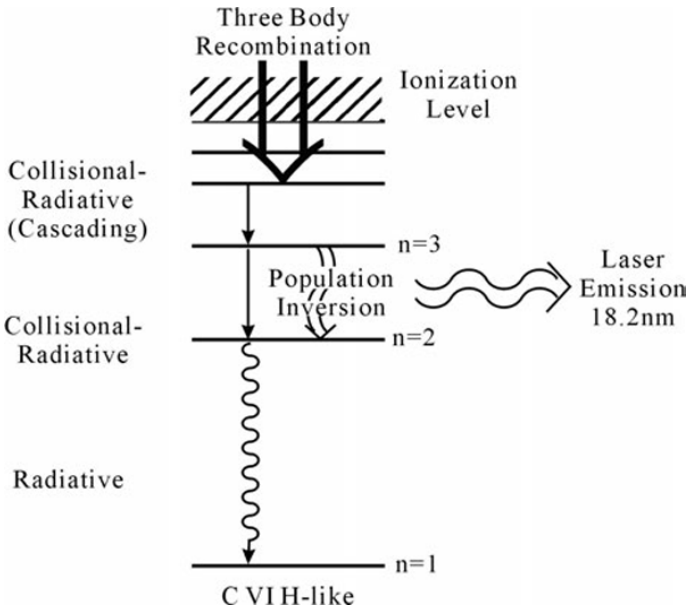

Figure 2.5: Simplified electron energy level diagram of H-like C showing the processes reponsible for the generation of population inversion between $n=3$ and $n=2$ levels in 18.2 nm C_{VI} recombination laser. from [12]

Achieving high gain in a fast recombining plasma is very desirable in the pursuit of SXRL. The amplification of soft x-rays by plasma recombination requires conflicting plasma conditions $--$ highly ionized plasma with very cold electron temperature. Solving this problem could allow the recombination scheme to be extended to the shorter wavelengths. Scaling with atomic number, Z, which leads to Z (hydrogen-like ions charge) dependence of the transition wavelength as $\lambda \sim Z^{-2}$, the electron temperature $T_e \sim Z^2$, electron density $n_e \sim Z^7$, the time scale $t \sim Z^{-4}$, the gain coefficient $g \sim Z^{7.5}$ and $g \sim Z^6$ for a Doppler-broadened line and Stark-broadened line respectively [14]. The recombining plasma can be rapidly cooled due to adiabatic expansion [15, 16], electron heat conduction to a nearby wall or colder neighbouring plasma [17], or radiation from high-Z ions introduced as impurities in to the plasma[18, 19]. Eventually, the two contradicting plasma conditions were traditionally solved adopting two-step process: 1) a heating pulse to generate highly ionized and dense plasma; 2) the plasma is rapid cooled down by the termination of the excitation pulse. All these cooling mechanisms have been utilized experimentally to generate the gain at soft x-ray wavelengths.

Pert [14] proposed a cylindrical fiber to meet the optimum recombination plasma condition. This idea was carried out by a French-English group performing a hydrogen-like carbon soft x-ray lasing experiment at Rutherford Appleton Laboratory [20] ten years later. Gain coefficient of $4.1\ cm^{-1}$ and gain-length product of 3.3 were achieved for the CVI $Balmer-\alpha$ transition at $18.2\ nm$. An similar improved experiment was conducted with driven laser of $2\ ps$, $20\ J$ using a $7\ \mu m$ diameter carbon fibre [21]. It demonstrated gain coefficient of $12.5\ cm^{-1}$ and gain-length product at 6. The line intensities of hydrogen-like ion $Balmer-\alpha$ and $Balmer-\beta$ lines as a function of plasma length are shown

in $Fig.\ 2.6$. The largest gain-length product achieved to date is $gl \approx 8$ using a carbon blade target [22, 23].

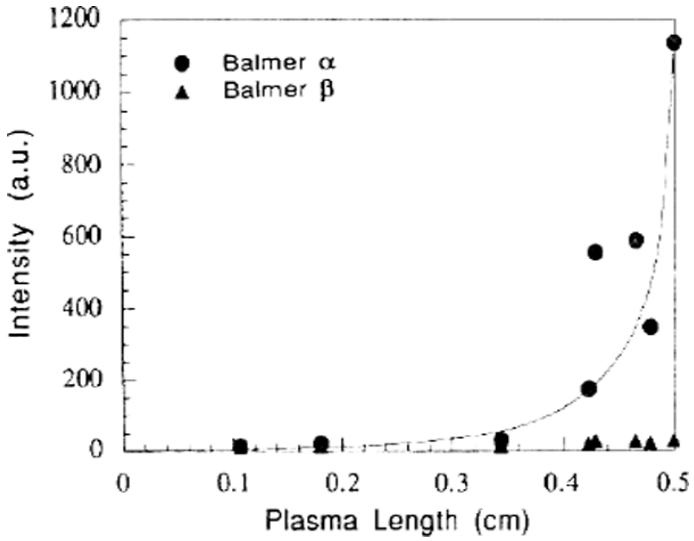

Figure 2.6: Intensity of $Balmer-\alpha$ (solid dots) and $Balmer-\beta$ (solid triangles) as a function of the plasma length. from [21]

2.3 Lithium-like ion recombination scheme

In 1978, Jaeglé with his group [24] found the population inversion in recombining aluminium plasma which was later identified as $3d-4f$ and $3d-5f$ transitions in lithium-like ions[15], as represented in $Fig.\ 2.7$ [25]. And soon Jamelot *et al.* [26]measured the gain coefficient as $1-2\ cm^{-1}$. This French group also pointed out the interesting aspects of this scheme: a) abundant in a large range of plasma densities and temperatures; b) helium-like ions emit an intense resonance line which could contribute to the plasma cooling; c) radiative decay between the two levels is very fast, hence, population of the lower level could reach very low value; d) ionization potential of the amplifying ion is lower for lithium like scheme than for any other, which means that this scheme requires a lower pumping power, for instance, $10^{12}\ Wcm^{-2}$ for $10\ nm$ lasing transition. Hara *et al.* [27] proposed a table-top lithium-like SXRL. Kawachi *et al.* [28, 29] performed a soft x-ray lasing experiment by irradiating 16 laser pulses ($80\ ps$ FWHM with $100\ ps$ separation) to a $3\ cm$ long aluminium slab target. Gain-length product of 4.2 and 4.5 for $15.4\ nm$line ($3d-5f$) and $10.5\ nm$ line ($3d^{'}4f$) were separately observed. Moreover, an enhancement by $1.8\ times$ of the $15.4\ nm$ lasing was achieved by adopting a multi-layer soft x-ray mirror placed at the end of plasma.

Although the recombination schemes inherently have many advantages, no saturation amplification has been demonstrated so far. The limitation is not merely caused by radiation trapping in the $2p-3d$ resonance line, because the detailed calculations show gain coefficient is not reduced too much when re-absorption is taken into account [30]. Even with stronger radiation trapping could not explain the effect consisting in gain coefficient growing gradually less when plasma length increases ($gl \approx 4-5$). Gain irregularities coming from non-uniform plasma irradiation, or possibly from plasma instabilities could, at

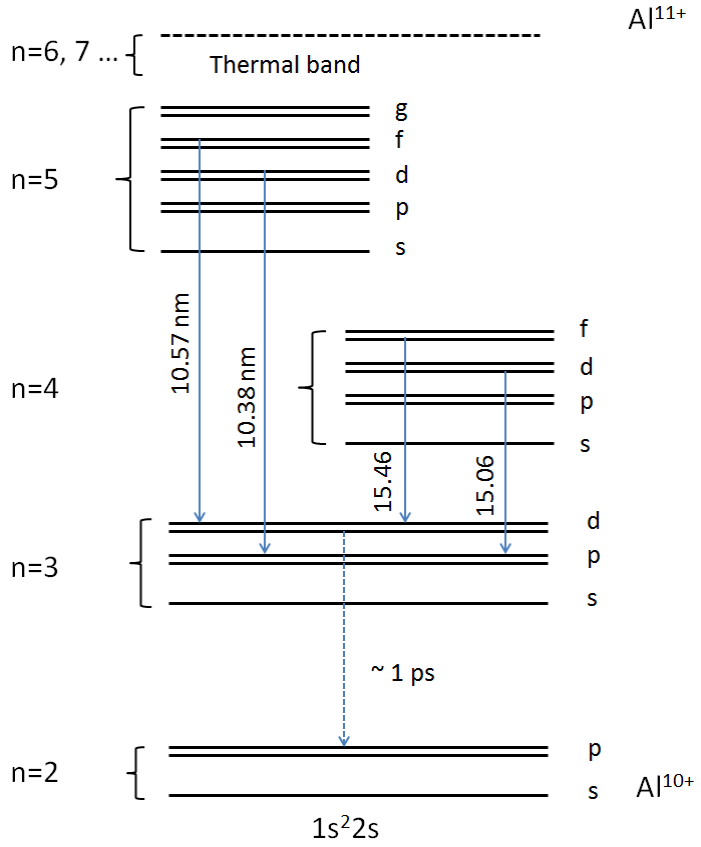

Figure 2.7: Atomic energy level diagram of Li-like ions for aluminium. The wavelengths of all the lasing lines are given in nanometers. from [25]

least partially, account for the drop of gain in longer plasmas. The non-uniformity of focal line, inherent to the geometrical aberrations of the focusing system, may also cause the gain decrease at longer plasma [32].

2.4 Optical-field-ionization recombination lasing in transition to ground state

ion An important advantage of the recombination scheme respected to the collisional excitation scheme (see **Section 5** in this chapter) is its rapid scaling to shorter wavelengths with low atomic number Z. Jones and Ali [33] firstly predicted that large transient gains could be generated in the $2-1$ transitions of H-like ions following recombination when plasma is totally ionized with low temperature. Within this concept, very short wavelength lines are able to be generated with a high quantum efficiency (QE), the ratio of the laser photon energy and the energy required to totally strip the atom, by moderating the ionization. $Fig.\ 2.8$ shows the simplified Grotrian diagram (a) and line wavelengths (b) of lasing transition for H-like ions under recombination scheme [34]. It is indicated that lasing at $13.5\ nm$ requires an initial plasma of totally stripped Li ions, while lasing at $3.37\ nm$ (so called "water window") can be obtained in

a C_{VI} plasma. For the first case, $QE = 0.45$, which is much higher than the lasing at $13.4\ nm$ based on the $3-2$ transition ($QE = 0.06$) in H-like N. This advantage allows the development of very short wavelength lasers with low excitation energy.

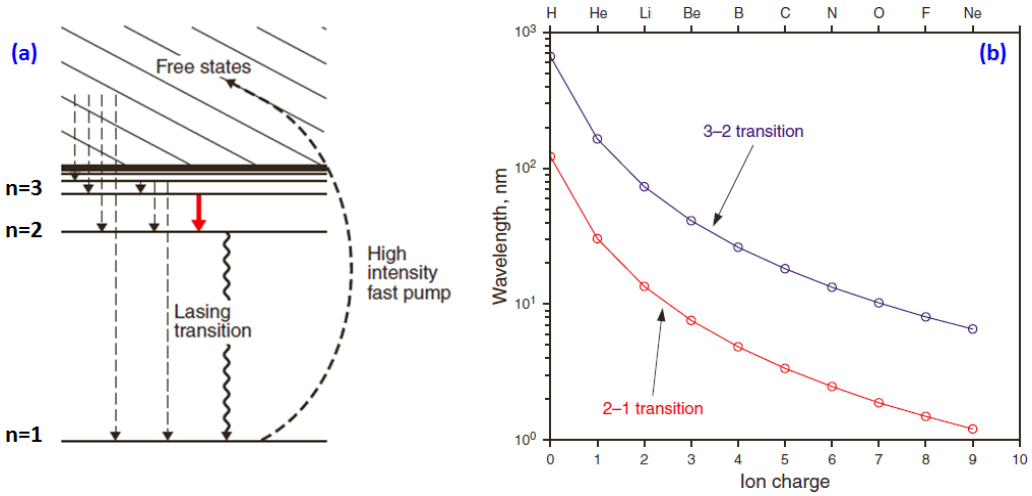

Figure 2.8: (a) Simplified Grotrian diagram with indication of lasing transition for H-like ions. (b) $3-2$ (blue line) and $2-1$ (red line) lasing transitions of H-like ions with recombination scheme. from [34]

However, in practical, for gain generation in H-like ions the atoms have to be totally ionized as the first step. Then, recombination has to be very rapid to allow for the large upper energy level population before the ground state ion level is significantly populated. Amplification in transitions to the ground state requires the generation of highly stripped ions in a plasma with low electron temperature ($\sim 10\ eV$) and high electron densities (in range of $10^{18} - 10^{20}\ cm^{-3}$ depending on nucleus charge Z). $2-1$ population inversion requires the ionizing pulse has to be very high intensity with very short duration, while for $3-2$ transitions, pulse duration can be much longer and its intensity much lower. In the early $1970's$, Peyraud *et al.* [35] suggested to use multi-photon ionization to produce a plasma of fully stripped ions and cold electrons on a time scale that is short compared to the recombination time. The initial experimental observations were demonstrated twenty years later [36, 37, 38] due to the powerful sub-picosecond lasers [39, 40, 41, 42] and understanding of above-threshold ionization (ATI) [43].

Based on this idea, optical-field-ionization (OFI) scheme using linearly polarized light was recognized [44] to create a cold plasma with highly stripped ions in which recombination can occur in sub-picosecond time scale. By means of this approach, the ultrashort wavelengths can be achieved. Electrons are compelled to return their quiver energy to the laser field within a linearly polarized laser pulse. This method can therefore create plasmas that are simultaneously highly ionized and cold in a time scale much shorter than recombination time. The first observation of amplification in an OFI plasma was demonstrated in the transition $2-1$ by Nagata *et al.* [36]. A linearly polarized pump pulse of $50\ mJ$, $0.5\ ps$ was longitudinally focused to an intensity of $1 \times 10^{17}\ cm^{-2}$ after the pre-pulse ($200\ mJ$, $20\ ns$) with a proper time delay. The $13.5\ nm$ lasing pulse, measured as FWHM duration $< 20\ ps$, was occurring about $20\ ns$ after the short pump laser pulse [45]. It indicated that the population inversion is not directly created by the short pump laser, but by collisional relaxation processes following collisional recombination. *Fig. 2.9* shows the measured lasing lines intensity variation with the plasma length, where a gain coefficient of $20\ cm^{-1}$ was obtained for $13.5\ nm$ line [46]. However, owing to the refraction

effect of propagating radiation in the plasma, the maximum amplification length was limited to about $2\ mm$, the resulting gain-length $gl \approx 4$. Similar results were obtained in the experiments conducted in Princeton [47] and Berkeley [48] using this method. An improvement experiment was carried out by performing a plasma waveguide in a LiF micro-capillary tube [37]. Plasma amplification length was increased to 5 mm,which is corresponding to $gl \approx 5.5$.

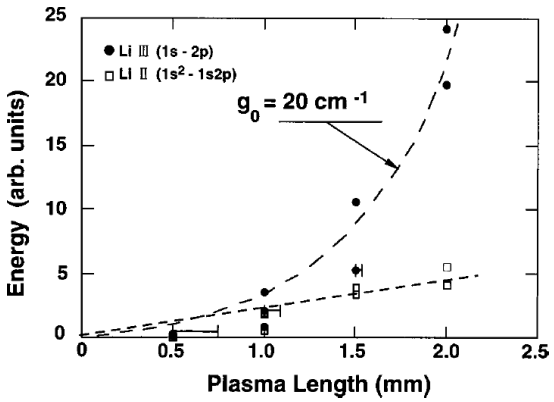

Figure 2.9: H-like Li 2-1 line in a recombination plasma pumped by OFI from [46]. Intensities of $13.5\ nm$ *(solid dots) and* $19.9\ nm$ *(hollow squares) lines as a function of plasma column length.*

Recent development on numerical model [49] predicted that high gain in the $2-1$ transition of recombining $LiIII$ ions can be achieved. This modelling takes into account several additional properties of OFI plasma, such as the non-Maxwellian nature of the plasma and its spatial distribution. This group even pushing this model to be feasible for achieving high gain in CVI ions in $2-1$ transition at $3.4\ nm$ by investigating the effects of different laser and plasma parameters [50]. Typical results are shown in $Fig.\ 2.10$, the H-like $C\ 2-1$ transition at $3.4\ nm$ line pumped by $50\ fs$ laser beam with diameter of $15\ \mu$m and $30\ \mu$m ($10^{19}\ W/cm^2$) as a function of time (gain time evolution in ps). Gain over $80\ cm^{-1}$ is expected in up to $2.5\ \mu$m and $6.0\ \mu$m in diameter for $15\ \mu$m and $30\ \mu$m (in diameter) pumping beams respectively, and lasing for $\sim 0.6\ ps$, which are very encouraging results. More recently, some preliminary experiment

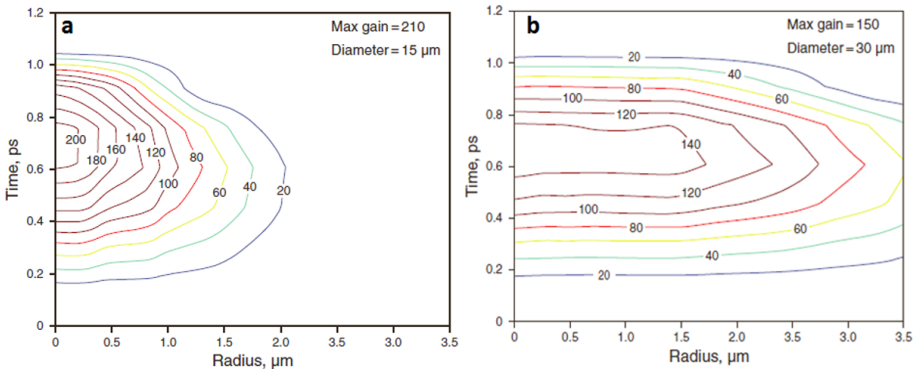

Figure 2.10: Gain map (in cm^{-1}*) for* $CVI\ 2-1$ *transition at* $3.4\ nm$ *with initial conditions of carbon density* $n_C = 10^{19}\ cm^{-3}$ *and hydrogen density* $n_H = 10^{20}\ cm^{-3}$ *with intensity* $I \sim 10^{19}\ W/cm^2$ *for OFI pumping beam diameters at (a)* $15\ \mu m$ *and (b)* $30\ \mu m$*. from [34]*

results of lasing on $2-1$ transition at $3.37\ nm$ from the OFI recombination plasma was reported [51],

as represented in in $Fig.\ 2.11$. The plasma was created by $100\ fs$, $200\ mJ$ pump pulse after a largely suppressed tens of picoseconds pre-pulse with a proper time delay. The effect of pump pulse duration, pre-pulse intensity and gas density on the lasing spectra has been investigated. Moreover, enhancement of this lasing at $3.47\ nm$ under OFI recombination scheme by employing a plasma waveguide was presented by the same team in the recent International conference of X-ray lasers (ICXRL2014) held in Colorado State University. However, no significant amplification from OFI recombination plasma has been demonstrated so far.

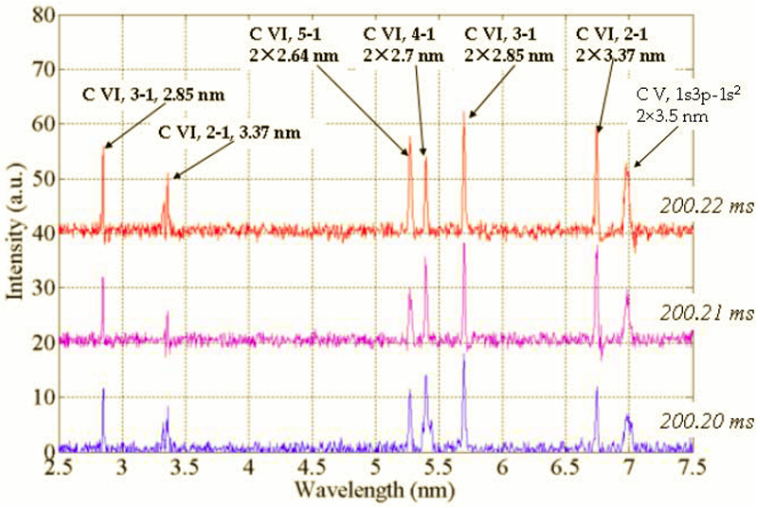

Figure 2.11: Carbon spectra of ethane plasmas created by $100\ fs$, $200\ mJ$ *pulse with suppressed pre-pulse for various initial gas densities. from [51]*

In general, the x-ray recombination scheme has been reported to generate amplification at wavelengths as short as $3.4\ nm$ with laser excitation energies of only $200\ mJ$. The x-ray recombination scheme requires relatively low pumping power with respect to collisional x-ray laser schemes (summarized in a later section). This combined with the high quantum efficiency achieved by transition to the ground state, makes the creation of a truly tabletop SXRL in "water window" ($2.2 - 4.4\ nm$) become more appealing. However, It has suffered the problem of not scaling adequately with plasma column length, the maximum gain-length product was obtained as 8 [22]. In the term of SXRL applications, the recombination schemes should be firstly developed to achieve the amplification saturation.

2.5 Inner-shell photoionization

The generation of large population inversions following the selective x-ray photoionization of inner shell electrons was originally proposed in 1967 [52]. The idea is based on the fact that cross section for photo-ionization of atom ot ion in deeper states can be larger than for more shallow state. In principle, recombination SXRL is based on a process of plasma relaxation which follows very rapid heating of cold matter, lasing in inner-shell transitions of ions should occur near the peak of plasma temperature. The very short heating phase generates free electrons associated with a distribution of inner-shell vacancies formed in ions. As a consequence, lasing can occur between highly populated level and inner shell

vacancies before equilibrium restoration. SXRL based on inner shell transitions in atoms and ions are very attractive for generating gain in compact systems at wavelengths in order of $1\ nm$ and below [53, 54]. Simplified energy level diagram of the K_α Ne laser is illustrated in $Fig.\ 2.12$. The filtered x-rays primarily

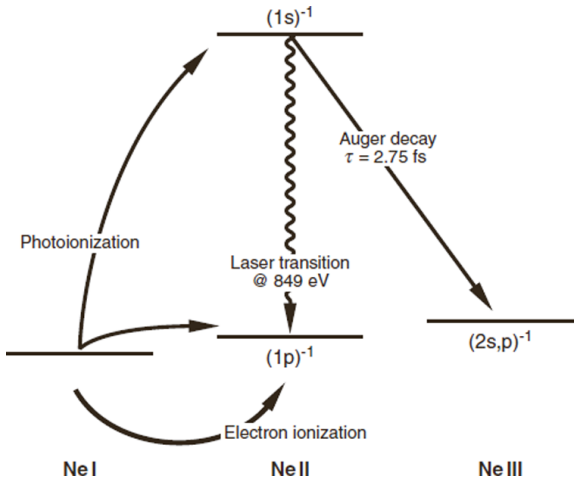

Figure 2.12: Simplified energy level diagram of inner-shell photoionization laser in the K_α transition of Ne at $1.46\ nm$. from [46]

photoionize the inner shell electrons to the upper level $(1s)^{-1}\ ^2S$ producing the population inversion respected to the lower level $(2p)^{-1}\ ^2P$ in $NeII$. While rapid Auger decay with a rate of $(2.75fs)^{-1}$ dominate the depopulation of upper level $(1s)^{-1}\ ^2S$. However the self-terminating life time is not the main limit of the gain duration, but the electron collisional ionization of natural neon atoms dominates this process. These two effects restrict the high gain and its duration. In another hand, the SXRL from inner shell photopumping is intrinsically ultrashort. Kapteyn [53] proposed to use travelling-wave excitation by a $10\ J$, $50\ fs$ pump laser for generating lasing in the K_α transition of NeI at $1.46\ nm$. A specific target of thin beryllium foil with a frozen mix of Ne-H on the other side was suggested. The beryllium would act as an absorber for low energy x-rays which are capable of producing outer-shell ionization, and also separates the hot x-ray emission region from the laser region, so that thermal ionization of Ne does not take place. Hydrogen would be used as an electron moderator in the lasing material to suppress electron collisional ionization. In addition, inner-shell lasing in C at $4.5\ nm$ with gain coefficient of $10cm^{-1}$ and a quite large gain-length product was predicted [48, 55] using a driven laser with the order of $1\ J$ energy. Recently , an very interesting study on generating femtosecond SXRL pulses at saturation from inner shell transition was reported [56], saturation regime was experimentally achieved by using PW-class laser accelerated electron bunches.

Thanks to the recent development of x-ray free-electron-laser (XFEL) [57, 58, 59], fast and intense x-ray sources are sufficient for the inner shell photo-ionization scheme in the x-ray regime. More recently, detailed calculation for neon pumped by XFEL radiation was presented [60] and followed by the experiment [61], as shown in $Fig.\ 2.13$. The XFEL beam was focused into a gas cell filled with neon to a focus spot of radius $1-2\ \mu$m. A flat-field x-ray grating was placed ∼4 m from the interaction region. Population inversion of the $1s^12s^22p^6$ to $1s^22s^22p^5$ transition was created by K-shell photo-ionization of neutral neon. Gain coefficient of $61-70\ cm^{-1}$ due to this inner-shell transition $(1.46\ nm)$ was achieved. Owing to the strong absorption of XFEL, the gain coefficient decreases as a function of propagation

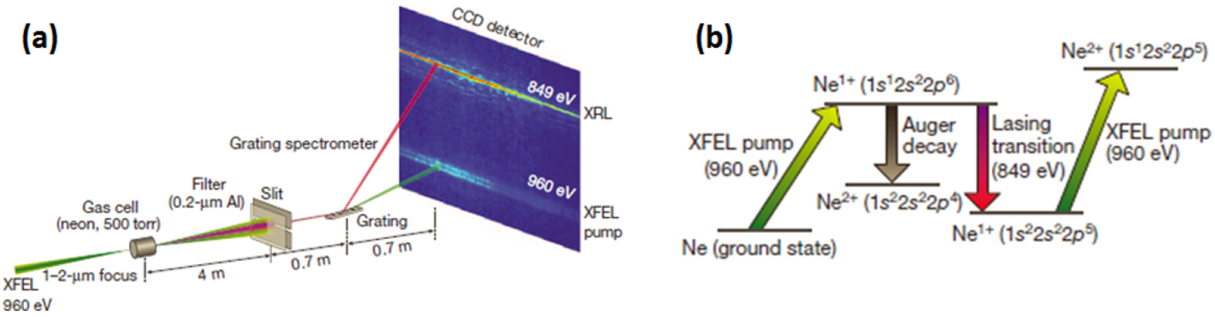

Figure 2.13: (a) Schematic diagram of experimental setup for K-shell photo-ionization of neutral neon producing lasing at $1.46\ nm$*. (b) Illustration of the simpled energy level scheme. from [61]*

depth, with a calculated decay length of 0.28 cm. With consequent, gain-length product was estimated as $gl = 17 - 19.3$. Measured output parameters of this neon SXRL by inner-shell pumping showed that single-shot energy is $1.1 \pm 0.4\ \mu J$, angular divergence of $1\ mrad$ and estimated peak brilliance reaches $4 \times 10^{29}\ photons\ s^{-1}\ mrad^{-2}\ mm^{-2}$ within a relative spectral bandwidth of 0.1% according to the predicted pulse duration of $5\ fs\ FWHM$ [60].

2.6 Electron collisional excitation pumping scheme

2.6.1 Atomic physics of SXRL by collisional pumping

Achieving high gain in a x-ray plasma amplifier is very desirable in the pursuit of SXRL sources. At present, all the SXRL that achieve very large brightness and saturated emission are electron collisional pumped lasers. The collisional electron excitation pumping scheme was firstly proposed in 1970s [62, 63, 64, 65, 66]. Principally, this SXRL scheme is due to the plasma free electrons of population inversions between multi-charged ion excited levels, which basically requires plasma densities a little larger than $10^{20}\ cm^{-3}$ and temperatures of a few hundreds eV [67]. The first successful observation of lasing at SXRL wavelengths utilizing this approach was demonstrated at Lawrence Livermore National Laboratory involved with the $3p - 3s$ transitions in neon like (Ne-like) Se [68] and Ne-like Y [69].

Ne-like, nickel like (Ni-like) and palladium like (Pd-like) ions have fully occupied outer shell (closed shell) of principal quantum number $n = 2$, $n = 3$ and $n = 4$, respectively, haven been successfully observed lasing with collisional excitation pumping. Schematic energy level diagrams for Ne-like, Ni-like and Pd-like quantum states involved in lasing are shown in $Fig.\ 2.14$ [70], lasing occurs between excited sub-shells $2p^5 3p \rightarrow 2p^5 3s$ (Ne-like), $3d^9 4d \rightarrow 3d^9 4p$ (Ni-like), $4d^9 5f \rightarrow 4d^9 5d$ (Pd-like) or $4d^9 5d \rightarrow 4d^9 5p$ (Pd-like). The upper level is predominantly excited by direct elect impact collision from the ground state of the each ion stage of interest, and it is metastable to decay to the ground state as the transition is electric dipole forbidden. However, the lower laser level can decay rapidly and directly to the ground state via the resonance dipole transitions $2p^5 3s \rightarrow 2p^6$ (Ne-like), $3d^9 4p \rightarrow 3d^1 0$ (Ni-like), $4d^9 5d \rightarrow 4d^1 0$ (Pd-like) or $4d^9 5p \rightarrow 4d^1 0$ (Pd-like).

Due to the higher QE, ratio of the laser photon energy to the energy of the upper laser level above the ground sate, lasing at shorter wavelengths have been observed with Ni-like ions [71, 72, 73, 74, 75]. More SXRL lasing lines in different wavelengths from Ne-like, Ni-like and Pd-like as a function of atomic

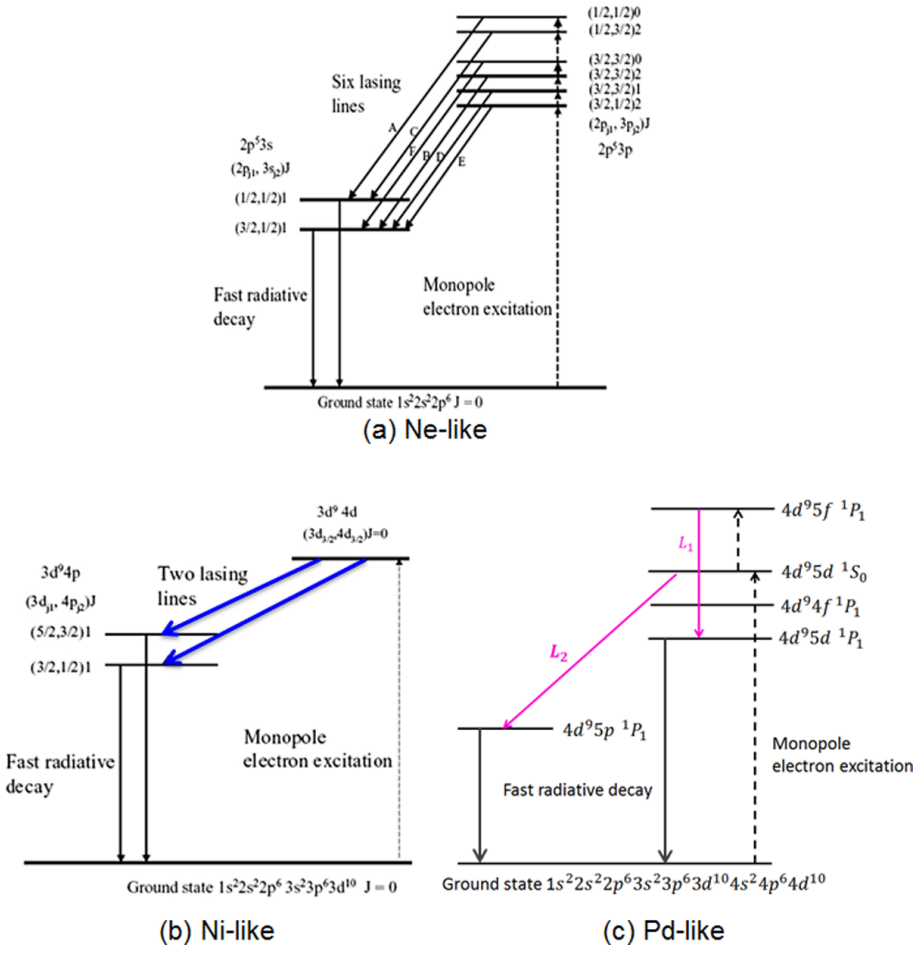

Figure 2.14: Simplified Grotrain diagram of (a) Ne-like, (b) Ni-like and (c) Pd-like ions. The Ne-like lasing lines are designated A-F following the nomenclature that A is the most intense lasing line. from [70]

number of the target material are demonstrated in the $Fig.\ 2.15$. In the simplified Grotrain diagram of Ne-like ions, the lasing lines are designated A-F following the nomenclature that A is the most intense lasing line. Therein, line A and F are shortly called as $J = 0 - 1$ line, line C, B and E are called as $J = 2 - 1$ line, and line D is $J = 1 - 1$ line. Lasing with shorter wavelength in the collisional scheme requires high-Z materials for plasma amplifier creation.

Because of the closed shells of principal quantum number $n = 2, n = 3$ and $n = 4$, Ne-like, Ni-like and Pd-like ions are stable to further ionization over a wide range of electron temperature ($100\ eV - 1\ keV$). This stability guarantees a large fractional abundance of Ne-like, Ni-like and Pd-like ions in the laser induced plasma. As it represented in $Fig.\ 2.16$, ion abundance as a function of the electron temperature for tin plasma [12] and tungsten plasma [76] respectively. It means that lasing ions are dominant species inside the plasma promising the aim of extracting high amount of energy from SXRL plasma amplifier.

McWhirter criterion [77] for local thermodynamic equilibrium (LTE) between two quantum state levels is written as

$$N_e \geq 1.9 \times 10^{16} {T_e}^{1/2} E_{ul} \quad cm^{-3}, \tag{2.11}$$

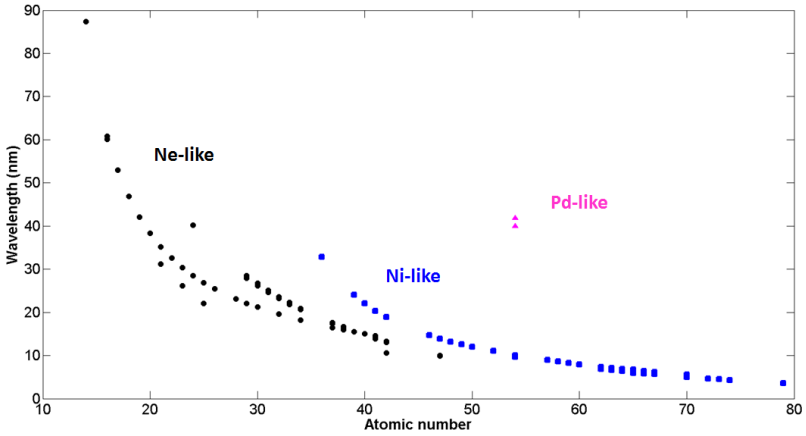

Figure 2.15: Lasing wavelengths by collisional pumping scheme from Ne-like (black dots), Ni-like (blue squares) and Pd-like (pink triangles) ions as a function of atomic numbers. data from [12]

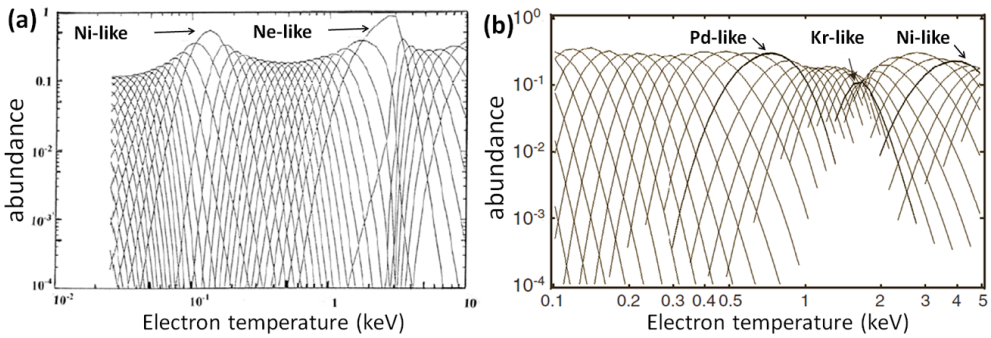

Figure 2.16: Ion abundance as a function of the electron temperature for (a) tin plamsa from [12] and (b) tungsten plasma from [76].

where N_e is the electron density measured in cm^{-3}, T_e is the electron temperature measured in eV and E_{ul} (in eV) is corresponding to the energy difference between the upper and lower levels. It implies that x-ray laser transitions of approximately 100 eV should be in equilibrium at densities greater than approximately $4 \times 10^{19}\ cm^{-3}$ for electron temperature $\sim 500\ eV$. However, in the SXRL collisional excitation pump scheme, population inversion is created by the rapid monopole excitation coupled with the lack of a compensating rapid decay rate back to the ground sate. The McWhirter criterion is not valid for calculating the proximity to LTE between the ground and upper lasing level because radiative decay to the ground is fundamentally forbidden. Instead of that, the relative population densities can be calculated by considering the relevant populating and de-populating collisional and radiative process. The population inversion happens between the upper and lower levels when the collisional excitation rate R_{gu} from ground state to the upper level is sufficiently high, which is described as [70]

$$R_{gu} = N_e N_i K(g,u), \tag{2.12}$$

where N_e and N_i is the free electron density and density of ions in ground state respectively. $K(g,u)$ is the monopole excitation rate coefficient which is given by

$$K(g,u) = 1.58 \times 10^{-5} \gamma_{gu} e^{-E_{gu}/T_e} / (E_{gu}\sqrt{T_e}) \quad cm^3 s^{-1}. \tag{2.13}$$

Here, the energy difference E_{gu} between the upper level and ground state and electron temperature T_e are measured in eV. γ_{gu} is varying slowly by the electron temperature and not too rapidly with atomic number Z [78].

2.6.2 Quasi-steady-state (QSS) pumping

The pioneering SXRL experiment on Ne-like selenium was demonstrated with an exploding foil target using several kJ driven laser energy delivered from glass laser system [68]. SXRL significant amplification of this experiment encouraged many experiments carried out using a smaller pumping laser system. Soft x-ray lasing in Ne-like germanium was then observed using solid slab target irradiated by a $600\ J$, $2\ ns$ glass laser [79]. From then on, the germanium laser coupled with the solid slab target technique became popular worldwide. However, the hydrodynamic time-scale is $\sim 100\ ps$ (variation in Electron density N_e and temperature T_e and atomic process in lasing ions are mostly in the range of $1-10\ ps$. Pumping with nanosecond to sub-nanosecond laser, SXRL plasma population inversion reaches LTE. This popular technique is so called Quasi-steady-state (QSS) pumping scheme.

In early work, the gain of different lasing lines corresponding to $Fig.\ 2.10$ have been predicted theoretically. For Ne-like ions, the $J=2-1$ and $J=0-1$ lines are pointed out in $Fig.\ 2.17$ and $Fig.\ 2.18$, respectively [80]. Population inversion is decreased at larger electron density owing to collisional mixing between levels. Gain coefficient of the lasing lines are varying with the atomic numbers. Meanwhile, Rosen *et al.* predicted that the gain of the $J=0-1$ transition is much higher than that of the $J=2-1$ transition via $3p-3s$ transitions in Ne-like selenium[69]. Hydrodynamical simulation results showed the scaling law for gain coefficient as a function of plasma electron density [81]

$$g \propto n_e \lambda / Z_i \quad . \tag{2.14}$$

Here, Z_i is the lasing ion charge and the lasing lines are dominated by Doppler profile. Taking into account the relations between λ and Z_i for $J=0-1$ and $J=0-2$ line, the scale relations can thus be written as

$$\begin{aligned} g &\propto n_e \lambda^2 \quad for \quad J=0-1 \quad lines \quad , \\ g &\propto n_e \lambda^{3/2} \quad for \quad J=0-2 \quad lines \quad . \end{aligned} \tag{2.15}$$

It shows that lasing at shorter wavelength requires higher plasma density to reach the same gain. In consequent, the plasma refraction effects on SXRL operation should be expected to increase at short wavelength. In addition, a crucial point of QSS collisionally pumped SXRL physics lies in the relation between the intensity of driven lasers and the wavelengths of lasing lines as [81]

$$I_{pump} \propto \lambda^{-4} \quad . \tag{2.16}$$

Therefore, with the single pumping pulse focused on to the lasing material, any process toward shorter laser wavelength will require a huge increase of pump intensity.

During the first ten years after the initial significant observation of SXRL [68], many efforts had been made for lasing of the transition $J=0-1$ [68]. However, this lasing line was unexpected low. Eventually, this issue was figured out when the simulation showed some aspects of the role played by pre-pulses [84], as illustrated in $Fig.\ 2.19$. It is apparent that pre-pulse reduces the steepness of the plasma density gradient. Consequently, the reducing of the laser beam trajectory curvature enhances

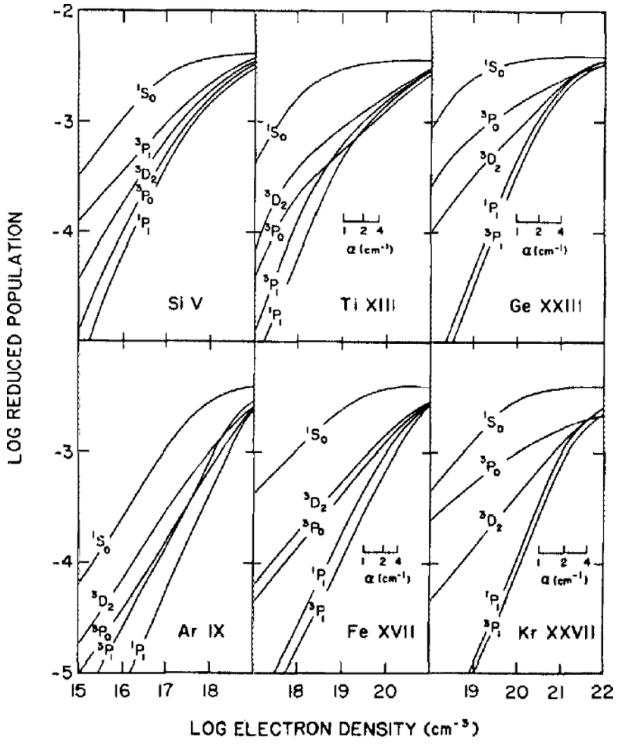

Figure 2.17: Level populations of Ne-like ions referred to the density number of these ions as a function of the electron density. The corresponding lasing lines are represented in $Fig.$ 2.14. from [80]

the travelling length in the narrow gain region of the plasma. Within the relaxed pre-plasma, radiation of the main pulse laser penetrates more deeply than it could do in the immediately dense plasma created by single-pulse scheme. In fact, the simulation has showed three benefits of pre-pulse pumping: a) an enhanced absorption of the main pulse energy during the earlier time of plasma expansion; b) an increase of the gain zone volume; c) a relaxation of electron density gradients.This idea was soon proved by sending small pre-pulse before the main pumping pulse [83, 82]. The controlled pre-pulse for producing pre-formed plasma makes the enhancement of the $J = 0 - 1$ lasing line.

Besides the pursuit of shorter wavelength, another aim is to push this SXRL source reaches saturated amplification. While the single flat slab target has a limitation in gain-length product due to the x-ray refraction caused by the electron density gradient in the SXRL plasma [85]. Many experiments were following up to improve the SXRL plasma amplifier to reach saturated amplification. First of all, the group at Osaka University in collaboration with the Irish group has demonstrated curved slab target, which was original proposed by Lunney [86], as it shown schematically in $Fig.$ 2.20 [87]. Within this refraction compensation for controlling x-ray laser beam propagation in the amplifying plasma, the intensity of $J = 0 - 1$ line at $19.6\ nm$ was $10\ times$ stronger than that with slab target.

Secondly, in this experiment, there was a x-ray mirror employed playing the role of half cavity to achieve double-pass plasma amplifier. This half-cavity configuration was initially performed by the French group [88, 89, 90]. Sequentially, multi-target configuration coupled with refraction-compensated pumping scheme achieved remarkable progress [73, 74, 91]. In $Fig.$ 2.21, saturated amplification Ni-like SXRL including samarium at $7.3\ nm$ was represented [74]. Plasma amplifier were generated by irradiating

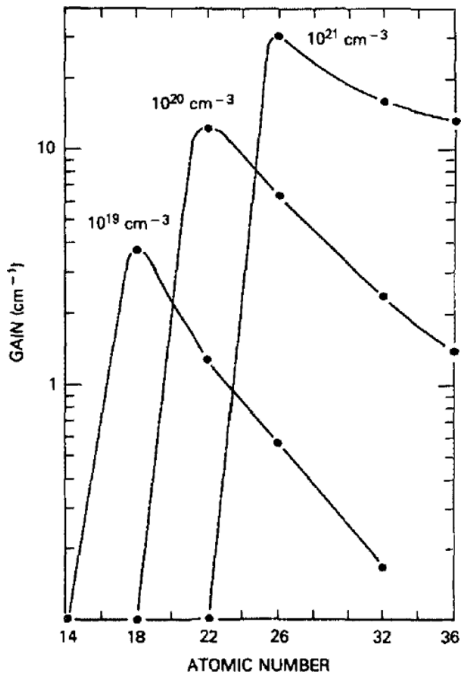

Figure 2.18: Gain coefficient of Ne-like $J = 0 - 1$ line calculated as a function of the atomic number for three electron densities. The electron temperature is defined one-half the ionization potential. from [80]

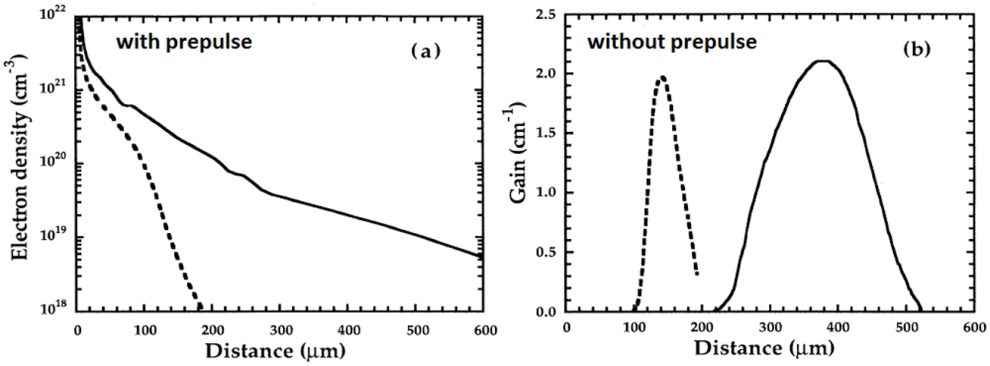

Figure 2.19: Electron density and gain coefficient distribution along the distance from target surface (a) with and (b) without pre-pulse. from [84]

three-pulse (with proper time delays) on the slab target surface with line focus. The pumping systems of the double plasma amplifiers were designed in 180^o opposition to generate opposed density gradient between each other, which is dedicated to compensate the refraction of the x-ray beam propagation in the plasma column. The coupling efficiency at the optimized separation was quite high because of small deflection and divergence angles. The gain coefficient was observed as $8.4cm^{-1}$. Output intensity no longer increases exponentially with target length longer than 18 mm, which corresponds to a gain-length product of 16, as illustrated in $Fig.$ 2.22. A saturated samarium x-ray laser beam has been demonstrated with an output energy of 0.3 mJ in 50 ps. Another interesting experiment was conducted with main pumping pulse of 140 J in 100 ps [91]. Gain coefficient of 19 cm^{-1} was inferred and saturated operation

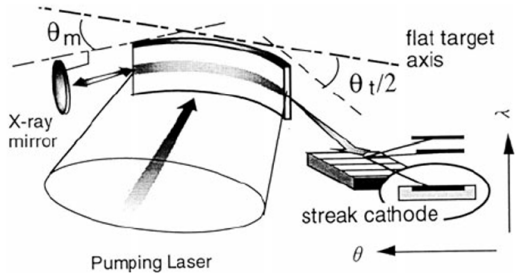

Figure 2.20: Schematic diagram of curved slab-target for compesentation of refraction effect. The notation t and m are the target bending angle and the angle of the mirror normal to the flat target axis. from [87]

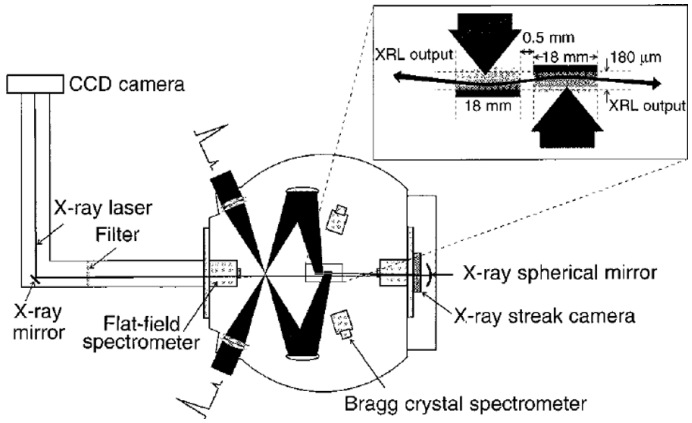

Figure 2.21: Schematic diagram of the saturated Ni-like SXRL experiemnt. from [74]

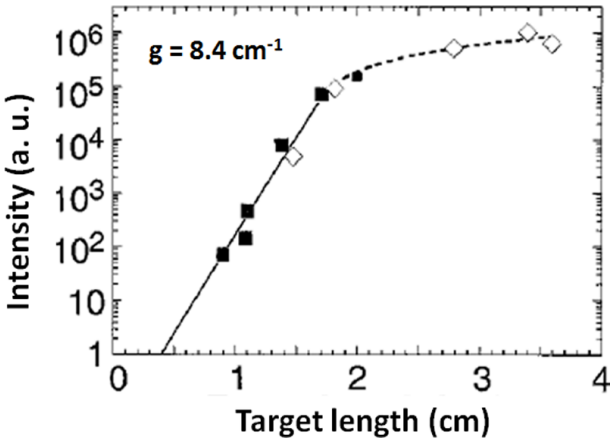

Figure 2.22: Peak intensities of nickel-like samarium x-ray laser as a function of target length. from [74]

ha been achieved with an 8-mm long plasma. $Fig.$ 2.23 shows the Saturated silver SXRL (13.9 nm) intensity and divergence as a function of the plasma amplifier length.

In order to increase the intensity and optical quality of the x-ray laser beam, a double-target with quasi-travelling-wave excitation technique was investigated. As demonstrated in $Fig.$ 2.24, the time- and

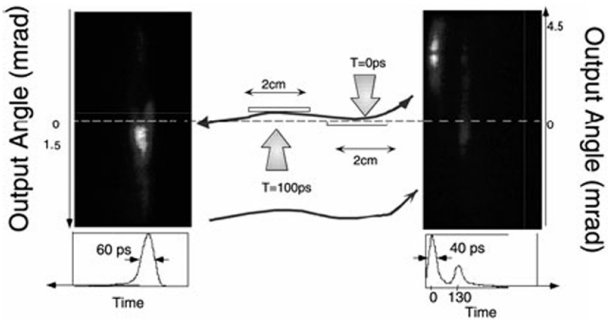

Figure 2.23: Temporal and angle-resolved profiles of a double-target $13.9\ nm$ *SXRL. The emission is in the left and backward emission is at right. from [91]*

angular-resolved spectra of the lasing line in the forward and the backward direction of the quasi-travelling wave pumping are compared. A weak increase of $10-20\%$ has been observed in the quasi-travelling wave direction, while the spatial as well as the temporal profiles of the lasing signals in both directions appear very different. This point is probably due the overlap of the double-target x-ray laser signal and the one coming only from the second target. More detailed discussion about this double-plasma configuration will be discussed in Chapter 3. Furthermore, after realizing the pre-pulse influence on pumping, SXRL saturation were achieved in a wide range of ions: Ne-like Zinc [92, 93, 94, 95], Germanium [96, 97, 98], Selenium [82], Yttrium[99] and Ne-like low Z elements[84, 101, 102, 103, 104, 105, 106], as well as Ni-like Tin [107], Samarium [74], Dysprosium [72], Palladium [108] and Silver [109], as represented in $Fig.\ 2.15$.

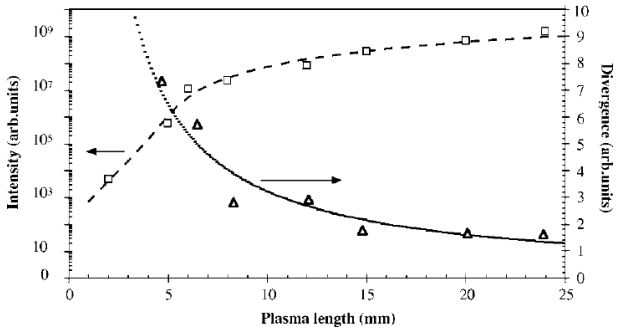

Figure 2.24: Saturated silver SXRL ($13.9\ nm$*) intensity and divergence as a function of the plasma amplifier length. from [91]*

In general, the pre-pulse pumping technique opened the way to shorter wavelength lasers (down to the "water window"). It is capable to reach SXRL saturated amplification within plasma length $1-2$ cm under the QSS pumping scheme. Maximum gain coefficient has been obtained is $\sim 18\ cm^{-1}$ [91]. Typical output of the SXRL from double-plasma amplifiers is $0.3\ mJ$ with pulse duration $\sim 50\ ps$. With respect to the pumping laser energy at the order of $100\ J$, the efficiency of this SXRL pumping scheme is extremely low. Refraction influence plays an important role in the plasma column at level of centimetre long. In term of the SXRL application, it is mandatory required to develop a more compact and higher efficient pumping scheme.

2.6.3 Transient collisional excitation (TCE) pumping

A novel two-step collisional pumping scheme with specific drive-pulse configuration was firstly proposed by Afanasiev and Shlyaptsev [110], which pointed out that gain coefficient could reach $1-2$ orders of magnitude larger than those obtained for the same transition in the QSS pumping scheme. This new pumping scheme is based on the difference between the population inversion lifetime (a few tens of picoseconds) and the ionization time (hundreds of picoseconds). Using a long pulse ($0.1-1\ ns$) of moderate energy to ionize the plasma at or slightly below the lasing ionization stage (population inversion is not created). Then an intense short pulse ($1-10\ ps$) so rapidly overheats the ions and free electrons ($0.5-1\ KeV$). The ions are reaching the lasing ionization stage (such as Ne-like, Ni-like and Pd-like), while the stimulated electrons are colliding with the lasing ions induce very strong pumping. As illustrated in $Fig.\ 2.14$, the bounded electrons stay at the ground state are rapidly collisional pumped to the upper level induce the abrupt increase of collisional-excitation rate. Owing to the fast decay time between the lower level and the ground state. During a short time of several picoseconds, the ions are not over-ionized placing the plasma very far from thermal equilibrium, and the transient population inversion can achieve extremely strong level with gain coefficient of $\sim 100\ cm^{-1}$. This improved regime is so called transient collisional excitation (TCE) pumping scheme.

This interesting pumping technique was firstly performed in the Ne-like titanium SXRL experiment demonstrated in the $Fig.\ 2.25$ [111, 112]. Two synchronized beams, delivering $1\ ns$ and $1\ ps$ pulses respectively, irradiating on the titanium slab target with various line focus lengths of $2\ mm$, $3\ mm$ and $5\ mm$. Time delay between the long ($1\ ns$) and short pulse ($1\ ps$) is $1\ ns$. It is interesting to note that both pulses energy are only several joules, which is much lower than the pumping energy required in QSS scheme (discussed in last section). Pumping laser intensity for long pulse and short pulse are $10^12\ W/cm^2$ and $10^15\ W/cm^2$ respectively. Gain coefficient deduced from a fit of experimental data on Lindford formula [113] was found to be $\sim 20\ cm^{-1}$ and gain-length product of 9.5. As illustrated in $Fig.\ 2.26$, the effective

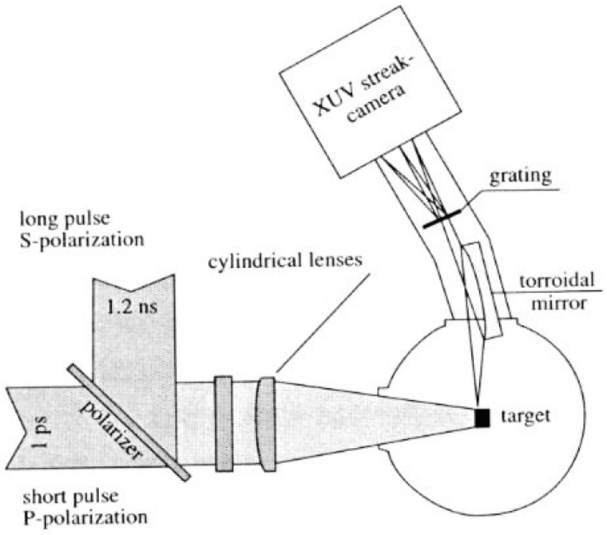

Figure 2.25: Schematic diagram of the experiment setup used to produce a TCE Ne-like plasma of titanium. from [111]

differential gain coefficient g_{eff} has values $\sim 100\ cm^{-1}$ at the shorter plasma length $L < 1\ mm$ and then

decreases to $\sim 10\ cm^{-1}$ at the exit of laser amplifier $L = 5\ mm$. Moreover, this lasing line at $32.6\ nm$ was confirmed as pulse duration of less than $20\ ps$. This breakthrough pumping technique attracts much attention of compact, intense SXRL source development [114, 115, 116, 117, 118] with the attractive properties: a) population inversion can occur at arbitrary electron density and it increases with larger electron density, (b) gain coefficient is much higher than the QSS and recombination pumping schemes, (c) there are no restrictions to an active media dimension, (d) pumping laser energy requirement are impressively low.

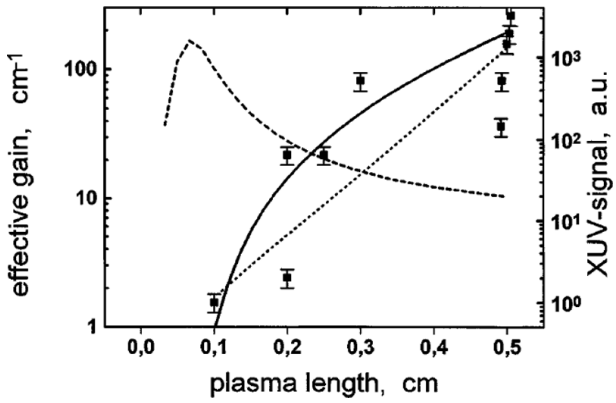

Figure 2.26: Lasing of the $3p - 3s$, $J = 0 - 1$ transition in Ne-like titanium at $32.6\ nm$ and effective gain as a function of plasma length: experimental results (solid squares), Linford formula fit of the data with $g = 19.4\ cm^{-1}$ (dotted line), RADEX calculated signal intensity (solid line) and calculated effective gain based on Linford fitting of RADEX calculated intensity (dashed line). from [112]

However, in the previous TCE pumping plasma experiment [112], laser saturation was not achieved. Note that the gain region had a very small lateral extension and it was characterized by a steep density gradient. The amplification is very sensitive to the plasma inhomogeneities and refraction. A modelling [119] addressed to this experiment provided some explanation. It demonstrated that the transient nature of the gain is due to the ionization balance in the plasma, where electron collisional excitation dominates rather than ionization because of the short period. Time delay between the pre-pulse and main short pulse plays a significant role in optimum density for short pulse heating the plasma. It also pointed out that beam propagation in the high gain and low gradients plasma region can actually contribute to the enhancement of the output SXRL. Moreover, as a matter of fact, the TCE pump configuration leaves unsolved the difficulty of fitting a short population inversion lifetime ($\sim 10\ ps$) to the propagation time of the amplified SXRL beam ($3.3\ ps/mm$). It limits the effective length of the laser because propagation partially occurs in a non-amplifying medium. This behaviour becomes to be obvious when the plasma length increases. However, this problem can be resolved using a travelling wave to the stationary lighting of the target by the short pulse, this technique is so called travelling wave (TW) implementation.

The purpose of TW excitation is to match the propagation of the ASE along the plasma column to the speed of light c. Two typical approaches have been worked out using a multi-segment stepped mirror and diffraction grating, which are described in $Fig.\ 2.27$ and $Fig.\ 2.28$, respectively. For the n steps mirror configuration illustrated in $Fig.\ 2.27$, the pump pulse turns out divided in to n temporally and spatially separated pulses arriving on the target surface. In order to get a continuous travelling wave along the target length L, the specific condition has to be met that light propagation time over each step should be

shorter than the pump pulse duration τ, therefore

$$\frac{L}{n}\frac{1}{c} \leq \tau. \tag{2.17}$$

For example, for the target length $L = 6\ mm$, the pump pulse duration τ should be longer than $5\ ps$ when

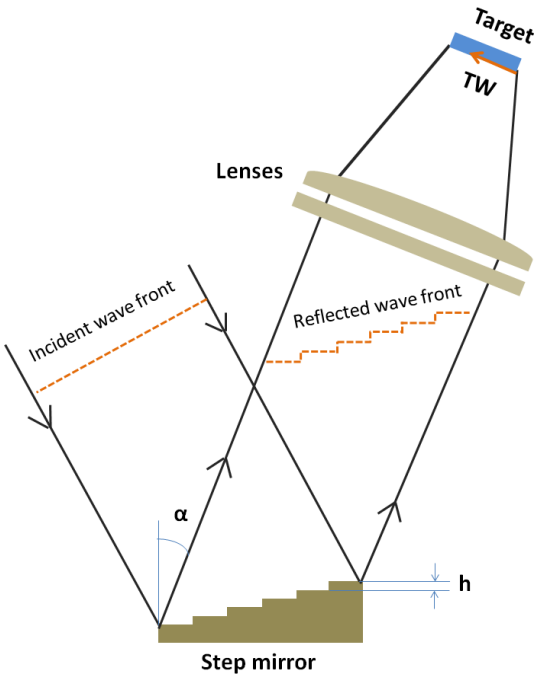

Figure 2.27: Traveling wave produced by a multi-step mirror.

using a 4-segment stepped mirror. On the other hand, when $\tau < 5\ ps$, only part of the pumping laser beam reflected from the stepped mirror will be useful for the plasma heating. Increasing the step number of the stepped mirror shows the way to reduce the pump pulse duration, however, it increases risk of optical damage by the beam diffraction from the step edges. Another technique by using a diffraction grating offer a flexible approach for the travelling wave pumping, as shown in $Fig.$ 2.28. Travelling wave velocity υ_{TW} related to the diffraction angle α can be written as [120]

$$\upsilon_{TW} = c/tan\alpha, \tag{2.18}$$

which indicates that the travelling wave velocity is faster than the light velocity when the diffraction angle is smaller than 45^o. Many efforts have been made to find out the optimal travelling wave velocity [121, 117]. A quasi-travelling wave pumping technique with a 6 steps mirror has been demonstrated by Kawachi *et al.*, as described in $Fig.$ 2.29. The step mirror has six steps with difference of 600 μm in the level and each step is corresponding to $1.2\ mm$ length in the line focus with time separation of 4 ps. Gain saturation was achieved for Ni-like silver x-ray lasing at 13.9 nm, and the gain coefficient was estimated to be $35\ cm^{-1}$. With the benefit of TW pumping technique, more saturated amplification have been observed under the TCE scheme using the solid target [118, 121, 122, 123] as well as gas-puff target [124, 125]. It is interesting to note that electron collisional excitation type Pd-like ion scheme using the optical OFI have achieved saturated amplification [126, 127] with $10\ Hz$ repetition rate. The saturated

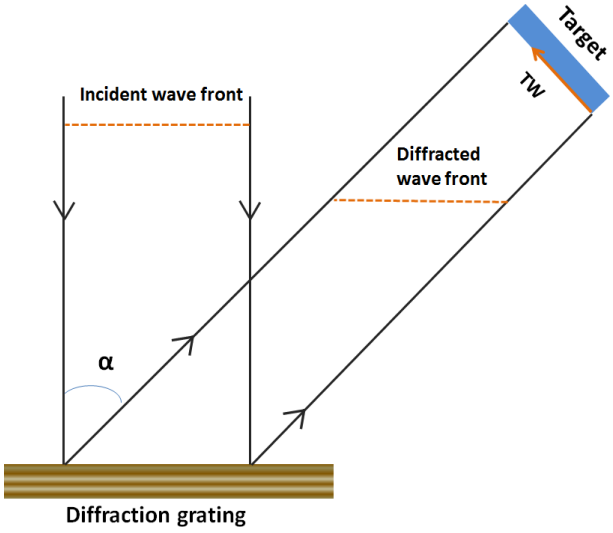

Figure 2.28: Traveling wave produced by diffraction on plane grating.

amplification SXRL provide the highest peak brightness x-ray source at present. In the seek of various SXRL applications, this level of lasing pulse is quite important not only for the photon flux but also for the beam quality.

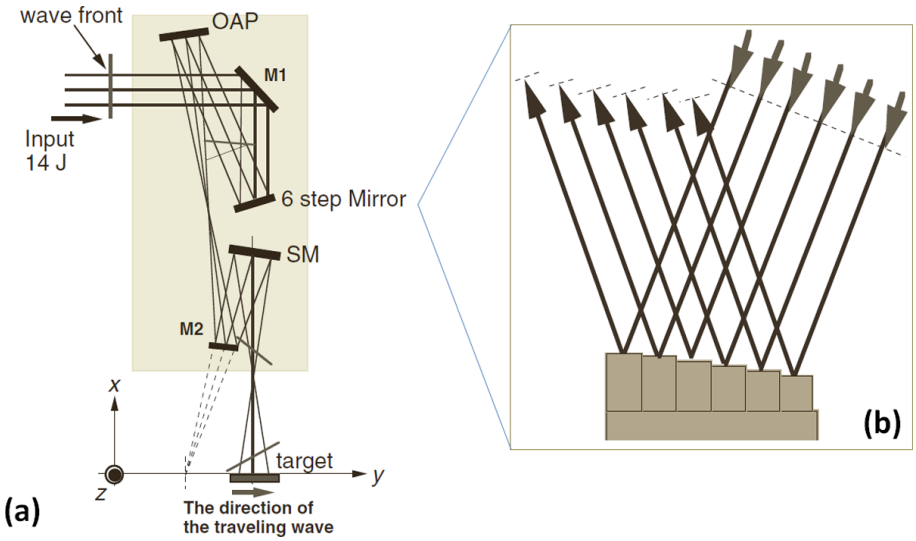

Figure 2.29: (a) Schematic diagram of the line-focus system, where step mirror for the TW pumping, an off-axis parabolic (OAP) mirror and a spherical mirror (SM) are contributed to the line-focusing. (b) An inset illustrqtion of the 6-step mirror for TW pumping. from [128]

Rapid progress towards much lower pump threshold was achieved using more appreciate pumping incidence angle [129]. It demonstrated a $10\ Hz$ Ni-like Molybdenum $4d-4p$ x-ray laser operating at $18.9\ nm$ pumped with $10\ mJ$ long pulse $(200\ ps)$ and $80\ mJ$ short pulse $(8\ ps)$. The novel pumping geometry is illustrated in $Fig.\ 2.30$, a long pulse $(200\ ps)$ line-focused on a slab at normal incidence performs a plasma column to create a tailored density profile. Sequentially, with a certain time delay, a

short pulse ($8\ ps$) is incident at a grazing angle (14^o) to the target surface in a line focus. The short pulse beam is refracted in the plasma amplifier at a chosen electron density , which is below critical, and is strongly absorbed.

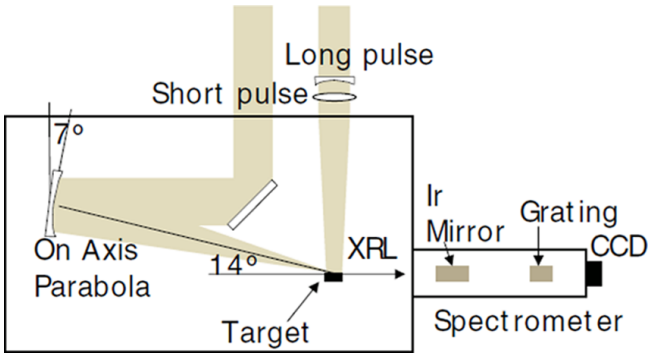

Figure 2.30: Experimental setup of grazing incident pumping for SXRL. from [129]

This novel pumping technique is so called grazing incident pumping (GRIP) scheme, which includes two-stage pumping. This pumping configuration improves laser coupling into the plasma gain region by using refraction to turn the short pump pulse back into the gain region, thus increase the path length and absorption in this specific plasma region. This higher efficiency realized with only a very low energy laser pump ($\sim 150\ mJ$ in total), provides a $10\ Hz$ repetition rate and represents more than one order of magnitude reduction in the pumping energy compared to the conventional transverse scheme. As represented in $Fig.\ 2.30$, lasing line at $18.9\ nm$ was achieved saturation for targets above $2\ mm$ in length, and the laser coefficient was determined as $55\ cm^{-1}$. Optimizing of the grazing incidence pumping angle was also worked out [130].

Another improved GRIP scheme combining the long pulse and short short pulse into the same beam, which is called double-pulse grazing incident pumping (DGRIP), was demonstrated several years later, as illustrated in $Fig.\ 2.31$ [131, 132]. This approach provided a simpler and more reliable operation scheme in compare to the standard GRIP. It could be helpful in the multi-plasma configurations, such as the oscillator-amplifier configuration [133].

Janulewicz and Kim [134] numerically analysed the GRIP scheme with performance of a Ni-like Ag SXRL pumped by a triple-pulse structure in the grazing incidence geometry as a function of the pumping conditions, as described in $Fig.\ 2.32(a)$. In this standard irradiation scheme, precursor and pre-pulse were at normal incidence angle with $15\ mJ$, $350\ ps$ (FWHM) and $263\ mJ$, $350\ ps$ (FWHM) respectively. Time delay between the two pulses was 5 ns at peak-to-peak, which were contributed to create a plasma approaching the Ni-like ionization stage. The plasma was then allowed to expand, and was subsequently heated by a $560\ mJ$, $8\ ps$ (FWHM) short pulse arriving at $300\ ps$ after the pre-pulse (peak-to-peak) with a specific grazing incidence angle at 18^o in respect to the target surface.

Calculated gain distribution perpendicularly along the target surface with optimizing time delays between the precursor pulse and short pump pulse (main pulse) is demonstrated in $Fig.\ 2.33(a)$. Gain coefficient over 200 cm^{-1} were obtained by playing with the time delay between pump pulses and the maximum gain region appeared at $\sim$20 μm deviated from the target surface. Moreover, the interesting pumping approach all-GRIP was also figured out by this modelling, as described in $Fig.\ 2.32(b)$, where the triple-pulse combined into one laser beam and with proper temporal separation were delivered to

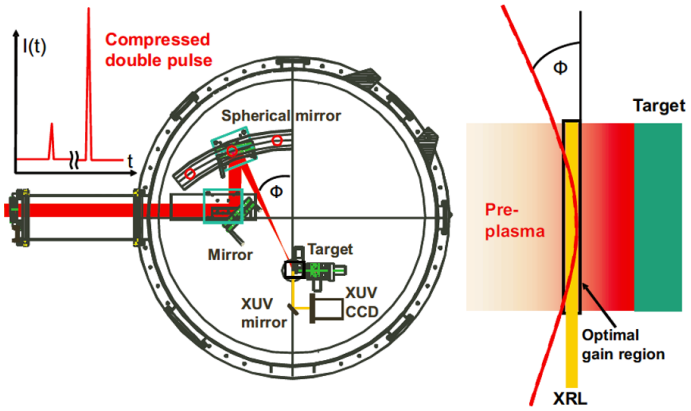

Figure 2.31: Schematical drawing of the experiment on plasma pumped with the DGRIP scheme and the SXRL dignostic sysytem. Inset on the right shows the non-normal incidence pumping and the refraction influence. from [131]

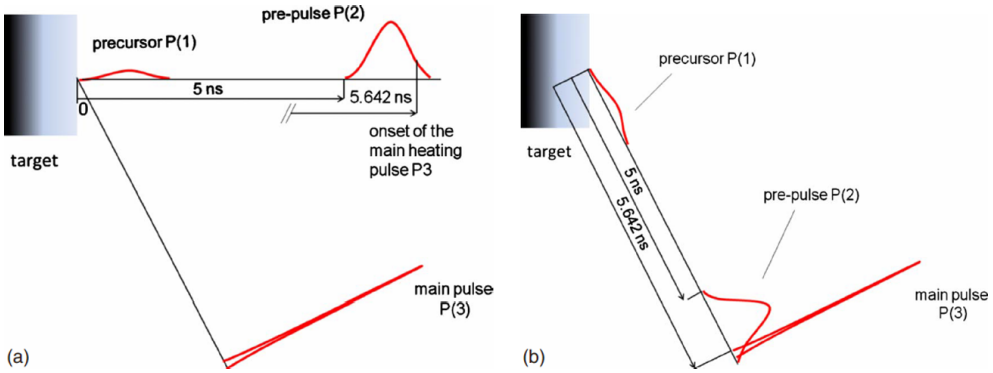

Figure 2.32: The design of triple-pulse pumping GRIP geometry. (a) Satandard irradiation scheme with precursor and pre-pulse at normal incidence angle and short pump pulse at grazing angle to the target surface. (b) Pump pulse structure of irradiation in the all-GRIP geometry: all the pulses are impinging on the target at a specific graing angle. The corresponding pulse parameters are: $P(1) - 15\ mJ$, $350\ ps\ (FWHM)$, $P(2) - 263\ mJ$, $350\ ps\ (FWHM)$ and $P(3) - 560\ mJ$, $8\ ps\ (FWHM)$. from [134]

the target at the specific grazing angle respected to the target surface. Similar results were obtained in $Fig.\ 2.33(b)$, while the maximum gain region took place at $\sim$8 μm apart from the target surface. The impressive GRIP schemes have encouraged the development of HH injection seeded SXRL based on the solid-plasma amplifier [135, 6, 136, 137]. Both GRIP techniques were widely carried out in our experiments on ASE-self seeding (oscillator-amplifier configuration) and HH injection seeded SXRL, which will be discussed in the following chapters.

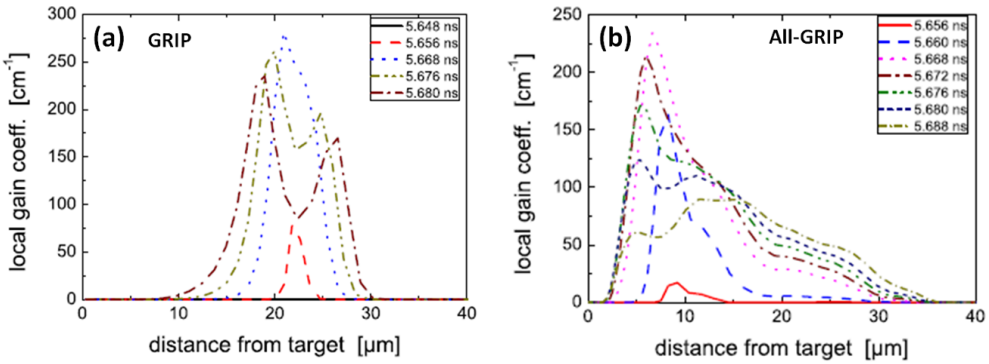

Figure 2.33: Gain distribution as a function of distance from the target surface at various time delay between the short pump pulse and the begining of the precursor pulse: (a) for standard GRIP related to $Fig.\ 2.32(a)$; (b) for full-GRIP corresponded to $Fig.\ 2.32(b)$. from [134]

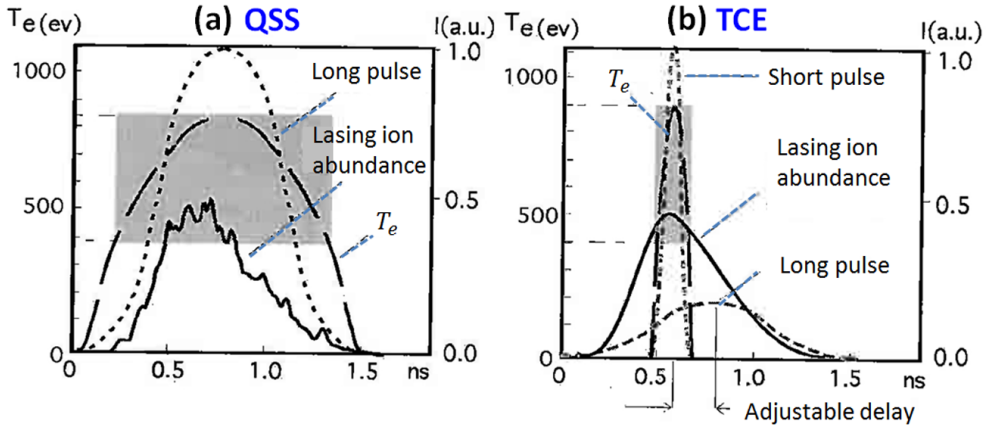

Figure 2.34: A visual comparison of temporal characteristics between (a) QSS and (b) TCE pumping scheme. Dotted line −− intensity of the pump laser, dashed line −− electron temperature T_e, solid lines are indicating the lasing ions abundance. Grey areas are corresponding to the regions where pumping is effective. from [81]

In summary, the two most important collisional pumping schemes, QSS and TCE have been discussed, as illustrated in $Fig.\ 2.34$. For QSS collisional pumping scheme using longer duration pump laser ($100\ ps - ns$), the plasma evolved slowly and atomic populations are placed in the quasi-steady sate (near LTE). The amplification coefficient is rather low ranging at $\sim 15\ cm^{-1}$ while the pumping laser energy is at the level of $100\ J$, which indicates extremely low pumping efficiency. Most of the pumping energy is lost in keeping the plasma hot. Moreover, saturated amplification reaches with plasma length $1-2\ cm$ accompanied with strong refraction during the SXRL propagation in the plasma. The life time of the gain is as similar level as the long pulse. However, for the TCE pumping scheme using much shorter pump pulse (typically few ps) the plasma is far from LTE with very high gain coefficient $10s$ to $100s\ cm^{-1}$. Pumping laser energy requirement are impressively low, normally less than $2\ J$. Saturation has been observed in a wide-range of materials within $2-5\ mm$ plasma length, which could significantly reduce the refraction influence. The gain life time is about $10\ ps$. Our experiments on HH-injected seeded SXRL demonstrated in this dissertation are all based on the TCE pumping scheme coupled with the impressive GRIP technique.

2.6.4 Solid-based X-ray plasma amplifier

The principle of producing a laser-induced plasma column with a solid slab target is presented in $Fig.\ 2.35(a)$, which is simulated using ARWEN code (see **Chapter 4, Section 4.1**). According to above discussion, the GRIP scheme, consists of long pulse ($100's\ ps$ to ns) in normal incidence and short pulse ($several\ ps$) in grazing incident angle, is normally adopted for creating and pumping a high density x-ray plasma amplifier. In consequent, the soft x-rays mostly emit along the plasma column as mentioned in Section 2.1. Especially, under the grazing incidence pumping scheme, ASE is mostly contributed in the forward direction, label as z axis in $Fig.\ 2.35(a)$. In most of the experiments included in this dissertation, Cylindrical and spherical optical systems are often used for the line-focusing onto the target surface, and three-pulse configuration composed of two long pre-pulses ($100's\ ps$) and a short pump pulse ($1-10\ ps$) is employed. A warm plasma is firstly generated by the normal incident long pulse. The second pre-pulse with much higher energy arrives at several ns later along the same beam path, which ionizing the plasma into highly charged and stable ionization stage (such as neon-like, nickel-like and palladium-like, see **Section 2.6.1**). Finally, short pump pulse arrives $100's\ ps$ later to further push the plasma to above stage and especially produce the large population inversion. The x-ray amplifying plasma is eventually created, as it displayed in $Fig.\ 2.35(b)$ which is showing the cross-sectional view of the x-ray plasma amplifier. One should be noted that the large population inversion region, which is so call gain zone, generated from $x = 25\ \mu m$ to $x = 50\ \mu m$. Here $x = 0\ \mu m$ is corresponding to the target surface. This results is in good agreement with the computation results using EHYBRID code [70].

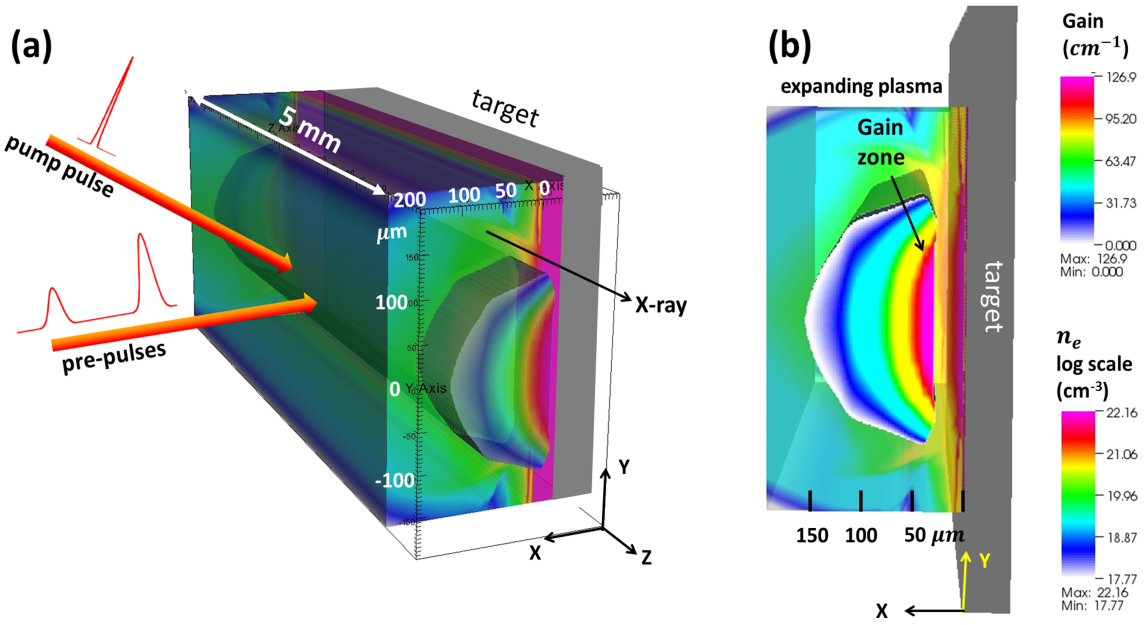

*Figure 2.35: 2D simulation of the x-ray plasma amplifier with ARWEN code (see **Chapter 4, Section 4.1**). (a) Production of a plasma column with line focusing using GRIP pumping scheme. (b) A cross-sectional view of the $200\ \mu m$ wide plasma. Density displayed in logarithm scale. (courtesy of T. T. Thuy Le, LPGP, University of Paris Sud)*

Energy transfer from the laser beam to plasma is basically due to the electron heating by electron-photon collisions in the ion electric field. For long pre-pulses, the typical process is inverse bremsstrahlung, most of the laser energy is considered to be absorbed during this process [138]. The absorption coefficient is given as [139]

$$\kappa_{ib} \approx 3.4\times10^{-6}\times\frac{(n_e/n_c)^2 Z ln\Lambda}{\sqrt{1-n_e/n_c}\lambda^2(kT_e)^{3/2}}, \tag{2.19}$$

where n_e is the electron density and n_c is the critical density in cm^{-3}, T_e is the electron temperature in keV, Z means the ion charge, λ corresponds to the lasing wavelength in nm, and $ln\Lambda$ is indicating to the Coulomb logarithm for inverse bremsstrahlung [140]. When the laser frequency ω is equalling to or even larger than the plasma frequency

$$\omega_p = (\frac{e^2 n_e}{m\varepsilon_0})^{1/2}, \tag{2.20}$$

the laser will be unable to propagate in the plasma. Here, m is the electron mass, e is the electron charge and ε_0 is the dielectric constant. Setting laser frequency $\omega = 2\pi c/\lambda$ to equal ω_p gives the critical density

$$n_c = \frac{4\pi^2 c^2 m\varepsilon_0}{e^2\lambda^2} \approx 1.1\times10^{27}\lambda^{-2}. \tag{2.21}$$

It is interesting to point out that the critical density [70] for IR pumping laser ($810\ nm$) is $\sim 1.7\times10^{21}\ cm^{-3}$, while it is $\sim 3.1\times10^{24}\ cm^{-3}$ for SXRL at $18.9\ nm$.

Once the x-ray plasma amplifier is created, evolution along the expanding direction x attracts much attention of the gain region. As it shown in $Fig.\ 2.35(b)$, which is associated with the evolutions of plasma density, temperature and expansion velocity along the x direction. A further simulation work with ARWEN two dimensional (2D) hydrodynamic code showed the density profile and temperature of the plasma amplifier along $x\ axis$ (see $Fig.\ 2.36$). The critical density is corresponding to the IR laser propagation limit. Beyond the critical surface, which is called conduction zone, plasma heating is only due to electron thermal conduction and possibly by x-ray radiations coming from the sub-critical region [139], which is also called plasma corona. The electron temperature is maximum in plasma corona, and stable in a certain distance, as described in $Fig.\ 2.36(b)$. Consequently, population inversions could happen in this specific region and give rise to x-ray emission.

It is interesting to mention that the plasma expansion velocity is approximately linear with distance and temperature is isothermal at densities below critical. $Fig.\ 2.35$ shows profiles at the time of peak gain. The velocity is still close to linear with distance and temperature is stable at densities close to critical. However, with the intense short pump pulse, ions are mostly pushed to a stable ionization stage and a high density region $\sim 25\ \mu m$ width along x axis, where $n_e > n_c$. It is indicated that in this region, the IR laser can not propagate, while soft x-rays (such as $18.9\ nm$) is free to pass. One should be aware of that this specific region is located in the plasma corona area. In addition, the plasma density distribution which is implying the gain region is shown in $Fig.\ 2.35(b)$, from $x = 25\ \mu m$ to $x = 50\ \mu m$. It is worth nothing that $x = 25\ \mu m$ is the location of critical surface in this simulation.

Furthermore, due to the plasma density gradient along x axis, a complex frequency dependent refractive index was discussed in [141]. However, the real component of the refractive index n can be written as

$$n = (1-\frac{n_e}{n_c})^{1/2} \approx (1-\frac{n_e\lambda^2}{1.1\times10^{27}})^{1/2}. \tag{2.22}$$

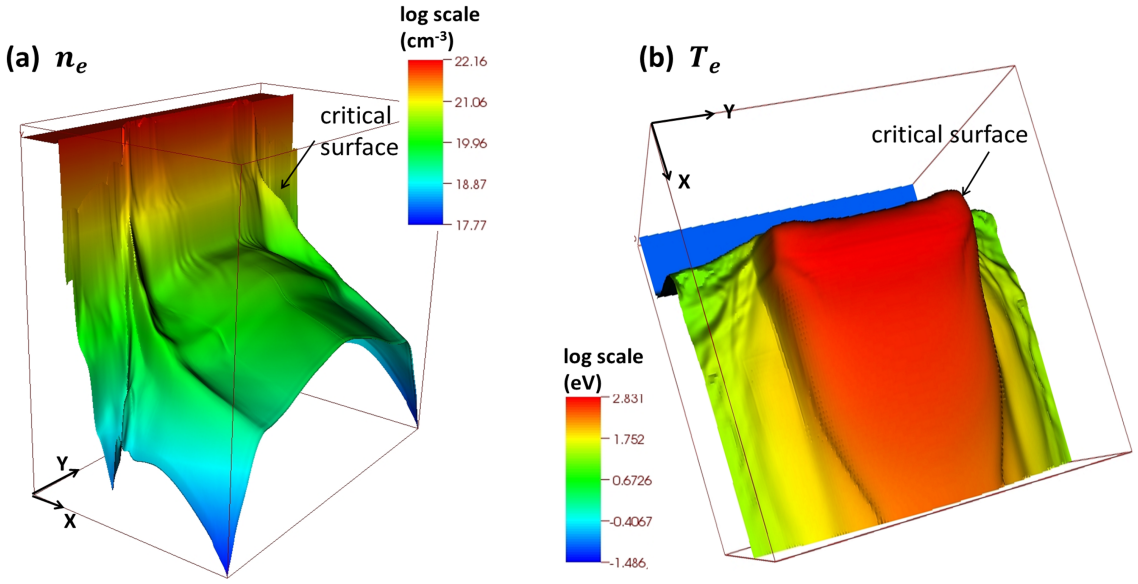

Figure 2.36: Distribution of (a) plasma density n_e and (b) temperature T_e in logarithm scale in the expanding plasma along the expanding direction x. (courtesy of T. T. Thuy Le, LPGP, University of Paris Sud)

Here, the λ is in nm. It is important to point out the refractive index of the plasma is inversely proportional to the square value of the soft x-ray wavelength.

Bibliography

[1] T. H. Maiman, Nature **187**, 493 (1960).

[2] P. Jaegle, S. Sebban, A. carillon, G. Jamelot, A. Klisnick, P. Zeitoun, B. Rus, F. Albert and D. Ros, *X-ray Lasers 1996 Conf. Lund, Sweden*, pp.1-pp.8 (1996)

[3] G. A. Gudzenko and L. A. Shelepin, Zh. Eksp. Teor. Fiz. **45**, 1445 (1963) [Sov. Phys. JETP 18, 998 (1964)].

[4] J. J. Rocca, V. Shlyaptsev, F.G. Tomasel, O. D. Cortazar, D. Hartshorn, and J. L. A. Chilla, Phy. Rev. Lett. **73**, 2192 (1994).

[5] Ph. Zeitoun, G. Faivre, S. Sebban, T. Mocek, A. Hallou, M. Fajardo, D. Aubert, P. Balcou, F. Burgy, D. Douillet, S. Kazamias, G. De Lacheze-Murel, T. Lefrou, S. Le Pape, P. Mercere, H. Merdji, A. S. Morlens, J. P. Rousseau, and C. Valentin, Nature **431**, 426 (2004).

[6] Y. Wang, E. Granados, F. Pedaci, D. Alessi, B. Luther, M. Berrill, and J. J. Rocca, Nat. Photonics **2**, 94 (2008).

[7] E., Ph. Zeitoun, M. Fajardo, G. Lambert, D. Ros, S. Sebban, and P. Velarde, Phys. Rev. A **84**, 013811 (2011).

[8] D. Attwood, *Soft X-rays and Extreme Ultraviolet Radiation*, Cambridge University Press, pp.274-pp.278 (1999).

[9] P. Jaegle, *Coherent Sources of XUV Radiation*, pp.114-p.120, Springer (2006).

[10] F. E. Irons and N. J. Peacock, J. Phys. B: At. Mol. Phys. **7**, 1109 (1974).

[11] R. J. Dewhurst, D. Jacoby , G. J. Pert and S. A. Ramsden , Phys. Rev. Lett. **37**, 1265 (1976).

[12] H. Daido, Rep. Prog. Phys. **65**, 1513-1576 (2002).

[13] W. T. Sifvast, *Laser Fundamentals*, p.26 (Cambridge University Press, Cambridge 1996).

[14] G, J. Pert, J. Phys. B: At. Mol. Phys. **9**, 3301-3315 (1976).

[15] P. Jaegle, G. Jamelot, A. Carrillon, A. Klisnik, A. Sureau, and H. Guennov,J. Opt. Soc. Am. B **4**, 563 (1987).

[16] A. Carillon, M. J. Edwards, M. Grande, M. J. C. Henshaw, P. Jaegle, G. Jamelot, M. H. Key, G. P. Kiehn, A. Klisnick, C. L. S. Lewis, D. O'Neill, G. J. Pert, S. A. Ramsden, C. M. E. Regan, S. J. Rose, R. Smith and O. Willi, J. Phys. B: At. Mol. Opt. Phys. **23**,147 (1990).

[17] H. Milchberg, C. H. Skinner, S. Suckewer, and D. Voorhees, Appl. Phys.Lett. **47**, 1151 (1985).

[18] S. Suckewer and H. Fishman, J. Appl. Phys. **51**, 1922 (1980).

[19] C. J. Keane and S. Suckewer, J. Opt. Soc. Am. B **8**, 201 (1991).

[20] C. Chenais-Popovics, R. Corbett, C. J. Hooker, M. H. Key, G. P. Kiehn, C. L. S. Lewis, G. J. Pert, C. Regan, S. J. Rose, S. Sadaat, R. Smith, T. Tomie, and and O. Willi, Phys. Rev. Lett. **59**, 2161 (1987).

[21] J. Zhang, M. H. Key, P. A. Norreys, G. J. Tallents, A. Behjat, C. Danson, A. Demir, L. Dwivedi, M. Holden, P. B. Holden, C. L. S. Lewis, A. G. MacPhee, D. Neely, G. J. Pert, S. A. Ramsden, S. J. Rose, Y. F. Shao, O. Thomas, F. Walsh, and Y. L. You, Phys. Rev Lett. **74**, 1335 (1995).

[22] S. Suckewer, C. H. Skinner, H. Milchberg, C. Keane, and D. Voorhees,Phys. Rev. Lett. **55**, 1753 (1985).

[23] S. Suckewer, C. H. Skinner, D. Kim, E. Valeo, D. Voorhees, and A. Wouters, *ibid.* **57**, 1004 (1986).

[24] P. Jaegle, G. Jamelot, A. Carillon and C. Wehenkel, Jpn. J. Appl. Phys. **17**, 483 (1978).

[25] P. Jaegle, *Coherent Sources of XUV Radiation*, pp.245, Springer (2006).

[26] G. Jamelot, A. Carillon, A. Klisnick and P. Jaegle, Appl. Phys. B **50**, 239 (1990).

[27] T. Hara, K. Ando , N. Kusakabe, H. Yashiro and Y. Aoyagi, Jpn. J. Appl. Phys. **28**, L1010 (1989).

[28] T. Kawachi, K. Ando, Y. Aoyagi, M. Aoyama, T. Hara and A. Sasaki, J. Opt. Soc. Am B **14**, 1863 (1997).

[29] T. Kawachi, K. Ando, H. Oyama, T. Hara and Y. Aoyagi, Jpn. J. Appl. Phys. **36**, 7048 (1997).

[30] D. Benredjem, A. Sureau, B. Rus and C. Moller, Phys. Rev. A **56**, 5152 (1997).

[31] G. Jamelot, P. Dhez, B.Gauthe, P. Jaegle, A. Klisnick and J. P. Raucourt, *X-Ray Lasers*, 1992, Inst. Phys. Conf. Ser. No. 125, IOP Publishing, p. 89 (1992).

[32] R. Li, Z. Zhang, Y. Liu, Z. Xu and Y. Cheng, Phys. Scripta, **56**m 472 (1997).

[33] W. W. Jones and A. W. Ali, Appl. Phys. Lett. **26**, 450 (1975).

[34] S. Suckewer and P. Jaegle, X-ray Laser: Past, Present and Future, Laser Phys. Lett. **6**, 411 (2009).

[35] J. Peyraud and N. Peyraud, J. Appl. Phys. **43**, 2993 (1972).

[36] Y. Nagata, K. Midorikawa, S. Kubodera, M. Obara, H. Tashiro, and K. Tokoda, Phys. Rev. Lett. **71**, 3774 (1993).

[37] D. Korobkin, C. H. Nam, S. Suckewer, and A. Golstov, Phys. Rev. Lett. **77**, 5206 (1996).

[38] B. N. Chichkov and B. Wellegehausen, in "X-ray Lasers 1998," *Proceedings of the 6th International Conference on X-ray Lasers*, edited by Y. Kato, H. Takuma and H. Daido, Institute of Physics, University of Berkshire, Reading (1999).

[39] S. Backus, C. G. Durfee III, M. Murnane, and H. C. Kapteyn, Rev. Sci. Instrum. **69**, 1207 (1998).

[40] D. P. Umstadter, C. Barty, M. Perry, and G. A. Mourou, Opt. Photonic News **9**, 41 (1998).

[41] C. P. J. Barty, T. Guo, C. Le Blanc, F. Raksi, C. Rose-Petruck, J. Squier, K. R. Wilson, V. V. Yakovlev, and K. Yamakawa, *X-Ray Lasers*, edited by S. Svanberg and C. G. Wahlstrom, Institute of Physics, University of Reading, Berkshi, Vol. 1511, p.282 (1996).

[42] Y. Kato, *X-Ray Lasers*, edited by S. Svanberg and C. G. Wahlstrom,Institute of Physics, University of Reading, Berkshi, Vol. 1511, p.274 (1996).

[43] P. B. Corkum, N. H. Burnett, and F. Brunel, Phys. Rev. Lett. **62**, 1259 (1989).

[44] N. H. Burnett and P. B. Corkum, J. Opt. Soc. Am. B **6**, 1195 (1989).

[45] Y. Nagata, K. Midorikawa, S. Kubodera, M. Obara, H. Tashiro, K.Toyoda, and Y. Kato, Phys. Rev. A **51**, 1415 (1995).

[46] J. J. Rocca, Rev. Sci. Instrum., **70**, 3799-3827 (1999).

[47] P. Polonsky, C. O. Park, K. Krushelnick, and S. Suckewer, *Proc. SPIE* **2012**, 61 (1993).

[48] D.C. Eder, P. Amendt, L.B. DaSilva, R.A. London, B.J. MacGowan, D.L. Matthews, B.M. Penetrante, M.D. Rosen, S.C. Wilks, T.D. Donnelly, R.W. Falcone, and G.L. Strobel, Phys. Plasmas **1**, 1744 (1994).

[49] Y. Avitzour and S. Suckewer, J. Opt. Soc. Am. B **23**, 925 (2006).

[50] Y. Avitzour and S. Suckewer, J. Opt. Soc. Am. B **24**, 819(2007).

[51] Y. Luo, *Toward Development of X-ray Lasers in ""Water Window"*, A Dissertation Presented to the Faculty of Princeton University, p.169 (2013).

[52] M. A. Duguay and P. M. Rentzepis, Appl. Phys. Lett. **10**, 350 (1967).

[53] H. C. Kapteyn, Appl. Opt. **31**, 4931(1992).

[54] G. L. Strobel, D. C. Eder, R. A. London, M. D. Rosen, R. W. Falcone, and S. P. Gordon, Proc. SPIE **1860**, 157 (1993).

[55] S.J. Moon, D.C. Eder, and G.L. Strobel,*Proc. of the 4th Int. Conf. on X-Ray Lasers* (Editors: D. Eder and D. Matthews), p. 262 (1994).

[56] M. Ribiere, S. Sebban, S. Jacquemot, B.G. Cheron, K. Ta Phuoc, J. Gautier, J. Grunenwald, P. Ribeiro, M. Kozlova, Ph. Zeitoun and A. Rousse, Appl. Phys. B **106**, 809–816 (2012).

[57] P. Emma, R. Akre, J. Arthur, R. Bionta, C. Bostedt, J. Bozek, A. Brachmann, P. Bucksbaum, R. Coffee, F.-J. Decker, Y. Ding, D. Dowell, S. Edstrom, A. Fisher, J. Frisch, S. Gilevich, J. Hastings, G. Hays, Ph. Hering, Z. Huang, R. Iverson, H. Loos, M. Messerschmidt, A. Miahnahri, S. Moeller, H.-D. Nuhn, G. Pile, D. Ratner, J. Rzepiela, D. Schultz, T. Smith, P. Stefan, H. Tompkins, J. Turner, J. Welch, W. White, J. Wu, G. Yocky and J. Galayda, Nature Photon. **4**, 641–647 (2010).

[58] W. Ackermann, G. Asova, V. Ayvazyan, A. Azima, N. Baboi, J. Bähr, V. Balandin, B. Beutner, A. Brandt, A. Bolzmann, R. Brinkmann, O. I. Brovko, M. Castellano, P. Castro, L. Catani, E. Chiadroni, S. Choroba, A. Cianchi, J. T. Costello, D. Cubaynes, J. Dardis, W. Decking, H. Delsim-Hashemi, A. Delserieys, G. Di Pirro, M. Dohlus, S. Düsterer, A. Eckhardt, H. T. Edwards, B. Faatz, J. Feldhaus, K. Flöttmann, J. Frisch, L. Fröhlich, T. Garvey, U. Gensch, Ch. Gerth, M. Görler, N. Golubeva, H.-J. Grabosch, M. Grecki, O. Grimm, K. Hacker, U. Hahn, J. H. Han, K. Honkavaara, T. Hott, M. Hüning, Y. Ivanisenko, E. Jaeschke, W. Jalmuzna, T. Jezynski, R. Kammering, V. Katalev, K. Kavanagh, E. T. Kennedy, S. Khodyachykh, K. Klose, V. Kocharyan, M. Körfer, M. Kollewe, W. Koprek, S. Korepanov, D. Kostin, M. Krassilnikov, G. Kube, M. Kuhlmann, C. L. S. Lewis, L. Lilje, T. Limberg, D. Lipka, F. Löhl, H. Luna, M. Luong, M. Martins, M. Meyer, P. Michelato, V. Miltchev, W. D. Möller, L. Monaco, W. F. O. Müller, O. Napieralski, O. Napoly, P. Nicolosi, D. Nölle, T. Nuñez, A. Oppelt, C. Pagani, R. Paparella, N. Pchalek, J. Pedregosa-Gutierrez, B. Petersen, B. Petrosyan, G. Petrosyan, L. Petrosyan, J. Pflüger, E. Plönjes, L. Poletto, K. Pozniak, E. Prat, D. Proch, P. Pucyk, P. Radcliffe, H. Redlin, K. Rehlich, M. Richter, M. Roehrs, J. Roensch, R. Romaniuk, M. Ross, J. Rossbach, V. Rybnikov, M. Sachwitz, E. L. Saldin, W. Sandner, H. Schlarb, B. Schmidt, M. Schmitz, P. Schmüser, J. R. Schneider, E. A. Schneidmiller, S. Schnepp, S. Schreiber, M. Seidel, D. Sertore, A. V. Shabunov, C. Simon, S. Simrock, E. Sombrowski, A. A. Sorokin, P. Spanknebel, R. Spesyvtsev, L. Staykov, B. Steffen, F. Stephan, F. Stulle, H. Thom, K. Tiedtke, M. Tischer, S. Toleikis, R. Treusch, D. Trines, I. Tsakov, E. Vogel, T. Weiland, H. Weise, M. Wellhöfer, M. Wendt, I. Will, A. Winter, K. Wittenburg, W. Wurth, P. Yeates, M. V. Yurkov, I. Zagorodnov and K. Zapfe, Nature Photon. **1**, 336–342 (2007).

[59] D. Pile, *X-rays: first light from SACLA*, Nature Photon. **5**, 456 (2011).

[60] N. Rohringer, and R. A. London, *Atomic inner-shell X-ray laser pumped by an X-ray free-electron laser*, Phys. Rev. A **80**, 013809 (2009).

[61] N. Rohringer, D. Ryan, R. A. London, M. Purvis, F. Albert, J. Dunn, J. D. Bozek, C. Bostedt, A. Graf, R. Hill, S. P. Hau-Riege and J J. Rocca, Nature **481**, 488-491 (2012).

[62] A. G. Molchanov, Sov. Phys. Usp. **15**, 124 (1972).

[63] R. C. Elton, Appl. Opt. **14**, 97 (1975).

[64] A. N. Zherikin, K. N. Koshelev, and V. S. Letokhov, Sov. J. Quantum Electron. **6**, 82 (1976).

[65] L. A. Vainshtein, A. V. Vinogradov, V. I. Safranova, and I. Vu. Skolev, Sov. J. Quantum Electron. **8**, 239 (1978).

[66] A. V. Vinogradov and V. N. Shlyaptsev, Sov. J. Quantum Electron. **10**, 754 1980!, and **13**, 303 (1980).

[67] A. V. Vinogradov, I. I. Sobelman, E. A. Yukov, Sov. J. Quant. Electron. **7**, 32 (1977).

[68] D. L. Matthews, P. L. Hagelstein, M. D. Rosen, M. J. Eckart, N. M. Ceglio, A. U. Hazi, H. Medecki, B. J. MacGowan, J. E. Trebes, B. L. Whitten, E. M. Campbell, C. W. Hatcher, A. M. Hawryluk, R. L. Kauffman, L. D. Pleasance, G. Rambach, J. H. Scofield, G. Stone, and T. A. Weaver, Phys. Rev. Lett. **54**,110 (1985).

[69] M. D. Rosen, P. L. Hagelstein, D. L. Matthews, E. M. Campbell, A. U. Hazi, B. L. Whitten, B. MacGowan, R. E. Turner, and R. W. Lee, ibid. **54**, 106 (1985).

[70] G. J. Tallents, J. Phys. D: Appl. Phys. **36**, R259-R276 (2003).

[71] B. J. MacGowan, L. B. Da Silva, D. J. Fields, C. J. Keane, J. A. Koch, R. A. London, D. L. Matthews, S. Maxon, S. Mrowka, A. L. Osterheld, J. H. Scofield, G. Shimkaveg, J. E. Trebes and R. S. Walling , Phys. Fluids B **4**, 2326 (1992).

[72] R. Smith, G. J. Tallents, J. Zhang, G.Eker, S. McCabe, G. J. Pert and E. Wolfrum, Phys. Rev. A **59**, R47 (1999).

[73] J. Zhang, A. G. MacPhee, J. Nilsen, J. Lin, T. W. Barbee, Jr., C. Danson, M. H. Key, C. L. S. Lewis, D. Neely, R. M. N. O'Rourke, G. J. Pert, R. Smith, G. J. Tallents, J. S. Wark, and E. Wolfrum, Phys. Rev. Lett. **78**, 3856 (1997).

[74] J. Zhang, A. G. MacPhee, J. Lin, E. Wolfrum, R. Smith, C. Danson, M. H. Key, C. L. S. Lewis, D. Neely, J. Nilsen, G. J. Pert, G. J. Tallents, and J. S. Wark, Science **276**, 1097 (1997).

[75] H. Daido, S. Ninomiya, M. Tagaki, Y. Kato, J. Opt. Soc. Am. B **16**, 296 (1999).

[76] A. Sasaki and I. Murakami, J. Phys. B: At. Mol. Phys. **46**, 175701 (2013).

[77] R. W. P. McWhirter, *Plasma Diagnostic Techniques*, edited by R. H. Huddlestone and S. L. Leonard (New York: Academic), p.206 (1965).

[78] H. Daido, S. Ninomiya, T. Imani, Y. Okaichi, M. Takagi, R. Kodama, H. Takabe, Y. Kato, F. Koike, J. Nilsen and K. Murai, Int. J. Mod. Phys. B **11**, 945-990 (1997).

[79] T. N. Lee , E. A. McLean and R. C. Elton, Phys. Rev. Lett. **59**, 1185 (1987).

[80] U. Feldman and J. F. Seely, J. Appl.Phys. **56**, 2475-2478 (1984).

[81] P. Jaegle, *Coherent Sources of XUV Radiation*, pp.141-143, Springer (2006).

[82] J. Nilsen and J. C. Moreno, Phys. Rev. Lett. **74**, 3376 (1995).

[83] H. Daido, Y. Kato, K. Murai, S. Ninomiya, R. Kodam, G. Yuan, Y. Oshikane, M. Takagi, H. Takbe and F. Koike, Phys. Rev. Lett. **75**, 1074 (1995).

[84] J. Nilse, J. A. Koch, J. H. Scofield, B. J. MacGowan, J. C. Moreno and L. B. Da Silva, Phys. Rev. Lett. **24**, 3713 (1993).

[85] P. Jaegle, *Coherent Sources of XUV Radiation*, pp.70, Springer (2006).

[86] J. G. Lunney, App. Phys. Lett. **48**, 891 (1986).

[87] R. Kodama, D. Neely, Y. Kato, H. Daido, K. Murai, G. Yuan, A. MacPhee, and C. L. S. Lewis, Phys. Rev. Lett. **73**,3215-3218 (1994).

[88] P. Jaegle, A. Carillon, H. Z. Chen, P. Dhez, L. Dwivedi, J. Jacoby, G. Jamelot, J. Zhang, M. H. Key, A. Kidd, A. Klisnick, R. Kodama, J. Krishnan, C. L. S. Lewis, D. Neely, P. Norreys. D. O. Neill, G. J. Pert, S. A. Ramsden, J. P. Raucourt, G. J. Tallents, J. Uhomoibhi, *X-ray Lasers*, Inst. Phys. Conf. Ser. No. 125 (1992).

[89] A. Carillon, H. Z. Chen, P. Dhez, L. Dwivedi, J. Jacoby, P. Jaegle, G. Jamelot, Jie Zhang, M. H. Key, A. Kidd, A. Klisnick, R. Kodama, J. Krishnan, C. L. S. Lewis, D. Neely, P. Norreys, D. O'Neill, G. J. Pert, S. A. Ramsden, J. P. Raucourt, G. J. Tallents and J. Uhomoibhi, Phys. Rev. Lett. **68**, 2917 (1992).

[90] B. Rus, T. Mocek, A. R. Prag, M. Kozlova, G. Jamelot, A. Carillon, D. Ros, D. Joyeux, and D. Phalippou, Phys. Rev. A **66**, 063806 (2002).

[91] S. Sebban, H. Daido, N. Sakaya, Y. Kato, K. Murai, H. Tang, Y. Gu, G. Huang, S. Wang, A. Klisnick, Ph. Zeitoun, F. Koike, and H. Takenaka, Phys. Rev. A **61**, 043810 (2000).

[92] P. Jaegle, A. Carillon, P. Dhez, P. Goedtkindt, G. Jamelot, A. Klisnick and B. Rus, *X-ray Lasers 1994*; AIP Conf. Proc. **332**, 25 (1995).

[93] B. Rus, A. Carillon, P. Dhez, B. Gauthe, P. Goedtkindt, P. Jaegle, G. Jamelot, A. Klisnick, M. Nantel, S. Sureau and Ph. Zeitoun, *X-ray Lasers 1994*; AIP Conf. Proc. **332**, 152 (1995).

[94] B. Rus, A. Carillon, P. Dhez, P. Goedtkindt, P. Jaegle, G. Jamelot, A. Klisnick, M. Nantel, and Ph. Zeitoun, Phys. Rev. A **55**, 3858 (1997).

[95] P. J. Warwick, C. L. S. Lewis, S. McCabe., A. G. MacPhee, A. Behjat, M. Kurkcuoglu, G. J. Tallents, D. Neely, E. Wolfrum, S. B. Healy and G. J. Pert, Opt. Comm. **144**, 192 (1997).

[96] S. Wang, G. Zhou, G. Zhang, J. Zheng and S. Chunyu, *X-ray Lasers 1994*; AIP Conf. Proc. **332**, 293 (1995).

[97] J. Nilsen, Y. Li, J. C. Moreno and E. E. Fill, Opt. Comm. **124**, 287 (1996).

[98] J. Zhang, P. J. Warwick, E. Wolfrum, M. H. Key, C. Danson, A. Demir, S. Healy, D. H. Kalantar, N. S. Kim, C. L. S. Lewis, J. Lin, A. G. MacPhee, D. Neely, J. Nilsen, G. J. Pert, R. Smith, G. J. Tallents, and J. S. Wark, Phys. Rev. A **54**, R4653(1996).

[99] J. Nilsen, J. C. Moreno, L. B. Da Silva and J. A. Koch, Proc. SPIE **2520**, 97 (1995).

[100] J. Nilsen, J. C. Moreno, B. J. MacGowan and J. A. Koch, Appl. Phys. B **57**, 309 (1993).

[101] E. E. Fill, Y. Li and G. Pretzler, IEEE J. Selected Topics Quant. Electron.**1**, 958 (1995).

[102] E. E. Fill, Y. Li, D. Schlogl, J. Steingruber and J. Nilsen, Optics Lett. **20**, 374 (1995).

[103] Y. Li, G. Pretzler and E. E. Fill, Optics Lett. **20**, 1026 (1995).

[104] Y. Li, G. Pretzler and E. E. Fill, Phys. Rev. A **51**, R4341 (1995).

[105] Y. Li, G. Pretzler and E. E. Fill, Phys. Rev. A **52**, R3433 (1995).

[106] Y. Li, G. Pretzler and E. E. Fill, Appl. Phys. B **63**, 125 (1996).

[107] J. Zhang, A. G. MacPhee, J. Lin, E. Wolfrum, R. Smith, C. Danson, M.H. Key, C.L.S. Lewis, D. Neely, J. Nilsen, G.J. Pert, G.J. Tallents, J.S. Wark and P.J. Warwick, Phys. Lett. A **234**, 410 (1997).

[108] R. Tommasini, F. Lowenthal and J. E. Balmer, Phys. Rev. A **59**, 1577 (1999).

[109] A. Klisnick, D. Ros, Ph. Zeitoun, F. Albert, A. Carillon, P. Fourcade, S. Hubert, P. Jaegle, G. Jamelot, C. L. S. Lewis, A. Mac Phee, R. O'Rourcke,R. Keenan, P. Nickles, K. Janulewicz, M. Kalashnikov, J. Warwick, J. C. Chanteloup, E. Salmon, C. Sauteret, J. P. Zou, D. Joyeux and D. Phalippou, *X-ray Lasers 1998*; Inst. Phys. Conf. Ser. No. 159, IOP Publishing, P.107 (1998).

[110] Y. A. Afanasiev and V. N. Shlyaptsev, Sov. J. Quantum Electron. **19**,1606 (1989).

[111] P. V. Nickles, M. Schnuer, M. R. Kalashnikov, I. Will and W. Sandner, Proc. SPIE **2520**, 373 (1995).

[112] P. V. Nickles, V. N. Shlyaptsev, M. Kalachnikov, M. Schnürer,I. Will, and W. Sandner, Phys. Rev. Lett. **78**, 2748-2751 (1997).

[113] P. Jaegle, *Coherent Sources of XUV Radiation*, pp.16, Springer (2006).

[114] Dunn J, Osterheld A L, Shepherd R, White W E, Shlyaptsev V N and Steward R E, Phys. Rev. Lett. **80**, 2825 (1998).

[115] P. J. Warwick, C. L. S. Lewls, M. P. Kalachnikov, P. V. Nickles, M. Schnurer, A. Behiat, A. Demir , G. J. Tallents, D. Neely, E. Wolfrum, J. Zhang and G. J. Pert , J. Opt Soc. Am. B **15**, 1808 (1998).

[116] M. Kado, A. Nagashima, K. Nagashima, T. Kawachi, N. Hasegawa, M. Tanaka, T. Hosokai, K. Sukegawa, A. Sasaki and Y. Kato, Proc. SPIE **3776** 242–248 (1999).

[117] C. L. S. Lewis, R. Keenan, A. G. MacPhee, B. Moore, R. M. N. O'Rourke, G. J. Tallents, S. Dobosz, J. Peschete, F. Strati, J. S. Wark, E. Wolfrum ,G. J. Pert, S. P. MacCabe, P. A. Simms, R. Allott, J. Collier, C. N. Danson, A. Djaoui and D. Neely, Proc. SPIE **3776**, 292–301 (1999).

[118] A. Klisnick, Ph. Zeltoun , D. Ros, A. Carillon, P. Fourcade, S. Hubert, G. Jamelot, C. L. S. Lewis, A. G. MacPhee, O. RourckeRMN, R. Keenan, P. V. Nickles, K. Janulewicz, M. Kalashnikov, J. Warwick, J. C. Chanteloup, A. Migus, E. Salmon, C. Sauteret and J. P. Zou, J. Opt. Soc. Am. B **17**, 1093 (2000).

[119] J. Nilsen, Y. Li and J. Dunn, J. Opt. Soc. Am. B **17**, 1084 (2000).

[120] P. Jaegle, *Coherent Sources of XUV Radiation*, pp.196-202, Springer (2006).

[121] M. P. Kalachnikov, P. V. Nickles, M. Schnürer, W. Sandner, V. N. Shlyaptsev, C. Danson, D. Neely, E. Wolfrum, J. Zhang, A. Behjat, A. Demir, G. J. Tallents, P. J. Warwick, and C. L. S. Lewis, Phys. Rev. A **57**, 4778 (1998).

[122] J. Dunn, Y. Li, A. L. Osterheld, J. Nilsen, J. R. Hunter and V. N. Shlyaptsev, Phys. Rev. Lett. **84**, 4834 (2000).

[123] Y Li, J. Dunn, J. Nilsen, T. W. Barbee, A. L. Osterheld and V. N. Shlyaptsev, J. Opt. Soc. Am. B **17**, 1098 (2000).

[124] H. Fiedorowicz, A. Bartnik, J. Dunn, R. F. Smith, J. Hunter, J. Nilsen, A. L. Osterheld and V. N. Shlyaptsev, Opt. Lett. **26**, 1403 (2001).

[125] P. Lu, T. Kawachi, M. Kishimoto, K. Sukegawa, M. Tanaka, N. Hasegawa, M. Suzuki, R. Tai, M. Kado, K. Nagashima, H. Daido, Y. Kato and H. Fiedorowicz, Opt. Lett. **27**, 1911-1913 (2002).

[126] S. Sebban, R. Haroutunian, Ph. Balcou, G. Grillon, A. Rousse, S. Kazamias, T. Marin, J. P. Rousseau, L. Notebaert, M. Pittman, J. P. Chambaret, A. Antonetti, D. Hulin, D. Ros, A. Klisnick, A. Carillon, P. Jaeglé, G. Jamelot, and J. F. Wyart, Phys. Rev. Lett. **86**, 3004 (2001).

[127] S. Sebban, T. Mocek, R. Haroutmain, B. Rus, Ph. Balcou, D. Ros, G. Grillon, A. Rousse, S. Kazamias, T. Marin, J. P. Roussean, L. Notebaert, M. Pittman, J. P. Chambaret, A. Antonett, D. Hulin, A. Klisnick, A. Carillon, P. Jaegle and J. F. Wyart, *Proc. SPIE* **4505**, 195–203 (2001).

[128] T. Kawachi, M. Kado, M. Tanaka, A. Sasaki, N. Hasegawa, A. V. Kilpio, S. Namba, K. Nagashima, P. Lu, K. Takahashi, H. Tang, R. Tai, M. Kishimoto, M. Koike, H. Daido, and Y. Kato, Phys. Rev. A **66**, 033815 (2002).

[129] R. Keenan, J. Dunn, P. K. Patel, D. F. Price, R. F. Smith, and V. N. Shlyaptsev, Phys. Rev. Lett. **94**, 103901 (2005).

[130] D. Ursescu, B. Zielbauer, T. Kuehl, and P. Neumayer, Phys. Rev. E **75**, 045401 (2007).

[131] D. Zimmer, B. Zielbauer, V. Bagnoud, U. Eisenbarth, D. Javorkova and T. Kuehl, Optics Exp. **16**, 10398-10403 (2008).

[132] D. Zimmer, B. Zielbauer, M. Pittman, O. Guilbaud, J. Habib, S. Kazamias, D. Ros, V. Bagnoud, and T. Kuehl, Optics Lett. **35**, 450-452 (2010).

[133] B. Ecker, E. Oliva, B. Aurand, D. C. Hochhaus, P. Neumayer, H. Zhao, B. Zielbauer, K. Cassou, S. Daboussi, O. Guilbaud, S. Kazamias, T. T. T. Le, D. Ros, P. Zeitoun, and T. Kuehl, Optic Exp. **20**, 25391-25399 (2012).

[134] K. A. Janulewicz and C. M. Kim, Phys. Rev. E **82**, 056405 (2010).

[135] Y. Wang, E. Granados, M. A. Larotonda, M. Berrill, B. M. Luther, D. Patel, C. S. Menoni, and J. J. Rocca, Phys. Rev. Lett. **97**, 123901 (2006).

[136] L. Li, Y. Wang, S. Wang, E. Oliva, L. Yin, T. T. T. Le, S. Daboussi, D. Ros, G. Maynard, S. Sebban, B. Hu, J. J. Rocca, and Ph. Zeitoun, Optics Lett. **38**, 4011-4014 (2013).

[137] Y. Wang, S.Wang, E. Oliva, L. Li, M. Berrill, L. Yin, J. Nejdl, B. M. Luther, C. Proux, T. T. T. Le, J. Dunn, D. Ros, Ph. Zeitoun and J. J. Rocca, Nature Photonics **8**, 381-384 (2014).

[138] W.L. Kruer, *The Physics of Plasma Laser Interactions*, Frontiers in Physics, Addison-Wesley, Redwood City, CA, 1988.

[139] P. Jaegle, *Coherent Sources of XUV Radiation*, pp.69-72, Springer (2006).

[140] T.P. Hughes, *Plasmas and Laser Light*, Adam Hilger, The Institute of Physics, Bristol, England, 1975.

[141] P. Jaegle, *Coherent Sources of XUV Radiation*, pp.23-28, Springer (2006).

CHAPTER 3

Optical Properties Study of Seeded SXRL

The promise of high beam quality of SXRL became clear after the pioneer x-ray imaging attempts from the $1970's$ to $1980's$, when Schmahl and Kirz with their colleagues proposed the development of full-field transmission [1, 2] and scanning transmission [3, 4] x-ray microscopies in synchrotron radiation source respectively. Nowadays, soft x-ray imaging at the nano- and micro-scale is of great interest for applications in physical, chemical and life sciences, such as x-ray microscopy [5, 6, 7, 8], error-free nano-patterning [9], photochemistry [10], materials characterization [11, 12], CDI [13, 14], x-ray holography [15, 16, 17] and development of nano-probe [18]. Many of the applications are calling for the excellent optical properties of the soft x-ray source.

We therefore performed three experiments to investigate the SXRL optical properties from different seeding approaches. In the **first Section**, SXRL generated by ASE self-seeded scheme with double plasma amplifiers (molybdenum) was carried out at GSI (Germany). ASE from the first plasma amplifier was rated as the seed injected to the second plasma amplifier using an injection mirror. In **Section 2**, SXRL coherent seeding experiment was conducted at LASERIX (France). HH pulse from argon gas cell was directly seeded into titanium-plasma amplifier without any imaging x-ray optics. The characteristics of the plasma amplifier and amplified HH pulse ($32.6\ nm$) were studied. In **Section 3**, another HH seeded SXRL experiment was carried out at Colorado State University (US). A toroidal mirror was adopted for the injection of HH pulse from neon gas puff into molybdenum plasma amplifier. Wave front of the HH seed pulse and amplified seed pulse ($18.9\ nm$) were comprehensively discussed.

3.1 ASE self-seeded SXRL at GSI

Since the first significant amplification on soft x-ray emission demonstrated in 1985 [19, 20], laser driven SXRL sources have achieved remarkable progress. Their size has been greatly reduced and repetition rate has been increased by several orders of magnitude, recently reaching 100 Hz [21] in a table-top. These advances are opening a wealth of applications in the fields of high resolution imaging, error-free nano-patterning, photochemistry, materials characterization, and the development of nano-probes [9]. Pulse energy of the x-ray emission from the laser-based plasma has demonstrated mJ level, which meets most of the energy requirements for the x-ray imaging. However, the poor beam properties in spatial coherence and pulse duration of this ASE, due to its stochastic nature, are limiting parameters in the development of the ultra-fast, high resolution CDI [22, 9]. Early efforts [23, 24] to improve the beam quality of the plasma-based ASE under the QSS pumping scheme, demonstrated saturated amplification, but no apparent improvement on pulse duration and spatial coherence. Ten years ago, Tanaka *et al.* [25] and Nishikino *et al.* [26] demonstrated a double-stage x-ray laser of near diffraction-limited divergence and highly spatial coherence. In both experiment, the oscillator-amplifier were pumped by double IR driven lasers incident onto the target in opposite. And TW was taken into account in oscillator plasma.

With the benefit of our DGRIP pumping scheme [27, 28] (see **Section 2.6.3**), which relies on two collinear pulses that are focused onto the targets in grazing incidence, we conducted this double-stage x-ray plasma amplifier experiment. This intrinsically provides travelling waves for both targets and allows for a more efficient pumping as compared to the normal incidence pumping. More importantly, the DGRIP scheme allows for an exceptionally compact and simple double-stage SXRL setup, as it relies only on two beams and one target. As reported in previous experiment [28], a first proof-of-principle experiment using this "Butterfly" scheme resulted in an amplified SXRL with $3\ ps$ pulse duration and $1\ \mu J$ pulse energy. In this section, we present the results of a follow-up experiment carried out at the PHELIX laser facility [29], using molybdenum ($18.9\ nm$) slab target in a very compact setup and working at low pump energy. In addition to the DGRIP technique, the influence of a third pumping pulse has been studied. Previously, it has been demonstrated that a third pulse can significantly reduce the energy required to pump the SXRL [30]. Also, it has been shown that a third pulse affects the near-field of the SXRL [31] and prolongs the lifetime of the target [32]. In this work, seeded SXRL operation has been demonstrated in both pumping schemes, resulting in an increased brilliance of two orders of magnitude compared to the original seed pulse.

3.1.1 Experimental setup

This experiment [33] was conducted at GSI using the PHELIX laser facility [34] in collaboration with the team of Prof. T. Kuehl. The PHELIX laser system is illustrated in $Fig.\ 3.1$. A Mach-Zehnder like interferometer, which was implemented in the short-pulse Front-End of the PHELIX laser, was used to create the chirped double-pulse structure required for the DGRIP scheme [27]. After compression, the pulse durations of the two pulses were $200\ ps$ (pre-pulse) and $2\ ps$ (main pulse), respectively. Using the PHELIX pre-amplifier section, the total pump energy amounted to $600\ mJ$, equally distributed between two individual pump beams.

Inside the target chamber, spherical mirrors (Sph.) have been used to focus the beams onto the Mo slab target, as illustrated in $Fig.\ 3.2$. The GRIP angle was 25° for both beams, which resulted in a TW of approximately $1.1\ c$ according to ray tracing simulations. The line focus providing the seed-plasma was $5\ mm \times 90\ \mu m$, leading to intensities of $8\times10^{10}\ Wcm^{-2}$ and $2\times10^{13}\ Wcm^{-2}$ for the pre-pulse and main pulse, respectively. The amplifier medium (amplifier-plasma) was pumped by a $2.5\ mm \times 220\ \mu m$ focus at intensities of $7\times10^{10}\ Wcm^{-2}$ for the pre-pulse and $1\times10^{13}\ Wcm^{-2}$ for the main pulse. The line foci were vertically separated by $\sim3\ mm$.

To inject the ASE seed into the amplifier-plasma, a spherical extreme ultraviolet (EUV/XUV) mirror (Inj., $f = 1.2\ m$) was installed at $275\ mm$ distance to the target. This distance defined the optimum delay between the two IR main pulses to $\tau = 1835\ ps$. In this way, the seed pulse arrives at the same time at the target as the IR pulse pumping the amplifier medium, as indicated in the inset 3.2(b). Using a fast rise-time photo-diode and a $12\ GHz$ oscilloscope, the timing of the two IR main pulses has been set with an uncertainty of $\pm15\ ps$. Within this time window, the ideal injection time had to be found experimentally, using a delay stage implemented in the beam-line that provided the pumping pulses for the amplifier medium. In the following, the delay of $1835\ ps$ will be referred to as $0\ ps$. It should be noted, that due to the large uncertainty of $\pm15\ ps$, only the relative delay provides useful information, the absolute values cannot be interpreted. As described in more detail in [28], the line foci pumping the seed and the injection mirror were tilted, in order to compensate the vertical separation between the seed- and the amplifier-plasma. Spatial overlap of the seed pulse with the amplification zone was estimated to 2%.

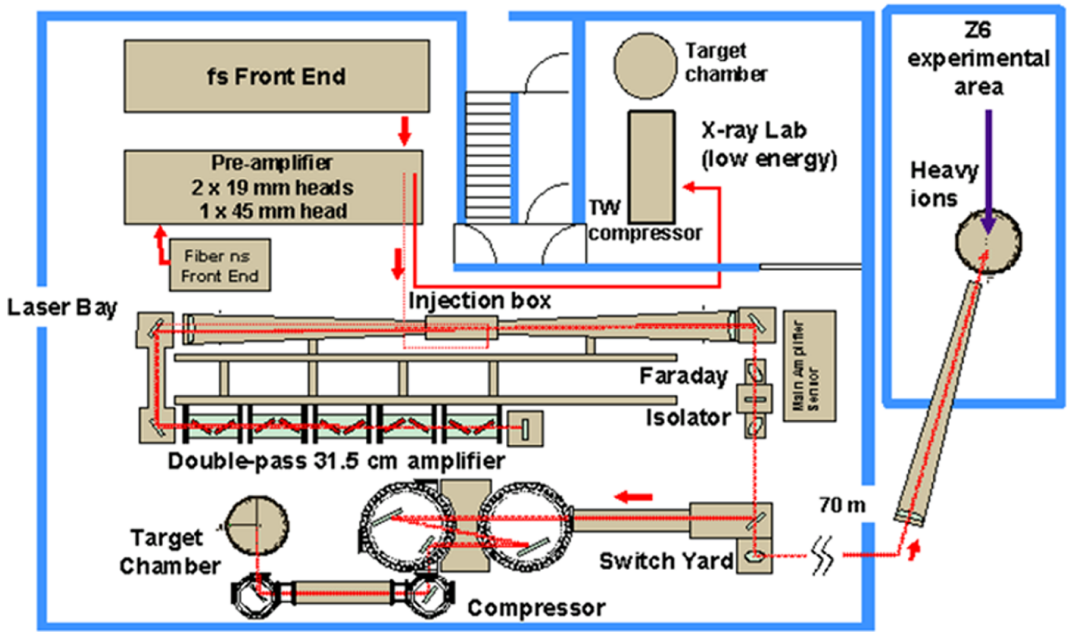

Figure 3.1: Schematics of the PHELIX laser system. The beam is presently used at three different target stations: 1) x-ray laser lab, 2) target chamber after the compressor, 3) target station "Z6" at the heavy-ion accelerator beam-line. from [34]

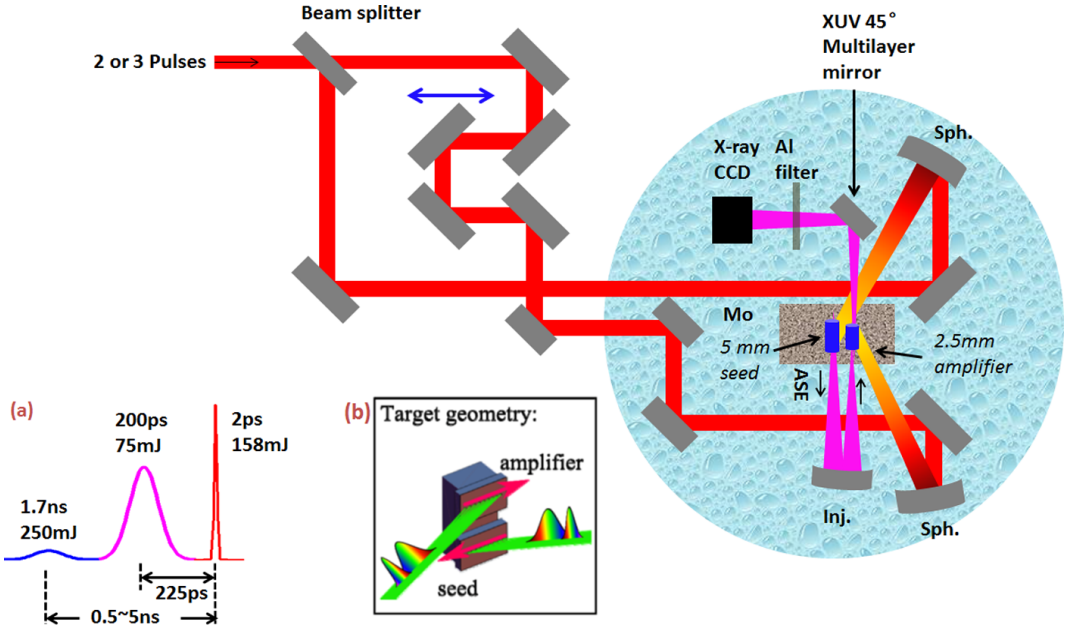

Figure 3.2: Sketch of experiment setup of ASE self-seeding with the three or two pulses GRIP shceme. Plasma driven laser pulses configuration is displayed in inset (a) and the seed-plasma and amplifiers are described in inset (b).

As a consequence, the setup should prove insensitive to pointing fluctuations of the ASE seed. To detect

the amplified seed signal, a $16-$bit back illuminated charge-coupled device (CCD) camera (Andor DX 434-BN) was positioned $40\ cm$ away from the target. In addition, a 45° XUV multilayer mirror, as well as set of aluminium filters of various thickness between $0.2\ \mu m$ and $4.1\ \mu m$ have been deployed. Finally, it should be noted that the experiments were carried out using the PHELIX front-end and pre-amplifier section only, which can be operated at a repetition rate of one shot in every two minutes.

3.1.2 Results in double grazing incident pumping

For ASE self-seeding operation using DGRIP, the following set of parameters has been used. Pulse durations of the pre-pulse and main pulse were chosen as $200\ ps$ and $2\ ps$, respectively, with an optimized delay of $225\ ps$ between each other. Each target was pumped by $300\ mJ$ of total pump energy, with an energy ratio of $25\% - 75\%$ for the pre-pulse and main pulse. In order to find the optimum injection time, the delay between the two IR heating beams has been varied in step of $1\ ps$. The first sign of amplification was observed in a $50\ \mu m$ wide region $40\ \mu m$ away from the target surface (see $Fig.\ 3.3$). This measurement series basically mapped the temporal development of the horizontal size of the gain zone, as represented in $Fig.\ 3.4$. During the first $6\ ps$ after injection the horizontal size of the gain zone increased, reaching its maximum of $170\ \mu m$ in a $1\ ps$ long time frame. Sequentially, the seed pulse amplification is decreasing due to the depletion of the population inversion within the amplifier medium. As expected, the vertical size of the gain zone, defined by the width of the line focus, remained constant. However, it should be noted that the measured vertical size of $30\ \mu m$ was significantly smaller compared to the $220\ \mu m$ width of the line focus. This discrepancy might indicate that the available amount of pump energy or intensity were not sufficient for this line focus width. According to $Fig.\ 3.4$, the life time of the gain (FWHM) can be estimated to $3\ ps$, which also presents the maximum duration of the amplified SXRL pulse. A maximum output pulse energy of 90 nJ was obtained as the gain medium reached its largest horizontal extension, corresponding to a total pumping efficiency (amplified seed pulse energy / total IR pump energy for both stages) of 2×10^{-7}. Defining an amplification factor by the ratio of photon counts of the ASE seed and the amplified seed, a maximum amplification of 60 was observed with $2.5mm$ long amplifier medium. $Fig.\ 3.3(a-c)$ show examples of the measured footprint patterns at different injection times, displaying the excellent homogeneity of the spatial profile of the amplified pulse. Its divergence amounts to $0.5\ mrad \times 4\ mrad$ at the optimum injection time ($Fig.\ 3.3(b)$), leading to a brilliance of $2\times10^{23}\ photons/s/mm^2/mrad^2$ in an estimated relative bandwidth of 5×10^{-5} [35].

3.1.3 Implementation of the third pumping pulse

According to above observations, with DGRIP scheme, the amplifier-plasma showed elliptical gain zone (optimum at $170\times30\ \mu m^2$) structure, and amplified beam showed asymmetrical divergence in horizontal and vertical as well as poor energy amplification (maximum 60 times) with high fluctuation. We therefore performed modified pumping scheme using a ns pre-pulse before the previous two pulses, as described in inset (a) of $Fig.\ 3.2$, which is so called TGRIP (GRIP with triple-pulse beam). The PHELIX laser system contains two independent Front-End delivering pulses of either nanosecond or femtosecond duration as depicted in $Fig.\ 3.1$. In front of the pre-amplifier section, the double-pulse created by the Mach-Zehnder interferometer in the short-pulse Front-End can be combined with the pulse generated by the long-pulse Front-End. Thus, the PHELIX pre-amplifier can provide two independent beams, each carrying an identical series of up to three collinear pulses. In contrast to the double-pulses of the short-pulse Front-End, the

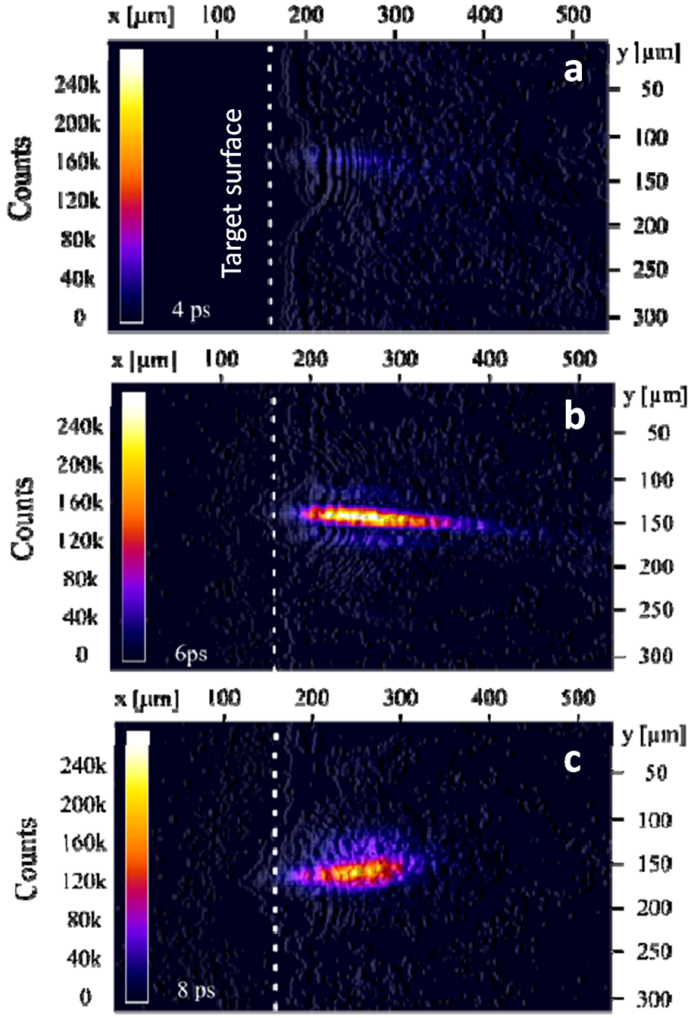

Figure 3.3: Amplified ASE seed beam profiles after $2.5\ mm$ *long plasma amplifier with different seed injection time at (a)* $4\ ps$*, (b)* $6\ ps$ *and (b)* $8\ ps$ *referred to the amplification curve displayed in* $Fig.$ 3.4*. The white dashed line indicated target surface location.*

pulses from the ns-Front-End are not chirped and will maintain their comparably long duration of $1.7\ ns$ while amplified to energies as high as $500\ mJ$. This energy is equally divided in the two pumping beams, leading to intensities of $\sim 2\times 10^{10}\ Wcm^2$ on both targets. In the following, these pulses will be referred to as ns-pulse, whereas the nomenclature of the pre-pulse and main pulse created by the short-pulse Front-End is maintained.

The influence of the preceding ns-pulse has been investigated using different pulse durations of the ns-pulse, and changing the delay between the pre-pulse and the main pulse. The delay between the maximum of the ns-pulse and the maximum of the main pulse has been varied from $5\ ns$ to $0.5\ ns$ by step of $0.5\ ns$. For these delays, several measurement series have been performed. Optimum amplified seed performance was achieved with the parameter set used in the DGRIP scheme described above, combined with a ns-pulse of 1.7 ns duration at a delay of $2\ ns$ - $3\ ns$. Here, it has been found that the third pulse has a beneficial effect on the properties of the amplified beam, as well as the magnitude of the gain,

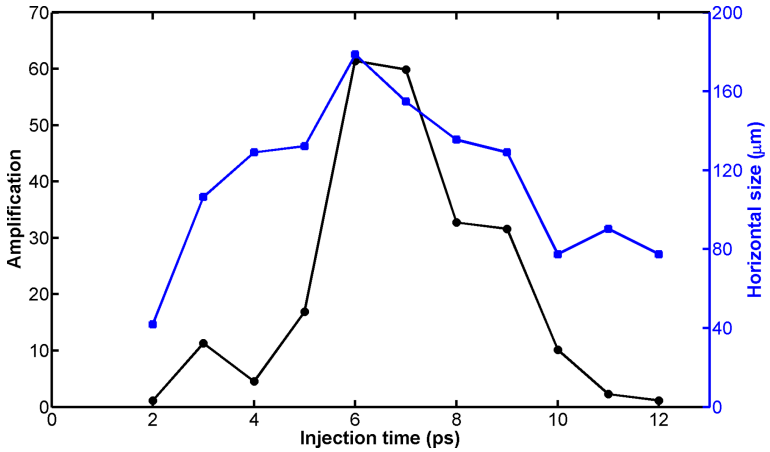

Figure 3.4: Temporal evolution of the amplification curve (black line) and horizontal size of the amplifier plasma gain zone (blue line). The injection time at $0\ ps$ *was not calibrated with respect to the pump pulse.*

which is consistent with the results presented by Cassou *et al.* [31]. The divergence of the final output beam added up to $2\ mrad \times 2\ mrad$, leading to a symmetric beam profile. As illustrated in $Fig.\ 3.5$, the footprint patterns of the amplified seed recorded in a series of consecutive shots on the same target position. The data also gives an account of the typical stability of the lasing. Remarkably constant are the shape and the horizontal position of the seeded SXRL beam. The vertical position showed a drift of $100\ \mu m/shot$ in the detection plane of CCD camera, probably due to a drift of a mechanical component inside the target chamber or of the pump laser pointing. An increasing trend of the energy of the SXRL pulses is related to the fact that a new target position was used at the beginning of this measurement series.

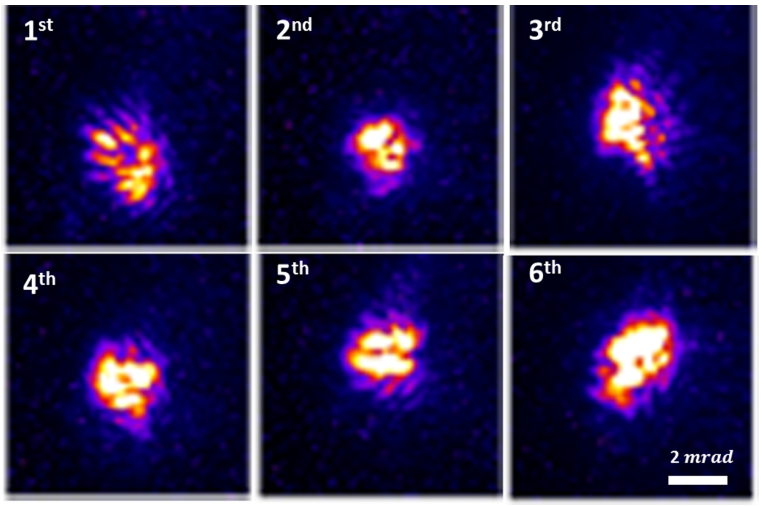

Figure 3.5: Shot-to-shot stability of the amplified seed beam through $2.5\ mm$ *plasma amplifier at DGRIP scheme.*

$Fig.\ 3.6$ shows the pulse energy of the seeded SXRL along injection times of the seed. As mentioned in the previous section, only the relative delays hold significant information while the absolute values cannot be interpreted. From this data, the lifetime of the gain within the Mo plasma can be deduced to $5\ ps$

(FWHM), which is longer compared to the $3\ ps$ (FWHM) observed in the double-pulse pumping scheme. At the optimum injection time ($12\ ps$), pulse energy of 240 nJ was achieved. Thus, the amplified seed pulse energy exceeded the energy of the original seed pulse ($120\ nJ$), despite the low spatial injection efficiency. The conversion efficiency obtained with triple-pulse pumping is identical to the efficiency achieved in DGRIP in a single target. The brilliance is improved by two orders of magnitude to 4×10^{23} $photons/s/mm^2/mrad^2$ with same relative bandwidth ($\sim5\times10^{-5}$).

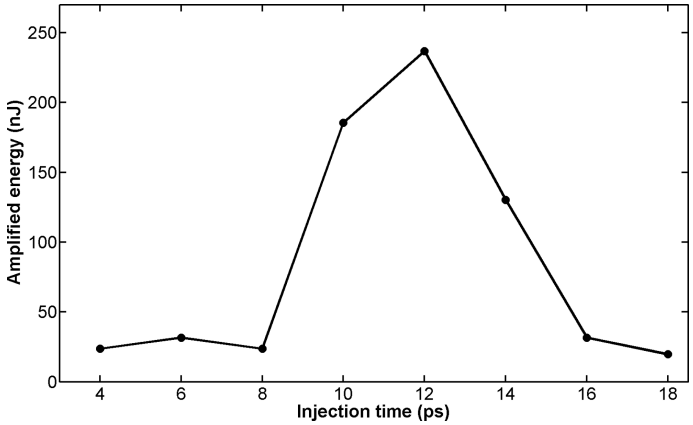

Figure 3.6: Energy evolution of the seeded SXRL pulse along the injection time.

3.1.4 Discussion and outlook

In this section, we demonstrated ASE self-seeded SXRL operated at $18.9\ nm$ using a double-stage plasma configuration with moderate pump energy. Applying a series of either two or three collinear pumping pulses under grazing incidence allowed for a remarkably simple and compact setup, relying only on a single target and two pumping beams. One of the most important results is a detailed mapping of the temporal development of the gain zone, providing valuable information for both Maxwell-Bloch codes and hydrodynamic codes (see **Chapter 4**). Despite the fact that a relatively low fraction of the seed pulse was injected, the amplified seed pulse energy of $100\ nJ - 250\ nJ$ was of the same order as the energy of the original seed pulse. However, due to the improvement of the beam quality, the brilliance of the amplified seed up to $4\times10^{23}\ photons/s/mm^2/mrad^2$ in the estimated relative bandwidth of 5×10^{-5} is two orders of magnitude larger respected to the seed.

The amplification factor of 60 observed in our experiments shows strong potential to reach higher SXRL pulse energy. The stable self-seeding operation demonstrated here indicates that the energy- and pointing-fluctuations of the original seed pulse were not limiting factors. Therefore a further increase of the spatial overlap between the ASE seed beam and the amplification medium should be possible without deteriorating the beam quality. This should lead to a more efficient energy extraction of the amplifier medium, until eventually saturation is reached. Using a higher pump energy in the amplifier zone with a wider line focus, much larger amplification medium could be generated, leading to a higher energy of the amplified SXRL pulse [36] (more discussion in Chapter 4). Moreover, due to the nature stochastic of incoherent ASE seed, this ASE self-seeding technique has several disadvantages, such as poor spatial coherence, long pulse duration (several ps) and inefficient amplification, which is extremely limited to

most of the high resolution SXRL phase imaging [22, 9]. A more efficient x-ray seeding approach with fully coherent seed source is required.

3.2 HH injection SXRL seeding experiment at LASERIX

Plasma-based ASE has attracted much attentions for the pursuit of high energy, ultrashort, coherent SXRL source over past three decades. Many practical techniques have been demonstrated achieving beam quality improvements, such as multi-pulse pumping [37, 38, 39], curved target [23], half-cavity configuration [35, 40, 41] and oscillator-amplifier system [28, 27, 83]. The proved mJ-class x-ray energy stored in the laser induced plasma [19, 20, 43] is attractive to the table-top SXRL development. Researchers realized that seeding is an expedient technique to extract the enviable energy from the laser-induced plasma.

As a practical attempt, ASE self-seeding was performed in above section. However, it is important to point out that the amplified output beam quality is fundamentally dependent on the optical properties of the seed pulse, as it occurs in the conventional amplification of Ti:sapphire lasers [44]. Owing to this inherited characteristic of the seeding technique, ASE with poor beam properties in spatial coherence, divergence and pulse duration are not adequate to achieve ultrashort, fully coherent amplified SXRL. Seeking for a fully coherent seed source becomes to be necessary. Coincidently, high order harmonic source was proposed towards soft x-ray region [45, 46] and was soon practically proved as fully temporal and spatial coherence in experiment [47]. This diffraction limited beam [48, 49] remains similar beam properties as the input driven laser beam, providing an excellent alternative for the seeding SXRL although the HH pulse energy is rather low ($< nJ$).

The first successful coherent x-ray seeding experiment was performed ten years ago [50], where fully coherent HH pulse was injected into a gas-based x-ray plasma amplifier. Final output exhibited as full saturation, strong energy ($\sim 1\ \mu J$), high coherence and full polarization inherited the resembling beam quality as the coherent HH seed, showing the attractive advantages of using coherent seed. Seeding with solid-plasma amplifier [51], which potentially stores much more energy in the x-ray plasma amplifier, was sequentially inspired. We therefore concentrate on this fully coherent seeded SXRL with solid-based x-ray plasma amplifier using the excellent HH seed.

3.2.1 Experiment details

The characteristics investigation of the HH-seeded SXRL was conducted at LASERIX laboratory (see $Fig.\ 3.7$). As illustrated in $Fig.\ 3.8$, high harmonics signal was generated by focusing $3\ mJ$, $50\ fs\ IR$ laser beam at the entrance of $1\ cm$ long argon gas cell (backup pressure $\sim 60\ mbar$) with $1\ m$ focal length. The titanium slab target was set $7\ cm$ away from the gas cell. Sequentially, the SXRL plasma amplifier was generated by the irradiation of three pulses to the Ti slab target—a ns-level long pre-pulse ($532\ nm$) coupled with two ps-level short pump pulses ($810\ nm$), which are described at the inset figure. Pre-pulse ($150\ mJ$, $6\ ns\ FWHM$ Gaussian pulse) from a Nd: YAG green laser ($532\ nm$) was focused into a $4\ mm \times 200\ \mu m$ line on the slab target with normal incidence by adopting a cylinder lens and a spherical mirror. The created warm plasma was subsequently expanding. The 1^{st} short pulse ($\sim 370\ mJ$, $5\ ps\ FWHM$ in Gaussian) was arriving at the target at $3\ ns$ after the peak of the YAG pre-pulse. It was focused into a same line as the pre-pulse and with 20° grazing incident angle to promote the plasma to

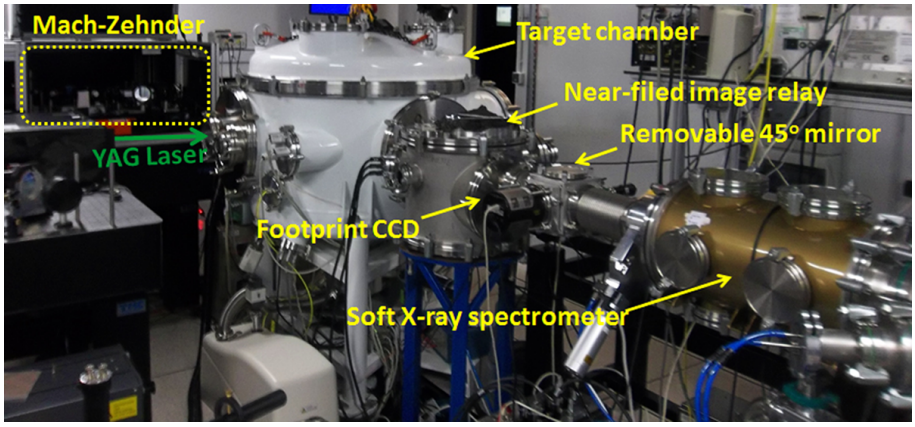

Figure 3.7: Picture of the seeding SXRL experiment beam line at LASERIX. The near-field image system constituted with a spherical mirror ($f = 0.5\ m$), a pair of $BK7$ flat mirrors, two removable Al filters and an x-ray CCD.

Ne-like ionization stage. Finally, plasma was heated by a 2^{nd} short pulse ($\sim 610\ mJ$, $5\ ps\ FWHM$ in

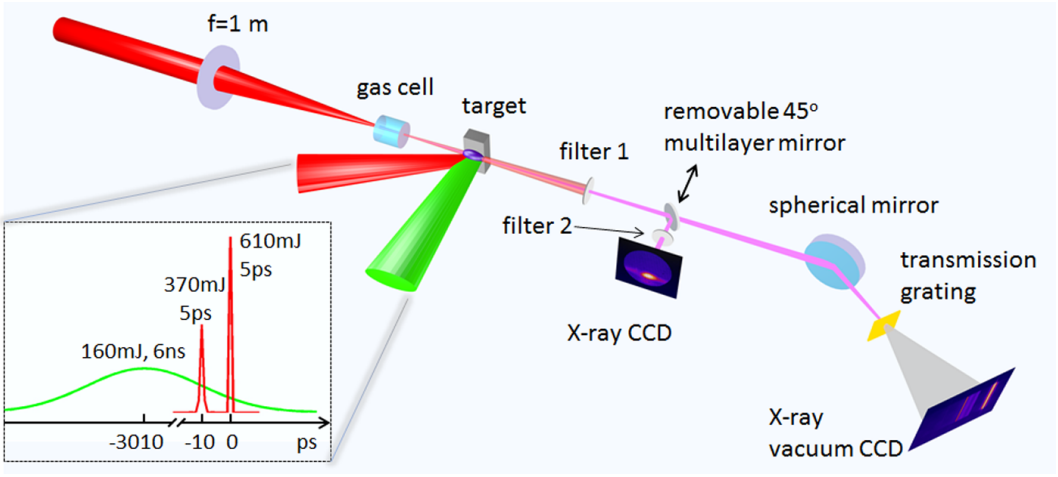

Figure 3.8: Schematic diagram of HH-injection seeded SXRL experiment in LASERIX.

Gaussian) following the 1^{st} short pulse beam path but with $10\ ps$ peak-to-peak time delay. Large population inversion between the upper lasing level and lower lasing level was eventually generated as explained in **Chapter 2, Section 2.6**. Grazing incident angle of the two short pump pulses are involving with the travelling wave compensation [52] (see **Chapter 2, Section 2.6.3**). Moreover, the two short pulses were generated employing a pellicle coupled with a wave-plate, as depicted in $Fig.\ 3.9$, where a detailed layout of the target chamber was described.

The seeded SXRL is emitted along the direction of the line focus and has a privileged amplification following the direction of the travelling wave. Final output was analysed by different systems. An aluminium filter with $300\ nm$ thickness was placed at $1\ m$ after the plasma amplifier to stop the IR laser. A removable 45° multilayer flat mirror was employed sending the beam to the x-ray CCD and spectrometer, respectively, which was positioned at $16\ cm$ after the first Al filter. The alternative diagnostics for footprint and spectral information of the final output SXRL was controlled by turning the 45° multilayer mirror. For

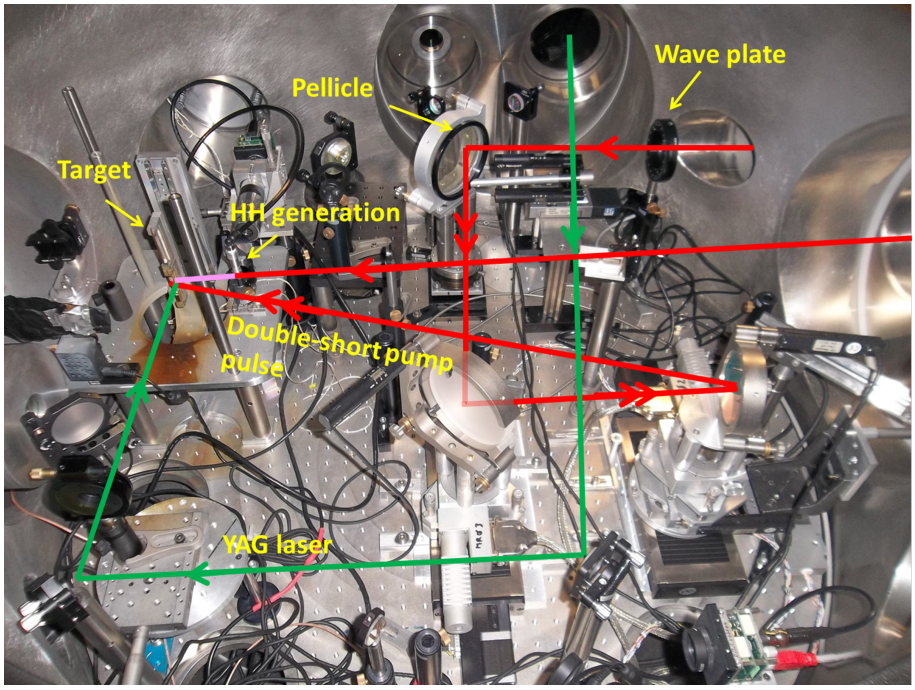

Figure 3.9: Layout of the target chamber with the four laser beams. YAG green laser irradiated to the titanium slab target is dedicated to create warm plasma, which was sequentially reaching the high ionization stage (Ne-like) and strong population inversion by the double-short lasers generated by the pellicle. The high harmonics beam was generated using a $1\ m$*-focal-length lens to focus the IR driven laser at the entrance of a* $1\ cm$ *long argon gas cell.*

the footprint beam detection, the 45° multilayer mirror has to be activated and an extra removable $300\ nm$ Al filter with grids was set in front of the x-ray CCD in order to avoid the detector saturation. The footprint CCD was installed at $10\ cm$ after the 45° mirror. However, without using the 45° multilayer mirror, the output SXRL is available for the spectrometer detection, which is composed with transmission grating ($13\times13\ mm^2$, $1000\ lines/mm$) and a vacuum x-ray CCD. A spherical mirror was employed delivering the SXRL beam to the transmission grating, which also allows a horizontal focusing effect.

In addition, there is a near-field imaging system for the exit of the plasma amplifier installed in the big target chamber and the followed smaller chamber as depicted in $Fig.\ 3.7$. It is constituted with a spherical mirror ($f = 0.5\ m$), a pair of $BK7$ flat mirrors, two removable Al filters ($1\ \mu m$ and $0.3\ \mu m$). The spherical mirror is for the imaging relay and $BK7$ mirrors are used to substantially reduce the IR driven laser and two removable filters are contributed to the flexible final near-filed detection of the exit of this plasma amplifier.

3.2.2 Characteristics of the coherent seeding

First of all, optimizing HH seed beam footprint and spectral profiles were performed, which is the guarantee of the SXRL seeding. HH beam ($<2\ mrad$) was generated from argon gas cell and the footprint image was illustrated in $Fig.\ 3.10\ (a)$. The spectra of the HH pulse was detected without the 45° multilayer mirror, as it shown in $Fig.\ 3.10\ (b)$. It is apparent that the left beam spots with symmetrical diffraction orders are contributed by the IR laser, which is not well stopped without using the 45° multilayer mirror. The zero

order of the IR laser ($810\ nm$) is located at the centre of the left spots. One could also observe the high order harmonics signals mixed with the diffraction signals at the right part of the spectral image. High har-

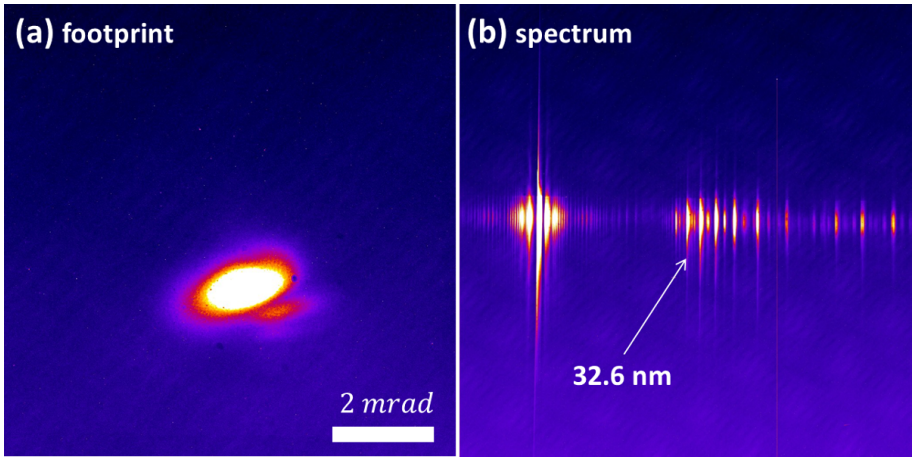

Figure 3.10: Footprint (a) and spectrum (b) of HH seed generated from argon gas cell.

monics generation is dependent on the quantum effect during IR laser interactions with the gas-plasma in the cell. All the orders are respected to the centre wavelength of the IR driven laser ($810\ nm$). The most interesting wavelength for the SXRL seeding experiment is $32.6\ nm$ as marked in the $Fig.\ 3.10(b)$ for the 25^{th} HH order. In the sake of the guarantee for SXRL seeding, shot-to-shot HH beam energy stability was measured and represented in $Fig.\ 3.11$, where three typical HH beam profiles were included. Energy stability from shot-to-shot was obtained as $\pm 16\%$ over 20 consecutive shots, which is sufficient for the input condition as coherent seed source for the SXRL seeding experiment.

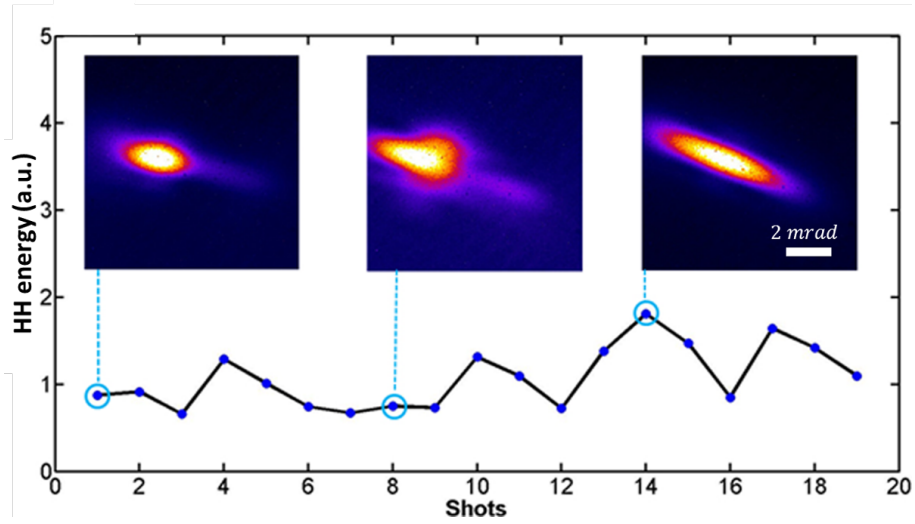

Figure 3.11: HH signal shot-to-shot stability for the SXRL seeding experiment. The three sample images indicate the typical beam profiles and energy statbility obtained as $\pm 16\%$.

By adopting a BBO crystal coupled with a normal camera, one can calibrate the arrival time of the HH seed and the peak of the 2^{nd} short pump pulse at the centre location of the target. This timing calibration

was done in the air using HH-driven laser (IR laser) instead of the HH seed to check the spatial and temporal overlap between the HH beam and peak of the 2^{nd} pump pulse. The spatial overlap can be easily checked by the camera vision. However, the time matching is due to the weak lasing light (double frequency) emitted between the two separated beams at afterwards of the overlap point. The $T = 0\ ps$ was eventually set as the same arrival time at the centre of the plasma amplifier between HH seed and the 2^{nd} short pump pulse. The timing error during the alignment is estimated as $\pm 0.3\ ps$. It is important to note that the distance between the centre of the gas cell and the centre of the plasma amplifier is $7\ cm$. By controlling the time window, HH seed was directly injected to the Ti-based plasma amplifier without any injection optics.

The 25^{th} HH order was then amplified due to the $3d^9 4d(J = 0) \rightarrow 3d^0 4p(J = 1)$ transition line in the $2\ mm$ long Ti plasma amplifier. Some typical footprint image of the final output beam are displayed in *Fig.* 3.12, from $t = -2.3\ ps$ to $t = 3\ ps$. It is worth nothing that the images with grids shadow were detected using double $300\ nm$ Al filters, and only one $300\ nm$ Al filter was employed for the rest. Fist of all, an apparent temporal evolution of the amplified seed beam was observed with maximum amplification appearing at $T = 0.3\ ps$. This is because of the collisional pumping conditions in the plasma amplifier which is due to the three pulses configuration for creation of the x-ray plasma amplifier (see the inset figure in *Fig.* 3.8). It is also the hydrodynamic behaviour of the dense plasma. Secondly, a deformed beam

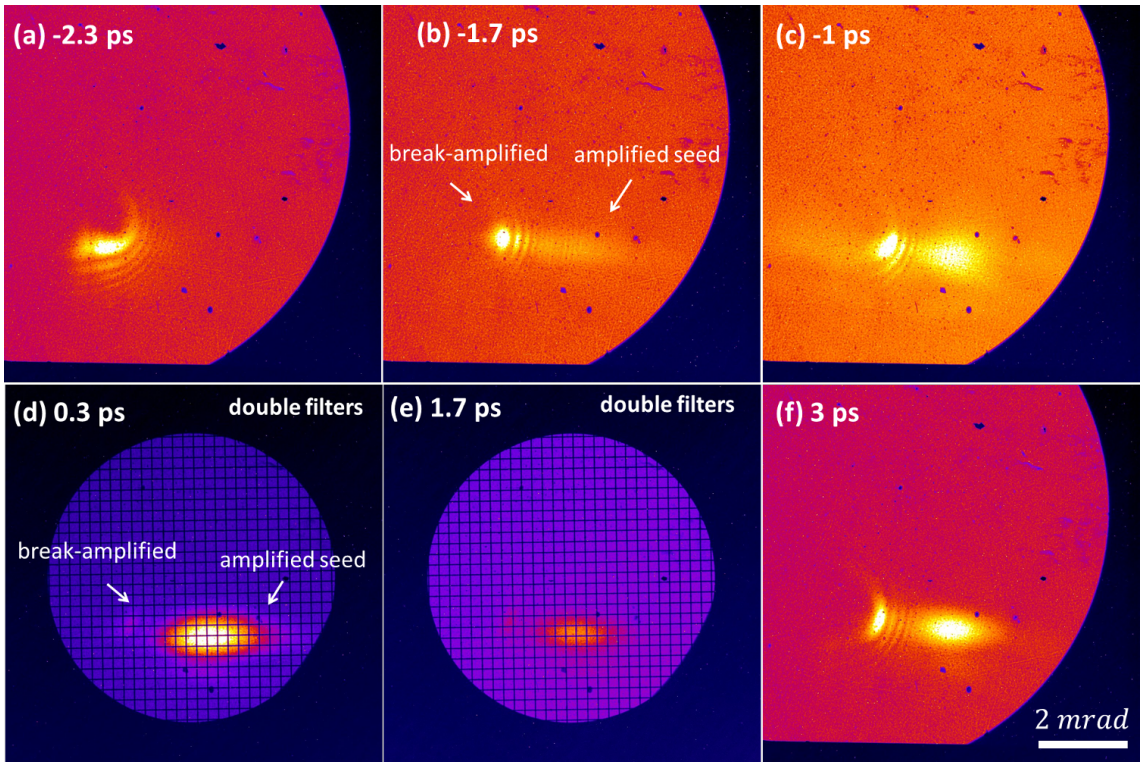

Figure 3.12: Footprint images of amplified SXRL at different delays between the peak of 2^{nd} short pump pulse and arrival of HH seed. The deflected angle of amplified SXRL was $4\ mrad$ with respect to the HH seed.

is visible at each delay by the left of the main amplified seed beam. The intensity of this deformed beam is varying from the different injection times of the HH seed. This is considered as the break-amplified HH seed, which is deflected by the dense plasma due to the density gradient. The refractive index of the x-ray

plasma is described by Eq. (2.22), which is proportional to λ^2. Coupled with divergent seeding approach of the HH injection (without any imaging optics), this strong refraction effect deflected the $32.6\ nm$ SXRL (more discussion in **Chapter 4, Section 4.3.3**). Another fact is the estimated HH beam size ($150\ \mu m$) at the plasma location is much bigger than the efficient gain zone ($\sim 40\ \mu m$), therefore, owing to the spatial mismatching, the un-amplified seed can be also detected. Both effects contributed to this double spots behaviour. Moreover, one could see the strong fringes between the two spots, which are caused by the interference between the two coherent beam (break-amplified seed and fully amplified seed) due to the deflection by the plasma.

We therefore extracted the amplified seed signal carefully from detection plane, and plotted the amplification curve as a function of seed injection time represented in $Fig.\ 3.13$. The rapid rising time and narrow gain life time ($3\ ps$ at FWHM) were observed due to the double short pumping pulse configuration. The red line is corresponding to the 2^{nd} short pump pulse. It is interesting to point out that the peak of the gain achieved at exactly the arrival peak time of the 2^{nd} short pump pulse.

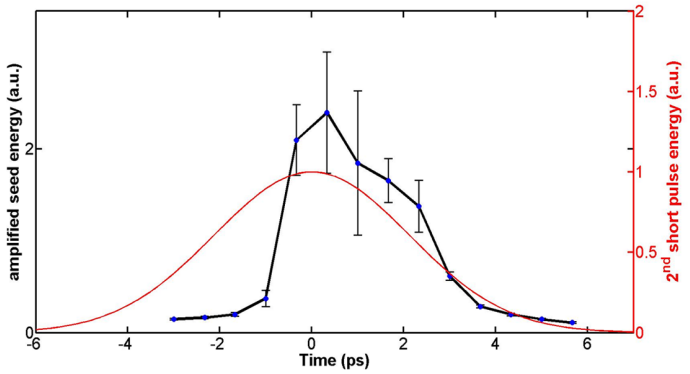

Figure 3.13: Black line represents the SXRL amplification curve by seeding the HH beam to $2\ mm$ long plasma amplifier with different delays between the peak of the 2^{nd} short pulse and arrival of HH seed. The time at $0\ ps$ is corresponding to the peak of the 2^{nd} short pulse with $5\ ps$ pulse duration (FWHM), as described in the inset of $Fig.\ 3.8$. The red line indicates the temporal profile of the 2^{nd} short pulse. add the horizontal time error bar

Thanks to the flexible imaging relay system, the near-field images of (a) HH seed, (b) ASE and (c) amplified seed at the exit of the $2\ mm$ plasma amplifier are obtained in $Fig.\ 3.14$. All the three cases were detected with same Al filter configuration ($300\ nm$). $Fig.\ 3.14(b)$ shows only the ASE images without seed. The near-field images are giving clear gain zone distribution. The right edge indicates the target surface. In $Fig.\ 3.14(c)$ the CCD saturation was achieved when seeding the HH pulse into the dense part of the plasma region (gain region). This encouraged us to make more near-field images from various plasma amplifiers. The exit of the plasma amplifier without any seed pulse were imaged as displayed in $Fig.\ 3.15$, with plasma column length from $1.5\ mm$ to $4\ mm$. ASE is significant increased with the plasma length from $2\ mm$ to $3\ mm$. Therefore, different filters were employed: $0.3\ \mu m$ thick Al for $1.5\ mm$ and $2.0\ mm$ long plasmas; $1\ \mu m$ thick Al for $3\ mm$ and $4\ mm$ long plasmas. One should note that there is a stronger/denser part of the plasma amplifier appear at certain distance (~ 15) μm from the target surface. A specific gain zone can be defined around this strongest region.

Furthermore, the near field images from a variety of plasma amplifier lengths with HH seeding were obtained (see $Fig.\ 3.16$). It is interesting to note that these images including three typical parts: the general warm plasma, high density region and amplified seed beam (bright spot). The HH seed beam

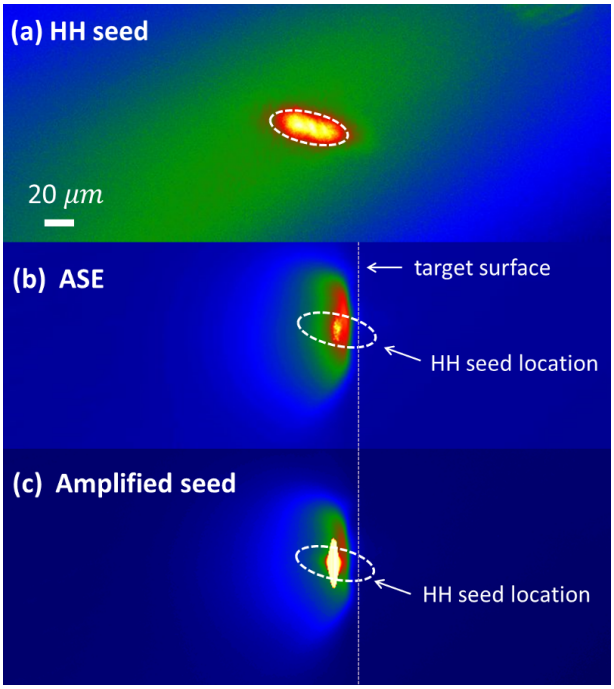

Figure 3.14: Near-field images at the exit of the $2\ mm$ *plasma amplifier.*

location is also marked by the dashed circle. There is a separation observed between the high density part of the plasma and amplified seed beam. It could be caused by the refraction when SXRL propagating in the dense plasma. As increasing the plasma length, separation between the amplified seed and the gain zone is becoming slightly larger. Especially in $Fig.\ 3.16(d)$, only the high density plasma was visible while amplified seed beam was deflected away and beyond the detection region of the detection system. It is implied that refraction effect becomes much stronger when increasing the plasma length. In comparison, we drew the HH beam for each near-field images with respect to the HH location without the plasma amplifier. One should beware of that the direct HH seeding approach indicates a divergent HH seed injection to the plasma amplifier.

In summary, we performed the first successful HH-injection seeded SXRL with Ne-like plasma at LASERIX. This direct injection configuration was observed with apparent amplification once propagation in the plasma amplifier. This seeding technique without coupling mirror makes simpler experiment operation and remains higher energy of the seed pulse. However, strong refraction was achieved, due to the divergent seed beam propagation in the large density gradient medium. In order to get efficient seeding approach with higher amplification, one would suggest using a compensated injection mirror for the seed pulse to a short plasma medium. Considering the plasma refractive index is proportional to the λ^2, shorter wavelength has also less contribution to the refraction. Further seeding experiment would be suggested to operate with shorter wavelength, shorter plasma amplifier, higher HH seed pulse and refraction compensation (such as injection imaging mirror and curved target).

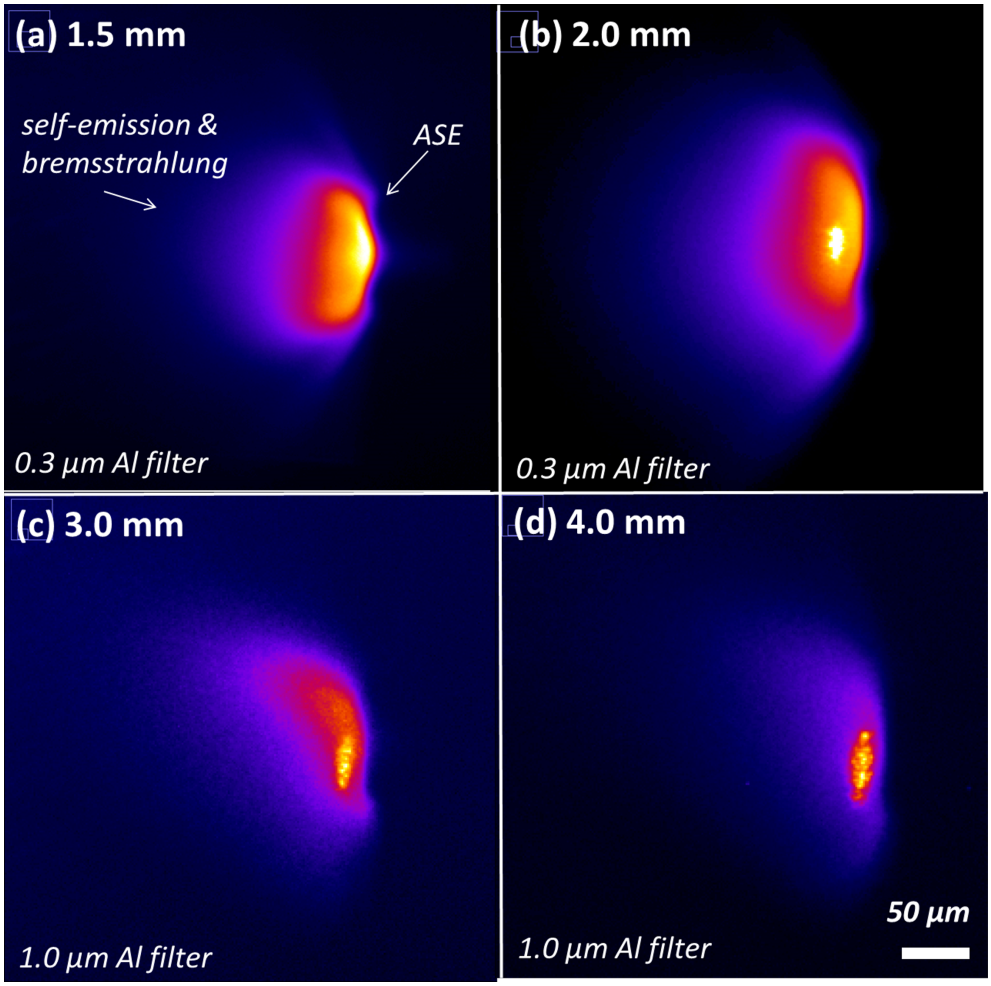

Figure 3.15: Near-field images of SXRL plasma amplifier ***without*** *seeding for (a)* $1.5\ mm$*, (b)* $2.0\ mm$*, (c)* $3.0\ mm$ *and (d)* $4.0\ mm$ *long Ti target. The short pump pulse duration is* $5\ ps$ *at FWHM. The size of the supposed lasing region was remarked in the lower right of each figure.*

3.3 Experiment on wave front of HH-seeded SXRL

Coherent seeding approach with x-ray plasma amplifier has brought a bright perspective to develop high saturation, fully coherent and ultra-fast table-top SXRL source. With the purpose of high resolution phase contrast and diffraction imaging, an increasing of spatial coherence is important. Besides, the wave front of the beam must also be excellent. Indeed, imaging a sample with a phase contrast microscope and a coherent source having an aberrated wave front will reduce the resolution and may even distort the image. On the other hand, wave front characterization is also related to the radiation intensity of the beam spot with micrometer dimension, as explained in the relation with Strehl ratio [53]. Furthermore, a good wave front of the beam source is contributed to match the subsequent spectral compensation, such as the proposed SXRL compressor [54] (see **Chapter 4, Section 4.7**). Previous work on wave front of the HH source [48] and gas-plasma-based seeded SXRL source [69] showed near-diffraction limited characteristics. However, the wave front of HH-seeded SXRL from solid-based plasma amplifier

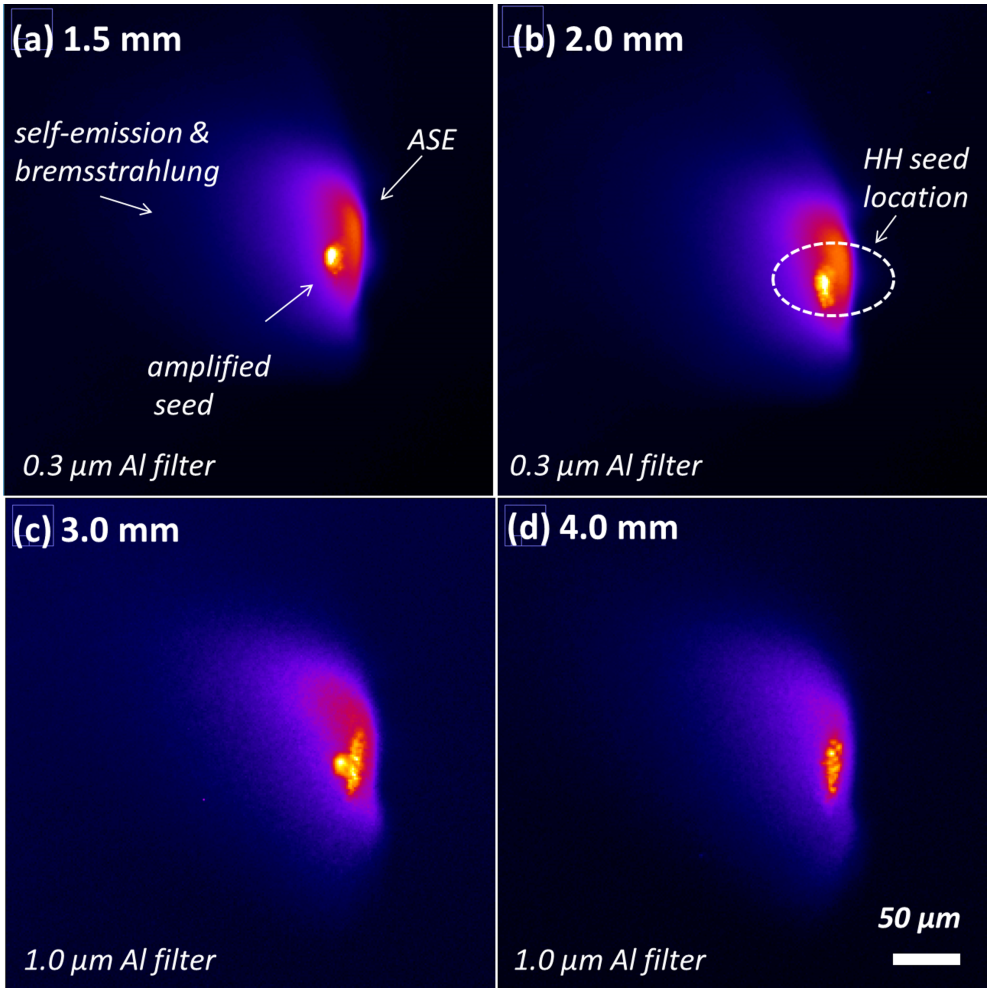

Figure 3.16: Near-field images of SXRL plasma amplifier ***with*** *HH seed for (a)* $1.5\ mm$*, (b)* $2.0\ mm$*, (c)* $3.0\ mm$ *and (d)* $4.0\ mm$ *long Ti target. The short pump pulse duration is* $5\ ps$ *FWHM and HH beam size in the plasma is ∼60* μm *FWHM. The seeded SXRL (SSXRL) source size (FWHM) is* $12\ \mu m$*, 16* μm *and 20* μm *for* $1.5\ mm$*,* $2.0\ mm$ *and* $3.0\ mm$ *long plasma amplifier, respectively. It is interesting to note that , for the case of* $4\ mm$ *long plasma, the amplified seed was deflected away from detection system due to the reflection.*

had not been studied prior to this work. Despite its crucial role in the applications and high intensity achievement.We therefore performed an experiment [55] at Colorado State University to measure the wave front of HH-seeded SXRL based on solid-plasma amplifier. X-ray Hartmann wave front sensor [56] was employed to detect the output beam.

In this section, we firstly described working mechanism of the x-ray Hartmann wave front sensor in **Section 3.3.1**. Then, the structure and calibration of the sensor was introduced in **Section 3.3.2**. Finally, the wave front study of HH seed and amplified seed coupled with the detailed discussion were represented in **Section 3.3.3**.

3.3.1 Theory of wave front sensor

A wave front sensor is commonly used which allows the measurement of the phase of the incoming light. In the SXRL region, there are several typical techniques to measure the wave front, such as Shack-Hartmann wave front sensor [57], Shearing Interferometer [58], AIS wave front sensor [59], Wigner distribution function [60, 61], curvature sensing and Hartman wave front sensor [56]. We use x-ray Hartman wave front for the seeded SXRL wave front measurement in this experiment.

3.3.1.1 Wave front sensor operation

The Hartmann sensor was invented a century ago to perform optical meteorology [62]. Subsequently these sensors have been adopted to a wide variety of applications including adaptive optics, ophthalmology, and laser wave front characterization. We chose this sensor for the SXRL wave front measurement in this experiment as a direct and efficient approach. This Hartmann wave front sensor [56] consists of an aperture array mounted a distance from the detection plane (CCD). $Fig.\ 3.17$ shows the schematic diagram of the sensor operation. Light incident on the sensor along $z-$axis first encounters the aperture array. Each of the aperture acts like an optical lever, displacing the diffracted spot proportional to the average phase tilt over the aperture. The wave front sensor measures the tilt over each aperture by comparing the measured positions of the diffracted spots to the positions of the diffracted spots for a reference input beam. If the overall wave front were flat, that is, if every isoplanatic region has zero tilt and all parallel, each aperture would produce an diffraction pattern at a null position between its own four pixel elements, as the black spots shown in $Fig.\ 3.17$, which is considered as the reference. When considering a coherent beam with distorted wave front, the isopanatic region is tilted, the corresponding diffraction image spot shifts and the four CCD elements record a unbalanced signal that indicates the exact displacement, as depicted in the right images of $Fig.\ 3.17$. The tilt measurements are then converted into a replica of the wave front by performing a form of integration called wave front reconstruction. The reference diffracted spots are normally recorded by with a plane wave or spherical wave, this process is so called sensor calibration, which will be discussed in Section 3.3.3.

3.3.1.2 Wave front recording

For the coherent beam, the first step in measuring a wave front with the Hartmann wave front sensor is to determine the location of the diffracted spots. We use the coordinate system shown in $Fig.\ 3.17$. The z-axis is the optical axis normal to the planes of the CCD and aperture arrays. The x and y axes are located in the plane of the CCD array. The sensor is calibrated by recording an image of a uniform plane wave or a spherical wave, as recorded as black spots in $Fig.\ 3.17$. It is important to note that, the diffracted spots from reference beam are illustrated as same tidy array as the aperture array, while diffracted spots from an arbitrary incident wave front are usually deviated from the tidy array. Diffracted spot locations are then determined from the reference image by calculating their centroids or first moments along both the x-axis and the y-axis. The centroid in the x direction, $\bar{x}$, of an arbitrary intensity pattern is given as [63],

$$\bar{x} = \frac{\int_{-\infty}^{\infty}\int_{-\infty}^{\infty} I(x,y)\cdot x\cdot dx\cdot dy}{\int_{-\infty}^{\infty}\int_{-\infty}^{\infty} I(x,y)\cdot dx\cdot dy}. \tag{3.1}$$

Where $I(x,y)$ is the intensity as a function of x location and y location. To apply this equation for Hartmann sensor, it needs to be modified. The CCD behind the Hartmann wave front sensor is comprised of a

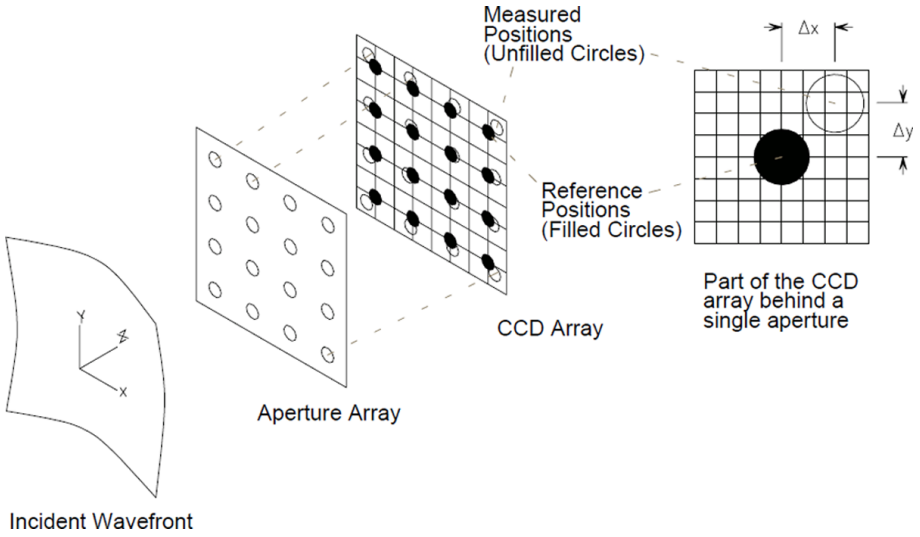

Figure 3.17: Drawing of the Hartmann wave front sensor operation. Showing an incident wave front traveling along the z-axis illuminating an aperture array and the diffracted spots illuminating a CCD and the displacement of a single diffracted spot from the reference location on the CCD. from [63]

set of discrete pixels that we describe by the variable i along the x-axis and j along the y-axis. It is allowed to replace the integral with a summation. A rectangular grid of apertures is typically used when building Hartmann wave front sensors to roughly match to the rectangular grid of photo-detectors in the CCD. To find the locations of all the diffracted spots, the image firstly divided into an array of small rectangular sections of pixels that are centered on the apertures with sides as long as the aperture spacing. Therefore, the general centroid equation can be written as [63],

$$\bar{x} = \frac{\sum_{i_{min}}^{i_{max}} \sum_{j_{min}}^{j_{max}} I(i,j) \cdot i}{\sum_{i_{min}}^{i_{max}} \sum_{j_{min}}^{j_{max}} I(i,j)} \cdot s. \tag{3.2}$$

Where $I(i,j)$ is the intensity measured by the pixel in the i^{th} row and j^{th} column, s is the spacing of pixels along the x or y axes. The same equation can be used to determine the position of the diffracted spot along the y-axis. The intensity used in the centroid calculation, $I(i,j)$, is actually a threshold limited intensity value. If the intensity is above the threshold the intensity value minus the threshold is used in the calculation. If the intensity is below the threshold, the intensity at this pixel is set to zero. Threshold limiting the intensity helps to minimize the effects of noise due to the camera and due to light diffracted out of the primary diffracted order.

The gradient of the wave front can be calculated based on the motion of the centroid of a diffracted spot. To perform any measurement, the Hartmann wave front sensor is illuminated with a beam whose wave front, $\Phi(x,y)$ is being measured and the diffracted spot positions are determined from the CCD image using the centroid algorithm. The slope of the measured wave front is determined by measuring the spatial displacement of a diffraction pattern from that due to a reference wave (plane or spherical wave front) incident on the same aperture array. As it presented in the right inset of *Fig.* 3.17, the average gradient of the wave front over the aperture diameter along the x or y axes is calculated using

the equation, [63]

$$\frac{d\phi(x,y)}{dx} = \frac{\triangle x}{l}, \tag{3.3}$$

$$\frac{d\phi(x,y)}{dy} = \frac{\triangle y}{l}, \tag{3.4}$$

here, l is the distance between the aperture array and the detector array.

3.3.1.3 Wave front reconstruction

Once the local wave front slopes have been determined, the wave front can be reconstructed by performing a type of integration on the gradient measurements. The HASO software can calculate the wave front surface in two primary wave front reconstruction algorithms types, which are Zonal and Modal. The Zonal wave front reconstruction is a type of numerical integration. The Modal wave front reconstruction fits the data to a set of orthogonal surface polynomials.

Zonal reconstruction mode is often used in beam alignment phases or in laser beam analysis, because it can be adopted to all types of pupil. Its local slope signal integration concept lets it preserve all the spatial high frequency information that makes the reconstructed wave front sensitive to any noise on a local slope. To choose an appropriate pupil size is fundamentally required. This is the only method that can be used for a special pupil shape, such as the seeded SXRL shapes. It is advantageous to use a Zonal reconstruction method in the adjustment phase because the beam moves on the sensor. The phase front can then be measured on all computable sub-apertures. In addition, the phase front is then displayed on the physical pupil. The pupil and the beam aberrations can then be viewed on the same window. The method used in this mode is attributed to Southwell, known as the Successive Over Relaxation Method [64]. The idea behind the Southwell's reconstructor is to minimize the error between the reconstructed wave front and the measured wave front slopes. To achieve this goal, a scan is made through the entire grid of wave front slope data and the wave front height is calculated at each point as average height predicted by each of the neighbours as follows [63],

$$\phi_{n,m} = \sum_{j=-1}^{1}\sum_{i=-1}^{1} I_{n+i,m+j}\cdot[\phi_{n+i,m+j} + (\frac{\frac{\partial\phi}{\partial x_{n,m}} + \frac{\partial\phi}{\partial x_{n+i,m+j}}}{2})\cdot\triangle] \tag{3.5}$$

where $\phi_{n,m}$ is the wave front at grid location (n,m), $\triangle$ is the separation between the (n,m) integration area and the $(n+i,m+j)$ integration area, and $I_{n+i,m+j}$ is the intensity measured in the $(n+i,m+j)$ integration area.

Modal reconstruction mode has the advantage of providing the best possible determination of the low spatial frequencies of the wave front such as tilts, curvature and third-order aberrations. This method calculates the coefficients of the reconstruction polynomials (Legendre or Zernike), which are often used in the field of optical metrology. The main disadvantage of this method is that it filters the high spatial frequencies during reconstruction. It also introduces a constraint: the pupil must have a simple shape (round or rectangular). This reconstruction is useful in solving problems involving the characterisation of optics. It is used when a list of polynomial coefficients needs to be calculated. It is not recommended when beams have high spatial frequencies (Fresnel lenses, etc.). Modal reconstruction requires a base of orthogonal polynomials on a fixed support. The well-known Zernike polynomials of particular interest in the case of circular and annular apertures as they are related to the classical aberrations [65] are

used. Legendre polynomials are used for a rectangular pupil. Some of the important low-order Zernike and Legendre polynomials are listed in the Appendix $Tab.\ A.1$ and $Tab.\ A.2$, respectively.

3.3.1.4 Wave front sensitivity

The sensitivity of the wave front sensor depends on the sensor's ability to determine the position of the diffracted spots on the CCD array. The error in determining the diffracted spot location includes a set of factors such as CCD detector noise, coherent optical crosstalk between diffracted spots from different apertures, and CCD digitization error and incoherent beam affect. CCD detection noise is often coming from the dark current due to the operation temperature. The interference between the diffraction patterns from adjacent array elements can be reduced by a specific design of the aperture shape. CCD digitization error often corresponds to the read out problem, which is sensitive with the trigger signal and shuttle controlling. In the x-ray seeding experiment, the incoherent signal (ASE) always occurs as the background signal full filled the detection plane. The RMS error in the diffracted spot location for the wave front sensor was measured by evaluating the spot position of a stable wave front repeatedly with the sensor and measuring the RMS error in the spot position location. The RMS wave front error is measured by illuminating the sensor with a beam of non uniform-intensity with a non-planar wave front. The sensor evaluates the wave front many times and determines the RMS difference between the individual measured wave front and an average value evaluated at each of the apertures. The RMS wave front error, ϕ_{RMS} , associated with a Hartmann wave front sensor is related to the quality of the reconstruction algorithm, the length of the apertures, the size of the apertures, and the RMS spot location error. The ϕ_{RMS} can be expressed as,

$$\phi_{RMS} \approx F_{reconstructor} \cdot \frac{d}{f} \cdot \triangle x_{RMS}, \tag{3.6}$$

where $F_{reconstructor}$ is a factor determined empirically by the type of reconstructor used, d is the size of an aperture in the Hartmann plate, and f is the aperture diffracted length. The reconstruction factor is usually between 1 and 10 for most reconstructor. When the HASO application reports the RMS wave front error, it is simply a measure of the average deviation of the reconstructed wave front from the plane wave case [63]:

$$\phi_{RMS} = \sqrt{\sum_n \sum_m \phi_{n,m}^2} \cdot \frac{1}{N}, \tag{3.7}$$

here, N is the pupils number taken into account in the calculation. Note that the wave front calibration limit (accuracy) of the Hartman sensor used for this experiment is $\lambda/32\ RMS$ at $18.9\ nm$ [48].

3.3.2 Structure and calibration of Hartmann wave front sensor

3.3.2.1 Sensor introduction

In this wave front measurement experiment, we used the Hartmann wave front sensor developed at Laboratoire d'Optique Appliquée (LOA) in collaboration with Imagine Optics and SOLEIL [56]. A photograph and schematic diagram of the sensor are demonstrated in $Fig.\ 3.18(a)\ and\ (d)$, respectively. In $Fig.\ 3.18(a)$, the metallic bellows system is for the mechanical alignment of this sensor. Structure

of Hartmann wave front sensor displays clearly the two basic components: Hartmann plate and x-ray CCD. Distance between the Hartmann plate and CCD detection plane is $310\ mm$. Hartmann plate plays the role of aperture array which is composed of 51×51 square holes with 80 μm size and separation of 380 μm. This $19\times19\ mm^2$ plate is made of 100 μm thick nickel. All the square holes are rotated by 22.5° to minimize the interference from the adjacent holes diffraction (coherent optical crosstalk between diffracted spots), as described in $Fig.\ 3.18(c)$. The back-illuminated CCD camera (PIXIS XO 1024B) is adopted for direct detection in a range of x-rays between $30\ eV$ and $20\ keV$. Quantum efficiency of this CCD over the wide bandwidth is displayed in $Fig.\ 3.18(d)$.

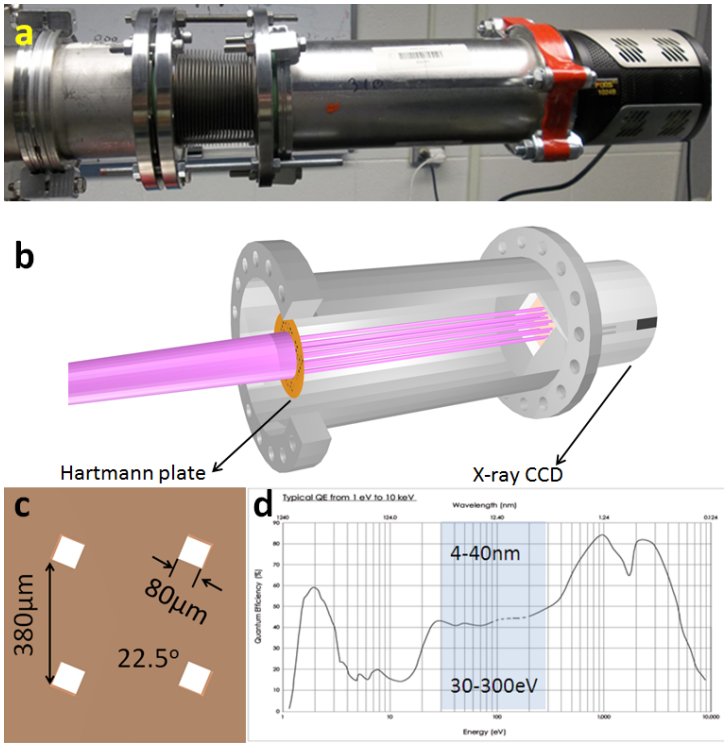

Figure 3.18: Photograph (a) and mechanism diagram (b) of Hartmann wave front sensor, with parameters of Harmann plate (c) and wide work bandwidth and quantum efficiency of x-ray CCD (d).

This Hartmann wave front sensor working scheme is described in **Section 3.3.1**. $Fig.\ 3.19$ shows a schematic drawing of the operation of the wave front sensor. Light travels to the sensor along the z-axis. Each of the square aperture acts as an optical lever, displacing the diffracted spot proportional to the average phase tilt over the aperture. The wave front sensor measures the tilt over each aperture by comparing the measured positions of the diffracted spots to the positions of the diffracted spots for a reference input beam. The reference diffraction patterns are recorded with a regular wave front (ideal one is flat wave front), as marked in white illuminated in $Fig.\ 3.19$. The tilt measurements are then converted into a replica of the wave front by performing a form of integration called wave front reconstruction. All these procedures are able to be processed with HASO EUV software.

Owing to the titled square aperture shape in the Hartmann plate, diffracted pattern is composed of a circular round shape with diffraction lights rotated by 22.5° from the four edges of square hole, which is so called star shape, as displayed in the right image of $Fig.\ 3.19$. It is worth nothing that the visibility

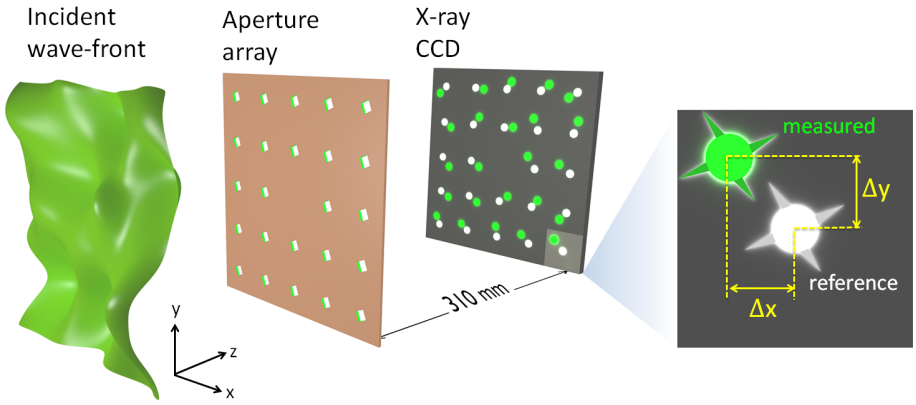

Figure 3.19: Drawing of the Hartmann wave front sensor operation. Showing an incident wave front traveling along the $z-axis$ illuminating an aperture array and the diffracted spots illuminating a CCD and the displacement of a single diffracted spot from the reference location on the CCD. The inset at right is indicating the diffraction pattern from reference and measurement beam.

of the diffraction pattern is dependent on the spatial coherence. Moreover, due to the array element size (square aperture), the diffraction cause by the aperture has the wavelength limit of several nanometres. Therefore, for very short wavelength (such as hard X-rays), the diffraction will not occur (no star shapes) when passing through this aperture. The experiment evidence will be shown in **Section 3.3.3**. When an incident light with flat wave front first counters the aperture array, all the diffraction spots are recorded in the detection plane (CCD) placed $310\ mm$ away. Each diffraction spot will take place at the centre position of its own pixel elements, as described in white patterns in $Fig.\ 3.19$, which are considered as the reference record. However, if the incident light with distorted wave front, the diffraction patterns detected in the CCD plane will shift and the CCD elements record an un balanced signal that indicates the exact displacement, see the green diffraction patterns in $Fig.\ 3.19$. The output from all of these minute detectors is computer analysed with theoretically reconstructed as described in Eqs. (3.1-3.5), HASO EUV software of this device calculates in a more complicated way [66].

It is interesting to note that there is a blinded hole at the centre of aperture array, which is used for the mechanical alignment of the incident beam and specially used for the algorithm to calculate the position of each barycentre, which is much faster than without this "black hole". It is necessary to make sure the projection pattern (shadow) of the blinded hole is exactly at the centre of detection plane before performing a wave front measurement, which indicates that the incident beam is perpendicular to the Hartmann plate. This can be realized by the adjustment of the mechanical bellows system in front of the sensor, as displayed in $Fig.\ 3.19$.

3.3.2.2 Recording and back propagation

The Hartmann wave front sensor is based on a pinhole array that divides the incoming beam into an array of smaller beams. The position and intensity are recorded with a CCD camera placed at a distance l from the holes array (see $Fig.\ 3.19$). The displacement of spot centroid Δx divided by l yields the local wave front gradient $\beta_{x,y}$ inside one sub-aperture relative to a known reference wave front. According to above description of wave front reconstruction method (see **Section 3.3.1**), summation over pixel data inside the individual sub-aperture yields the intensity distribution or beam profile $I(x,y)$.

When considering a coherent beam, the knowledge of the beam profile and wave front allows calculation of the beam parameters using the moments method [67]. The central second spatial (x,y) and angular(u,v) moments are computed from the intensity distribution and the local wave front slopes $\beta_{x,y}$ according to [68]

$$< x^2 >= \frac{\sum_{ij}(x_{ij}- < x >)^2 I_{ij}}{\sum_{ij} I_{ij}}, \tag{3.8}$$

$$< xu >= \frac{\sum_{ij}(\beta_{x,ij}- < \beta_x >)(x_{ij}- < x >) I_{ij}}{\sum_{ij} I_{ij}}, \tag{3.9}$$

$$< u^2 >= \frac{\sum_{ij}(\beta_{x,ij}- < \beta_x >)^2 I_{ij}}{\sum_{ij} I_{ij}} + (\frac{\lambda}{2\pi})^2 \frac{\sum_{ij}((\partial_x I)^2/I)}{\sum_{ij} I_{ij}}, \tag{3.10}$$

where $< x >$ and $< \beta_x >$ are the first moments over x and β_x, and the index (ij) denotes the sub-aperture. The yielded beam with d, divergence θ, beam propagation factor M^2, beam waist diameter d_0, Rayleigh length z_R and waist position z_0 are expressed as [68]

$$d = 4\sqrt{< x^2 >}, \qquad \theta = 4\sqrt{< u^2 >}, \tag{3.11}$$

$$M^2 = \frac{4\pi}{\lambda}\sqrt{< x^2 >< u^2 > - < xu >^2}, \tag{3.12}$$

$$d_0 = \frac{4M^2\lambda}{\pi\theta}, \qquad z_R = \frac{d_0}{\theta}, \tag{3.13}$$

$$z_0 = \frac{z_R < xu >}{| < xu > |}\sqrt{(\frac{d}{d_0})^2 - 1}. \tag{3.14}$$

Once the intensity and phase of the beam are known from Hartmann measurement, the complex amplitude of the electric-magnetic field on the sensor plane can be written as [69]

$$I(x,y,z_H) = \sqrt{I_{SXRL}(\theta_x,\theta_y)} \times exp[i\frac{\pi}{\lambda}(\frac{x^2+y^2}{z_H} + 2\delta(\theta_x,\theta_y))]. \tag{3.15}$$

Here, z_H is the distance between detector and exit of the plasma, $\theta_x = x/z_H$ and $\theta_y = y/z_H$ are the beam divergence in the two directions perpendicular to the beam axis. I_{SXRL} is the SXRL intensity on the detection plane. $\delta(\theta_x,\theta_y)$ represents the fluctuation of the wave front and $\delta(\theta_x,\theta_y) = 0$ is corresponding to a fully coherent, diffraction-limited beam. It is possible to make the reconstruction of the complex amplitude of seeded SXRL on the path of the beam by using a χ^2 minimization fit which are projected on a Hermit-Gauss basis [70]. One should be noted that when back propagating the HH seed beam without plasma amplification, and the seed was assumed as monochromatic beam, such as $18.9\ nm$ in this study.

3.3.2.3 Sensor calibration

According to the above description, it is necessary to have the sensor calibrated before any measurements. Two steps are normally performed to a complete calibration of such a wave front sensor: fist step in visible light using the Talbot effect [71, 72]; next step at the operation SXRL wavelength to save the final calibration file as the reference.

Talbot calibration was performed by using a 780 nm laser diode injected in a single mode fibre, then adjust the distance between the Hartmann plate and the fibre output. It is possible to retrieve a camera signal that is much closer to the expected camera signal at the wavelength. This approach allows aligning the aperture array relatively to the CCD and finding the main parameters of the Hartmann sensor, such as the exact pitch of the aperture array and the distance between the plate and CCD. There is a sample image acquired in this configuration illustrated in $Fig.\ 3.20$. It is interesting to note that the Talbot effect removes the "balck hole" as diffraction mixes beams from several sub-pupils, as it shown in the right figure. Finally, we obtained grid pitch (aperture size) of 13.863 pixels, which corresponds to 180.224 μm. The absolute accuracy on the curvature measurement is $\pm 4.5 \times 10^{-3} m^{-1}$.

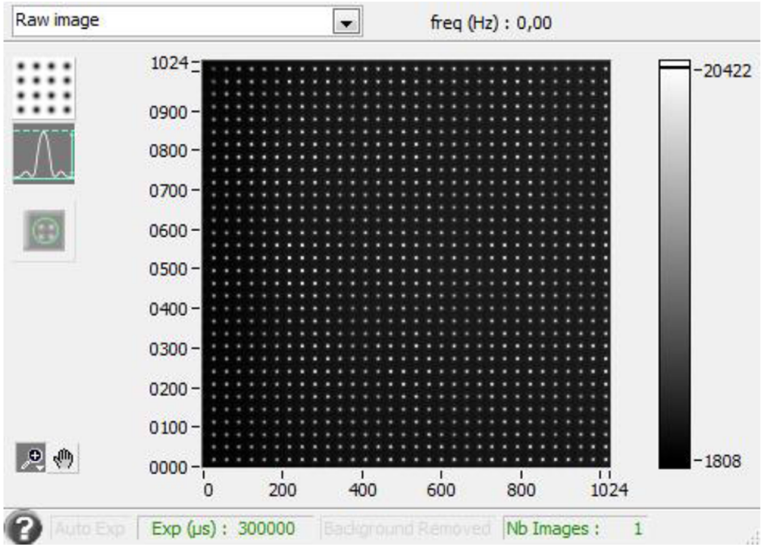

Figure 3.20: Sample image of Talbot calibration, note that the Talbot effect removes the "non hole" as diffraction mixes beams from several sub-pupils.

To finalize the calibration and estimate the final specification of this wave front sensor, we conducted the experiment with the kHz HH beam line in Salle Orange at LOA, France. A photograph and the schematic diagram of this experiment are separately presented in $Fig.\ 3.21$ and $Fig.\ 3.22$. HH gener-

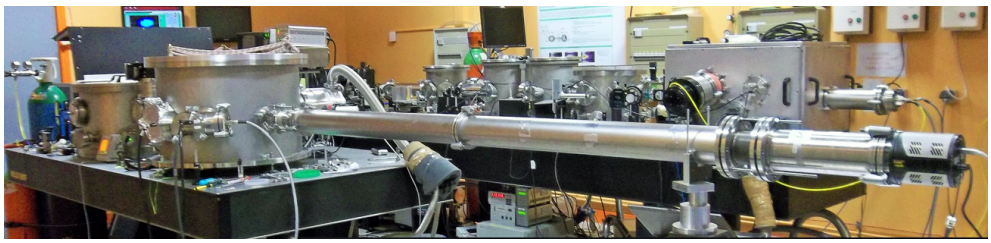

Figure 3.21: Picture of Hartmann wave front sensor calibration at Salle Orange of LOA.

ation was performed focusing 6 mJ, $52\ fs$ IR laser (beam size of $14.8\ mm$ in diameter) into a $15\ mm$ long gas cell filled with $\sim 50\ mbar$ argon gas by a lens ($f = 1\ m$). The generated HH beam (wavelength around $30\ nm$) sequentially countered a $5\ \mu m$ pinhole (in diameter) placed at 17 cm after the cell. This pinhole diffracts a beam and creates a spherical wave front. Hartmann wave front sensor was set at 2.9

m after the pinhole. 300 nm thick Al filter was employed to stop IR laser at $0.8\ m$ away from the gas cell. Since the pinhole reduce the beam intensity by several orders of magnitude, a long acquisition time was indeed. The CCD camera temperature was adjusted at $2°C$. It should be aware of that when the operation temperature is too low (below $0°C$) some dust can be glued on the CCD chip. A three dimensional motor was employed for the pinhole holder, which could provide a relative adjustable detection.

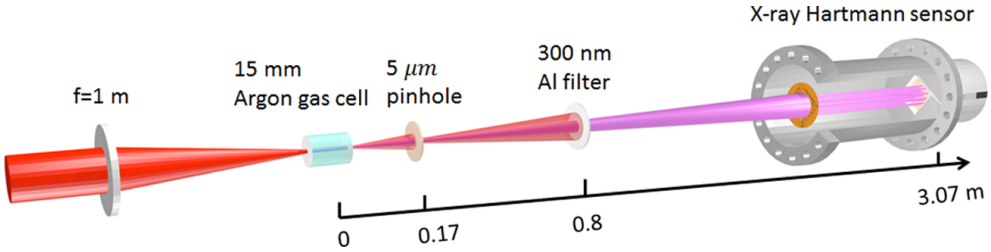

Figure 3.22: Schematic sketch of Hartmann wave front sensor calibration at Salle Orange of LOA using $5\ \mu m$ pinhole.

First of all, the tiny $5\ \mu m$ pinhole was roughly aligned using He-Ne laser coupled with a normal camera without vacuum. Then the pinhole was moved out of the HH beam line when generating the HH under vacuum. Once the HH beam was optimized by changing the gas pressure, adjusting the aperture size and varying the focal position at the gas cell, the pinhole was set back to the HH beam line. Estimated HH beam size at the pinhole position is $170\ \mu m$ according to the divergence ($\sim 2\ mrad$) of HH beam, the spatial filtering by the $5\ \mu m$ pinhole caused three orders of magnitude energy reducing. Therefore, long acquisition time with the pinhole was required. Two different acquisition times were performed during this calibration: $30\ s$ and $300\ s$ are separately displayed in $Fig.\ 3.23$ and $Fig.\ 3.24$. The maximum

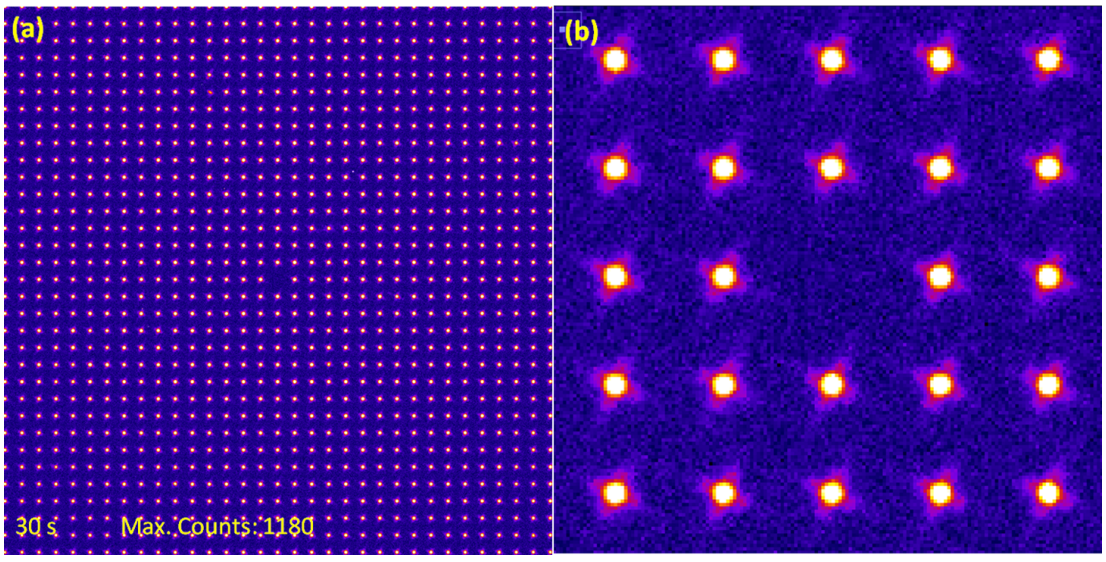

Figure 3.23: Full raw image (left) of HH beam detected with $30\ s$ acquisition time detected at $2.9\ m$ away from the pinhole. A zoomed-in image around the centre ("black hole") is displayed at right.

counts was observed from 1180 to 8000 when increasing the acquisition time from $30\ s$ ($\sim 3\times 10^4$ shots) to $300\ s$ ($\sim 3\times 10^5$ shots), while the background signal for each was around 10 counts. The "black hole"

was well aligned at the centre of the CCD chip (pixel position $[512, 512]$). Otherwise, the calibration may be wrong as it could be subtracted with a shift between sub-pupils. From the left full images, detected HH beam homogeneously distributed on the CCD chip. In the right close-up figure, it is apparent that diffraction patterns with " star shape " (described in **Section 3.3.2**) are all tilted by $22.5°$ respected to the normal vertical and horizontal coordinates. This is due to the intended design to minimize the coherent crosstalk between diffracted spots from adjacent apertures. It is important to note that, in the full images, the diffraction patterns by the chip edges were only partially detected. This could cause the calibration error by these edges. In consequence, more measurements were carried out shifting the "black hole" by 20 pixels in each direction from the centre. In that case, one could get full diffraction pattern of each edge. Finally, the calibration will be able to cover the whole CCD chip. The slope maps then obtained which includes all the grid defects. This calibration purpose is to save the slope maps and include them in the calibration file in order to ensure the absolute calibration of the sensor is taken into account in all the configurations.

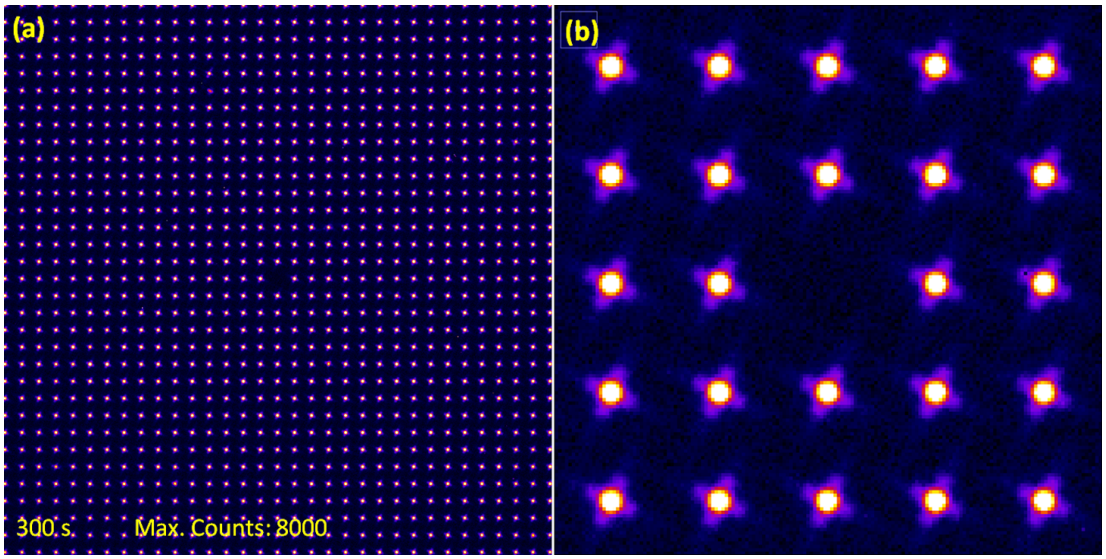

Figure 3.24: Full raw image (left) of HH beam detected with $300\ s$ *acquisition time detected at* $2.9\ m$ *away from the pinhole. A zoomed out image around the centre ("black hole") is displayed at right.*

After the calibration, we sequentially reopen the image file ($300\ s$ acquisition time) with HASO software to measure the quality of this calibration. Intensity map (left) and wave front (right) maps are displayed in $Fig.\ 3.25$. Wave front residual around $\lambda/46$ RMS (after subtracting tilt and focus at $30\ nm$) was obtained with the beam occupied the full pupil. Therefore, Hartmann sensor accuracy of $0.65\ nm$ RMS and $4.62\ nm$ peak-to-valley (PV) for the full pupils were achieved in the bandwidth $4 - 40\ nm$. To further understand the tilt (in both vertical and horizontal) and focus effect, we measured the tilt and focus alone as illustrated in $Fig.\ 3.26(a)$ and $Fig.\ 3.26(b)$, respectively. It is extremely difficult to replace the source under measurement at exactly the same location as it was in the calibration. The observed tilt as $3.57\ \mu m$ RMS and focus as $2.49\ \mu m$ RMS, which are in negligible level with respect to the $3\ m$ long diagnostic system. While the detected wave front distortions are normally in nm level. Therefore, during

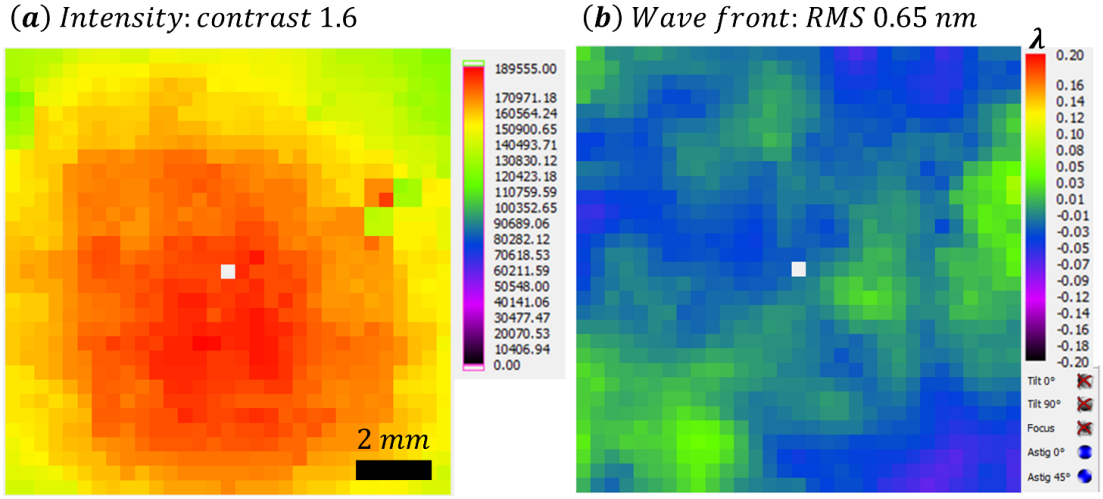

Figure 3.25: Intensity (left) and wave front (right) maps of HH beam with 300 s acquisition time using HASO software after the sensor calibration.

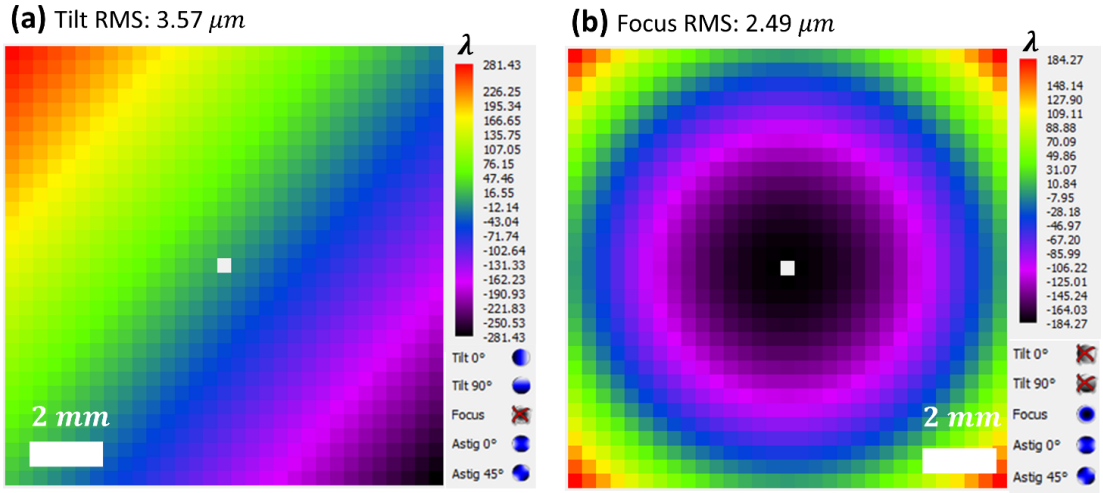

Figure 3.26: Tilt (left) and focus (right) aberration effect of the sensor detection after calibration.

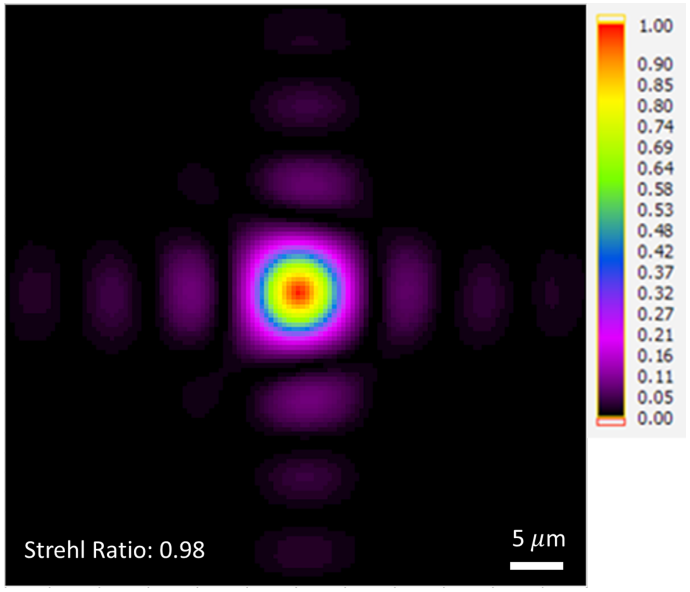

Figure 3.27: Back propagation image using point spread function showing the HH source condition from 5 μm pinhole.

the wave front measurement using this Hartmann wave front sensor, the "Tilt $0°$", "Tilt $90°$" and "Focus" options ($Fig.\ 3.26(b)$) are ticked out as long as they remain this level. In addition, a back propagation image using point spread function is represented in $Fig.\ 3.27$, which shows the source size as $6\ \mu m$ FWHM. Note that this image was detected $2.9\ m$ away from a $5\ \mu m$ pinhole.

3.3.3 Wave front study of HH-seeded SXRL

3.3.3.1 Experiment condition and preparation

After the soft x-ray Hartmann sensor calibration at LOA in France, the experiment was sequentially carried out at Colorado State University (US) in cooperation with Prof. Rocca's group. The aim was to measure the wave front of HH seed and seeded SXRL at $\lambda = 18.9\ nm$, $4d^1S_0 \rightarrow 4p^1P_1$ line of nickel-like Mo, using Hartmann wave front sensor developed at LOA in collaboration with Imagine Optics and SOLEIL [56], as described in **Section 3.3.2**. The main $1.5\ J$ IR laser beam with $200\ ps$ pulse duration from the Ti:Sapphire laser ($810\ nm$) system was firstly divided into two arms using a beam splitter with the energy proportion of 50% (reflected) and 50% (transmitted), respectively. As described in $Fig.\ 3.28$, to the first arm, the reflected beam then encountered the second beam splitter. This reflected beam was sent to a pulse compressor to create $60\ mJ$, $60\ fs$ pulse. However, an additional beam splitter was employed for the transmission beam. Here, the transmitted beam firstly encountered a polariser plate, then through a delay line, and finally delivered to a Brewster window [73] which allows most of the energy passing by adjusting the polarization of the beam. This Brewster window also combined these two separated branches together into a beam path with proper time delay between each other. These two pulses were considered as the pre-pulses for the plasma amplifier creation. The second arm was sent to single-pass grating pair compressor, the output beam with $6\ ps$ pulse duration was used as the pump laser for the x-ray plasma amplifier.

Thanks to the delay line described in the $Fig.\ 3.28$, both $200\ ps$ pulses were separated by $5\ ns$ in time (peak-to-peak): fist pulse with $30\ mJ$ energy and second pulse is $250\ mJ$. Sequentially, the two long pulses, separately considered as precursor pulse and pre-pulse, were focused into a line ($40\ \mu m \times 4\ mm$), by the combination of a spherical lens and a cylindrical lens, on the Molybdenum slab target surface with normal incidence, which can create a plasma approaching the Ni-like ionization stage. The warm plasma was subsequently expanding. However, population inversion between the upper lasing level ($4d^1S_0$) and lower lasing level $4p^1P_1$ was not substantially produced, more pumping energy is fundamentally required. Then, after $600\ ps$ (from the peak of the 2^{nd} pulse), a $500\ mJ$ short pulse ($6\ ps$ duration) was arriving and focused into a similar line as the pre-pulse, but with $23°$ grazing incident angle respected to the target surface. The plasma was rapidly heated and reaching the electron density of $\sim 2.6\times10^{20}\ cm^{-3}$ [51], which is adequate to achieve large population inversion between the two lasing levels [74]. By here, the x-ray plasma amplifier is basically ready for the seeding experiment. It is interesting to mention our previous x-ray seeding experiment conducted in LASERIX in France (see **Section 3.2**), where the GRIP scheme is composed of one green light ($6\ ns$ duration, $532\ nm$) as the normal incident pre-pulse and two short pump pulse with grazing incidence of $20°$. That is a GRIP configuration to generate narrow gain life time, as shown in $Fig.\ 3.13$.

Moreover, it is worth nothing that first shot with above three-pulse on the well-polished Molybdenum slab target is normally inefficient to obtain high electron density plasma due to the reflection of the target

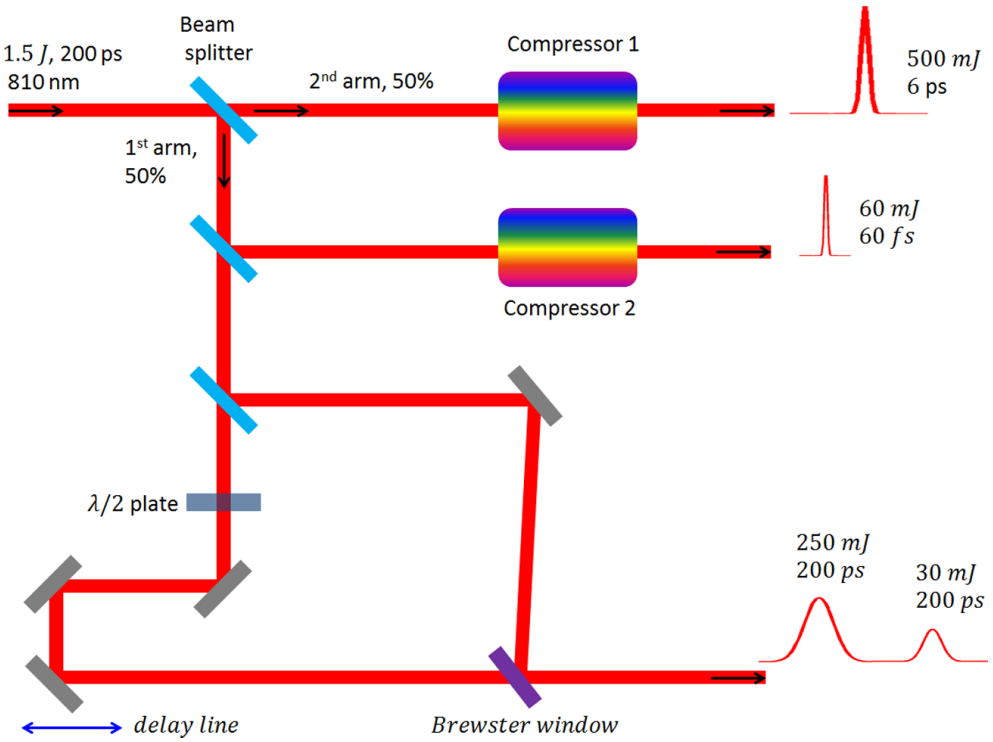

Figure 3.28: Layout of multi-IR-laser system from the Ti:Sapphire CPA laser.

surface. However, the second shot on the target becomes much more efficient. Therefore, during this soft x-ray seeding experiment, all the data acquisition were taken from the second shot of each new target, which means that each molybdenum target (new position on the slab) was only used for two shots, as it displayed in $Fig.\ 3.29$ in comparison with the target surface before and after shooting with several hours, where slightly blazed abrasion after shooting is observed. One should also beware of that, shooting on the same target position for over 10 shots would cause ablation damage on the target surface which could make some influence of the plasma condition.

In another hand, part of the fs beam ($\sim 13\ mJ$) was focused into a neon gas jet (backing pressure $\sim 1.5\ bar$) by adopting a $f = 1.1\ m$ focal lens. A toroidal mirror ($f = 0.25\ m$), designed to operate at a grazing incidence angle of $9.65°$, imaged the harmonic source with a magnification of one at the centre of plasma amplifier. Consequently, distance ($0.5\ m$) between gas cell and toroidal mirror was the same as the separation between toroidal mirror and plasma amplifier, as illustrated in $Fig.\ 3.30$. HH seed was injected into the plasma at a grazing angle of $5\ mrad$. Times matching between the seed pulse injection and the peak of the short pump pulse were optimized using a BBO double-frequency crystal as explained in **Section 3.2.1**. At proper injection time, the 43^{rd} order ($18.9\ nm$) of the HH pulse can be significantly amplified in this x-ray plasma amplifier with large population inversion between upper lasing level ($4d^1S_0$) and lower lasing level $4p^1P_1$ [77, 51, 74]. A $300\ nm$ thick aluminium filter was used to stop the straight IR lasers. In the sake of measuring the wave front of amplified seed beam, we firstly set the Hartmann wave front sensor directly along the output of the amplified seed beam at $1.6\ m$ far from the plasma amplifier.

When the HH driven IR laser (fs pulse) was set as P polarization, single-shot of the output beam detected by the Hartmann wave front sensor is represented in $Fig.\ 3.31$. Full raw image is illustrated

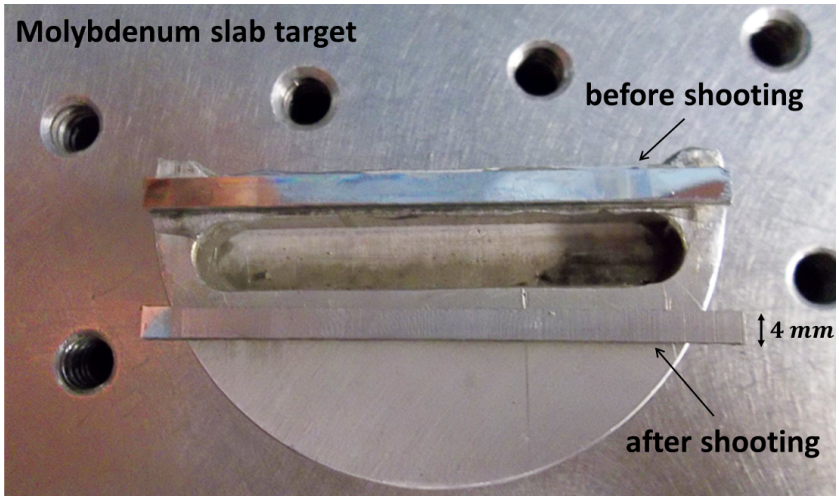

Figure 3.29: Molybdneum slab target before and after shooting with serveral hours by the three pulses.

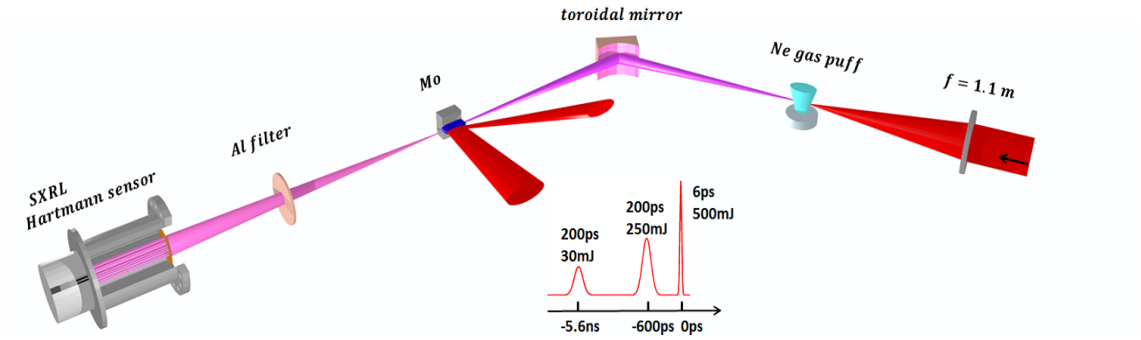

Figure 3.30: Experimental setup of direct measurement of seeded SXRL wave front using SXRL Hartmann sensor.

in $Fig.\ 3.31(a)$ where the "back hole" is obvious at the centre of the detector. However, no diffraction pattern was observed, as displayed in the close-up image ($Fig.\ 3.31(a)$) of the region of interest (ROI) in $Fig.\ 3.31(b)$. The illuminated patterns are showing the same shape as the square apertures in the Hartmann plate described in $Fig.\ 3.18$ and $Fig.\ 3.19$, respectively. This means that there is no diffraction occurred (or in negligible level) in the aperture array, which indicating that the amplification of the seed is not achieved. Owing to this high dense plasma, hard x-rays are considered as the main contributor of this observed light. Consequently, we changed the polarization of HH driven IR laser to S polarization. As seen in $Fig.\ 3.32$, single-shot full raw image (a) shows a bright beam around the central "black hole" as well as the homogeneous hard x-ray background. Enlarged picture of this interesting region is displayed in $Fig.\ 3.32(b)$. It is apparent that diffraction patterns are appeared in this bright beam, which are showing " star shapes " with diffraction lights tilted by 22.5° as discussed in **Section 3.3**. This obvious diffraction is contributed by the amplified seed. The peak counts of the pattern with diffraction is ~ 36000, while it is only ~ 10000 in the pattern without diffraction. And the diffraction lines (tilting pattern) is only 1000 at maximum. It is implying that the hard x-rays dominated the final output from plasma amplifier.

Although the observed beam size of amplified seed (seeding) is much smaller than that of the hard x-ray emission, which is corresponding to the beam divergence, the intensity contrast between the seeding

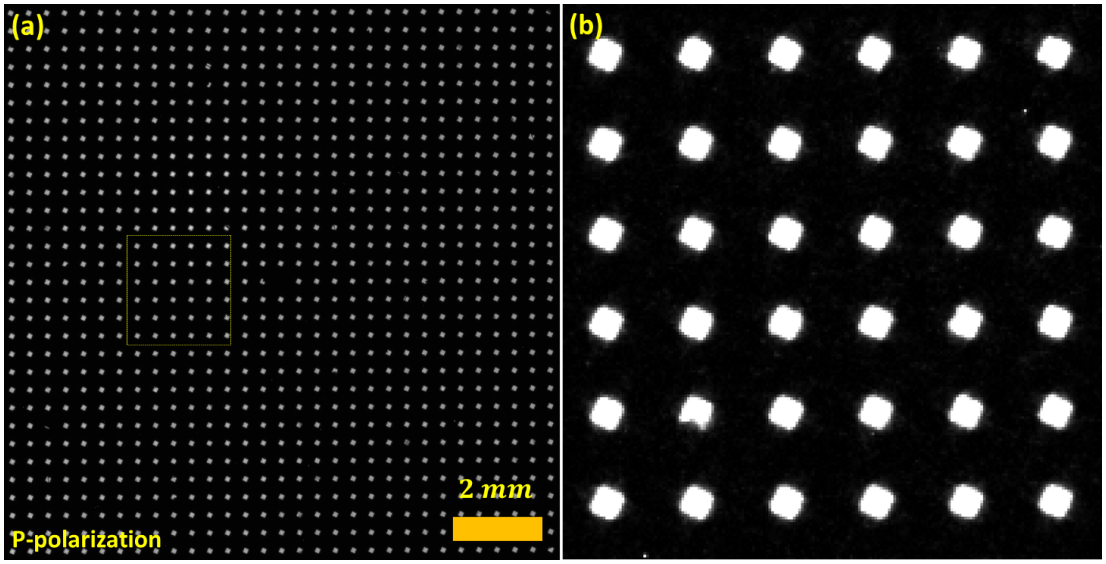

Figure 3.31: (a) Full and (b) region of interest raw image of the output beam detected with Hartmann wave front sensor in the experiment setup demonstrated in Fig. 3.30. The HH driven laser was set as P polarization.

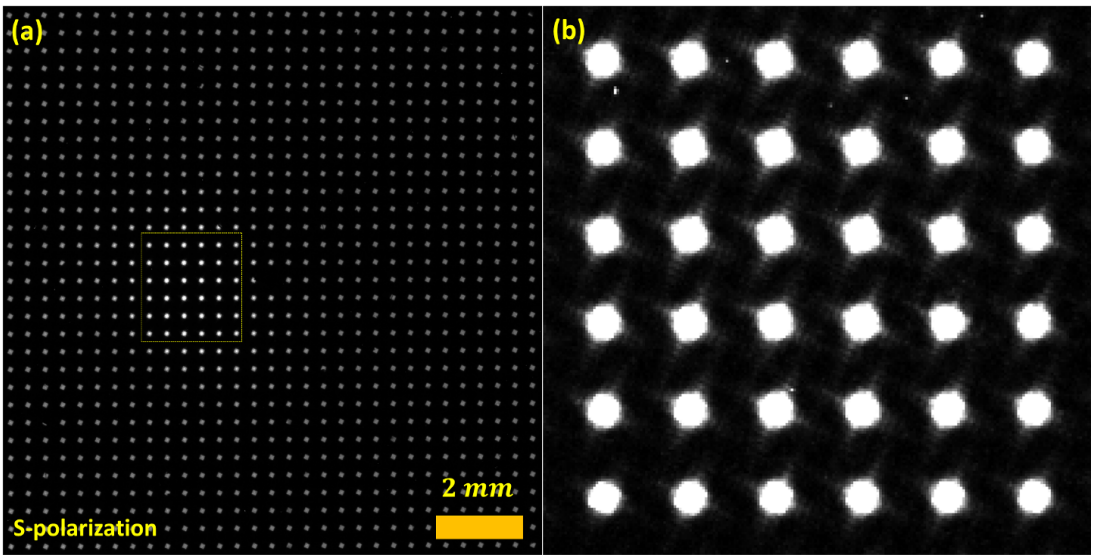

Figure 3.32: (a)Full and (b) region of interest raw image of the output beam detected with Hartmann wave front sensor in the experiment setup demonstrated in Fig. 3.31. The HH driven laser was set as S polarization.

and hard x-rays shows no concern with the detection distance from the plasma amplifier as explained in the following formula:

$$\frac{\rho_{seeding}}{\rho_{hard-x-ray}} = \frac{E_{seeding}}{E_{hard-x-ray}} \cdot \left(\frac{\theta_{hard-x-ray}}{\theta_{seeding}}\right)^2 \quad , \tag{3.16}$$

where ρ is the energy density, E is the total pulse energy, θ is the beam divergence. In another hand, seeded SXRL beam doesn't take sufficient pupil numbers on the Hartmann plate for the following wave front analysing (minimum 10 pupils). One might improve it by increasing the detection distance from

plasma amplifier, but this is limited by the experiment condition as illustrated in $Fig.$ 3.33, where the sensor was already installed against the wall. Therefore, the direct diagnostics of the seeded SXRL wave front has the physical and technical challenges due to the effect of hard x-rays and the low divergence of seeded SXRL. However, this direct wave front detection is suitable for the HH seed without plasma amplifier, which will be discussed in **Section 3.3.3.**

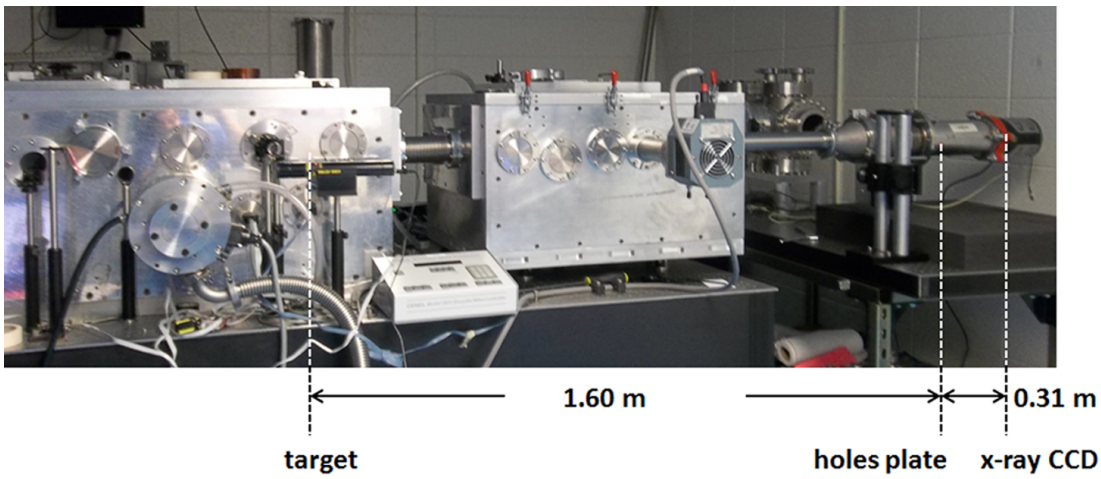

Figure 3.33: Photograph of the beam line for direct wave front diagnostics of the seeded SXRL using Hartmann wave front sensor. The detection distance is limited at $1.6\ m$ *from the plasma amplifier due to the wall of laboratory.*

One solution of the seeded SXRL wave front detection was coming up by employing a Mo-Si 45° multilayer mirror. The flatness of this mirror is $\lambda/10$ tested at $632\ nm$ for the full pupil of $25\ mm$. It was placed at $0.86\ m$ after the plasma amplifier, where the estimated seeded SXRL beam size is ~ 1 mm, thus the wave front aberration from this mirror could be neglected [78]. Simultaneously, due to the narrow bandwidth of the efficient reflection of this multilayer mirror (specified for $18.9\ nm$), the effect of the hard x-rays was substantially reduced. In addition, the detection distance could be settled further with respect to the direct diagnostics, which allows a sufficient seeded SXRL beam size for the Hartmann wave front sensor detection. As it shown in $Fig.$ 3.34, the sensor was positioned $3.5\ m$ away from the plasma amplifier. In this case, the schematic diagram of the experiment setup is depicted in $Fig.$ 3.35,

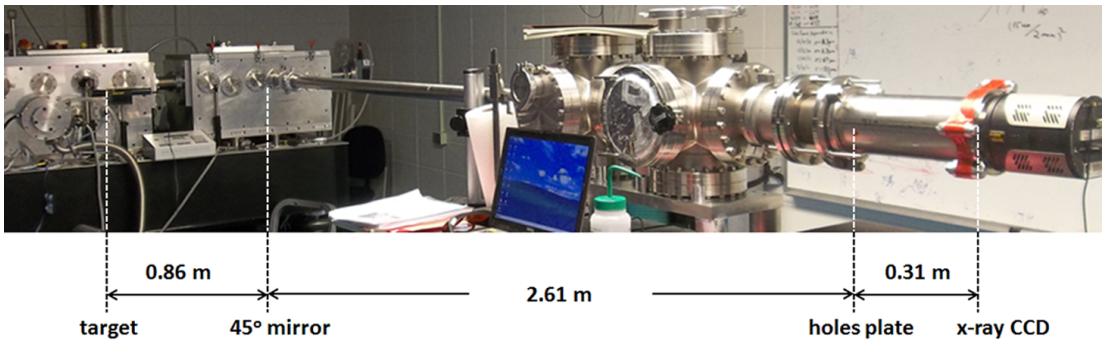

Figure 3.34: Picture of experimental beam line for HH-injection seeded SXRL wave front measurement with Hartmann sensor. A 45° *multilayer mirror designed for* $18.9\ nm$ *was employed.*

where the HH generation and plasma creation parameters are as the same as described in $Fig.$ 3.30. With the benefit of using this 45° multilayer mirror, hard x-rays were not observed in the detection plane. Instead, ASE took place of the background signal which exhibits the same behaviour as the hard x-rays described in Eq. (3.16). However, as the intensity of ASE signal is much lower than the amplified seed intensity, the energy intensity reduction due to the increasing of the detection distance makes most of the ASE signal below the detection threshold of Hartmann wave front sensor, while the amplified signal is still significantly above the calibration limit. More details of the seeded SXRL wave front measurement will be discussed in **Section 3.3.3** and all the seeded SXRL wave front measurements in **Section 3.3.3** were performed using this experiment setup illustrated in $Fig.$ 3.35.

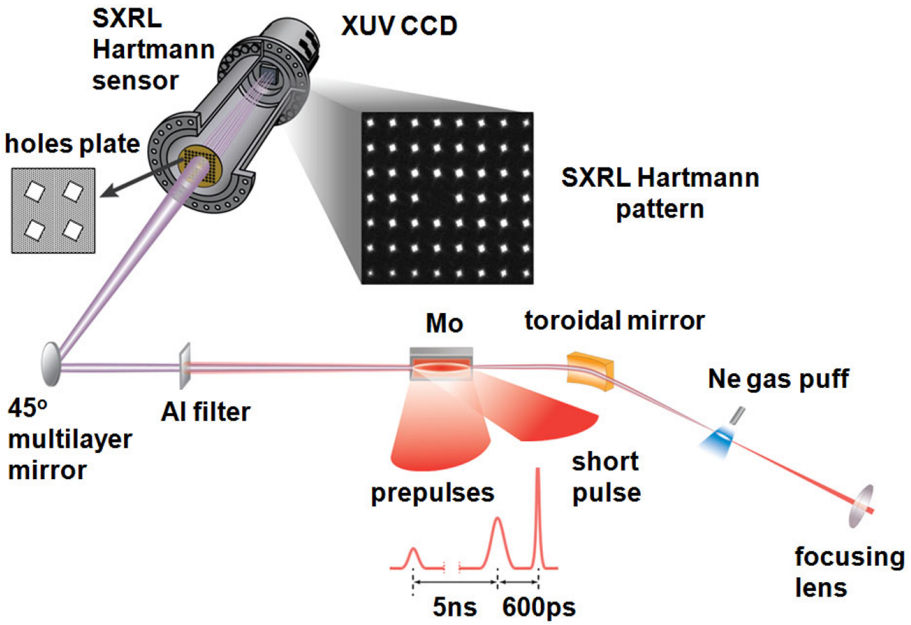

Figure 3.35: Schematic diagram of the experimental setup to measure the wave front of an HH-injection-seeded SXRL based on solid target plasma with x-ray Hartmann sensor. from [55]

3.3.3.2 Wave front of HH seed

To promise the sufficient single-shot energy for wave front detection, the HH seed wave front was measured settling Hartmann sensor directly along the HH beam propagation without the 45° multilayer mirror, as described in $Fig.$ 3.30 (without plasma amplifier). SXRL Hartmann sensor was placed $1.6\ m$ away from the HH imaging spot of the toroidal mirror. A raw image from single-shot HH pulse, which is set to be a typical sample data processing, recorded by the Hartmann sensor was represented in $Fig.$ 3.36. Low divergent HH beam passed through the Hartmann plate, and the illuminated pupils indicating the beam size at the aperture array location. Apparently, the vacancy ("black hole") at the image centre is corresponding to the blinded hole in the plate, which is the absolutely important reference for system alignment and the algorithm to calculate the position of each barycentre as mentioned in **Section 3.3.2**. Clear diffraction patterns are adorable for the phase analysing, while the weaker pupils are blurry and challenging the exploration of the wave front. Consequently, we made the line-out of the average value

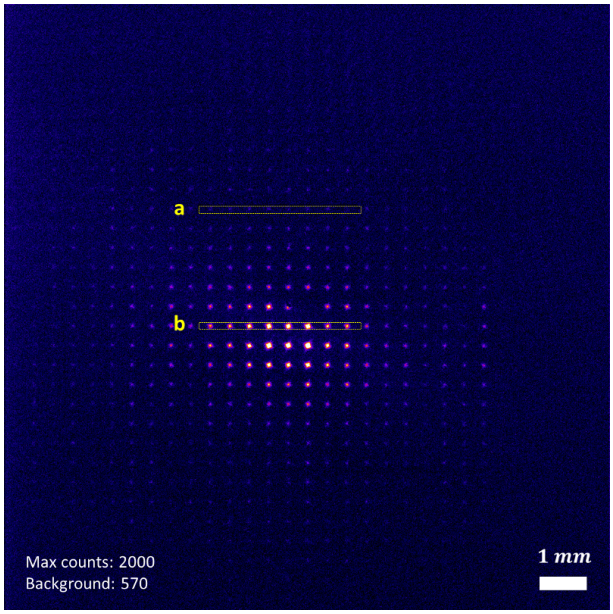

Figure 3.36: Raw image of HH seed beam without plasma amplifier, which is directly detected by Hartmann wave front sensor placed at $1.6\ m$ *away from the source without 45° multilayer mirror.*

in the two marked regions in $Fig.\ 3.36$, as illustrated in $Fig.\ 3.37(a)$ and $Fig.\ 3.37(b)$, respectively. The bright region are showing apparently separated spots while the signal-to-noise ratio is too low in the weakly illuminated region to get sufficient accuracy for wave front detection with Hartmann sensor. Then the first problem coming along is to choose the appropriate pupils for wave front analysis.

Full intensity (left figure) and wave front (right figure) images of the sample illustrated in $Fig.\ 3.36$ are displayed in $Fig.\ 3.38(a)$, where the wave front value (right image) consists of lower signal and noise causing low sensor detection accuracy. In order to reduce the effect of lower signal, we firstly picked up the ROI by setting intensity threshold, it is showed in $Fig.\ 3.38(b)$. The chosen area still remains 75% of the energy respected to the full image, while the PV and RMS wave front value are substantially improved. Another alternative option is to use fixed ROI, thereby we used circular ROI with respect of the HH beam shape, as demonstrated in $Fig.\ 3.38(c)$. Resembling improvement of the wave front was obtained as by the intensity threshold approach. The circular ROI takes 78% of the energy from full image. Based on this context, the two approaches were worked out for the 27 consecutive HH shots. In $Fig.\ 3.39$, the lower blue line (right coordinate) indicates energy stability from shot-to-shot, and the upper black lines are corresponding to the energy proportion from the full image for each shot in different approaches—intensity threshold (solid line), $6\ mm$ of diameter circular ROI (dotted line) and $5.5\ mm$ of diameter circular ROI (dashed line).

Moreover, there are several different methods to analyse the SXRL wave front in HASO software developed by Imagine Optics. Zonal and Modal are the two main wave front reconstructor modes. The Zonal wave front reconstruction is a type of numerical integration and Modal wave front reconstruction fits the data to a set of orthogonal surface polynomials (described in **Section 3.3.1**). In $Fig.\ 3.38$, the treatment was preformed within Zonal mode, where only several main aberrations are specifically taken into account– tilt, focus, astigmatism and coma (see **Appendix** $Fig.\ A.1$). During the wave front measurements, there are very strong horizontal and vertical tilts as well as spherical aberrations, which are

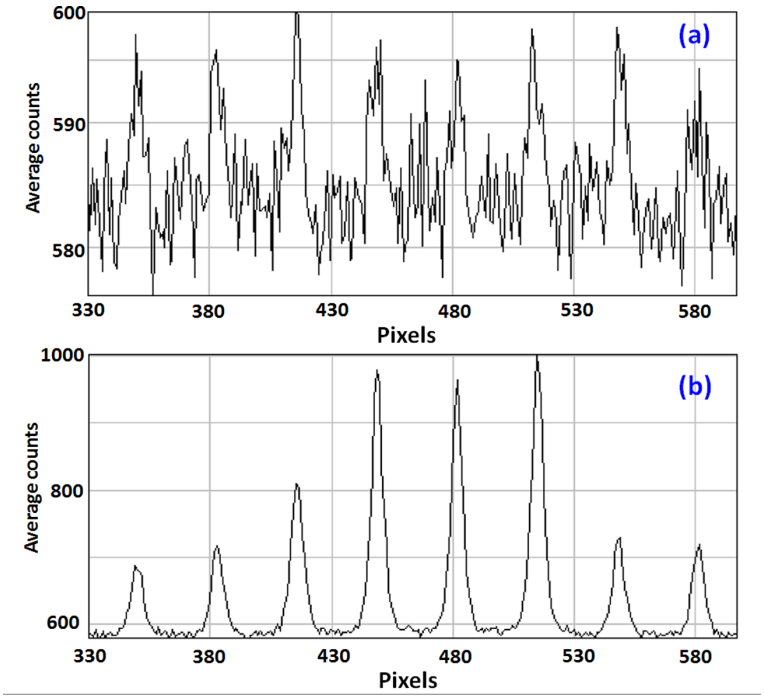

*Figure 3.37: Average line-out of the marked regions in $Fig.\ 3.36$: (a) line **a** and (b) line **b**.*

originated from the sensor calibration as discussed in Section 3.3.1. The sensor has been calibrated with high harmonics signal using a tiny pinhole ($5\ \mu m$) placed at $3\ m$ upstream (see **Section 3.3.3.1**). Obviously, it is extremely difficult to replace the source under measurement at exactly the same location as it in the calibration. Tilts are sub-100 λ (λ=18.9 nm) meaning a positioning error near or lower than a couple of micrometers. Considering the distance, it is already a good alignment. Nevertheless, tilt does not make any impact on wave front optimization as long as it remains at this level. It means that the tilt (in vertical and horizontal) and focus do not bring any impact on imaging or focusing experiments. Therefore, during this experiment, the options of tilt 0°, tilt 90° and focus were ticked out, as demonstrated in $Fig.\ 3.38(c)$, in order to make the main aberrations with great clarity.

In the Modal reconstructor mode, there are two different functions performing wave front analysis– Zernike polynomials and Legendre polynomials, which are represented in **Appendix** $Tab.\ A.1$ and $Tab.\ A.2$, respectively. In comparison, we performed the two treatments with circular pupils of $6\ mm$ diameter illustrated in $Fig.\ 3.40$ and $Fig.\ 3.41$ separately. The left figures are showing the wave front map with PV and RMS value, and right figures presenting the wave front deviation values under different orders of the mathematical polynomial. There are 8, 12 and 20 terms taken into account in (a), (b) and (c) of both figures, respectively. In principle, the accuracy of final wave front RMS value is dependent on the number of Zernike or Legendre polynomials (commonly referred to as terms). For Zernike and Legendre polynomials, the number of terms should be more than 20 to achieve a desired accuracy respected to the wave front obtained under Zonal mode. Considering the practical purpose of this experiment, we finally adopted the Zonal reconstructor mode for all the data processing of HH seed and seeded SXRL.

Within the Zonal reconstructor mode, the two approaches of intensity threshold ($Fig.\ 3.38(b)$) and circular ROI ($Fig.\ 3.38(c)$) were proceeded over 27 consecutive shots of HH seed. In $Fig.\ 3.42$, both

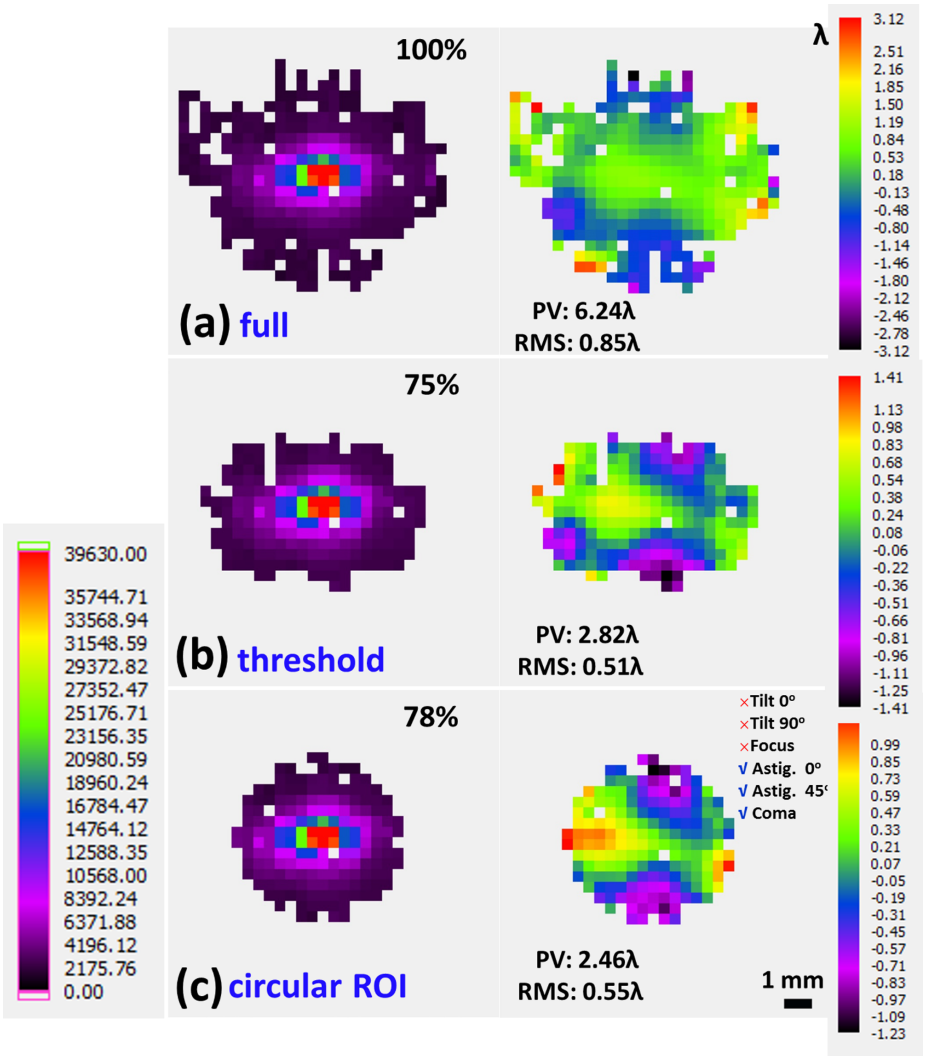

Figure 3.38: HH seed intensity (left) and wave front (right) under various data processing approaches: (a) full image, (b) clipping pupils by intensity threshold and (c) circular pupils as the ROI.

PV (black lines) and RMS (blue lines) residual wave front value of a series of successive HH shots are processed with approaches of (a) intensity threshold, (b) circular pupil size of 6 mm and (c) circular pupil size of 5.5 mm under Zonal reconstructor mode. According to $Fig.$ 3.39, the ROI energy proportions respected to the full beam of these three methods: (a) $82\%\pm3\%$, (b) $81\%\pm2\%$ and (c) $77\%\pm2\%$. The circular pupil technique shows good stability on the energy occupancy which is due to the stable circular shape of the HH seed beam. The detected wave front PV value is over 5 times higher and stability of the wave front PV value is $\sim$5 times lower than the observed wave front RMS value over the three approaches. The technique with 5.5 mm circular pupil shows better stability of wave front PV value in comparison with the other two approaches, while the ROI energy is resembling to the others. For the point view of seeding application, wave front RMS value is more concerning, which remains the same level for the three approaches: (a) $0.54\lambda\pm0.06\lambda$ (intensity threshold), (b) $0.57\lambda\pm0.04\lambda$ (6 mm circular pupil) and (c) $0.51\lambda\pm0.03\lambda$ (5.5 mm circular pupil).

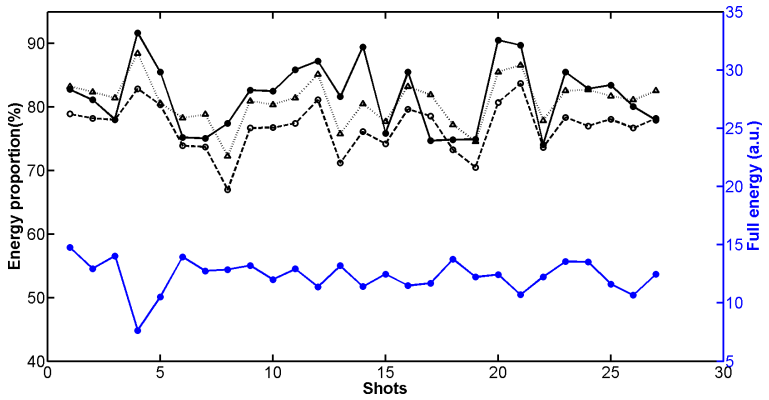

Figure 3.39: HH seed beam stability (right coordinate) from shot to shot (blue line), and energy proportions (left coordinate) of the chosen pupils respect to the full-pupil in three methods: clipping pupils by intensity threshold (black solid line), circular pupil size of $6\ mm$ *(black dotted line) and* $5.5\ mm$ *(black dashed line).*

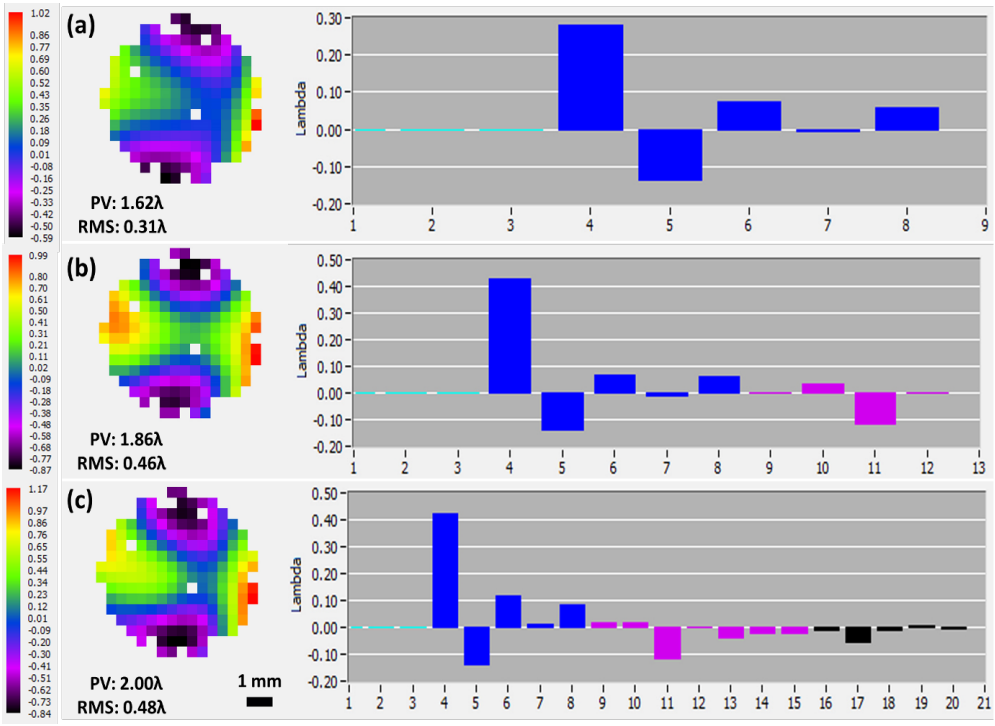

Figure 3.40: Wave front analysis with Zernike fuction by choosing $6\ mm$ *circle pupil size under the Modal reconstruction mode in the HASO software. Various parameters were taken into account for the wave front calculation:(a)* 8 *parameters, (b)* 12 *parameters and (c)* 20 *parameters, as illustrated in the right figures. All the parameters in the horizontal coordinate are corresponding to the physical phases in* ***Appendix*** $Tab.\ A.1$.

According to above understanding, we therefore only took account of the three most important aberrations – coma, astigmatism at 0° and astigmatism at 45° for the full characterization of HH seed beam. As the wave front sensor allows for independent measurement of different aberrations, see $Fig.\ 3.43$, we plotted the three strongest aberrations (phase in RMS) over the 27 consecutive shots for each processing

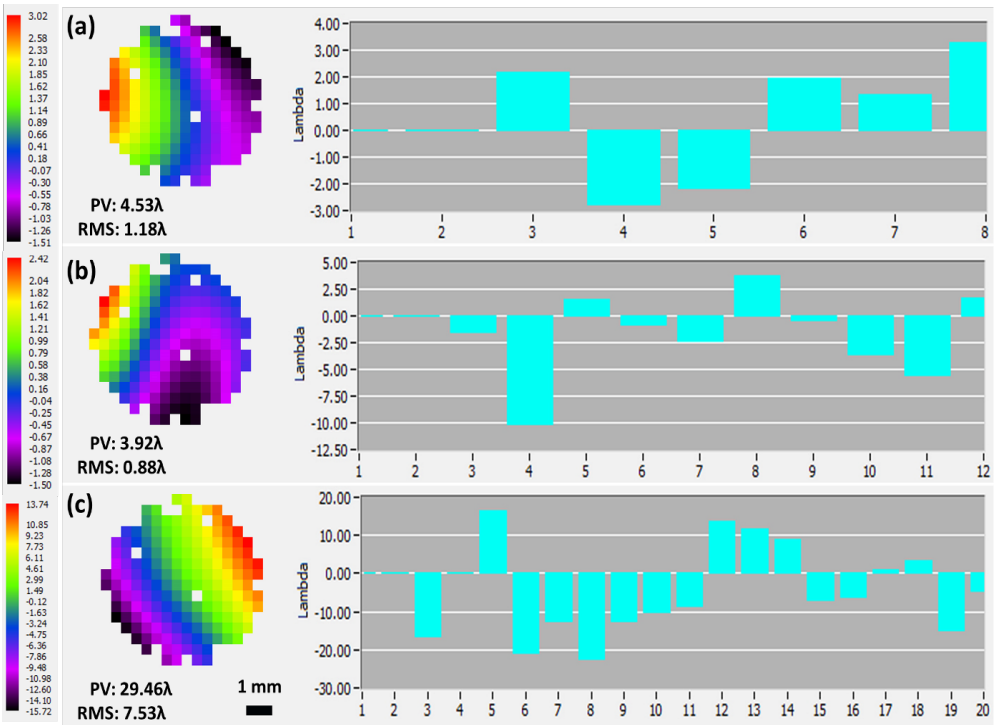

Figure 3.41: Wave front processing by Legendre fuction with 6 *mm circular pupil size under the Modal reconstruction mode in the HASO software. Several parameters were taken into account for the calculation:(a)* 8 *parameters, (b)* 12 *parameters and (c)* 20 *parameters, as displayed in the right figures. All the parameters in the horizontal coordinate are corresponding to the physical phases in* ***Appendix*** $Tab.\ A.2$.

case (a) intensity threshold, (b) 6 *mm* circular pupil and (c) 5.5 *mm* circular pupil. The black dashed lines are indicating the calibration limit (0.03λ RMS) of Hartmann wave front sensor (discussed in **Section 3.3.3**). Coma (blue lines) dominated the overall aberrations of HH seed: (a) $0.42\lambda \pm 0.03\lambda$ (intensity threshold), (b) $0.46\lambda \pm 0.03\lambda$ (6 *mm* circular pupil) and (c) $0.41\lambda \pm 0.03\lambda$ (5.5 *mm* circular pupil), which is considered to be caused by using toroidal mirror [79] for the HH seed imaging-injection. Astigmatism at 0° (green lines) was only a quarter of the coma distortion, while the astigmatism at 45° was below the sensor calibration limit. It is interesting to note that stability of astigmatism at 0° improves when changing the data processing approach from intensity threshold to circular pupils. In addition, all the wave front RMS value as well as the various aberrations were represented in Table 3.1 in comparison with the wave front of seeded SXRL (see **Section 3.3.3**). Except the aberration effect from toroidal mirror, one should also take account of the beam quality of the HH driven IR laser, which could directly impact on the HH beam wave front.

Furthermore, the electromagnetic field of the HH seed source at the imaging spot, where supposed to be the centre position of plasma amplifier when performing the seeding afterwards, can be reconstructed using the point spread function in a free space. Distance between HH seed image spot and Hartmann sensor holes-plate for 5.5 *mm* and 6 *mm* pupil size were calculated out by back propagation the detected HH beam on the sensor, as represented in $Fig.\ 3.44(a)$ ad $Fig.\ 3.44(b)$, respectively. This calculation is strongly dependent on the beam shape on the detection plane, which were considered as circular beam with (a) 5.5 *mm* and (b) 6 *mm* in diameter, respectively. The computed source position (HH imaging

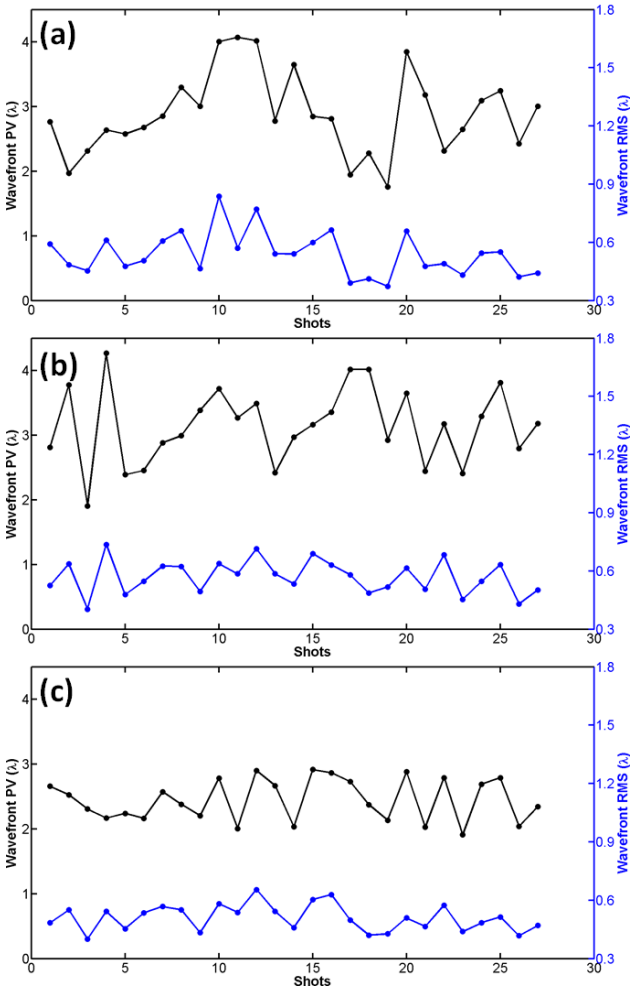

Figure 3.42: Wave front RMS (blue lines, right cooradinate) and PV (black lines, left coordinate) values of HH seed beam from shot-to-shot processed by the three different approaches: (a) clipping pupils by intensity threshold, (b) circular pupil size of 6 mm and (c) circular pupil size of $5.5\ mm$.

spot) is estimated as between $1940\ mm$ to $1950\ mm$ from the detection plane for both approaches. The source distance estimated range within $1\ cm$ implies rather high accuracy of this Hartmann sensor with respect of the $\sim 1.9\ m$ long distance. This computed distance is also in good agreement with our roughly measurement during the experiment as described in $Fig.\ 3.33$. So that, the estimated beam divergence of HH seed is eventually obtained as $1.3\ mrad$. Moreover, the Rayleigh length [70] of this HH beam under the toroidal mirror imaging system is about $2\ cm$. This high precision source position computing is adorable for the following back propagation.

Sequentially, using the point spread function, we calculated the transverse intensity distribution at different locations along the beam propagation axis ($Z = -20,\ -10,\ 0,\ 10$ and $20\ mm$), as illustrated in $Fig.\ 3.45$. $Z = 0\ mm$ corresponds to the centre of the source and also to the region of least confusion. Negative value indicates the direction deviated from the sensor. The reconstructed HH source shows elongated profile in vertical, and $\sim 20\ \mu m$ in horizontal. It could be caused by the toroidal imaging system. The beam quality of HH pulse from laser interaction with gas puff also needs to be taken into

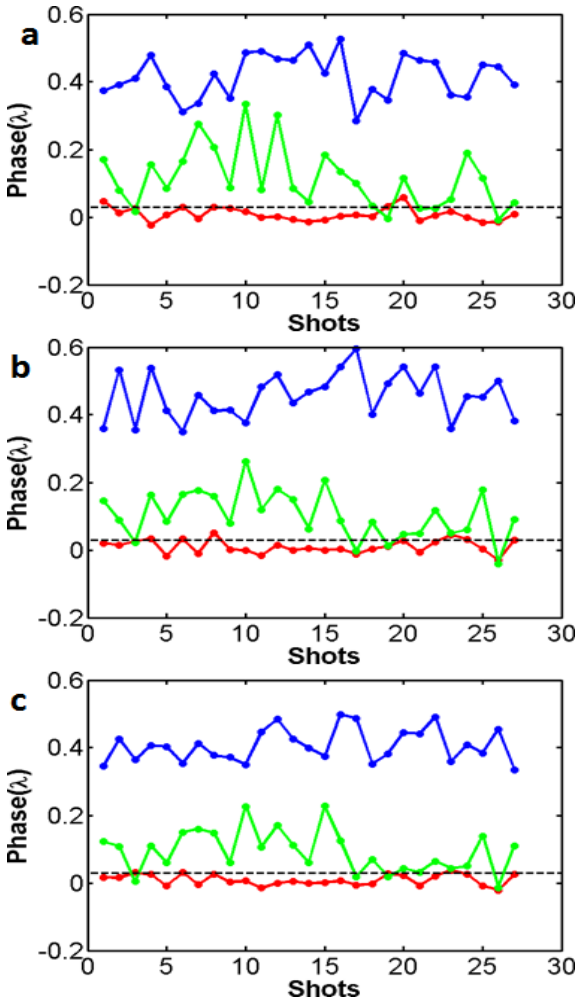

Figure 3.43: The three main aberrations — coma (blue line), astigmatism at 0^o (green line) and astigmatism at 45° (red line) of consecutive HH seed shots analysed with following approaches: (a) intensity threshold, (b) $6\ mm$ circular pupil and (c) $5.5\ mm$ circular pupil.

account, which is sensitive to many parameters, such as gas pressure, focal spot position and IR beam quality. Nevertheless, the spatial evolution along the beam propagation implies that the most convergent beam profile occurs at $Z = 0\ mm$, which is supposed to be the imaging point and seeding point. In consequence, we performed more back propagation HH seed source profiles at $Z = 0\ mm$, as illustrated in $Fig.\ 3.46$, where the shot numbers are corresponding to the shot numbers in $Fig.\ 3.42$ and $Fig.\ 3.43$. It is apparent that all the reconstructed source profile is demonstrated as elongated shape in vertical, while the horizontal size is remaining at $\sim 20\ \mu m$ level. One should also observe that there are multi-spot in elongated vertical and with a main spot at the top. This can be caused by the synthesis process of HH generation in the gas puff and the imaging from the toroidal mirror. Further understanding of this behaviour would require a non-linear simulation of the HH generation in the gas puff with equivalent experiment parameters. The impact to the SXRL seeding with plasma amplifier will be discussed in **Section 3.3.3.3**. Nevertheless, there are more than many efforts can be done to improve the HH seed beam quality.

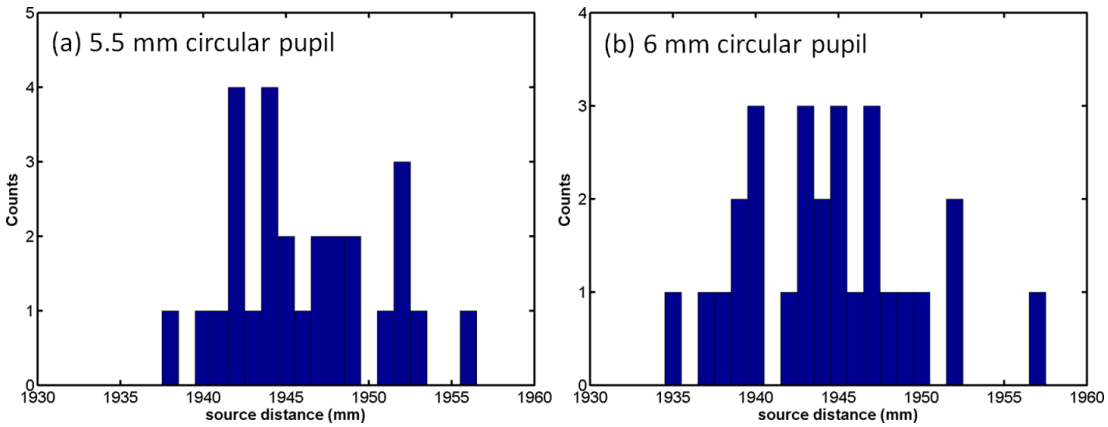

Figure 3.44: Histogram of source distance betweeen imaging spot of HH seed (location of plasma centre) and Hartmann plate computed by back propagation with (a) $5.5\ mm$ and (b) $6\ mm$ circular pupils, respectively.

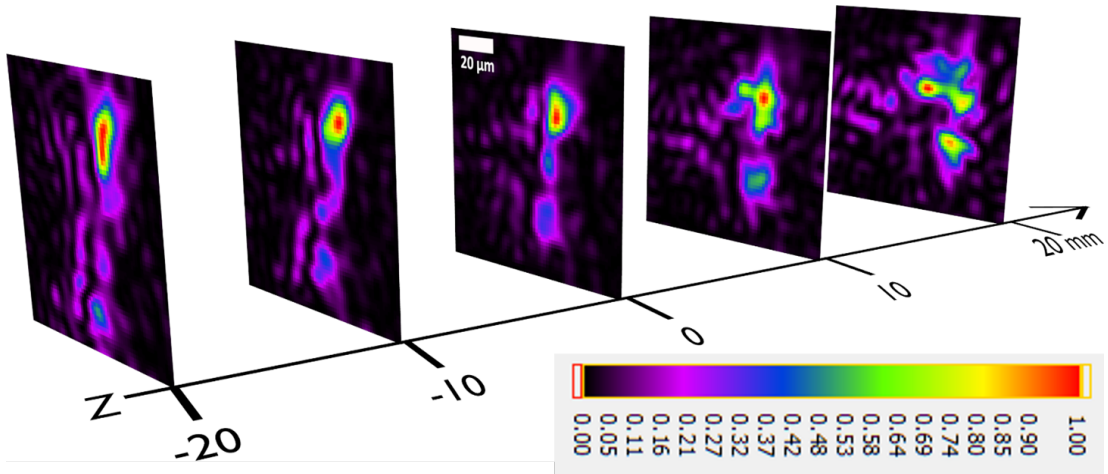

Figure 3.45: The retro-propagation of the HH seed source field along the Rayleigh length from $-20\ mm$ to $20\ mm$. It is calculated by point spread function in the free space. $Z = 0\ mm$ corresponds to the centre of the source and also to the region of least confusion. Negative value indicates the direction deviated from the sensor.

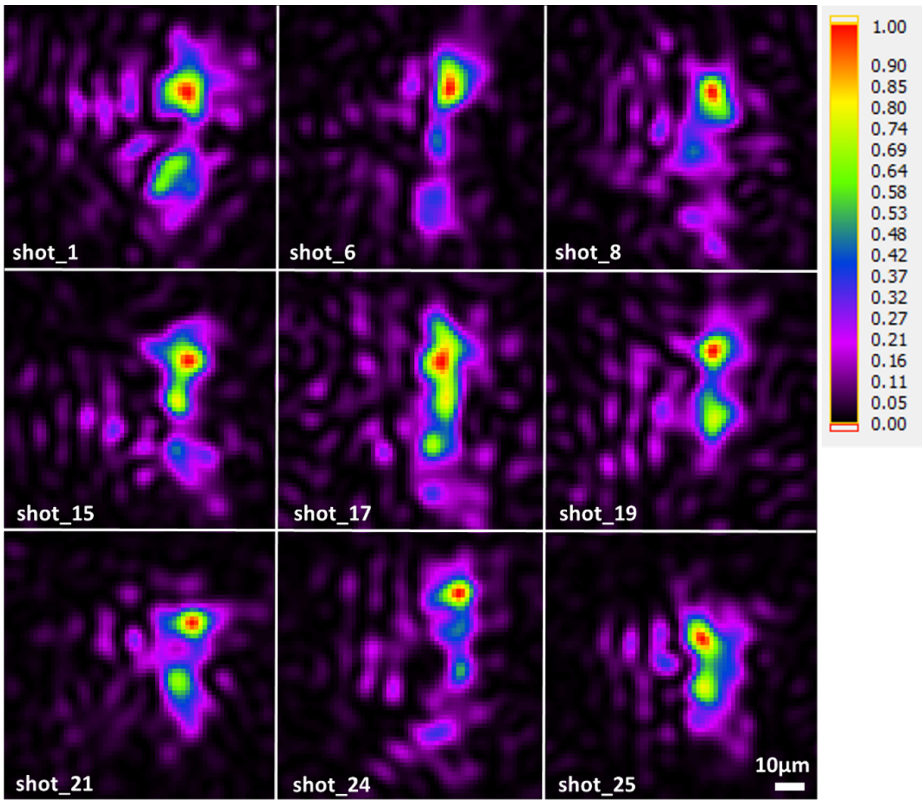

Figure 3.46: Retro-propagation of the HH seed intensity field of the source at $Z = 0$ mm by point spread function over nine different shots. The shot numbers are corresponding to the shot numbers demonstrated in $Fig.$ 3.42 and $Fig.$ 3.43.

3.3.3.3 Wave front of seeded SXRL

According to the discussion in **Section 3.3.3.1**, the HH driven laser was eventually set to S polarization to achieve significant amplification after seeding. The HH beam was injected into a x-ray plasma amplifier employing a toroidal mirror with a magnification of one time. HH seed injection angle was $5\ mrad$ deviated from $4\ mm$ long Molybdenum slab target surface, and injection time was at $2\ ps$ after the peak of short pump pulse (peak-to-peak). Seeded SXRL was consequently detected by the Hartmann wave front sensor located $3.5\ m$ away with a 45° multilayer mirror placed at $0.9\ m$ after the plasma amplifier, as schematically illustrated in $Fig.\ 3.35$.

A sample raw image of seeded SXRL (shot number 22 in $Fig.\ 3.55$) recorded by Hartmann wave front sensor was represented in $Fig.\ 3.47$. There are three interesting regions in the full image ($Fig.\ 3.47(a)$). First of all, the brightest beam primarily located in the second quadrant of the image is corresponding to the amplified seed with clear diffraction patterns tilted by 22.5°, as displayed in the close-up ($Fig.\ 3.47(b)$). The diffraction pattern is referred to the explanation in **Section 3.3.3**. Secondly, the weak part as illustrated in $Fig.\ 3.47(c)$ is principally contributed by the ASE, where the diffraction is obscure. It is important to note that ASE signal is overspread on the CCD chip. Phase analysing by the sensor is extremely dependent on the diffraction pattern, and the ASE signal may reduce the accuracy of wave front measurement. Therefore, carefully clipping the ASE during the wave front processing is mandatory. Finally, it is interesting to point out that there is a secondary bright beam observed in the first quadrant of the image as marked with dashed ellipse, which is smaller and less bright than the main amplified seed. However, the diffraction pattern of this secondary beam is apparent. It is implying that this secondary beam is coherent SXRL and considered as amplified seed as well.

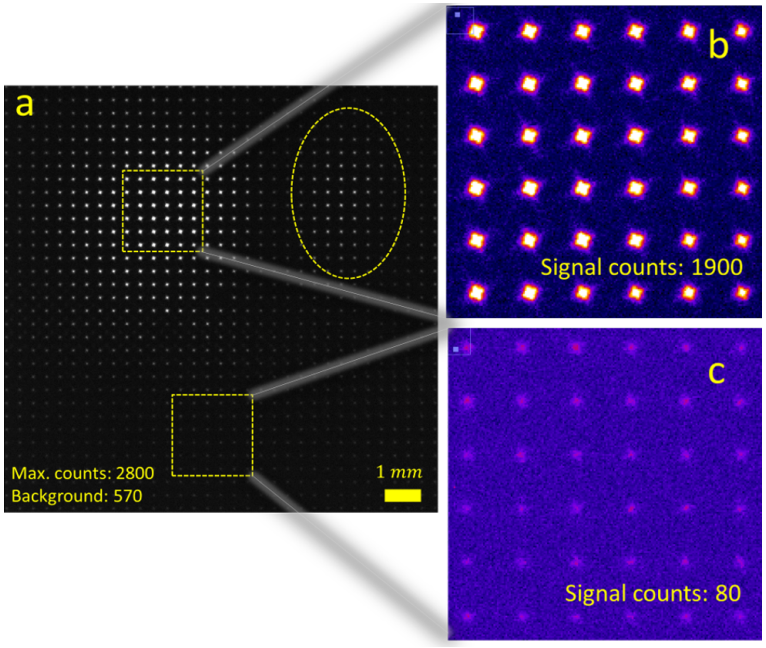

Figure 3.47: (a) Raw image of seeded SXRL with plasma amplifier measured by the Hartmann wave front sensor. (b) The region of interest coupled with amplified soft x-ray and ASE. (c) only with divergent ASE signal.

One should be noted that this multi-spot behaviour occurred among most of the shots during the suc-

cessive 27 shots in this measurement. In order to figure out this issue, we firstly checked out the footprint of HH seed without plasma amplifier and it showed a single round spot shape. Sequentially, we verified the footprint of seeded SXRL by placing x-ray CCD at $30\ cm$ after the 45° multilayer mirror, and it is shown in $Fig.\ 3.48$. Multi-spot were observed in the footprint of final output from the plasma amplifier. This obtained footprint image consists of 1) a smooth curved edge, 2) bright and homogeneous background inside the curved shape, 3) a big bright beam spot coupled with secondary and tertiary beam spots. First of all, the clear curved edge without diffraction pattern is normally coming from closing object respected to the CCD detector. In this experiment condition, it could be caused by the 45° multilayer mirror which is placed only $30\ cm$ far from the detection plane. Then, the bright and homogeneous light full filled the 45° multilayer mirror is considered as the self-emission (ASE) from the x-ray plasma amplifier. Finally, the observed multi beam spots are in consistent with the multi-spot behaviour observed with Hartmann wave front sensor, which are considered as the amplified seed signals. It is worth nothing that only two beam spots were obtained with Hartmann wave front sensor while three beam spots were apparent in the footprint image. The difference of detection distance for footprint CCD ($\sim 1.2\ m$) and Hartmann sensor ($3.5\ m$) respected to the plasma amplifier should be taken into account. One can assume a cross angle between the multi-beam, the separations between these beam spots on the detection plane $1.2\ m$ and $3.5\ m$ away should be much difference. So that the Hartmann wave front sensor placed at longer distance is only adequate to detect double beam spots, where the Tertiary is out of the detection region.

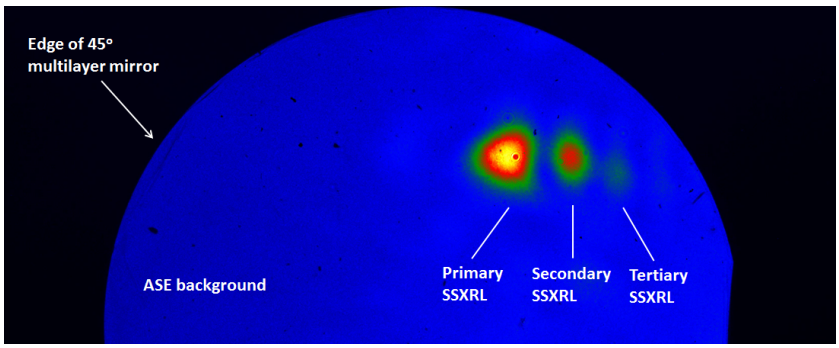

Figure 3.48: Footprint image of final ouput signal from x-ray plasma amplifier with HH seeding recorded by x-ray CCD placed at $30\ cm$ after the 45° degree mirror.

We are therefore concerning on the original reason causing the multi-beam amplification behaviour. The first considered effect is the refraction caused by the density gradient when SXRL beam propagation in the plasma amplifier. As explained in Chapter 2, **Section 2.1**, refraction occurs when wave propagation in a medium of atomic density. Here, the operated wavelength is very short ($18.9\ nm$), approaching atomic dimensions and the photon energy is comparable to the binding energy of the atomic electrons. When one considers the propagation in the forward direction, the frequency dependent refractive index has to be taken into account (see **Chapter 2, Section 2.6.4**). Indeed, it is the sum of forward-scattered radiation from all the atoms that interferes with the incident wave to produce modified propagating wave, compared to that in vacuum. Secondly, it is important to mention that, in previous section, multi HH spots separated by $10 - 20\ \mu m$ were observed in the back-propagated near-field images at the injection area (see $Fig.\ 3.45$ and $Fig.\ 3.46$). Coupled with the refraction effect with complex refractive index, this multi-seed-source can definitely cause the separated multi amplified SXRL beams as displayed in the far-field images in $Fig.\ 3.47$ and $Fig.\ 3.48$. Note that due to the variety refractive indexes in the plasma, which

caused by the density evolution and distribution, the HH seed propagating along the plasma column is still not clear. A 3D hydrodynamic simulation code is required for further understanding. Moreover, the back-propagation of the seeded SXRL will be discussed later in this Section, which will provide a comprehensive picture of this issue.

Based on above understanding, we started to treat the obtained wave front data with HASO software. Full images of intensity and wave front are displayed in $Fig.\ 3.49(a)$ and $Fig.\ 3.49(b)$, respectively. The beam arrived on the detection plane is composed of ASE, main amplified seed and the secondary amplified seed. While the incoherent ASE beam cannot be taken into account for wave front analysing, since the wave front is only meaningful to coherent light. It is apparent that the ASE background causes loss

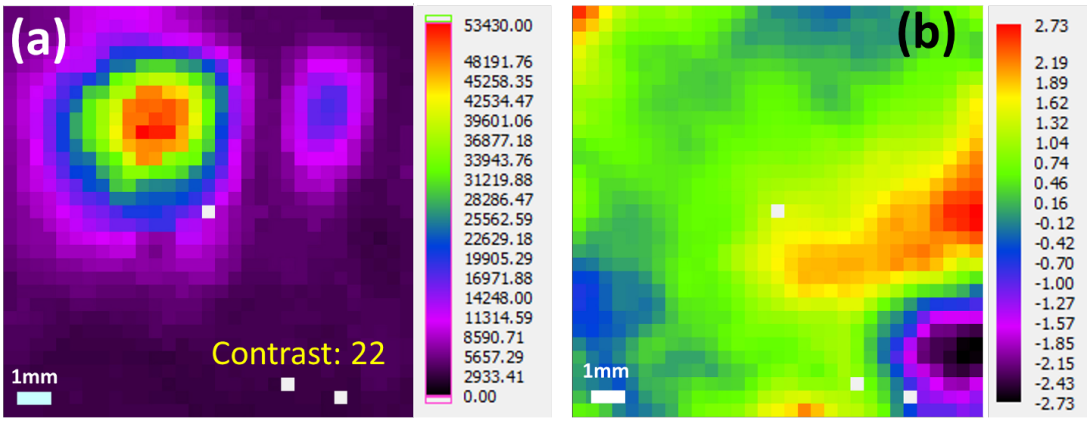

Figure 3.49: Sample full image of the deteced beam by Hartmann wave front sensor:(a) intensity and (b) wave front. This sample corresponds to the shot number 22 in $Fig.\ 3.56$

of accuracy during seeded SXRL wave front detection, as the preliminary analysed wave front value 3λ in PV displayed in $Fig.\ 3.49(b)$. Consequently, it is necessary to adequately choose the ROI for wave front processing. However, $Fig.\ 3.50$ shows six different shots of seeded SXRL, the number of each shot is corresponding to the shot number in $Fig.\ 3.56$. It implied that the beam shape was variously irregular from shot-to-shot and the multi-beam spots behaviour appeared over all the shots. On this account, one cannot choose a consistent regular shape of ROI as the approach demonstrated in previous section for the HH seed (see $Fig.\ 3.38(c)$).

It is interesting to pint out that, with the benefit of high divergence of ASE beam, the intensity contrast ratio between seeded SXRL and ASE is as high as 22. We hence performed an effective approach to select the appropriate ROI for wave front analysis setting the energy threshold. As demonstrated in $Fig.\ 3.51$, the energy threshold factor is set as 8% respected to the peak energy region, which means that all the detected beam shape with the part below 8% of the peak value is removed. The effect of ASE is substantially reduced within this technique, and the analysed wave front RMS value is improved by two times. However, the secondary seeded SXRL beam is still remained after the clipping by energy threshold. As we explained before, this beam spot is not the interest of our investigation in this experiment. This double-spot beam shape may cause a loss of wave front reconstruction accuracy (see **Section 3.3.1**). Therefore, the secondary beam is manually eliminated in further data processing.

Moreover, the final output beam position detected on Hartmann sensor was observed with a vibration within $6\ mm$ (see the vertical position changing in $Fig.\ 3.50$), while the HH seed beam position was extremely stable from the measurement in previous section. It can be indicated that this vibration in space

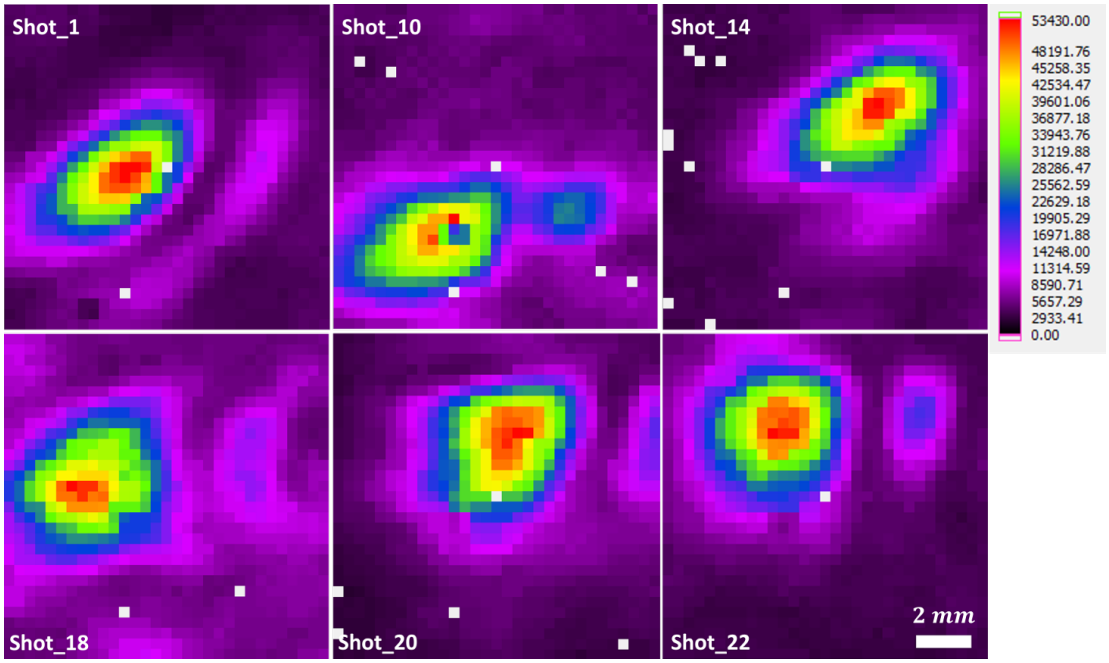

Figure 3.50: Shot-to-shot final output beam intensity profiles recorded by Hartmann wave front sensor. The shot numbers are corresponding to that in $Fig.\ 3.56$.

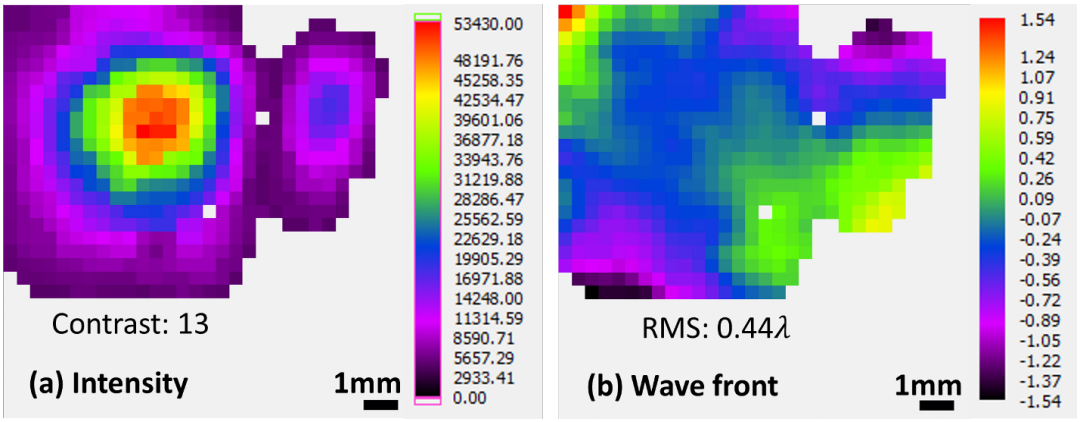

Figure 3.51: Processed (a) intensity and (b) wave front images with energy threshold of 8%.

is caused by the HH seed beam propagation in the plasma amplifier. Basically, the gain zone size of the amplifier is around $30\ \mu m$ [74] and the HH seed beam size is about two times larger (see discussion in **Section 3.3.3**). One can be sure that the observed $5\ mm$ vibration in spatial is not coming from the spatial matching between the seed and amplifier. Considering the long detection distance $(3.5\ m)$, a slight change of the output beam emergence angle from the plasma amplifier is a natural, such as a small change by $2\ mrad$ would cause $\sim 7\ mm$ shifting on the detection plane. The emergence angle of the amplified seed beam is strongly dependent on the complex refractive index evolution in the plasma amplifier.

A preliminary single beam treating was then displayed in $Fig.\ 3.52(a)$ including the intensity map

(left), phase map (middle) and reconstructed source shape (right) by point spread function (PSF) to the exit of the plasma amplifier with the Strehl ratio (SR) ~ 0.2 [53]. We assume the selected beam profile by this step contains full energy of the main seeded SXRL beam, so that the energy reference of "100%" is defined. However, one can still observe some ASE signal in the selected beam in $Fig.\ 3.52(a)$. As

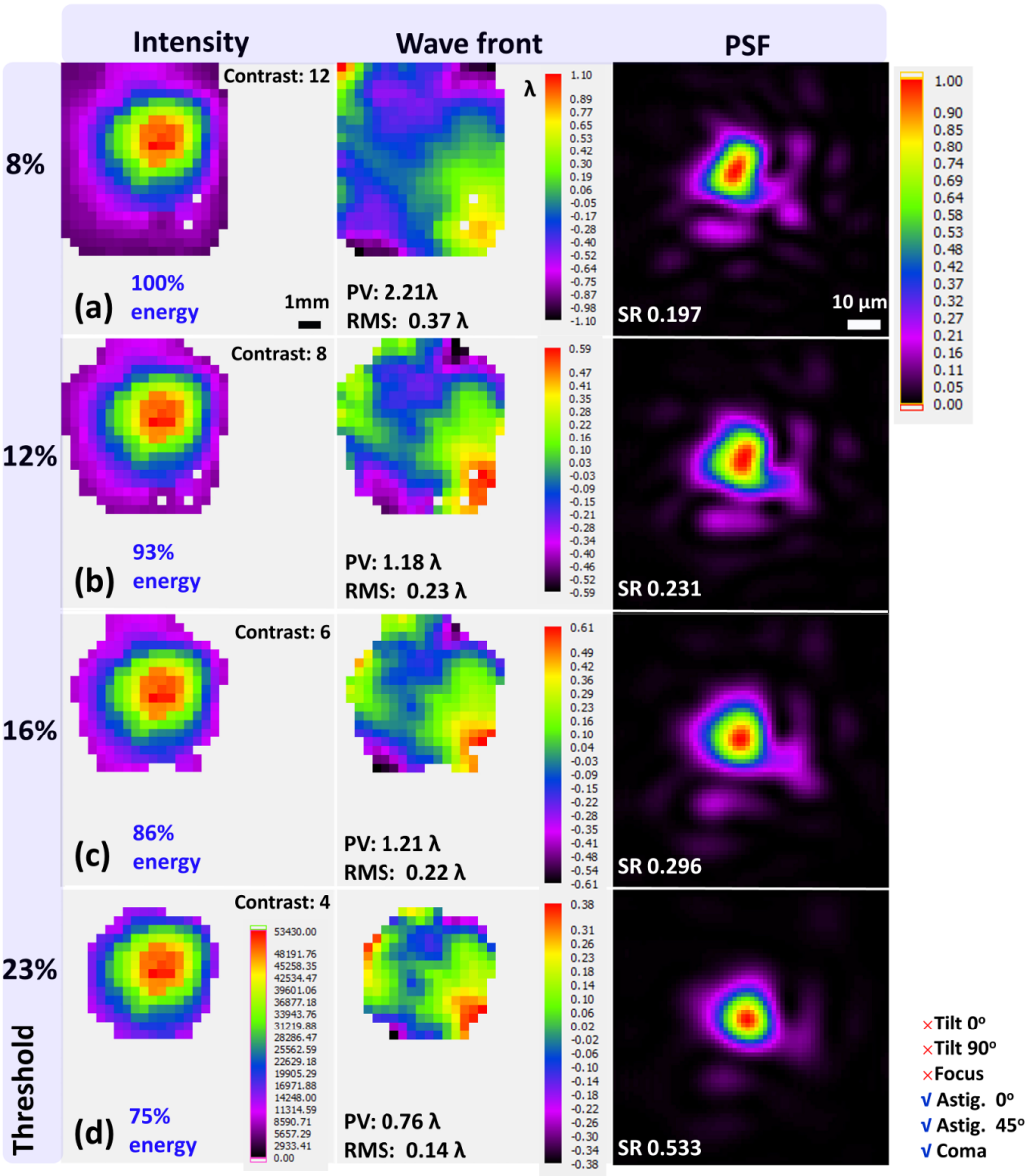

Figure 3.52: Data processing by adopting the approach of energy threshold: (a) 8%, (b) 12%, (c) 16% and (d) 23%.

explained in $Fig.\ 3.37(b)$, the incoherent ASE signal prevents the HASO software to converge well on the real wave front. More efforts should be done to minimize this effect during the wave front analysing. Therefore, a variety of energy thresholds were taken into account as illustrated in $Fig.\ 3.52$: (a) 8%, (b) 12%, (c) 16% and (d) 23%. It should be noted that the obtained wave front RMS value improved from

$0.37\ \lambda$ to $0.23\ \lambda$ when changing the energy threshold from 8% to 12%, where the full beam energy is 93% (respected to the "100%" reference). However, the wave front RMS value remains the same level when increasing the energy threshold from 12% to 16%, where full beam energy is 86%. This interesting behaviour shows the sensitivity of the ASE effect in wave front analysing. An even higher energy threshold (23%) was carried out in $Fig.\ 3.52(d)$, the energy contained in the beam was rapidly dropped down to 75%, while wave front improvement was not as sensitive as from (a) to (b). It is apparent that only the most intense central part of the seeded SXRL beam was considered, as the implying of Strehl ratio (0.53) from the reconstructed source. Eventually, the optimized pupil size was set at $Fig.\ 3.52(b)$, where most part of the ASE signal was removed and more than 90% of the full seed SXRL beam energy was reserved.

Sequentially, this processing approach was extended to 27 successive seeded SXRL shots from this measurement. Energy stability of the full amplified seed beam (resembling to $Fig.\ 3.52(a)$ is plotted as the blue line (right y axis) in $Fig.\ 3.53$, implying the energy stability is $\pm 17\%$, which is depressed comparing to that of HH seed ($\pm 6\%$) shown in $Fig.\ 3.39$. That may be caused by the refraction evolution of the plasma amplifier as mentioned before, the changing of the emergence angle from the plasma amplifier would have impact on the effective seed propagation distance in the gain zone, which is indicated to the amplification energy. It is worth nothing that the HH seed beam without plasma amplifier was directly detected without using 45° multilayer mirror. So a compensation of the mirror reflectivity should be taken into account when comparing the pulse energy between HH seed and amplified seed. In addition, the measured HH beam is consisted of several high order wavelengths, and only the 43^{rd} order is adequate to the amplification. In the wave front comparison (later in this section) between the HH seed and amplified seed beam, we assume the wave front of the recorded HH orders are remaining the same level. However, the energy proportion of this specific HH order (the 43^{rd}) in the detected HH beam is not figured out in this experiment. The detailed HH seed pulse energy amplification after the plasma amplifier is particularly discussed in the experiment demonstrated in Chapter 5.

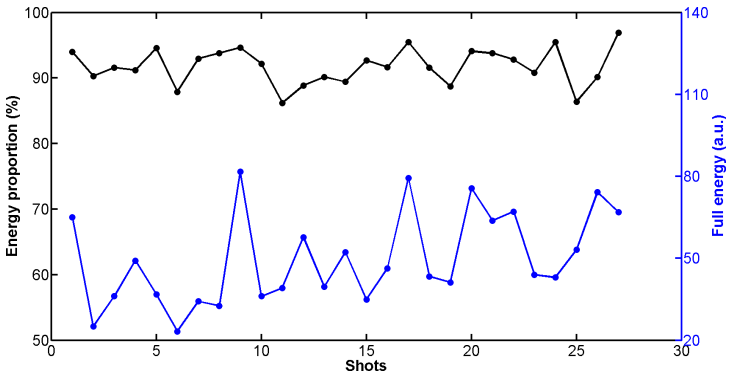

Figure 3.53: Seeded SXRL full energy stability from shot-to-shot (blue line, right coordinate) and energy proportions with the threshold data-processing approach (black line, left coordinate).

The black line illustrated in $Fig.\ 3.53$ indicating to the energy proportion ($92\% \pm 1\%$) of the selected beam respected to the assumed "100%" full energy of the main seeded SXRL beam. This treatment follows the criteria described in $Fig.\ 3.52(b)$. Subsequently, substantial wave front distortion analysing is performed in $Fig.\ 3.54$, where tilt 0°, tilt 90° and focus distortions are not taken into account as explained in **Section 3.3**. Black line with the left y axis is indicating PV wave front value for 27 consecutive shots,

and the shot-to-shot wave front RMS value is plotted in blue line (right y axis). The standard deviation of PV value is 20%, while standard deviation of wave front RMS value is down to 12%. Furthermore, in contrast with the wave front RMS value of HH seed $0.51\lambda \pm 0.03\lambda$, the value of seeded SXRL was improved to $0.23\lambda \pm 0.01\lambda$. Here, the error of the wave front corresponds to the half value of standard deviation over 27 consecutive shots. It is interesting to note that not only the SXRL wave front distortion was improved by over two times with plasma amplifier, but also the wave front stability was optimized by three times.

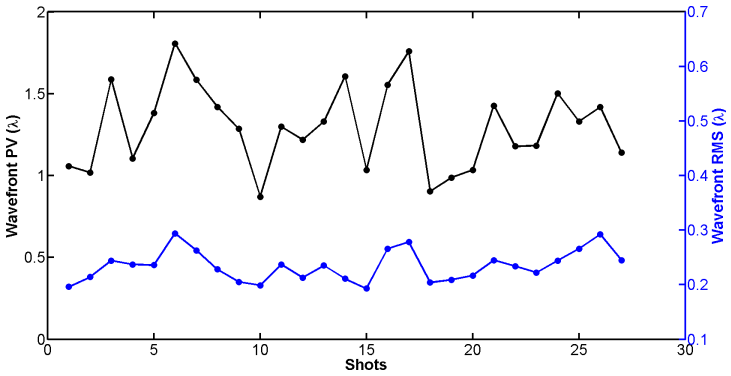

Figure 3.54: RMS (blue line, right coordinate) and PV (black line, left coordinate) wave front value of amplfied SXRL with $4\ mm$ *long plasma-amplifier crossing 27 consecutive shots.*

The observed beam improvement is resembling to the previous work of LOA group which showed a strong improvement in the wave front of seeded SXRL in a gas-amplifier [69]. However, the geometries of the two experiments and the physical processes influencing the gain creation are different. Consequently, as described in $Fig.\ 3.55$, the gain zone shapes are different between gas and solid amplifiers [51, 74] : (a) in SXRL gas-plasma amplifier, the shape of the gain region in the direction perpendicular to the laser propagation is decreasing sharply at the edge of the gain zone; (b) in the SXRL solid-plasma amplifier, the gain zone is evolving gently respected to the gas-plasma amplifier. Therefore, the effect of spatial filtering is much more efficient in gas-plasma amplifier. The coupling between seed and gain zone cannot follow the same optimization procedure and thus merits a specific study.

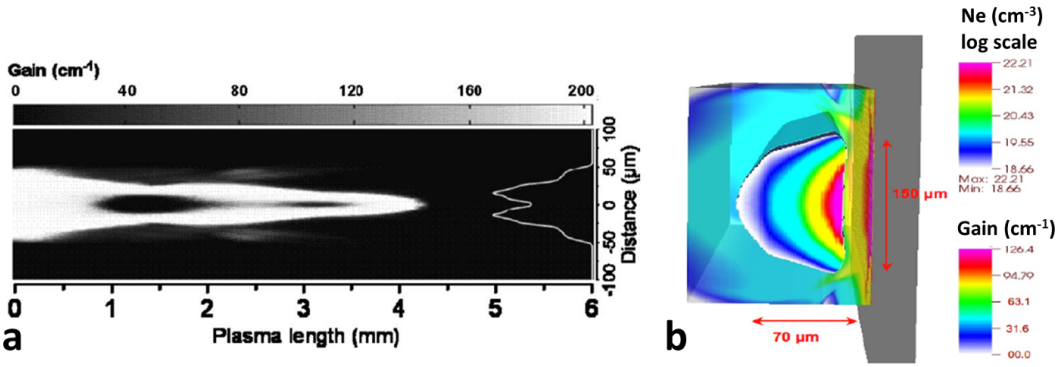

Figure 3.55: Calculated 2D distribution of the maximum gain coefficent in SXRL (a) gas-amplifier from [69] (transverse view) and (b) solid-amplifier from [75] (cross-sectional view).

Hartmann wave front sensor under Modal reconstructor mode allows for independent measurement of the three most important aberrations: coma, astigmatism at 0° and 45° (see **Appendix** $Fig.\ A.1$). Here the measured coma aberration is combined with coma, trefoil and the other aberrations, while coma is absolutely dominating. In $Fig.\ 3.56$, we plotted the three strongest aberrations in RMS value over 27 shots. Blue line is coma, green line and red line are corresponding to astigmatism at 0° and 45°, respectively. The black dashed line indicates the calibration limit (0.03λ RMS) of Hartmann wave front sensor [56]. In respect of HH seed aberrations analysed in $Fig.\ 3.43$, seeded SXRL astigmatism at 0° dropped from ∼0.10λ RMS to the calibration limit, while astigmatism at 45° did not show significant changes. Moreover, over two times improvement on coma was observed from $0.4l\lambda\pm0.02\lambda$ (HH seed, $Fig.\ 3.43$) to $0.18\lambda\pm0.01\lambda$ (seeded SXRL). Coma normally generates a central spot surrounded by many rays extending far from it [76]. This spot was selectively amplified while the surrounding rays were much less amplified, generating the observed drop of coma aberration, which is so-called spatial filtering effect [69].

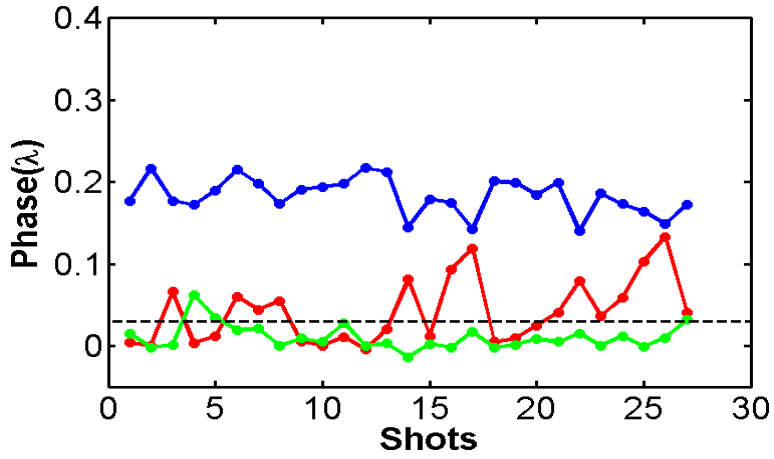

Figure 3.56: Shot-to-shot evolution of the three main aberrations, coma (blue line), astigmatism at 0^o) (green line), and astigmatism at 45^o (red line) for seeded SXRL with $4\ mm$ long plasma amplifier. The black dashed line is indicating the calibration limit of Hartmann wave front sensor.

In order to further verify this spatial filtering effect, we studied the influence of the plasma column length on the seeded SXRL wave front (see $Fig.\ 3.57$). Black data dots are indicating the wave front RMS value and blue data points are corresponding to the pulse energy of seeded SXRL. Each error-bar is corresponding to five shots. At $3\ mm$ length, the wave front of seeded SXRL remains at $0.5l\ \lambda\pm0.09\lambda$, while it improves to $0.31\lambda\pm0.09\lambda$ and $0.23\lambda\pm0.01\lambda$ for $3.5\ mm$ and $4\ mm$, respectively. In another hand, the output energy of seeded SXRL is increasing by the plasma amplifier length and reaching saturation around $3.5\ mm$, which is in consistence with previous experiment results [77, 51]. In addition, an apparent improvement of wave front stability with respect of HH seed was observed after plasma amplifier across the three plasma lengths. This result meets the interest of SXRL diffraction imaging applications [22], which requires for high pulse energy with good wave front. In the sake of comparison, we summarized the wave front RMS value and corresponded aberrations of HH seed (with different processing approaches) and seeded SXRL (with variety of plasma lengths), as represented in Table 3.1. The measurement error for seeded SXRL (SSXRL) with $3\ mm$ and $3.5\ mm$ plasma amplifier are corresponding to the standard deviation of five individual shots, while the others are indicating to the

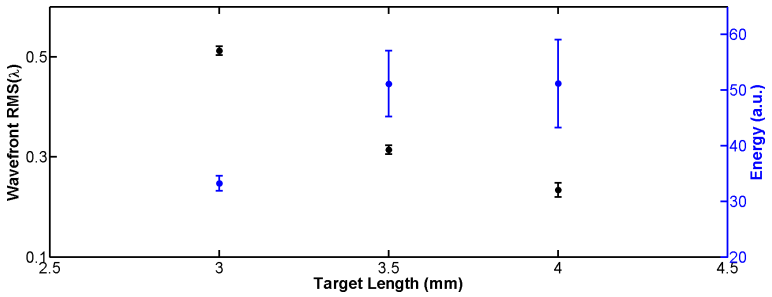

Figure 3.57: Residual wave front RMS value of seeded SXRL from $3.0\ mm$, $3.5\ mm$ *and* $4.0\ mm$ *long plasma amplifiers.*

standard deviation over 27 consecutive shots.

Table 3.1: Wave front analysis of HH seed with appropriate processing pupils and seeded SXRL with variety of plasma-column lengths.

Source	Approach	RMS(λ)	Coma(λ)	Astig. $0^o(\lambda)$	Astig. $45^o(\lambda)$
HH seed	energy threshold	0.54 ± 0.06	0.42 ± 0.03	0.11 ± 0.05	0.01 ± 0.01
HH seed	6.0 mm Pupils	0.57 ± 0.04	0.46 ± 0.03	0.10 ± 0.04	0.01 ± 0.01
HH seed	5.5 mm Pupils	0.51 ± 0.04	0.41 ± 0.03	0.09 ± 0.03	0.01 ± 0.01
SSXRL 3.0 mm	energy threshold	0.51 ± 0.01	0.28 ± 0.03	0.13 ± 0.06	0.09 ± 0.03
SSXRL 3.5 mm	energy threshold	0.31 ± 0.01	0.24 ± 0.01	0.03 ± 0.01	0.04 ± 0.02
SSXRL 4.0 mm	energy threshold	0.23 ± 0.01	0.18 ± 0.01	0.01 ± 0.01	0.04 ± 0.02

Owing to the refraction during the wave propagation in the plasma amplifier, HH seed injection angle might be the interest of final output beam wave front investigation. As a reminding, in all the seeding conditions prior to this discussion in the experiment, the injection angle was set to $5\ mrad$ deviated from Molybdenum slab target surface. We therefore changed this angle from $0\ mrad$ to $7.5\ mrad$, and measured wave front as well as the aberrations analysing are represented in Table 3.2 [84]. Slightly optimized wave front RMS value was obtained at injection angle of $5.0\ mrad$. However, the coma and astigmatism at 0° of all these amplified seed beams were remaining the same characteristics and a slightly changing of the astigmatism at 45° was observed. The amplified seed beam wave front doesn't show obvious function with the seed injection angles indicating that the refraction effect in our current experiment with $4\ mm$ long plasma amplifier does not cause much energy loss during the propagation. Nevertheless, in this experiment, the HH seed injection angle was set to $5.0\ mrad$ grazing incident angle in respect of the target surface.

In addition, the source distance between centre of plasma amplifier and Hartmann sensor holes-plate computed by back propagation with appropriate pupils were added up over 27 successive laser shots in $Fig.\ 3.58$. The most probable source distance of $3456\ mm$ with uncertainty of $7\ mm$ was obtained, which reveals the accuracy of source distance detection as high as 0.2%. Associating with observed beam size ($\sim 8\ mm$ in diameter) on the Hartmann sensor, the divergence of seeded SXRL as low as $\sim$1.1 $mrad$ was estimated, which is comparable to the HH seed ($1.3\ mrad$). It is worth nothing that this beam divergence of seeded SXRL is the most comparable to that of nowadays x-ray FEL beam achieved

Table 3.2: Wave front analysis by varying the HH injection angles into the plasma amplifier. from [84]

HH Injection Angle($mrad$)	wave front RMS(λ)	Coma(λ)	Astig. $0^o(\lambda)$	Astig. $45^o(\lambda)$
0	0.30±0.03	0.17±0.02	0.00±0.01	0.13±0.03
2.5	0.26±0.03	0.17±0.02	0.00±0.01	0.09±0.03
5.0	0.24±0.02	0.18±0.01	0.01±0.01	0.05±0.02
7.5	0.29±0.03	0.18±0.02	0.00±0.01	0.10±0.02

μrad level. As the intensity and phase of the SXRL beam were both recorded in the Hartmann

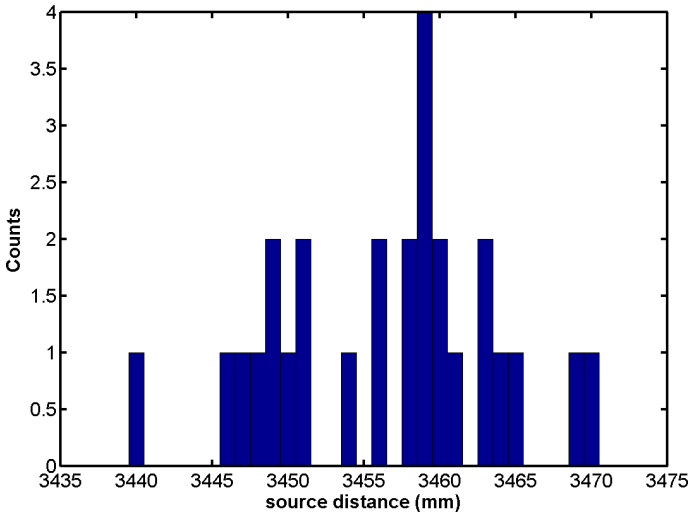

Figure 3.58: Histogram of source distance betweeen plasma amplifier center and Hartmann plate computed by HASO software with approprate pupils.

sensor, the complex amplitude of the electric-magnetic field on the sensor plane can be reconstructed by back propagating to the exit of plasma amplifier (see the discussion in **Section 3.3.2.2**). We remind that the main issue during the retro-propagation is the choice of the pupil size for the beam analysing. Large pupils contain noise from plasma ASE that has to be removed. Conversely, reducing too much of the pupil generates incorrect intensity distribution, spatial resolution and also results in smoothing of the outer part of the beam where aberrations imprint most of the wave front defects. We thus selected the largest pupils so as to contain more than 92% of the full detected energy and still remove most of the noise, as demonstrated in $Fig.$ 3.52 and $Fig.$ 3.53. It is important to note that, in $Fig.$ 3.52 the reconstructed seeded SXRL source profile as well as its Strehl ratio are sensitive with the pupil size (beam size) chosen for the back-propagation.

The second issue when one reconstructs the intensity distribution near the source location is the spatial resolution along both the transversal and longitudinal axis. As given by the numerical aperture of the beam, the transverse resolution is about 10 μm while the Rayleigh length is about 20 mm. Consequently, we were not able to resolve the fine structure of the gain zone. However, it was possible to follow the change of the source size and shape for the different time delays, which will be discussed later. Source from several different locations (-20 mm, -10 mm, 0 mm and 10 mm, 20 mm) along

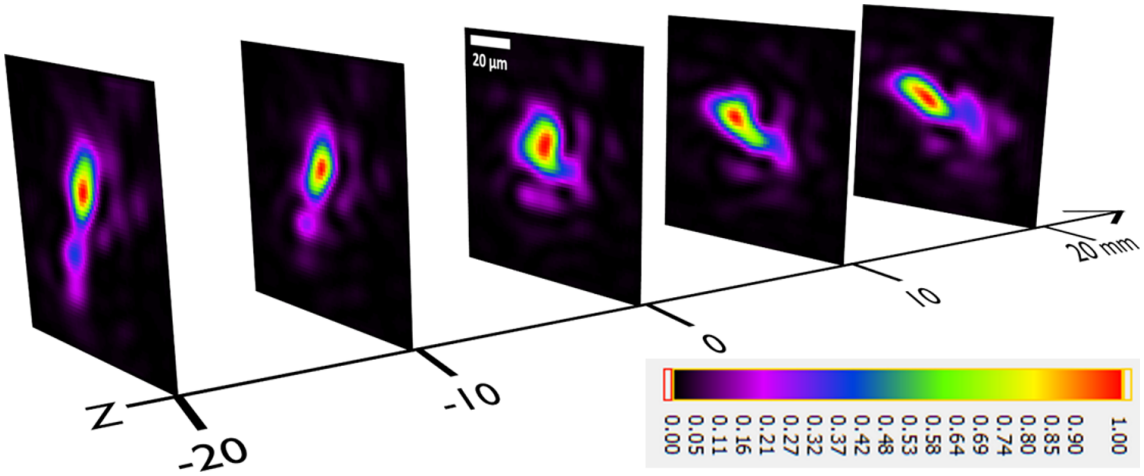

Figure 3.59: The back-propagation of the seeded SXRL along the Rayleigh length from -20 mm to 20 mm. It is calculated by point spread function in the free space. $Z = 0$ mm corresponds to the exit of the plasma amplifier. Negative value indicates the direction deviated from the sensor.

the beam propagation are illustrated in $Fig.$ 3.59. The 0 mm location corresponds to the exit of the plasma amplifier and negative value is indicating the direction deviating from the detection sensor. Source intensity profiles were reconstructed by back propagation the wave-field. For $z = -10$ mm and $z = 10$ mm, astigmatism produces elongated beams and with main axis rotated by $\sim 45°$. The source at $z = 0$ mm is relatively symmetrical shape with spot size of 20 $\mu m \times 20$ μm FWHM.

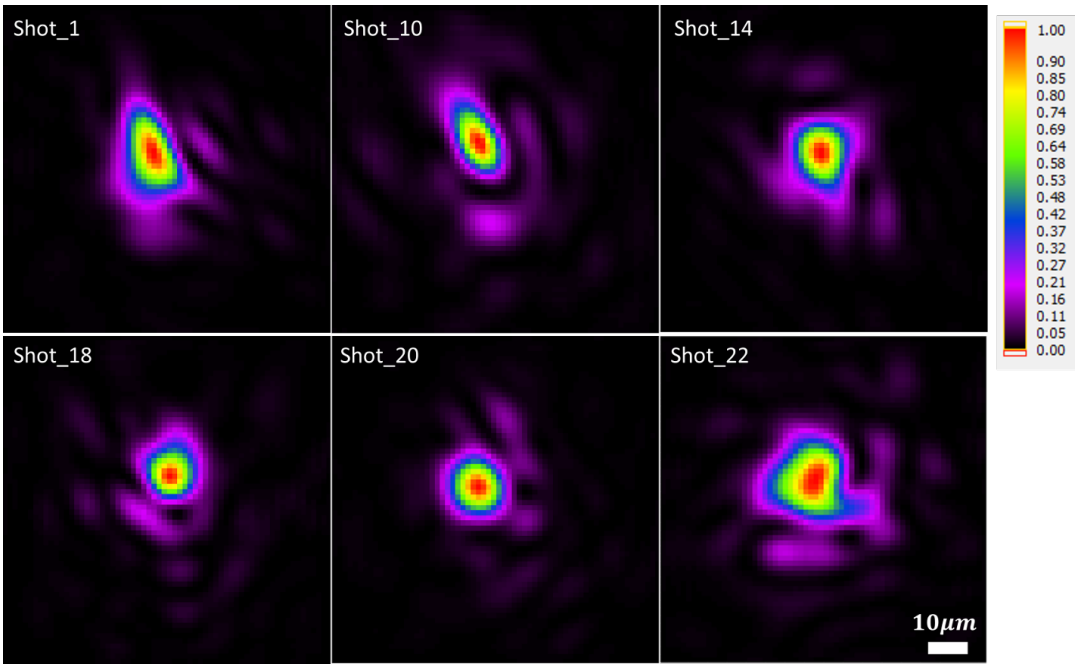

Figure 3.60: Seeded SXRL source intensity field reconstruction at the location of $Z = 0$ mm over different shots with shot numbers displayed in $Fig.$ 3.50.

Moreover, shot-to-shot reconstructed source intensity maps are illustrated in $Fig.\ 3.60$, where the shot numbers correspond to that in $Fig.\ 3.50$. As represented in $Fig.\ 3.61$, the average seeded SXRL source size over 27 consecutive shots, corresponded to the cross-sectional gain zone area at exit of the plasma amplifier, was obtained as $27\mu m\pm3\ \mu m$ in horizontal and $34\ \mu m\pm3\ \mu m$ in vertical. The Strehl ratio of the constructed SXRL source is 0.30 ± 0.04, which is s excellent parameter at soft x-ray domain.

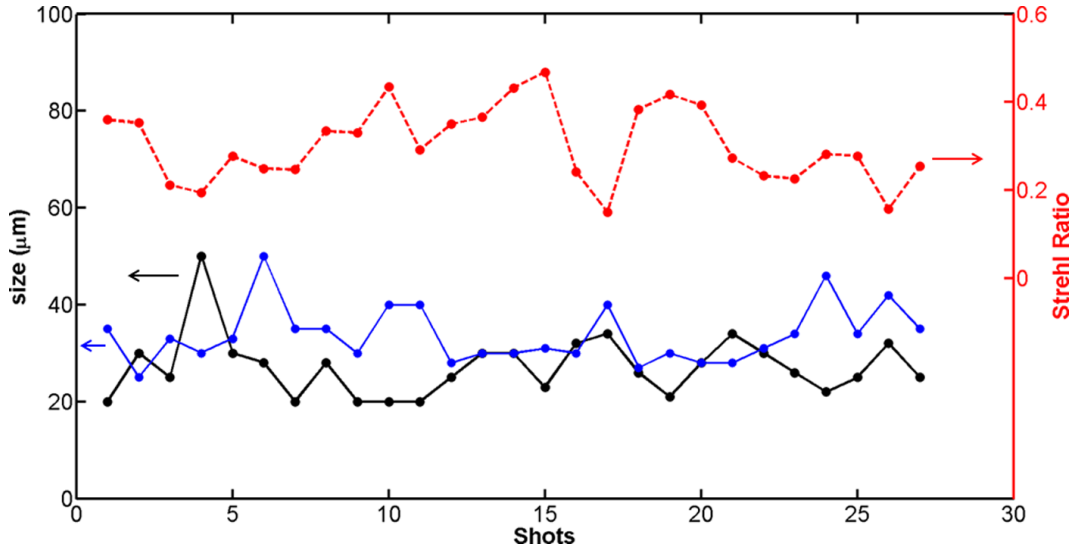

Figure 3.61: Back-propagated source size in horizontal (balck line) and vertical (blue line) at the exit of plasma amplifier over 27 consecutive shots, as well as the Strehl ratio (red line) for each.

Solid-plasma amplifiers pumped by a combination of long and short pulses have been known to experience hydrodynamic evolution that may impact on the wave front of the amplified HH seed. To study this effect, the HH seed was injected at different delays ranging from $0\ ps$ (seed synchronized with the peak of short pump pulse) to $5\ ps$ delay. The typical sample intensity and wave front images from each injection time are illustrated in $Fig.\ 3.62$. The ROI beam shapes were chosen with the energy threshold processing approach as described in $Fig.\ 3.52$. It is interesting to note that due to the temporal evolution of the gain (population inversion), at $5\ ps$, the peak intensity of amplified seed signal was only two times stronger than the ASE background which normally causing the inaccuracy during the signal extraction.

Furthermore, energy curve of the seeded SXRL as a function of time delay between HH seed and peak of short pump pulse was emerged with the blue dashed line (right y axis) in $Fig.\ 3.63$. This curve is associated with the gain curve obtained in our previous experiments under this GRIP pump scheme [51, 77]. After $5\ ps$ delay, the intensity of amplified signal is too weak to enable single-shot wave front detection with Hartmann wave front sensor. Therefore, we conducted measurements for a span of $5\ ps$ for a $4\ mm$ long plasmas amplifier. An optimum wave front of 0.23λ was observed at $2\ ps$ time delay, while the wave front aberration increases up to 0.41λ at longer delays.

To make further efforts, the three main aberrations varied by the time delay were analysed in $Fig.\ 3.64$. Black dashed line indicates the calibration limit of Hartmann wave front sensor. Astigmatism at 45° decreased from 0.12λ RMS at $0\ ps$ to the calibration limit at $5\ ps$, and astigmatism at 0° was observed to increase with the delay, while coma aberration showed little variation with injection time. In both above figures, the error bars correspond to the standard deviation of $5-10$ laser shots.

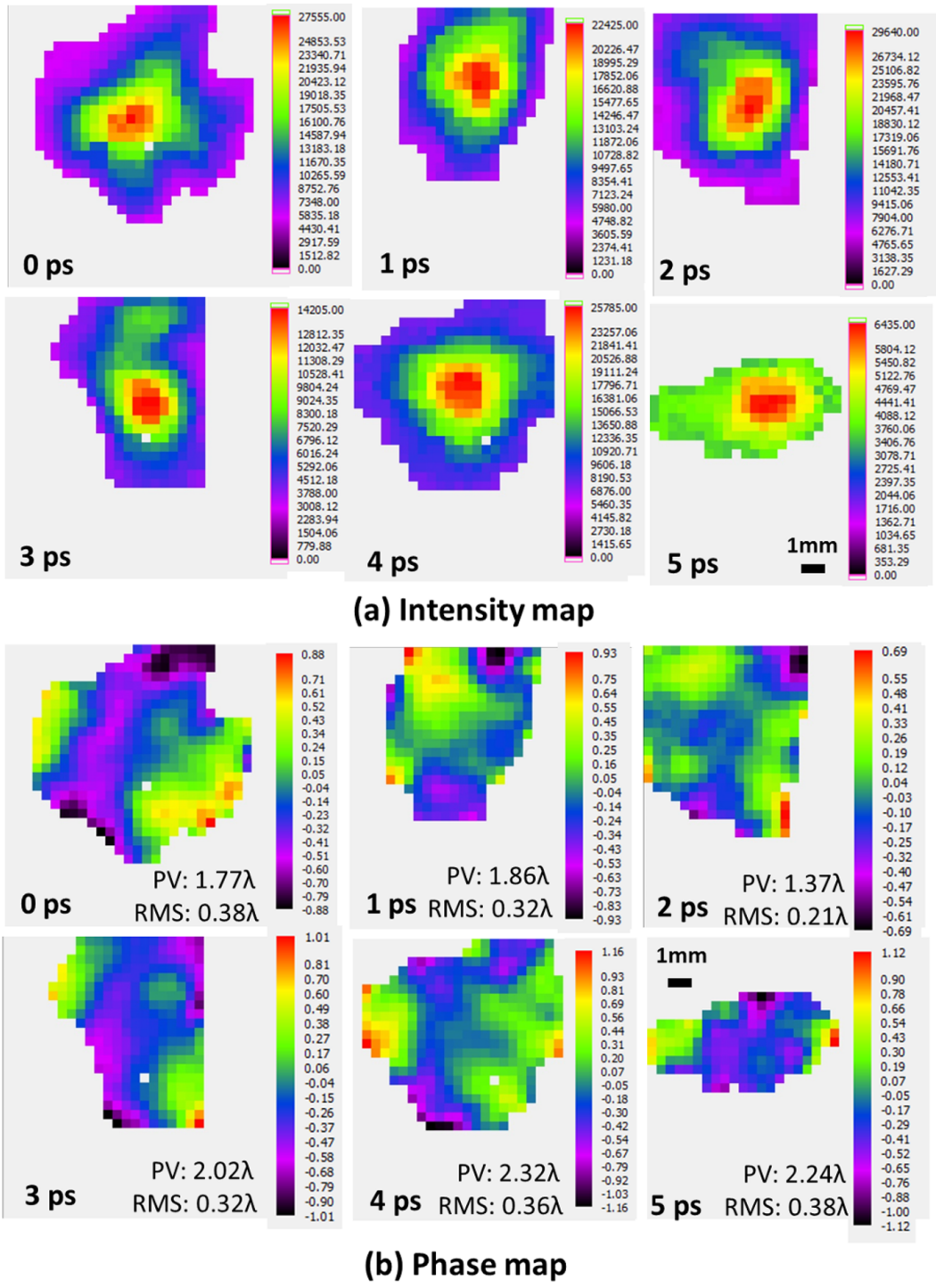

Figure 3.62: Detected (a)intensity and (b)wave front map of the sample shots for the variety of delays between HH injection time and the peak of arrival short pump pulse. The time of 0 ps is corresponding to the peak of short pump pulse.

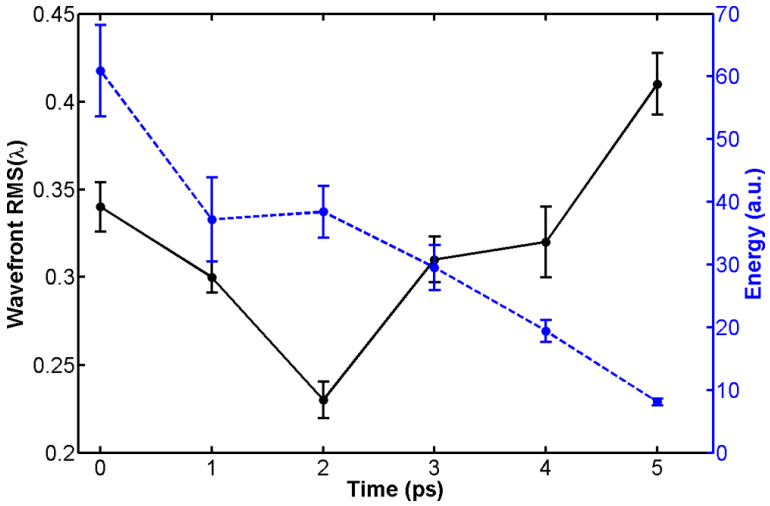

Figure 3.63: The wave front RMS value (black line, left y axis) and intensity curve (blue line, right y axis) of seeded SXRL versus the delay between injection time of HH seed and the peak of short pump pulse.

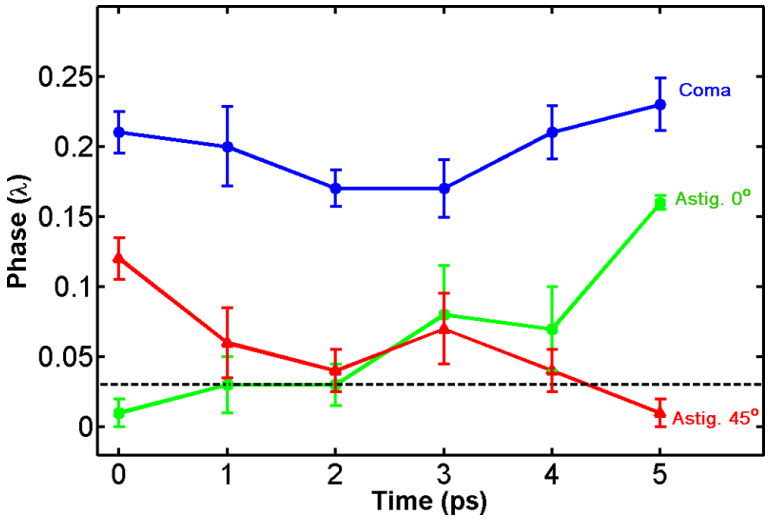

Figure 3.64: Evolution of three main aberrations, coma (blue line), astigmatism at 0°) (green line), and astigmatism at 45° (red line) of seeded SXRL versus the delay between injection time of HH seed and the peak of short pump pulse with $4\ mm$ long plasma amplifier. The black dashed line is indicating the calibration limit of Hartmann wave front sensor.

The above trends are associated with the evolution of plasma parameters such as density gradients, size, shape, and position of the gain region, a completely understanding of these results requires coupling $3D$ Maxwell-Bloch codes with $2D$ or $3D$ hydrodynamic codes. So far, to our best knowledge such model does not exist, while the back-propagation to the exit of plasma amplifier could provide further understanding the impact of hydrodynamic conditions on the seeded SXRL source. We hereby chose a typical laser shot for each delay and presented the (a) intensity maps and (b) phase maps from the detection plane of Hartmann wave front sensor in $Fig.\ 3.62$. On the basis of this, the retro-propagation to the exit of the plasma amplifier ($z = 0\ mm$) of wave-field was performed, as illustrated in $Fig.\ 3.65$,

with time delay at (a) $0\ ps$, (b) $1\ ps$, (c) $2\ ps$, (d) $3\ ps$, (e) $4\ ps$ and (f) $5\ ps$. The minimum source size at $20\ \mu m \times 18\ \mu m$ was observed at the time delay of $2\ ps$, which is consistent with the best wave front appearing delay shown in *Fig.* 3.64. Furthermore, the reconstructed source profile at $0\ ps$ shows a slightly elongated tilt with an angle of $\sim 45^{\circ}$ with respect to the vertical axis. This might be caused by the astigmatism at that direction. Owing to the phase quality of HH seed beam, the amplified seed beam is sensitive to the gain zone temporal evolution. Once again, a completely understanding of these results requires coupling 3D Maxwell-Bloch codes with 2D or 3D hydrodynamic codes.

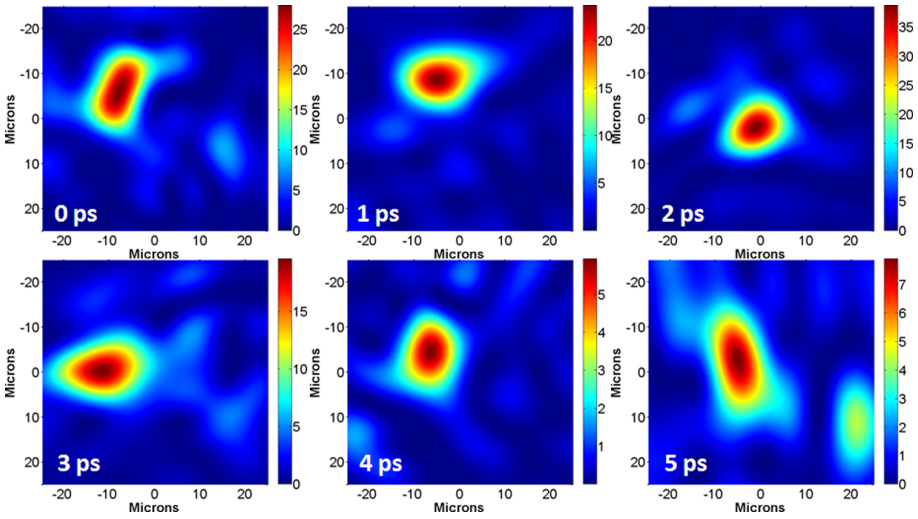

Figure 3.65: The source intensity reconstruction of seeded SXRL as a function of time delays between seed injection time and the arrival of the peak of short pump pulse for $4\ mm$ *long plasma amplifier:(a)* $0\ ps$*, (b)* $1\ ps$*, (c)* $2\ ps$*, (d)* $3\ ps$*, (e)* $4\ ps$ *and (f)* $5\ ps$*.*

3.3.4 Summary on wave front of HH-seeded SXRL

In summary, we have measured the wave front of an HH-seeded SXRL created by irradiation of a solid target as well as the wave front of HH seed without plasma amplifier by using a soft x-ray Hartmann wave front sensor. The main conclusion of this experiment is that SXRL solid-based plasma amplifier ($4\ mm$ long) produce a good wave front with distortions reaching $\lambda/5$ RMS, although it is significantly denser than gas-based amplifier. Previous work on gas-plasma amplifier [69] showed that the small size of gain region acts as spatial filtering of the incoming beam and results in a reduction of the wave front aberration for the amplified signal. Meanwhile, the back propagation of HH seed and seeded SXRL in this study verified the spatial filtering effect in more direct way.

According to this experiment, one could make following conclusions: i) the wave front RMS value and its stability of amplified seed improve ~ 2.5 times and over 4 times, respectively, with respect to that of HH seed; ii) the main optimization is coma aberration due to the spatial filtering; iii) an improvement of seeded SXRL wave front was observed by increasing the plasma amplifier length, and saturation amplified energy was achieved under this condition; iv) the seeded SXRL wave front is strongly dependent on the seed beam quality which was observed with strong coma aberrations caused by the toroidal injection mirror [79]; v) the optimized wave front occurs at $2\ ps$ time delay between HH seed and the peak of short

pump pulse ($6\ ps$), where astigmatism is the most sensitive distortion and coma is relatively stable with the delay; v) HH-seeded SXRL is capable to reach diffraction-limited ($\lambda/14$) beam by optimizing the HH seed beam quality, such as lower gas pressure for HH generation and better imaging mirror for HH seed injection to the plasma amplifier.

In order to perform a more detailed study of the impact of plasma hydrodynamic, an image relay system must be couple to the wave front sensor to achieve a higher numerical aperture and higher spatial resolution. Moreover, the statistical studies observed that the wave front of the seeded SXRL beam is more stable than that of the HH seed, opening the possibility to implement static or active wave front correction. Alternatively, the improvement of wave front, from HH seed to seeded SXRL, gives the great promise of the beam properties for the upcoming SXRL CPA system [54, 80] and matches the follow-up process, such as phase guaranty for SXRL compressor. It would also positively contribute the achievement of high peak intensity. Taking account of the pulse duration ($\sim 1\ ps$) [85] achieved nowadays of HH seeded SXRL from solid-plasma amplifier, the peak intensity could reach $5\times10^{15}\ W/cm^2$ for the diffraction-limited SXRL. Finally, this measurement of the source size of a seeded solid target SXRL confirms the high brightness of $\sim 1\times10^{26}\ photons\cdot s^{-1}\cdot mm^{-2}\cdot mrad^{-2}$. In contrast, the SXRL peak brilliance from free-electron laser in FLASH is 1×10^{29}-$1\times10^{31}\ photons\cdot s^{-1}\cdot mm^{-2}\cdot mrad^{-2}$/0.1%BW.

Bibliography

[1] G. Schmahl and D. Rudolph, Optik **29**,577-585 (1969).

[2] B. Niemann, D. Rudolph D. and G. Schmahl, Appl. Opt. **15**,1883-1884 (1976).

[3] H. Rarback, D. Shu, S. C. Feng, H. Ade, J. Kirz, I. McNulty, D. P. Kern, T. H. P. Chang, Y. Vladimirsky, N. Iskander, D. Attwood, K. McQuaid and S. Rothman, Rev. Sci. Instrum. **59**,52-59 (1988).

[4] J. Kirz, H. Ade, E. Anderson, D. Attwood, C. Buckley, S. Hellman, M. Howells, C. Jacobsen, D. Kern, S. Lindaas, I. McNulty, M. Oversluizen, H. Rarback, M. Rivers, S. Rothman, D. Sayre and D. Shu, Phys. Scripta **T31**,12-17 (1990).

[5] B. A. V. Fresnel, J. Opt. Soc. Am. **51**, 405–412 (1961).

[6] J. Miao, T. Ishikawa, B. Johnson, E. H. Anderson, B. Lai, and K. O. Hodgson, Phys. Rev. Lett. **89**, 088303 (2002).

[7] Y. Takahashi, Y. Nishino, R. Tsutsumi, H. Kubo, H. Furukawa, H. Mimura, S. Matsuyama, N. Zettsu, E. Matsubara, T. Ishikawa, and K. Yamauchi, Phys. Rev. B **80**, 054103 (2009).

[8] E. Lima, L. Wiegart, P. Pernot, M. Howells, J. Timmins, F. Zontone, and A. Madsen, Phys. Rev. Lett. *103*, 198102 (2009).

[9] A. Sakdinawat and D. Arrwood, Nature Photonics **4**, 840-848 (2010).

[10] D. Collison, C. D. Garner, C. M. McGrath, J. F. W. Mosselmans, M. D. Roper, J. M. W. Seddon, E. Sinn and N. A. Young, J. Chem. Soc., Dalton Trans., 4371-4376 (1997).

[11] S. Eisebitt, J. Lüning, W. F. Schlotter, M. Lörgen, O. Hellwig, W. Eberhardt and J. Stöhr, Nature **432**, 885–888 (2004).

[12] B. Vodungbo, J. Gautier, G. Lambert, A. B. Sardinha, M. Lozano, S. Sebban, M. Ducousso, W. Boutu, K. Li, B. Tudu, M. Tortarolo, R. Hawaldar, R. Delaunay, V. López-Flores, J. Arabski, C. Boeglin, H. Merdji, Ph. Zeitoun and J. Lüning, Nature Communication **3**, 999(2012).

[13] A. Barty, C. Caleman, A. Aquila, N. Timneanu, L. Lomb, T. A. White, J. Andreasson, D. Arnlund, S. Bajt, T. R. M. Barends, M. Barthelmess, M. J. Bogan, C. Bostedt, J. D. Bozek, R. Coffee, N. Coppola, J. Davidsson, D. P. DePonte, R. B. Doak, T. Ekeberg, V. Elser, S. W. Epp, B. Erk, H. Fleckenstein, L. Foucar, P. Fromme, H. Graafsma, L. Gumprecht, J. Hajdu, C. Y. Hampton, R. Hartmann, A. Hartmann, G. Hauser, H. Hirsemann, P. Holl, M. S. Hunter, L. Johansson, S. Kassemeyer, N. Kimmel, R. A. Kirian, M. Liang, F. R. N. C. Maia, E. Malmerberg, S. Marchesini, A.V. Martin, K. Nass, R. Neutze, C. Reich, D. Rolles, B. Rudek, A. Rudenko, H. Scott, I. Schlichting, J. Schulz, M. M. Seibert, R. L. Shoeman, R. G. Sierra, H. Soltau, J. C. H. Spence, F. Stellato, S. Stern, L. Strüder, J. Ullrich, X. Wang, G. Weidenspointner, U.Weierstall, C. B. Wunderer and H. N. Chapman, Nature Photonics **2**, 415 (2008).

[14] S. G. Podorov, K. M. Pavlov and D. M. Paganin, Opt. Express **15**, 9954–9962 (2007).

[15] I. McNulty, J. Kirz, Ch Jacobsen, E H. Anderson, M. R. Howells and D. P. Kern, Science **256**, 1009–1012 (1992).

[16] A. Morlens, J. Gautier, G. Rey, Ph. Zeitoun, J. Caumes, M. Kos-Rosset, H. Merdji, S. Kazamias, K. Cassou and M. Fajardo, Optics Lett. **31**, 3095 (2006).

[17] H. N. Chapman, S. P. Hau-Riege, M.l J. Bogan, S. Bajt, A. Barty, S. Boutet, S. Marchesini, M. Frank, B. W. Woods, W. H.y Benner, R.A. London, U. Rohner, A. Szöke, E. Spiller, T. Moller, C. Bostedt, D. A. Shapiro, M. Kuhlmann, R. Treusch, E. Plönjes, F. Burmeister, M. Bergh, C. Caleman, G. Huldt, M. M. Seibert and J. Hajdu, Nature **448**, 676 (2007).

[18] M. A. Pfeifer, G. J. Williams, I. A. Vartanyants, R. Harder, I. K. Robinson, Nature **442**, 63–66 (2006).

[19] D. Matthews, P. Hagelstein, M. Rosen, M. Eckart, N. Ceglio, A. Hazi, H. Medecki, B. MacGowan, J. Trebes, B. Whitten, E. Campbell, C. Hatcher, A. Hawryluk, R. Kauffman, L. Pleasance, G. Rambach, J. Scofield, G. Stone, and T. Weaver, Phys. Rev. Lett. **54**, 110 (1985).

[20] S. Suckewer, C. H. Skinner, H. Milchberg, C. Keane, and D. Voorhees, Phys. Rev. Lett. **55**, 1753 (1985).

[21] B. A. Reagan, K. A. Wernsing, A. H. Curtis, F. J. Furch, B. M. Luther, D. Patel, C. S. Menoni, and J. J. Rocca, Opt. Lett. **37**, 3624 (2012).

[22] H. N. Chapman and K. A. Nugent, Nature Photonics **4**, 833-839 (2010).

[23] R. Kodama, D. Neely, Y. Kato, H. Daido, K. Murai, G. Yuan, A. MacPhee, and C. L. S. Lewis, Phys. Rev. Lett. **73**,3215-3218 (1994).

[24] J. Zhang, A. G. MacPhee, J. Lin, E. Wolfrum, R. Smith, C. Danson, M. H. Key, C. L. S. Lewis, D. Neely, J. Nilsen, G. J. Pert, G. J. Tallents, and J. S. Wark, Science **276**, 1097 (1997).

[25] M. Tanaka, M. Nishikino, T. Kawachi, N. Hasegawa, M. Kado, M. Kishimoto, K. Nagashima, and Y. Kato, Opt. Lett. **28**, 1680–1682 (2003).

[26] M. Nishikino, M. Tanaka, K. Nagashima, M. Kishimoto, M. Kado, T. Kawachi, K. Sukegawa, Y. Ochi, N. Hasegawa, and Y. Kato, Phys. Rev. A **68**, 061802 (2003).

[27] D. Zimmer, B. Zielbauer, V. Bagnoud, U. Eisenbarth, D. Javorkova, and T. Kuehl, Optics Express, **16**, 10398 (2008).

[28] B. Ecker, E. Oliva, B. Aurand, D. C. Hochhaus, P. Neumayer, H. Zhao, B. Zielbauer, K. Cassou, S. Daboussi, O. Guilbaud, S. Kazamias, T. T. T. Le, D. Ros, P. Zeitoun, and T. Kuehl, Optic Exp. **20**, 25391-25399 (2012).

[29] V. Bagnoud, B. Aurand, A. Blazevic, S. Borneis, C. Bruske, B. Ecker, U. Eisenbarth, J. Fils, A. Frank, E. Gaul, S. Goette, C. Haefner, T. Hahn, K. Harres, H.-M. Heuck, D. Hochhaus, D. H. H. Hoffmann, D. Javorková, H.- J. Kluge, T. Kuehl, S. Kunzer, M. Kreutz, T. Merz-Mantwill, P. Neumayer, E. Onkels, D. Reemts, O. Rosmej, M. Roth, T. Stoehlker, A. Tauschwitz, B. Zielbauer, D. Zimmer, and K. Witte, Appl. Phys. B. **100**, 137-150 (2010).

[30] J. E. Balmer, F. Staub, C. Imesch, and D. Bleiner, Proc. SPIE **8140**, 81400X-81400X-5 (2011).

[31] K. Cassou, S. Kazamias, D. Ros, F. Plé, G. Jamelot, A. Klisnick, O. Lundh, F. Lindau, A. Persson, C.-G. Wahlström, S. de Rossi, D. Joyeux, B. Zielbauer, D. Ursescu, and T. Kühl, Opt. Lett. **32**, 139–141 (2007).

[32] J. Habib, O. Guilbaud, B. Zielbauer, D. Zimmer, M. Pittman, S. Kazamias, C. Montet, T. Kuehl, and D. Ros, Opt. Express **20**, 10128–10137 (2012).

[33] B. Ecker, B. Aurand,D. C. Hochhaus,P. Neumayer, B. Zielbauer, E. Oliva, L. Li, T. T. T. Le, Q. Jin, H. Zhao, K. Cassou, S. Daboussi, O. Guilbaud, S. Kazamias, D. Ros, Ph. Zeitoun and T. Kuehl, Journal of Physics B: Atoms, Molecular and Optical Physics, *In Press* (2015).

[34] T. Kuehl, B. Aurand, V. Bagnoud, B. Ecker, U. Eisenbarth, J. Fils, D. Hochhaus, D. Javorkova, P. Neumayer, B. Zielbauer, D. Zimmer, J. Habib, S. Kazamias, A. Klisnick, D. Ros and D. Ursescu, Proc. of SPIE, **7451**, 74510M-1-74510M-8 (2009).

[35] B. Rus, T. Mocek, A. R. Präg, M. Kozlová, G. Jamelot, A. Carillon, D. Ros, D. Joyeux, and D. Phalippou, Phys. Rev. A **66**, 063806 (2002).

[36] E. Oliva, P. Zeitoun, P. Velarde, M. Fajardo, K. Cassou, D. Ros, S. Sebban, D. Portillo, and S. le Pape, Phys. Rev. E **82**, 056408 (2010).

[37] M. D. Rosen, P. L. Hagelstein, D. L. Matthews, E. M. Campbell, A. U. Hazi, B. L. Whitten, B. MacGowan, R. E. Turner, and R. W. Lee, ibid. **54**, 106 (1985).

[38] H. Daido, Y. Kato, K. Murai, S. Ninomiya, R. Kodama, G. Yuan, Y. Oshikane, M. Takagi, H. Takbe, F. Koike, Phys.Rev. Lett. **75**, 1074 (1995).

[39] J. Nilsen, Y. Li, J. C. Moreno and E. E. Fill, Opt. Comm. **124**, 287 (1996).

[40] P. Jaegle, A. Carillon, H. Z. Chen, P. Dhez, L. Dwivedi, J. Jacoby, G. Jamelot, J. Zhang, M. H. Key, A. Kidd, A. Klisnick, R. Kodama, J. Krishnan, C. L. S. Lewis, D. Neely, P. Norreys. D. O. Neill, G. J. Pert, S. A. Ramsden, J. P. Raucourt, G. J. Tallents, J. Uhomoibhi, *X-ray Lasers*, Inst. Phys. Conf. Ser. No. 125 (1992).

[41] A. Carillon, H. Z. Chen, P. Dhez, L. Dwivedi, J. Jacoby, P. Jaegle, G. Jamelot, Jie Zhang, M. H. Key, A. Kidd, A. Klisnick, R. Kodama, J. Krishnan, C. L. S. Lewis, D. Neely, P. Norreys, D. O'Neill, G. J. Pert, S. A. Ramsden, J. P. Raucourt, G. J. Tallents and J. Uhomoibhi, Phys. Rev. Lett. **68**, 2917 (1992).

[42] D. Zimmer, B. Zielbauer, M. Pittman, O. Guilbaud, J. Habib, S. Kazamias, D. Ros, V. Bagnoud, and T. Kuehl, Optics Lett. **35**, 450-452 (2010).

[43] T. Ditmire, M. H. R. Hutchinson, M. H. Key, C. L. S. Lewis, A. MacPhee, I. Mercer, D. Neely, M. D. Perry, R. A. Smith, J. S. Wark and M. Zepf, Phys. Rev. A **51**, R4337 (1995).

[44] P. F. Moulton, J. Opt. Soc. Am. B **3**, 125-133 (1986)

[45] A. McPherson, G. Gibson, H. Jara, U. Johann, T. S. Luk, I. A. McIntyre, K. Boyer and C. K. Rhodes, J. Opt. Soc. Am. B **4**, 595 (1987).

[46] M. Ferray, A. L'Huillier, X. F. Li, L. A. Lompre, G. Mainfray and C. Manus, J. Phys. B: At. Mol. Opt. Phys. **21**, L31 (1988).

[47] A. L'Huillier, K. J. Schafer and K. C. Kulander, J. Phys. B: At. Mol. Opt. Phys. **24**, 3315-3341 (1991).

[48] J. Gautier, P. Zeitoun, C. Hauri, A.-S. Morlens, G. Rey, C. Valentin, E. Papalarazou, J.-P. Goddet, S. Sebban, F. Burgy, P. Mercère, M. Idir, G. Dovillaire, X. Levecq, S. Bucourt, M. Fajardo, H. Merdji and J.-P. Caumesm, Eur. Phys. J. D **48**, 459–463 (2008).

[49] G. Lambert, F. Tissandier, J. Gautier, C. P. Hauri, P. Zeitoun, C. Valentin, T. Marchenko, J. P. Goddet, M. Ribiere, A. Sardinha, M. Fajardo, F. Hamouda, G. Maynard, G. Rey, and S. Sebban, EPL, **89**, 24001 (2010).

[50] Ph. Zeitoun, G. Faivre, S. Sebban, T. Mocek, A. Hallou, M. Fajardo, D. Aubert, P. Balcou, F. Burgy, D. Douillet, S. Kazamias, G. De Lacheze-Murel, T. Lefrou, S. Le Pape, P. Mercere, H. Merdji, A. S. Morlens, J. P. Rousseau, and C. Valentin, Nature **431**, 426 (2004).

[51] Y. Wang, E. Granados, F. Pedaci, D. Alessi, B. Luther, M. Berrill, and J. J. Rocca, Nat. Photonics **2**, 94 (2008).

[52] R. Keenan, J. Dunn, P. K. Patel, D. F. Price, R. F. Smith, and V. N. Shlyaptsev, Phys. Rev. Lett. **94**, 103901 (2005).

[53] V. N. Mahajan, J. Opt. Soc. Amer. **71**, 75 (1981).

[54] E. Oliva, M. Fajardo, L. Li, M. Pittman, T. T. T. Le, J. Gautier, G. Lambert, P. Velarde, D. Ros, S. Sebban, and P. Zeitoun, Nat. Photonics **6**, 764 (2012).

[55] L. Li, Y. Wang, S. Wang, E. Oliva, L. Yin, T. T. Thuy Le, S. Daboussi, D. Ros, G. Maynard, S. Sebban, B. Hu, J. J. Rocca, and Ph. Zeitoun, Optics Lett. **38**, 4011-4014 (2013).

[56] P. Mercere, Ph. Zeitoun, M. Idir, S. L. Pape, D. Douillet, X. Levecq, G. Dovillaire, S. Bucourt, K. A. Goldberg, P. P. Naulleau, and S. Rekawa, Opt. Lett. 28, 1534 (2003).

[57] S. Le Pape, Ph. Zeitoun, M. Idir, P. Dhez, J. J. Rocca and M. François Phys. Rev. Lett. **88**, 183901 (2002).

[58] F. Pfeiffer, O. Bunk, C. Schulze-Briese, A. Diaz, T. Weitkamp, C. David, J. F. van der Veen, I. Vartanyants, and I. K. Robinsonm Phys. Rev. Lett. **94**, 164801 (2005).

[59] R. Miyakawa, X. Zhou, M. Goldstein, D. Ashworth, K. Cummings, Y.-J. Fan, Y. Shroff, G. Denbeaux, Y. Kandel and P. Naulleau, Proc. SPIE 9048, *Extreme Ultraviolet (EUV) Lithography V*, **90483A** (2014).

[60] P.Boggiatto, A. Oliaro and P. Wahlberg, J. Fourier Anal Appl **18**,410–438 (2012).

[61] B. Schäfer, K. Mann, B. Keitel, S. Kreis, M. Kuhlmann, E. Plönjes and K. Tiedtke, Proc. SPIE 8778, *Advances in X-ray Free-Electron Lasers II: Instrumentation*, **87780H** (2013).

[62] J. Hartmann. "Bemerkungen uber den Bau und die Justirung von Spektrographen," Z. Instrumentenkd., **20**, 47 (1900).

[63] *Hartmann Wavefront Analyzer Tutorial*, Spiricon, Inc. (2004).

[64] W. H. Southwell, J. Opt. Soc. Am, **70**, 998-1006 (1980).

[65] J.T. Wang, D.E. Silva, Appl. Opt. **19**, 1510-1518 (1980).

[66] *HASO software user guide*, Imagine Optics (2011).

[67] B. Schafer and K. Mann, Appl. Opt **41** 2809–2817 (2002).

[68] B. Floter, P. Juranic, S. Kapitzki, B. Keitel, K. Mann, E. Plonjes, B. Schäfer1 and K. Tiedtke, New Journal of Physics **12** 083015 (2010).

[69] J. P. Goddet, S. Sebban, J. Gautier, P. Zeitoun, C. Valentin, F. Tissandier, T. Marchenko, G. Lambert, M. Ribieres, D. Douillet, T. Lefrou, G. Iaquaniello, F. Burgy, G. Maynard, B. Cros, B. Robillard, T. Mocek, J. Nejdl, M. Kozlova, and K. Jakubczak, Opt. Lett. **34**, 2438 (2009).

[70] A. E. Siegman, *Lasers*, University Science Books, pp. 664–669 (1986).

[71] H. F. Talbot, "Facts relating to optical science" No. IV, Philos. Mag. 9 (1836).

[72] J. Filevich, J. J. Rocca, E. Jankowska, E. C. Hammarsten, K. Kanizay, M. C. Marconi, S. J. Moon, and V. N. Shlyaptsev, Phys. Rev. E **67**, 056409 (2003).

[73] M. Born and E. Wolf, *Principles of Optics*, 7^{th} (expanded) edition, Cambridge University Press, pp.45 (1999).

[74] M. Berrill, D. Alessi, Y. Wang, S. R. Domingue, D. H. Martz, B. M. Luther, Y. Liu, and J. J. Rocca, Opt. Lett. **35**, 2317 (2010).

[75] Ph. Zeitoun, E. Oliva, T. T. T. Le, D. Ros, S. Sebban, L. Li, P. Velarde and M. Fajardo, Applied Sciences **3**, 581-592 (2013).

[76] M. Born and E. Wolf, *Principles of Optics*, 7^{th} (expanded) edition, Cambridge University Press, pp.520 (1999).

[77] Y. Wang, E. Granados, M. A. Larotonda, M. Berrill, B. M. Luther, D. Patel, C. S. Menoni, and J. J. Rocca, Phys. Rev. Lett. **97**, 123901 (2006).

[78] I. A. Artioukov, R. M. Fechtchenko and A. V. Vinogradov, J. Opt. A: Pure ppl. Opt. **4**, 233-236(2002).

[79] L. Poletto, F. Frassetto, F. Calegari, S. Anumula, A. Trabattoni, and M. Nisoli, Optics Express **21**, 13040-13051 (2013).

[80] Y. Wang, S.Wang, E. Oliva, L. Li, M. Berrill, L. Yin, J. Nejdl, B. M. Luther, C. Proux, T. T. T. Le, J. Dunn, D. Ros, Ph. Zeitoun and J. J. Rocca, Nature Photonics **8**, 381-384 (2014).

[81] Y. Wang, M. A. Larotonda, B. M. Luther, D. Alessi, M. Berrill, V. N. Shlyaptsev, and J. J. Rocca, Phys. Rev. A **72**, 053807 (2005).

[82] K. A. Janulewicz and C. M. Kim, Phys. Rev. E **82**, 056405 (2010).

[83] D. Zimmer, B. Zielbauer, M. Pittman, O. Guilbaud, J. Habib, S. Kazamias, D. Ros, V. Bagnoud, and T. Kuehl, Optics Lett. **35**, 450-452 (2010).

[84] L. Li, Y. Wang, S. Wang, E. Oliva, L. Yin, T. T. Thuy Le, S. Daboussi, D. Ros, G. Maynard, S. Sebban, B. Hu, J. J. Rocca, and Ph. Zeitoun, *Wavefront of a seeded soft x-ray laser based on a solid-target plasma amplifier*, Proceedings of the SPIE, Volume **8849** (2013).

[85] Y. Wang, M. Berrill, F. Pedaci, M. M. Shakya, S. Gilbertson, Zenghu Chang, E. Granados, B. M. Luther, M. A. Larotonda, and J. J. Rocca, Phys. Rev. A **79**, 023810 (2009).

CHAPTER 4

Route towards high energy, ultra-short pulse, fully coherent SXRL

Emergence of ultra-fast coherent SXRL driven by LINAC (i.e. FEL) have opened new paradigm in coherent nano-imaging at the femtosecond time-scale leading to major breakthroughs in biology, solid state physics, astrophysics. The primary challenges for all the SXRL to ensure nano- femto-imaging are pulse energy, pulse duration, beam coherence and wave front. In parallel to the development of huge and costly FEL [1, 2, 3], table-top SXRL have achieved remarkable progresses in the past three decades. Since the first demonstration of x-ray lasing from a plasma created by intense laser beam in 1985 [4, 5], several table-top SXRL schemes have been developed: ASE based on laser-induced plasma [6, 7], HH generation from gas target [8] and solid surface [9], gas-discharged SXRL [10, 11] and the HH-injection seeded SXRL [12, 13]. Although high energy and broad wavelength range have been achieved in the laser-induced plasma ASE x-ray source, its low beam quality on pulse duration and spatial coherence is extremely hard to come over. HH sources being fully coherent temporally and spatially, have attracted multi-type of applications [14, 15, 16]. Indeed, the short pulse duration $(10's\ of\ attoseconds)$ of HH generated from solid surfaces brings a bright perspective [9]. However, the intrinsically poor pulse energy is limited to single-shot ultra-fast imaging. Another compact SXRL created by an electric discharge on gas has been optimized to reach mJ pulse energy with high degree of spatial coherence [4, 17, 18]. However, saturation level was obtained only at a wavelength of $46.9\ nm$ with long pulse duration ($\sim ns$).

Seeding soft x-ray plasma amplifier with HH pulse has achieved remarkable progress in the past two decades. The first attempt to seed plasma amplifier with femtosecond HH pulse was demonstrated in 1995 [19]. A specific order harmonics (the 21^{st}) from helium gas jet was tuned to overlap the 25.11 nm $J = 2 - 1$ laser transition of the ne-like Ga x-ray plasma, and then amplified after injection. However, the observed x-ray amplification was not as high as expected. Two main factors were taken into account: the spectral line-width coupling efficiency and spatial overlap between seed beam and the gain region. Dawn was beginning to show after the excited experiment in 2004 [12], where a deeply saturated, highly energetic, excellently coherent and fully polarized SXRL was reported with gas-plasma amplifier. Inspired by it, the HH-injection seeding concept was soon extended to the solid target [20, 13]. So far, there are two main divisions of this table-top coherent seeded SXRL source, which are based on the gas-plasma amplifier [12] and solid-plasma amplifier [20, 13] respectively. Both SXRL sources have showed their impressive advantage of high-brightness pulse with full temporal and spatial coherence [12, 20, 13] as well as aberration free beam [21, 22]. However, the restricted pulse duration [23] and inefficient energy amplification are still limiting their interest for coherent femto- nano- imaging [24]. In this study, we concentrated on the seeded SXRL based on solid-plasma amplifier due to the higher energy in the plasma reservoir respected to the gas-plasma amplifier, aiming to come over the limits on pulse duration and energy amplification simultaneously.

So far, there have been several modelling codes dedicated to this specific seeded SXRL scheme.

The first Maxwell-Bloch code, COLAX [25], originally developed for SXRL in a single- and double-pass configuration using a half-cavity mirror [26], was then updated to take into account seeding by HH as well as coupled with a hydrodynamics and collisional-radiative code. Achieving ultra-short ($\sim 10\ fs$) amplified HH seed was recently proposed [27, 28] using tricky system geometry and HH pulse parameters by this 2D Maxwell-Bloch code. Another 1D model based on Maxwell-Bloch equations investigating the amplification of HH pulse in an active x-ray plasma was developed by a south Korean group [29, 30], in which the temporal shape and polarization of the seeded SXRL were taken into account. In addition to these codes, the COFIXE numerical code [31, 32, 33] was applied to OFI SXRL based on the gas-plasma amplifier. A 2D hydrodynamical simulation code of SXRL solid-plasma amplifier was developed by the team of Colorado State University [34], which was particularly designed for the SXRL seeding experiment based on solid-plasma amplifier. It is interesting to note that a resembling code was recently reported for the two-stage x-ray plasma amplifier by a Russian group [35].

In this chapter, we firstly reviewed the previous work of our group on 2D hydrodynamic code ARWEN in **Section 4.1**. It presented a significant enhancement of the seeding energy amplification by tailoring plasma gain zone [36, 37]. Sequentially, in **Section 4.2**, the time-dependent 1D Maxwell-Bloch code DEEPONE developed by E. Oliva [38, 39] was briefly presented. This code is dedicated to simulate the HH injection seeded SXRL in the thesis work. In **Section 4.3**, previous efforts of our group as well as our current simulations work on HH seeding with single- and multi-stage x-ray plasma amplifier were discussed at in the first two subsections. In the third subsection (Section 4.3.3), a recent experiment to test multi-stage and wide plasma amplifier was studied. After the efforts with enlarging the cross-sectional area of plasma amplifier, we turned to the enlargement in time. In **Section 4.4**, the fast gain recovery behaviour in the x-ray plasma amplifier after the population inversion depletion when seeding a ultrashort coherent pulse was predicted [40] using the DEEPONE code. As a consequence, in **Section 4.5**, we suggested changing the seed pulse temporal properties to take advantages of this recovery behaviour and extract much more energy from the plasma amplifier as coherent emission. Seeding a train of coherent pulses or a stretched seed pulse were considered. Owing to the feasibility in experiment, we therefore proposed the x-ray CPA scheme [40, 41, 42]. Final output towards multi-tens of GW fully coherent femtosecond SXRL is extremely attractive to the single-shot coherent phase imaging applications [43] which are showing many advantages of reaching high temporal and spatial resolution nowadays. In this x-ray CPA scheme, future pulse shortening near to the Fourier-limited beam was proposed in **Section 4.6**. Finally, the key technique of the x-ray CPA system was briefly mentioned in **Section 4.7** adopting conical diffraction gratings.

4.1 2D Hydrodynamic modelling

Early simulation work of our group started with a 2D hydrodynamic code ARWEN [44], which has been used in several fields, such as inertial confinement fusion (ICF) [45], laboratory astrophysics [46] and the present plasma-based seeded SXRL [36, 47]. This 2D hydrodynamic code with radiation-transport solves radiation hydrodynamics equations enhanced with the treatment of electron thermal conduction. Electron thermal conduction and radiation transport are solved with matrix-free solvers and Sn multi group methods respectively. Owing to the Adaptive Mesh Refinement technique, it saves computational time by refining the mesh only in a small part of the simulation domain. Section 4.1.1 and 4.1.2 are the

brief introduction of the ARWEN code as a courtesy from E. Oliva [37], and more details are described in [48]. In section 4.1.3, optimization of x-ray amplifier by tailoring the plasma hydrodynamics is discussed.

4.1.1 ARWEN code

The ARWEN code is a 2D hydrodynamic code incorporating radiation transport that was developed at the *Instituto de Fusión Nuclear* of the Universidad Politécnica de Madrid, Spain. The equations solved are those of radiation hydrodynamics with thermal conduction:

$$\frac{\partial \rho}{\partial t} + \nabla \cdot (\rho \mathbf{u}) = \mathbf{0}, \tag{4.1}$$

$$\frac{\partial \rho \mathbf{u}}{\partial t} + \nabla \cdot (\rho \mathbf{u}\mathbf{u}) = -\nabla(\mathbf{P_m} + \mathbf{P_r}), \tag{4.2}$$

$$\frac{\partial \rho E_m}{\partial t} + \nabla \cdot [\rho E_m \mathbf{u} + (\mathbf{P_m} + \mathbf{P_r})\mathbf{u}] = S_E + \nabla \cdot \mathbf{q_c} + \nabla \cdot \mathbf{q_r}, \tag{4.3}$$

$$\Omega \cdot \nabla I + \kappa \cdot I = \varepsilon, \tag{4.4}$$

$$\nabla \cdot \mathbf{q_c} = -\nabla \cdot \mathbf{k_e} \nabla \mathbf{T}, \tag{4.5}$$

$$\nabla \cdot \mathbf{q_r} = \int (\kappa \cdot \mathbf{I} - \varepsilon) \mathbf{d}\nu, \tag{4.6}$$

$$E_r = \frac{1}{c} \int I d\Omega d\nu, \tag{4.7}$$

$$P_r = \frac{1}{3} E_r, \tag{4.8}$$

where ρ is the density, $\mathbf{u}$ is the velocity vector, P_m and P_r are, respectively, the matter and radiation pressure tensors, E_m is the energy of the matter, S_E is the laser energy source, $\mathbf{q_c}$ and $\mathbf{q_r}$ are, respectively, the heat fluxes due to conduction and radiation, c is the light celerity, I is the radiation intensity, Ω is the solid angle, κ and ε are, respectively, the opacity and the emissivity of the medium, k_e is the thermal conductivity, ν is the frequency of the radiation and E_r is the energy of the radiation field.

The Navier-Stokes equations (Eqs. (4.1)-(4.3)), including radiation pressure P_r and radiation heat transfer $\mathbf{q_r}$, are solved with an Eulerian scheme using a high- order Godunov type method with an approximate Riemann solver based on [49]. Flux-limited thermal electron conduction (Eq. (4.5)) and radiation

transport (Eq. (4.4)-(4.5)) are treated with multi-grid [50] and S_n multi-group methods [51, 52], respectively. Matrix-free solvers for thermal conduction are available in the new version of the code.Laser energy deposition is treated with a simple model, explained later in this paper. The laser energy is treated as a source term for Eq. (4.5). Planar and cylindrical geometries are available.Equation of state (EOS) data are obtained from the QEOS [53] equation of state, and the multipliers are adjusted to fit experimental data as Hugoniot curves. Opacities are computed with JIMENA [54] code, also developed at the *Instituto de Fusión Nuclear*.

The ARWEN code (and thus all its packages) is based on the adaptive mesh refinement technique [55, 56]. It is common in plasma hydrodynamics simulations to have small zones where high resolution is needed (i.e., shockwaves or high energy zones), whereas the majority of the computational domain is well resolved with coarser grids. The AMR technique consists of putting patches of finer grids where they are needed, producing a uniform numerical error and saving computational time. The structure of levels and grids is created and controlled by the C++ library BoxLib [57].

The output of the code is in both our native format (rwm) and also the standard HDF format to facilitate post-processing with other codes, such as our atomic model or codes that model the injection and amplification of radiation in the plasma, such as SHADOX [58].

4.1.2 The atomic model

The hydrodynamic parameters obtained from ARWEN were postprocessed to obtain 2D maps of atomic data as small-signal gain (which we will call "gain" in the rest of the paper) and saturation fluence, among others. This post-processing is done with a simple three-level atomic model that computes the gain and saturation fluence on the $2p^5_{1/2}3s_{1/2}$ J=1 $\rightarrow$ $2p^5_{1/2}3p_{1/2}$ J=0 Ne-like Fe^{16+} transition occurring at $\lambda = 25.5nm$, as it illustrated in $Fig.$ 4.1. This calculation slightly overestimates the gain [59]. In our model, we follow the classical assumption that assumes that the fundamental level (0) is much more populated than the other two levels. There is a forbidden transition between the fundamental level and the upper lasing level (2). The lower lasing level (1) depopulates quickly toward the fundamental level (0), creating a population inversion between the two lasing levels (1,2) by collisional excitation, as shown in [60]. This phenomenon was confirmed later by [61], demonstrating that for the high temperatures that typically exist in transient collisional excitation [62], collisional excitation is the dominant process populating the laser levels.

The objective of the model is to compute the small signal gain coefficient $g_0(\nu = \nu_0)$ and saturation fluence $F_{sat}(\nu = \nu_0)$ at the lasing line central frequency ν_0. For simplicity of notation, we will later use $g_0(0)$ and $F_{sat}(0)$:

$$g_0(\nu = \nu_0) = \left(N_2 - \frac{\gamma_2}{\gamma_1}N_1\right)\sigma_{stim}(\nu = \nu_0), \tag{4.9}$$

$$F_{sat}(\nu = \nu_0) = \frac{h\nu_0}{\sigma_{stim}(\nu = \nu_0)}. \tag{4.10}$$

In these formulas, N_i and γ_i are, respectively, the population and degeneracy of the i^{th} level of the transition, and σ_{stim} is the stimulated emission cross section. These last four values are computed at the line center. The populations of the levels are computed by solving the stationary rate equations of our

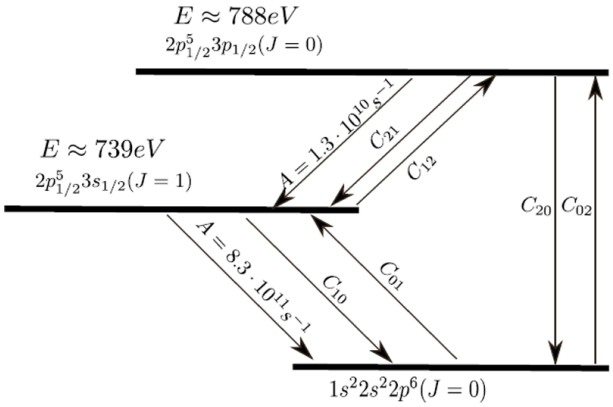

Figure 4.1: Simplified Grotrian scheme and transitions obtained from [63, 64] for Ne-like Fe.

three-level model:

$$\frac{dN_i}{dt} = \sum_j C_{ij} n_e N_j + \sum_j A_{ij} N_i, \tag{4.11}$$

$$\frac{dN_i}{dt} = 0, \tag{4.12}$$

where the C_{ij} are the collisional excitation rates between levels i and j, the A_{ij} are the spontaneous emission and absorption coefficients, the N_i are the populations of the corresponding level i and n_e is the electron density. The plus or minus sign is included in the coefficients depending on the effect of the transition (populating or depopulating level i).

The upper (numbered 2) and lower (numbered 1) lasing levels are $2p^5_{1/2}3p_{1/2}$ J=0 and $2p^5_{1/2}3s_{1/2}$ J=1, respectively. The fundamental level (numbered 0) is $2p^6$ J=0. The mechanisms taken into account in our model are collisional excitation between the fundamental and the two lasing levels ($0 \rightarrow 2$, $0 \rightarrow 1$), collisional de-excitation and radiative transitions ($2 \rightarrow 1$,$1 \rightarrow 0$). Electron collisional rates are Van Regemorter´ s rates [65], which depend on the electron temperature and electron density. The rates are calculated assuming that the electrons have a Maxwellian distribution of velocities.

$$C_{ij} \approx 1.6 \times 10^{-5} \frac{f_{ij} < g >}{\Delta E_{ij} \cdot \sqrt{kT_e}} e^{-\frac{\Delta E_{ij}}{kT_e}}, \tag{4.13}$$

$$C_{ji} \approx \frac{\gamma_i}{\gamma_j} C_{ij} \cdot e^{\frac{\Delta E_{ij}}{kT_e}}, \tag{4.14}$$

where f_{ij} is the oscillator strength, $< g >$ is the Gaunt factor (assumed to be $< g >= 0.2$), ΔE_{ij} is the difference of energy between levels i and j, k is Boltzmann's constant and T_e is the electron temperature.

The stimulated emission cross section is computed as follows:

$$\sigma_{stim}(\nu) = \Phi(\nu) \frac{\lambda^2}{8\pi} A_{21}, \tag{4.15}$$

where A_{21} is Einstein´ s coefficient of the $2 \rightarrow 1$ transition and $\Phi(\nu)$ is the spectral line profile. We assume only a Doppler profile. Neglecting collisional broadening reduces the profile width, artificially augmenting the gain and underestimating the saturation fluence [39], as shown in [64].

The Doppler effect is the principal mechanism of line broadening. In addition to this, we computed the value of the gain at the center of the line profile. Then, the peak Doppler value is:

$$\Phi_D(0) = \lambda \left(\frac{m}{2\pi k T_i} \right)^{1/2}, \tag{4.16}$$

where m is the atomic mass of the lasing ions, k is Boltzmann's constant and T_i is the ion temperature.

Because these simulations were performed with a one-temperature hydrodynamic version of the ARWEN code, we made the assumption that the plasma is in quasi local thermodynamic equilibrium, meaning that the temperature is the same for electrons and ions. This assumption has been validated in several experiments and modelling of plasmas heated with nanosecond pulses. This scheme is called QSS. For shorter pulses, this assumption fails. In the specific case of transient collisional excitation pumping, using a combination of a long nanosecond pulse and a short picosecond pulse, the peak gain appears only after interaction with the picosecond pulse, when the electron temperature has been dramatically increased, while the ion temperature has changed only negligibly. Consequently, we calculated the gain at the instant of the peak value, using the ion temperature before the interaction with the short pulse and the electron temperature as the value given by ARWEN at the moment of the pulse interaction.

4.1.3 Plasma amplifier optimization by tailoring plasma hydrodynamics

We benchmarked our numerical code addressing the successful coherent seeding experiment based on solid-plasma experiment [13]. In that experiment, TCE pumping scheme (as described in Section 2.6) was employed, combining a long IR pulse that creates the plasma at the proper ionization stage followed after a variable delay by a short (ps) pulse that produces the population inversion. All modelling showed in this chapter was done using this scheme: the plasma is created by a $100\ ps$ IR pulse ($I = 1.2\times10^{12}\ Wcm^{-2}$) preceded by a $1\ ns$ pre-pulse($I = 1.2\times10^{11}\ Wcm^{-2}$); free-electrons are heated up directly by the short IR pulse ($0.5\ ps$, $I = 1.1\times10^{15}\ Wcm^{-2}$) and later by thermal conductivity; then, they collide with the lasing ions populating both the lower (1) and upper (2) lasing levels. On a simplified but realistic description, population inversion is created because the upper level is metastable (the radiative transition between the fundamental and the upper level is forbidden) and the lower level is coupled to the ground-state (0) by a very fast E2 transition. Lasing ions considered here are either neon-like (10 bound electrons) or nickel-like (28 bound electrons). Einstein's coefficients for the different transitions involved on this scheme are $A_{21} = 1.3\times10^{10}\ s^{-1}$ and $A_{10} = 8.3\times10^{11}\ s^{-1}$ for the $2p^5 3s(J=1)\rightarrow 2p^5 3p(J=0)$ neon-like Fe transition occurring at $\lambda = 25.5\ nm$; $A_{21} = 1.8\times10^{10}\ s^{-1}$ and $A_{10} = 1.0\times10^{12}\ s^{-1}$ for the $2p^5 3s(J=1)\rightarrow 2p^5 3p(J=0)$ neon-like Zn transition at $\lambda = 21.2\ nm$ and $A_{21} = 4.4\times10^{11}\ s^{-1}$ and $A_{10} = 4.2\times10^{11}\ s^{-1}$ for the $4p^1(J=1)\rightarrow 4d^1(J=0)$ nickel-like Mo transition occurring at $\lambda = 18.9\ nm$.

In $Fig.$ 4.3, a map of the plasma and of the gain region is displayed. This plasma is assumed to be homogeneous along the longer (Z) dimension. In Wang *et al.*'s experiment [13], the pump laser was focused over a $30\ \mu m \times 5\ mm$ line. At first glance, we observed that the plasma is almost three times the size of the focal width along the target surface (Y). Such a strong plasma flow was not expected, leading to a larger gain region, about $50\ \mu m$ wide. It is interesting to observe that the gain zone extends only over $10\ \mu m$ along the pump laser axis (X). The gain peaks at about $62\ cm^{-1}$ agreeing very well with Wang *et al.*'s data. It decreases very fast when the distance from the target surface increases. The saturation fluence calculated over the gain region is roughly stable at $2.3\ mJ/cm^2$ agreeing well with Wang *et al.*'s article (fluence of $1.8\ mJ/cm^2$). These two results are striking. Although most plasma-based soft

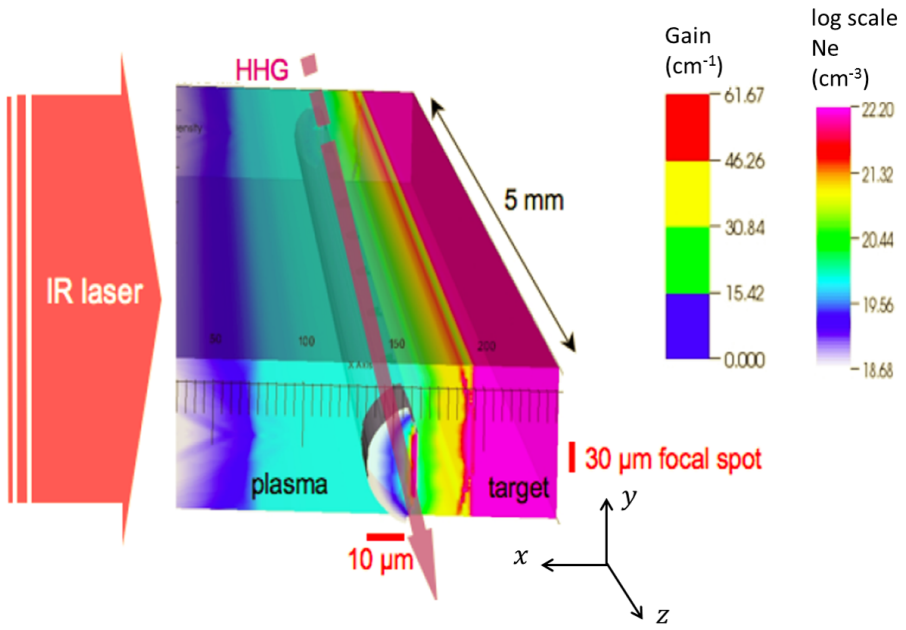

Figure 4.2: X-ray plasma amplifier created by two laser pulses and the gain region map in false color. This modelling has been used to benchmark ARWEN code against Wang et al.'s experiment [13]. from [42]

X-ray lasers are running at about 10 times the saturation fluence, in order to break the mJ threshold, one needs to produce a gain region of $0.1\ cm^2$ (to be compared to $5\times10^{-6}\ cm^2$ for Wang *et al.*). We therefore explored the possibility of enlarging the gain region. The most accessible solution consists in enlarging the focal width while keeping the intensity constant. We modelled plasmas created with focal widths from $30\ \mu m$ up to $2\ mm$ ($Fig.\ 4.2$). It is striking to observe that peak gain increases very quickly from 62 to $126\ cm^{-1}$ when enlarging the focal width from $30\ \mu m$ to $100\ \mu m$. Then, peak gain remains constant for widths larger than $100\ \mu m$ [36]. Note that the gain region increases nearly 8 times along the x direction from $10\ \mu m$ to $76\ \mu m$ while the vertical flow becomes negligible maintaining the gain region near the focal width size. When the focal width is larger than $100\ \mu m$, the gain zone is rather homogeneous. These changes are due to a reduction of the thermal losses by lateral conduction and radiation cooling as well as the inhibition of the lateral expansion when increasing the focal width [37].

However, the plasma vertical extension will generate a spurious effect already observed on Ti:Sa lasers: the transverse lasing. With a gain of about $130\ cm^{-1}$ and a transverse amplification length of $2\ mm$, the gain-length product can be as high as 26. However, it is commonly observed that SXRL saturates at a gain-length product of about 18. Thus the self-emission emitted from one side of the plasma will be amplified along y direction above saturation with the result to extract most of the energy stored. Actually, considering 18 as the saturation gain-length, the transverse lasing will be problematic for plasma larger than $1.4\ mm$. One solution we explore consists in reducing the pumping intensity so as to decrease the gain. For a reduction of 50% of the pump energy of the short pulse, the gain can be halved. In that case, $2\ mm$ large plasma does not generate too strong transverse lasing. With this condition, we estimate the total output energy to be around $44\ \mu J$.

Considering a $1\ mm$ large plasma that may be created with a sub-PW laser, about $0.4\ mJ$ is stored on the population inversion. This value, although too low for the most demanding experiments like biological

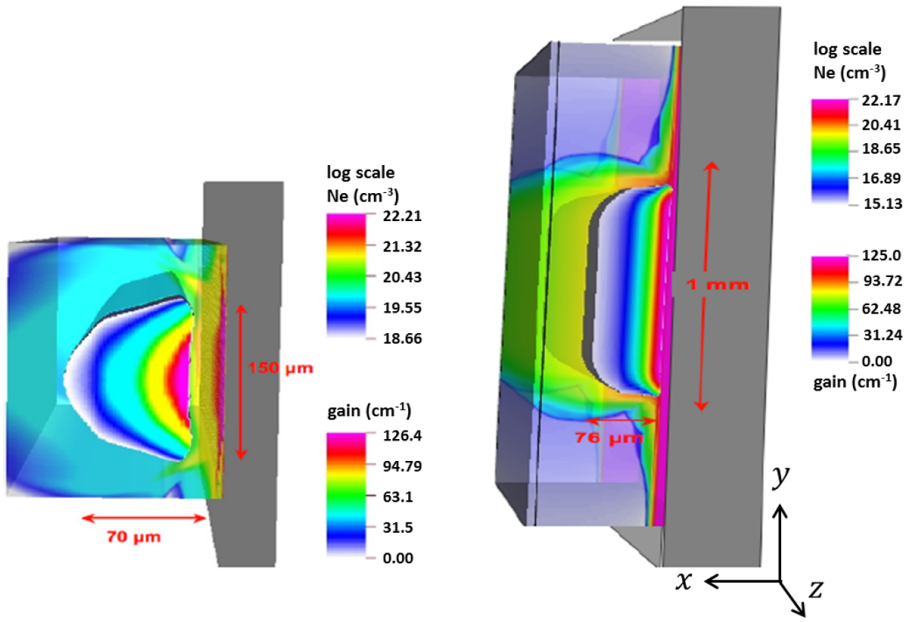

Figure 4.3: Image in false colors of plasmas created by $100\ \mu m$ *(left) and* $1\ mm$ *(right) focal width. For* $1\ mm$ *large width, the plasma along the target surface is very weak. from [42].*

imaging, represents a huge step forward. However, using only a hydrodynamic code is not sufficient to give a precise estimate of the output energy when seeding this amplifier with high harmonics. Several issues still remain to be studied numerically to define the best seeding conditions and thus the highest output energy and shortest duration achievable.

4.2 The time-dependent Maxwell-Bloch model

When the SXRL beam propagates in the plasma medium, the only amplification bounds are set by gain coefficient distribution and the refraction effects within the amplifying plasma. There is no mode selection as in the most lasers. Once population inversion is achieved, brightness and coherence of the laser are basically depending on the conditions of propagation in the plasma. The propagation of an electric field in a plasma is generally described by the Maxwell wave equation [66]

$$\nabla^2 E - \frac{1}{c^2}\frac{\partial^2 E}{\partial t^2} = \mu_0 \frac{\partial^2 P}{\partial t^2} - \frac{{\omega_p}^2}{c^2} E \quad , \tag{4.17}$$

where $\nabla^2 E$ is the Laplacian of the electric field E, c is the speed of light, P is the plasma polarization density and ω_p is the plasma frequency. Polarization (the first term at right side of equation) depends on the population inversion density and to the field amplitude E. The second term represents the interaction of the field with the plasma free electrons, which introduces the refraction of the beam in the wave equation. Refraction is given by the Laplacian term, while in one-dimensional model, the transverse Laplacian is neglected, retaining only the derivatives on the Z coordinate. Therefore, the electric field can be written as $E_z = Re[Ee^{(-i\omega_o t + i\kappa z)}]$, where ω_o is the frequency of the field and κ is the wave number.

Polarization density can be expressed in a similar way. With this simplification we lose the capacity of studying refraction and diffraction effects but the resolution of the equations is significantly simplified. Moreover, in the case of HH-injection seeded SXRL, the seed pulse ($\sim 30\ fs$) is normally much shorter than the time scale of the atomic response of the lasing ions (few ps) due to the electron-ion elastic and non-elastic collisions. It has nothing to do with the slowly varying envelope approximation in classical Maxwell equation ($Eq.\ 4.17$). It is not necessary to resolve the high frequency oscillations of the electric field due to the short seed pulse. We therefore assume that the second derivatives of the envelope function $E(z,t)$ can be neglected. Then the wave equation can be written as [38]

$$\frac{2i\omega_o}{c^2}\left(\frac{\partial E}{\partial t}+c\frac{\partial E}{\partial z}\right)=-\frac{{\omega_o}^2}{c^2}\left(-\frac{{\omega_p}^2}{{\omega_o}^2}E+\mu_o c^2 P\right). \tag{4.18}$$

Therefore, with the coordinate change $\tau = c - \frac{z}{c}$, which is so called reduced time, and defining $\zeta = c\tau$, the first order ordinary differential equation for the propagation and amplification of the electric field in plasma is described as [38, 41]

$$\frac{\partial E}{\partial \zeta}=\frac{i\omega_o}{2c}\left[\mu_o c^2 P-\left(\frac{\omega_p}{\omega_o}\right)^2 E\right]. \tag{4.19}$$

The polarization density is normally given by $P = Tr(\rho d)$, ρ is the density operator and d is the atomic electric dipole. According to [68], the equation related to the matrix element z_{21} is written as

$$\frac{\partial \rho_{21}}{\partial \tau}=-\gamma\rho_{21}+\frac{iE}{\hbar}Z_{21}(N_2-N_1), \tag{4.20}$$

where γ is the depolarization rate which is proportional to the electron-ion collisional frequency [26] and N_2 and N_1 are the population of the upper and lower level, respectively. Multiplying the equations that give the evolution of the density matrix elements by Z_{21} (non-diagonal elements) and N_0 (diagonal elements), we get the following equations:

$$\frac{\partial P}{\partial \tau}=\Gamma-\gamma P-\frac{i{z_{21}}^2}{\hbar}E(N_2-N_1), \tag{4.21}$$

$$\frac{\partial N_2}{\partial \tau}=\sum_k C_{k2}N_k+Imag(E*P)\frac{1}{2\hbar}, \tag{4.22}$$

$$\frac{\partial N_1}{\partial \tau}=\sum_k C_{k1}N_k+Imag(E*P)\frac{1}{2\hbar}, \tag{4.23}$$

where Γ is a stochastic source term corresponding to the spontaneous emission. The evolution of the plasma polarization density is demonstrated in Eq. (4.21), spontaneous emission has been taken into account. The random term Γ is properly normalized to obtain the expected Lorenzian lasing line profile [26]. Finally, the populations of the upper and lower levels involved on the lasing transition are respectively represented in Eq. (4.22) and Eq. (4.23), which are coupled with collisional excitation/de-excitation and radiative de-excitation rates (C_{k2} and C_{k1}) and with the SXRL electric field through

polarization density. This time-dependent Block-Maxwell code, so called DEEPONE, allows to study several processes required to understand the amplification of soft x-ray emissions in a plasma as Rabi oscillations or amplification of a noisy ASE mixed with a non-random signal (HH-seeded SXRL).

4.3 Single- and multi-stage x-ray amplification schemes

All the seeding experiments [12, 13, 19, 20, 69] prior to this study have demonstrated energy amplification up to two orders of magnitude and excellent hereditary optical-quality with respect to the fully coherent HH seed source. However, the energy is limited to $0.1\ \mu J$ which is far from the requirement of high-resolution ultra-fast single-shot imaging [43, 70]. The efforts on single- and multi-plasma-amplifier schemes are discussed in this section.

4.3.1 Single-plasma-amplifier scheme

Previous efforts using DEEPONE code have showed the effect of seed pulse properties in the polarization density [38], as illustrated in $Fig.\ 4.4$. Modelling of Wang *et al.*'s experiment [13], we observed well-known weak amplification of the HH seed followed by a wake field that is amplified [25, 30] and contains most of the energy in a $2\ ps$ pulse ($Fig.\ 4.4(a)$ and $Fig.\ 4.4(b)$. The incapacity of such plasma in amplifying the seed comes from the mismatch between the polarization characteristic time (0.1-$0.2\ ps$) and the HH pulse duration ($30\ fs$). Also, the long lasting (several picosecond) wake originates from the long duration of the polarization induced by the seed. Indeed, depolarization mainly occurs through electron-ion collisions that have a characteristic time of several picoseconds.Therefore, longer HH seed pulse ($200\ fs$) injection to high-density plasma was proposed, showing the results in $Fig.\ 4.4(c)$ and $Fig.\ 4.4(d)$, which presents a faster depolarization time scale and thus a shorter wake. This modelling pointed out that increasing the duration of the HH seed is not only interesting to the transfer of energy from to wake to the seed, but also to enhance the polarization, which would allow more efficient SXRL amplification through the plasma.

ARWEN modelling (Section 4.1) showed that plasmas larger than $100\ \mu m$ have the adequate conditions. Seeding with these parameters (and $50\ nJ$ energy to maintain the seeding intensity) a $100\ \mu m$ wide plasma enhances the coupling HH-plasma. The combination of the fast depolarization of the plasma (due to electron collisions) and the strong saturation of the population inversion by the HH field inhibits the creation and amplification of the wake, conserving the femtosecond duration of the seed. Furthermore, as observed on classical lasers [71, 72], amplification in this deep-saturation regime is only efficient during the first part of the HH pulse while the second half of the pulse encountering a reduced population inversion is weakly amplified. This phenomenon results in the pulse shortening observed for lengths above $2\ mm$ ($Fig.\ 4.4(d)$). This single plasma amplifier scheme leads to the generation of a $1.4\ \mu J$, $80\ fs$ pulse after passing through a $2.5\ mm$ length plasma ($Fig.\ 4.4$). It is not worth to use longer plasmas as the ASE and the wake are strongly developed after this optimal length.

Kim *et al.* [30] suggested that adjusting the injection time of the seed allows the coherent amplified seed to dominate the output beam. We performed a modelling in DEEPONE, as illustrated in $Fig.\ 4.5$, for a $4\times1\ mm^2$ plasma seeded with a $100\ nJ$, $200\ fs$ HH pulse at $2\ ps$ before the maximum gain value

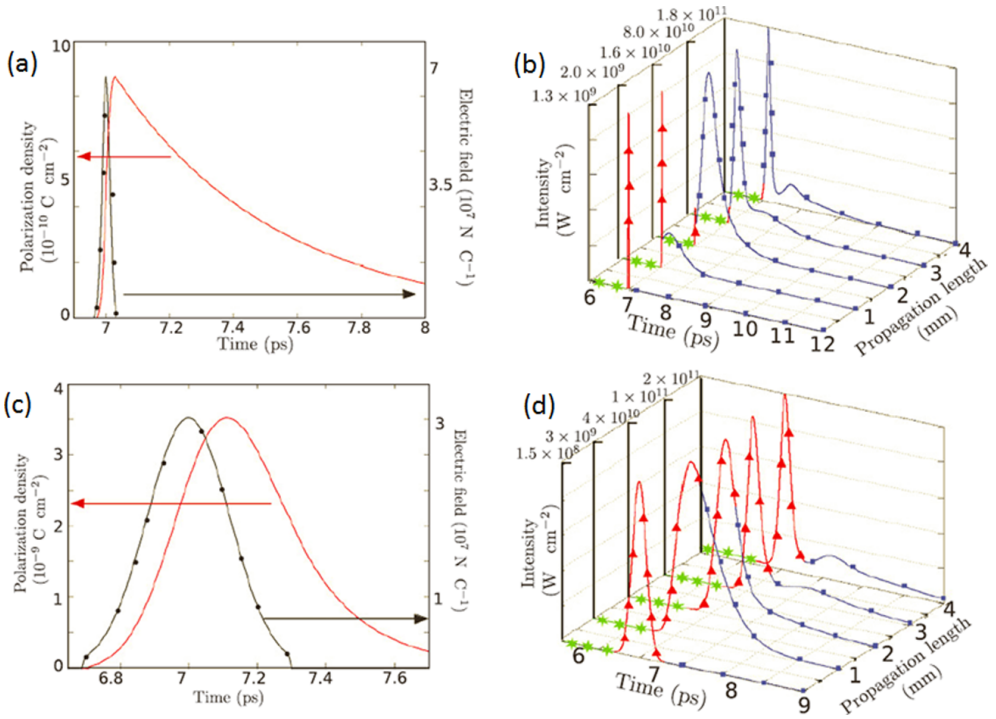

Figure 4.4: Electric field (black lines) and computed polarization (red lines) at $z = 0$ mm of (a) 1.5 nJ, 30 fs and (b) 1.5 nJ, 200 fs HH seeded in a plasma with $n_e = 2.2\times10^{20}$ cm^{-3} and $Te = 531$ eV. The temporal profiles of both cases are displayed in (c) and (d) respectively. The colours represent the ASE (green stars), HH seed (red triangles) and wake signal (blue squares). from [38].

($Fig.$ 4.5(a)) and 1 ps after the gain peak ($Fig.$ 4.5(b)) respectively. It is clearly seen that adjusting the seeding time has a strong impact on the output beam temporal profile. When seeding earlier, the structure composed of HH and wake signal is completely developed and clearly differentiated from the ASE which appears before the HH pulse and after the wake. On the other hand, when seeding later the ASE is strongly amplified. The seed appears as strong spike while the wake cannot be amplified due to the low gain it encounters. Nevertheless, from $Fig.$ 4.5, it is apparent that optimizing the seeding time is not sufficient to destroy the ASE signal and, in addition to this, the output pulse will have the complicated structure described above, during several picoseconds and preventing to obtain single short and intense pulses (100 fs or less). In order to get rid of the wake and ASE obtaining a short, energetic single pulse, one strategy is that seeding earlier is better than later as explained by Kim *et al.* [30]. The ASE and wake need some millimetres of plasma to develop, shortening the plasma would inhibit these structure at the cost of decreasing the output energy.

Another approach is to seed HH pulse with higher intensities. In this case, the HH pulse will saturate the plasma, destroy the population inversion and thus prevent the development of the ASE and wake. In $Fig.$ 4.6, the output pulse obtained by seeding 100 nJ, 200 fs HH pulse into 2×1 mm^2 plasma amplifier ($Fig.$ 4.6(a)) and seeding 2.2 μJ, 200 fs HH pulse into 4×1 mm^2 plasma amplifier ($Fig.$ 4.6(b)) respectively. Although the output pulse is improved for both of them, none of the beams is optimal for applications. When the length of the plasma is reduced ($Fig.$ 4.6(a)) the wake is still developed, and reducing more the length of the plasma would be impractical as the HH seed would not be amplified

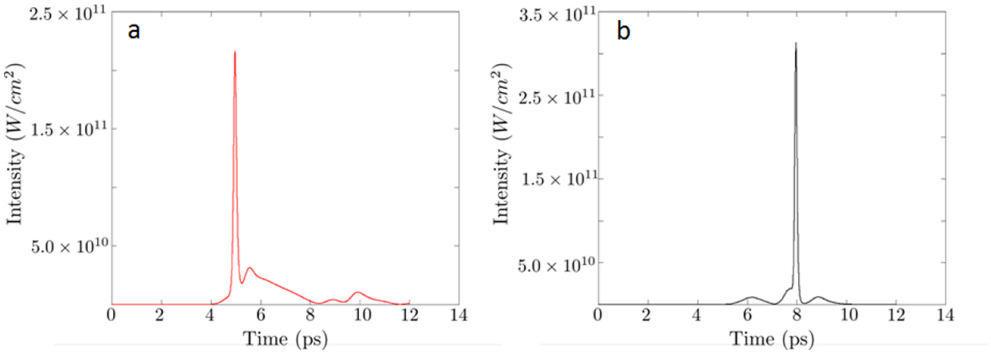

Figure 4.5: Temporal profile of output beam from a $4\times1\ mm^2$ *plasma seeded with a* $100\ nJ$, $200\ fs$ *HH seed pulse at* $2\ ps$ *before the maximum gain (left) and* $1\ ps$ *after the gain peak (right).*

enough. Seeding at higher energies ($Fig.\ 4.6(b)$), as expected, saturates the amplifier and prevents the wake and ASE to appear after the HH pulse. However, even for this high-density plasma, the spectral width of the soft X-ray laser is about $30\ times$ narrower than the spectral width of the HH pulse [73], meaning that we need $30\ times$ more HH seed pulse energy. Nevertheless, as the gain on this kind of plasmas has a duration of several picoseconds, the population inversion is recovered some picoseconds (discussed in Section 4.4) after the HH seed and the wake and ASE appear later in the beam. All these seeding strategies with single plasma amplifier are working relatively well but not adequate to obtain an optimized beam for the single-shot CDI [43, 70].

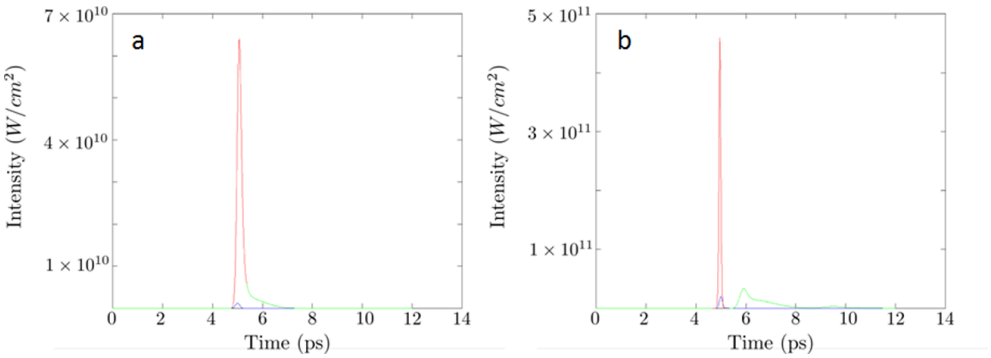

Figure 4.6: Temporal profile of output beam from a $2\times1\ mm^2$ *plasma seeded with a* $100\ nJ$, $200\ fs$ *HH seed pulse (left) and from a* $4\times1\ mm^2$ *plasma seeded with a* $2.2\ \mu J$, $200\ fs$ *HH seed pulse (right). Blue lines are the HH seed, amplified HH seed is in red, and green line are corresponding to the wake and ASE signals*

4.3.2 Multi-stage x-ray amplification scheme

Consequently, we proposed a multi-stage x-ray amplification scheme [41, 42] schematically illustrated in $Fig.\ 4.7$. The idea is to combine all the above strategies and seed a short (less than $2\ mm$), wide ($1\ mm$) plasma amplifier with an intense ($>1\ \mu J$, $200\ fs$) structure-free coherent seed pulse. The combination of these techniques should have all the advantages whereas the drawback of losing amplification power by shortening the plasma is overcome by seeding at higher energy. However, as our best knowledge,

common HH sources provide tens of nJ, which is clearly insufficient to directly seed these plasmas. Plasma-based SXRL easily achieve this energy but resulting in incoherent beam. The optimize source to seed these wide plasmas would be another plasma, narrower ($100\ \mu m$), directly seeded with HH pulse, which is considered as the pre-amplifier as described in $Fig.\ 4.7$. This pre-amplifier stage must augment the energy of the seed from several tens of nJ to several μJ, while maintain the duration of the pulse ($\sim 150\ fs$). In addition to this, the output beam of the pre-amplifier must present a structure free of ASE or wake, as these undesirable features will be strongly amplified in the $1\ mm\ plasma$ (main-amplifier) and thus increase the pulse duration. The pulse described earlier in this section is ideal in terms of energy, duration and temporal structure to seed wide, dense plasmas.

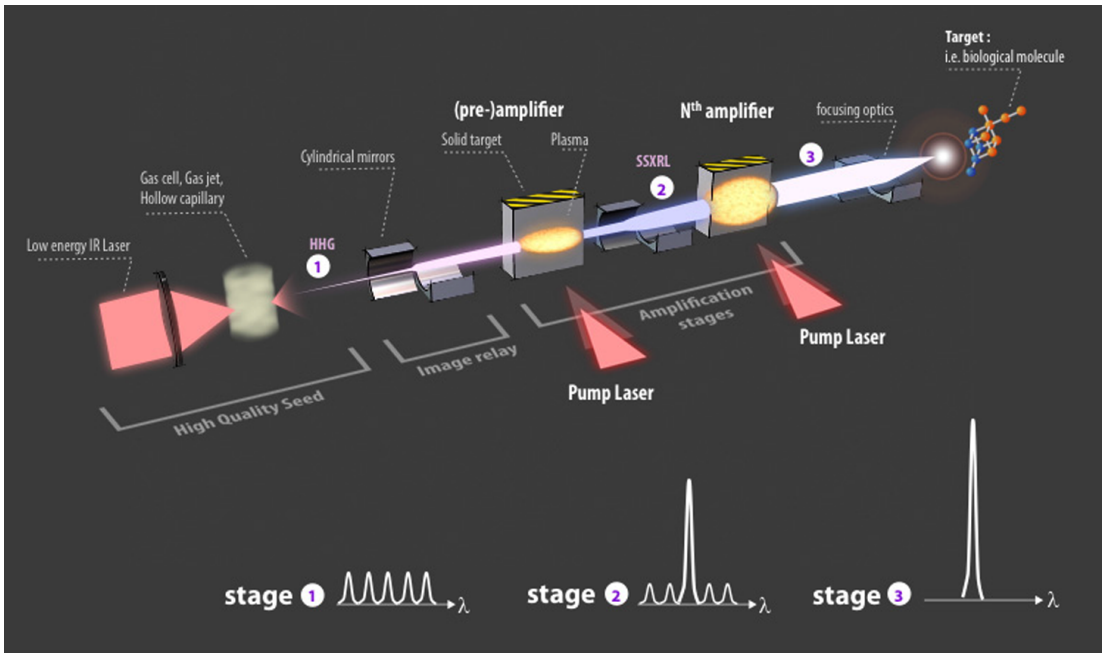

Figure 4.7: Artistic view of an multi-stage x-ray amplification chain, starting from left to right, consists of HH source, focusing optics of image relay, pre- and main-amplifier. from [42]

As shown in $Fig.\ 4.8(a)$, the $50\ nJ$, $120\ fs$ HH seed beam is amplified to $1.8\ \mu J$ through a $2.5\ mm \times 100\ \mu m$ pre-amplifier. Owing to the short plasma amplifier and intense seed pulse, the output beam contains negligible level of the wake ($49\ nJ$) and the ASE ($0.2\ nJ$). Saturation effects reduce the duration of the pulse to $80\ fs$ (more discussion in Section 4.5). In order to reduce the amplification of the wake, this pre-amplified beam was then seeded into the $3 \times 1\ mm^2$ main-amplifier with $1\ ps$ time delay. Final output beam consists of amplified seed ($46.6\ \mu J$, $160\ fs$), ASE ($21.6\ \mu J$) and the wake ($2.8\ \mu J$) as illustrated in $Fig.\ 4.8(b)$. Here, 20% of the input energy loosing has been taken into account due to the coupling efficiency. It is important to note that the beam intensity is not improved as much as the energy, because the amplifier SXRL beam size after the main amplifier is increased by $1000\ times$ which promises the total energy improvement. If the amplifier is shortened to $2\ mm$, the output pulse has a total energy of $24.8\ \mu J$ in $80\ fs$. The wake and the ASE takes only 4% and 8% of the energy. It is interesting to note that about $30\ J$ is necessary to create this kind of main plasma, which is achievable using commercial $10\ Hz$ lasers nowadays.

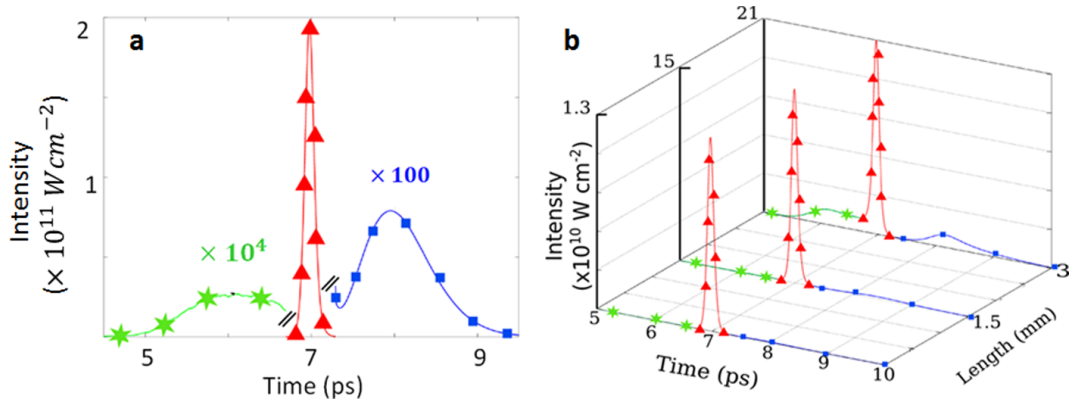

Figure 4.8: (a) Temporal profile of output beam from $2.5\ mm \times 100\ \mu m$ *pre-amplifier seeded with a* $50\ nJ$, $120\ fs$ *HH seed pulse. The ASE (green asterisk) and wake (blue squares) are zoomed* 10^4 *times and 100 times, respectively. Red triangles are corresponding to the amplified seed. (b) Output intensity through the* $1.5 \times 1\ mm^2$ *main-amplifier seeded with by the output beam from pre-amplifier. The energy lose of* 20% *due to the coupling efficiency has been taken into account. [41]*

4.3.3 Experiment on ASE self-seeding with wide plasma amplifier

An experiment using a wider plasma amplifier with ASE self-seeding was conducted in GSI (Germany) in collaboration with the teams of Prof. T. Kuehl (GSI, Germany), Prof. M. Fajardo (IST, Portugal) and Prof. D. Ursescu (ELI-NP, Romania). This IR laser ($1064\ nm$) system is similar to that described in Section 3.1. The nanosecond long pulse was from a fibre laser system (ns Front-End), as illustrated in $Fig.\ 3.1$, which only delivers nanosecond long pulses and runs independently from the femtosecond Front-End. The two short pulses were generated and combined into a collinear beam with $200\ ps$ delay of peak-to-peak in the femtosecond Front-End. The three pulses were then combined into a collinear beam before sending them to the pre-amplifier section ($Fig.\ 3.1$). The amplified triple-pulse beam with total energy $\sim 5.7\ J$ was finally sent into a compressor. Energy proportion and time delays of the three pulses after compression are described in the inset (a) of $Fig.\ 4.9$. A $1\ ns$ long pulse with $170\ mJ$ energy was delivered $1.5\ ns$ before the first short pulse ($3\ ps$, $0.8\ J$), the second short pulse ($3\ ps$, $2\ J$) was arriving $200\ ps$ later than the first short pulse. As illustrated in $Fig.\ 4.9$, this triple-pulse beam was divided into two arms by a mirror clipping. The top part of the beam ($\sim 30\%$ of the full energy), through a delay line, delivered into the target chamber and line-focused by a spherical mirror, was used to create the seed plasma ($50\ \mu m$ wide) by irradiating on a $5.4\ mm$ long molybdenum slab target with 28° grazing incident angle. In order to create a much broader amplifier-plasma respected to the experiment discussed in Section 3.1 ($30\ \mu m$), much higher intensity is requested at the focal line of the amplifier-plasma. The other arm (lower part of the clipped beam) with $\sim 70\%$ of the full beam energy was sent to an OAP mirror with $f = 350\ mm$, as depicted in inset (b). Another spherical mirror was set after the focal spot by OAP mirror and used to focus this divergent beam into a short intense line. It was subsequently sent to a $2\ mm$ long molybdenum slab target with incident angle of 68° comparing to the driven laser of seed plasma, which is dedicated to generate much broader plasma ($300\ \mu m$) as the main amplifier in this ASE self-seeding experiment, as it called amplifier plasma. This GRIP technique (as described in Section 2.6.3) coupled

with triple-pulse combining is so called TGRIP scheme. It is interesting to note the that the beam shapes of the two clipped arms remarked in $Fig.\ 4.9$ with different energy proportion are finally contributed to the line focusing for the creation of narrow seed-plasma and broader amplifier-plasma.

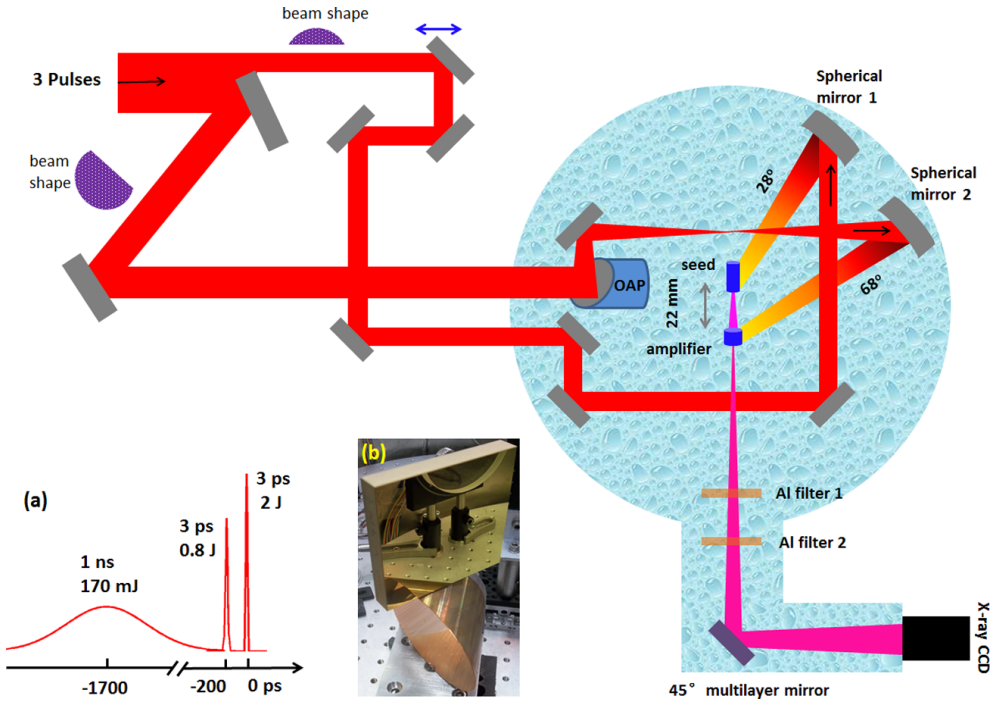

Figure 4.9: Schematic overview of the ASE self-seeding experiment with the $5.4\ mm \times 50\ \mu m$ *seed plasma and* $2\ mm \times 300\ \mu m$ *amplifier plasma. Inset* (a) *is describing the parameters of three pulses. The reflection mirror and OAP mirror at the entrance of the target chamber are delivering the seed-plasma driven laser and amplifier-plasma driven laser, respectively, as illustrated in inset* (b).

Centre-to-centre distance between the two targets is $22\ mm$, which are controllable independently in three dimensions, as displayed in $Fig.\ 4.10$. By adjusting the delay line, one could change the injection time of the seed plasma ($5.4\ mm \times 50\ \mu m$) on the broader amplifier-plasma ($2\ mm \times 300\ \mu m$). The final output was detected by a x-ray CCD camera coupled with a $45°$ multilayer mirror. $Fig.\ 4.11(a)$ and $Fig.\ 4.11(b)$ are showing the output of seed-plasma and amplifier-plasma alone, respectively. It is worth nothing that the signal is clipped by the edge of the second target. The estimated energy of the ASE seed was $0.5\ \mu J$ and beam divergence was $\sim 15\ mrad$ in vertical $\sim 8\ mrad$ in horizontal. The slight fringes are produced by the diffraction of the target edge. However, detected ASE signal from the shorter and wider amplifier-plasma ($2\ mm \times 300\ \mu m$) was showing very homogeneous energy distribution and much bigger source size due to the broader plasma. Both images were obtained with same detection conditions. Sequentially, the divergent ASE seed beam was naturally injected to the amplifier-plasma. $Fig.\ 4.12$ shows the amplification curve obtained when scanning the injection time. The narrow temporal amplification curve ($3.6\ ps$ duration) agrees with our previous experiment conducted in LASERIX (see $Fig.\ 3.13$) using a long pulse and two short pulse configuration for the plasma amplifier creation, as represented in Section 3.2. The long pulse was to generate a warm, expanding plasma. Then the first short pulse heats the plasma and ionizes it, attaining the Ni-like stage. After several hundreds

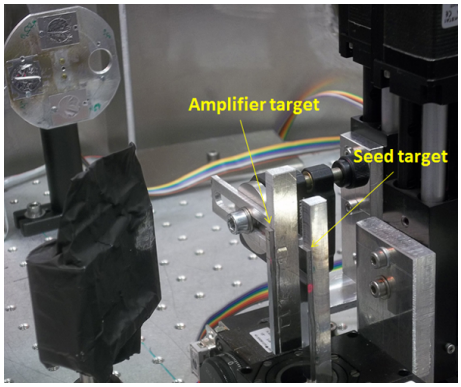

Figure 4.10: Photograph of the two independent controllable targets.

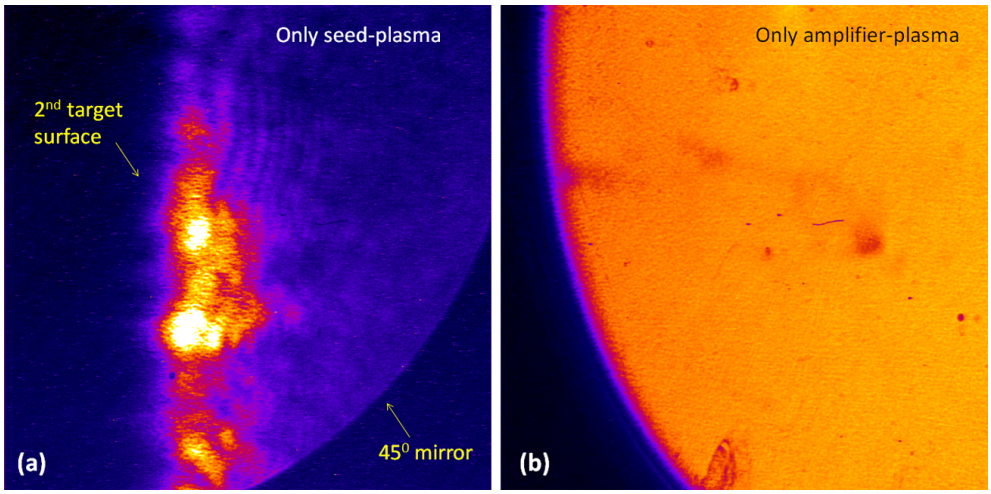

Figure 4.11: Foot-print images of the ASE signal from (a) seed-plasma and (b) amplifier-plasma alone, respectively.

picoseconds, the final short pulse heats the free electrons of the plasma. These electrons will create the population inversion by collisional excitation. Due to the short duration of pump pulse, the maximum population inversion was achieved $1\ ps$ after the arrival of the peak of pump pulse, as represented in $Fig.\ 4.12$. one need to be aware of that the $T = 0\ ps$ is not exactly calibrated, but the relative time is corresponding to the delay between injection time of the seed and peak of the 2^{nd} short pump pulse for amplifier-plasma.

There are three amplified seed images from different time delays as the insets illustrated in $Fig.\ 4.12$. It is apparent to see the energy changing from $T = 0\ ps$ to $T = 2.7\ ps$. Due to the strong refraction effect by the density gradient in the amplifier-plasma, part of the amplified seed beam was out of the detection region, only half of the beam was captured by the detection system. We assume the beam is symmetrical in horizontal direction to calculate the output energy. The maximum amplification factor achieved (at $T = 0.9\ ps$) was 6.5. It is interesting to point out that the "bubble" shape caused by the plasma refraction appears well before the population inversion is created. Thus, we can conclude that it is due to the dense plasma created from the second target. This bubble shape is implying the dense

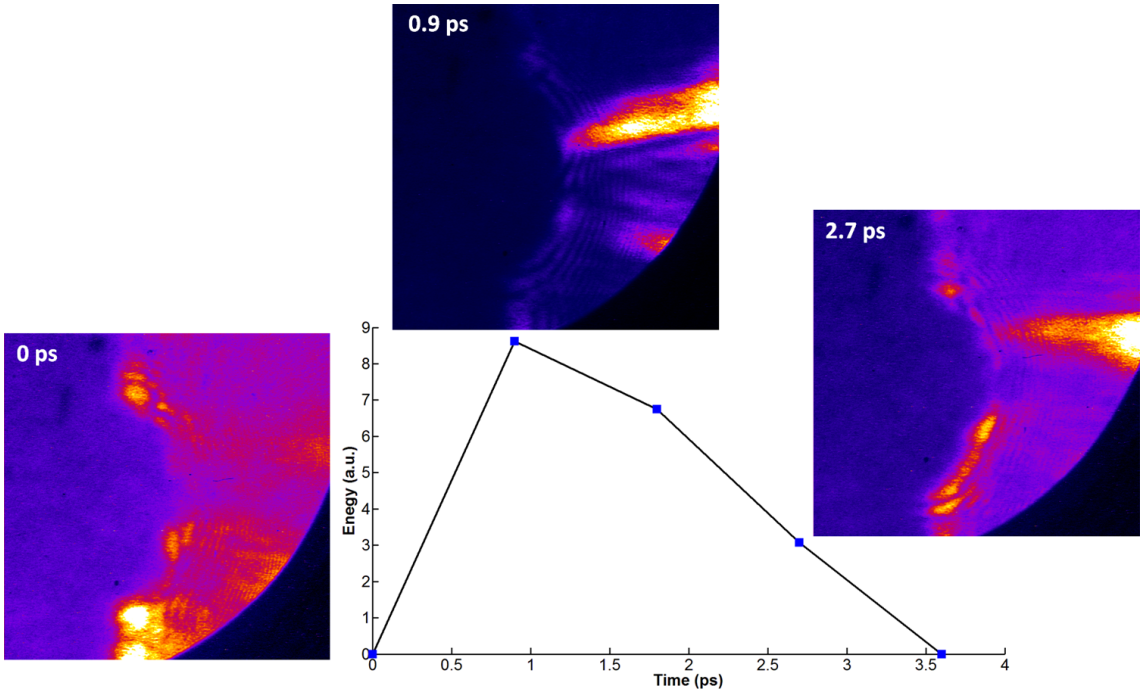

Figure 4.12: Temporal evolution of amplification for the ASE seed from $5.4\ mm \times 50\ \mu m$ *plasma injected to* $2\ mm \times 300\ \mu m$ *wider plasma. Three sample images are showing the amplification at* $T = 0\ ps$, $T = 0.9\ ps$ *and* $T = 2.7\ ps$ *respectively.* $T = 0\ ps$ *time is corresponding to the zero delay between seed injection and arrival of the peak of the* 2^{nd} *short pump pulse for amplifier-plasma.*

plasma shape created on the second target surface. During the experiment, we found that the "bubble" shape is due to the second target location in the clipping direction. The visibility of observed fringes shoes an interesting behaviour. Comparing the three images illustrated in $Fig.\ 4.12$, it is clearly seen that the visibility of the fringes is strongly dependent on the amplification energy. These fringes come from the interference between the amplified seed and the refracted un-amplified beam. Refraction by the edge of the dense plasma also contributes to them.

Further understanding of this deflection behaviour in the plasma amplifier, we compared the HH seeding from Chapter 3, Section 3.2.2 (x-ray seeding experiment at LASERIX) with this ASE self-seeding experiment, as illustrated in $Fig.\ 4.13$. $Fig.\ 4.13(a)$ and $Fig.\ 4.13(b)$ are taken from $Fig.\ 3.12$ with the HH seeding time at $-2.3\ ps$ and $3\ ps$, respectively. At $-2.3\ ps$, the amplification of the plasma is negligible as it is shown in the gain curve in $Fig.\ 3.13$. This implies that the large population inversion region (so called "gain zone"), which is considered as density homogeneous, is not created. The density distribution along the plasma expanding direction $x\ axis$ is shown on $Fig.\ 2.36(a)$, where a steep density gradient is presented. Consequently, one could explain the deflection of seed beam with "bubble shape" described in $Fig.\ 4.13(a)$ owing to the density gradient. $Fig.\ 4.13(b)$ is the mixture of deflected HH seed and amplified seed at $3\ ps$, when the population inversion remains a certain level. Part of the beam was allowed to be amplified, and the rest was refracted. The two output beams were then interfered causing the fringes.

In term of ASE self-seeding, it is interesting to note that in $Fig.\ 4.13(c)$, the ASE seed was delivered to the amplifier at $-27\ ps$ which is much earlier than the arrival of the short pump pulse for

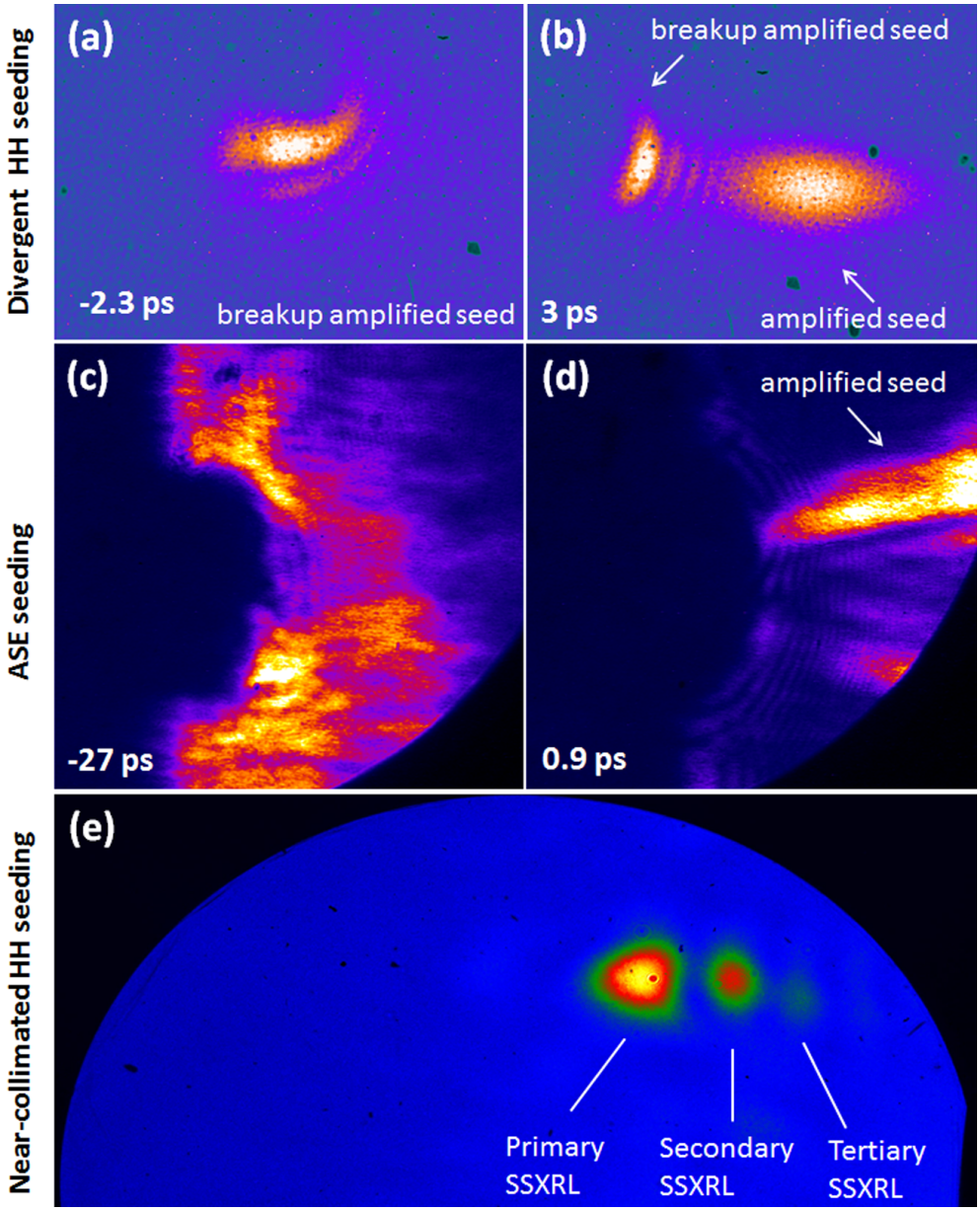

Figure 4.13: Divergent HH seed (a, b – at LASERIX, France), divergent ASE seed (c, d – at GSI, Germany) and near-collimated HH seed (e – at Colorado State University, US) injected to the plasma amplifier.

amplifier-plasma. It is indicated that in this case, the amplifier-plasma is only irradiated by the pre-pulses. owing to lack of short pump pulse, the population inversion is considered at negligible level. The seed beam can not be amplified, however, it was substantially refracted due to the density gradient, which produced the "bubble shape". Similar behaviour was reported recently as x-ray plasma mirage [35]. In $Fig.\ 4.13(d)$, ASE seeding time at $0.9\ ps$, which is observed as the peak of the gain. Both amplified seed and deflected "bubble shape" , as well as their interference, were apparently obtained.

In contrast with the near-collimated seeding approach in our experiment conducted at Colorado State University (US), where a toroidal mirror was adopted for the image-relay injection, $Fig.\ 3.48$ is displayed in $Fig.\ 4.13(e)$. The main amplified seed was observed as a single clean beam as marked as "Primary SSXRL" in the figure. One should be noted that the secondary and tertiary SSXRL are caused by the separated HH seed sources in the plasma amplifier as explained in Chapter 3, Section 3.3. Therefore, no fringes were observed.

We therefore blocked out the following sketch to simplify this behaviour caused by plasma refraction with different seeding approaches. In $Fig.\ 4.14$, (a) divergent and (b) collimated seed pulses injection to the plasma amplifier were taken into account. $Fig.\ 4.14(a)$ shows the divergent seed propagating in the expanding plasma. In this case, divergent beam passing through a x-ray plasma amplifier associated with a gain zone. As our previous description in $Fig.\ 2.35$, gain zone is considered as homogeneous region with much higher density than its surrounding. Part of the seed will be avoided from the gain zone due to the refraction and some part of the beam can pass into the dense gain zone. Owing to the divergent property, most of the seed beam can not propagate along the whole gain zone, it experiences only part of the distance in the gain zone then turns into the expanding plasma, which is so call breakup amplified seed. The big density gap between the gain zone and its surrounding area causing a strong deflection. Only the beam centre along the gain zone can be fully amplified through the whole amplifier. The breakup amplified will beam will be separated from the fully amplified beam on the detection plane, as displayed in $Fig.\ 4.13(a)$. Interference between the breakup amplified seed beams and the full amplified beam can be occurred. The refractive index is discussed in Chapter 2, Section 2.6.4. This deflection behaviour of the seed beam could also cause a reduction of the effective gain-length product[67]. Moreover, the amplified seed has a divergence of $15\times4\ mrad$ in horizontal and vertical directions, compared to the divergence of the seed $(8\times15\ mrad)$ (see $Fig.\ 4.11$). The divergence improved in the vertical direction a factor of ~3.5 while it becomes larger in the horizontal direction, which might be caused by the above explanation in $Fig.\ 4.14(a)$. Further detailed explanation of the elongate amplified seed, more information about the gain zone of the amplifier-plasma is required. One can measure the amplified seed using x-ray Hartmann sensor (described in Chapter 3), which allows back-propagation of the detected beam.

However, in the collimated seeding configuration represented in $Fig.\ 4.13(b)$, most of the seed beam can pass through the whole gain zone to reach fully amplification. The un-amplified beam is deflected due to the plasma gradient. Most of the amplified seed beams are in parallel at the output, therefore, one cannot observe the interference. In this case, breakup amplified seed are significant prevented.

In conclusion, preliminary results from ASE self-seeding with wide plasma amplifier $(300\ \mu m)$ demonstrated an energy amplification of $6.5\ times$ and vertical divergence $\sim3.5\ times$ smaller than the seed. This is the best amplification achieved within the self-seeding scheme [74]. A more efficient seeding approach and detection system are required to reduce the refraction effect, such as using convergent seeding instead of the divergent injection, optimizing the pumping pulse configuration (as the improvement discussed in Section 3.1), seed with coherent beam source, employment of X-ray Hartmann sensor and more flexible operation for the full detection of the amplified signal. Nevertheless, the wider plasma amplifier has showed its attractive advantages. However, the experiments confirmed the conclusion based on our modelling that the output energy of seeded transient x-ray laser would not exceed several $10's$ of μJ, far from our mJ-range goal. Consequently, we have had to consider a totally different approach, that is described in the next chapter.

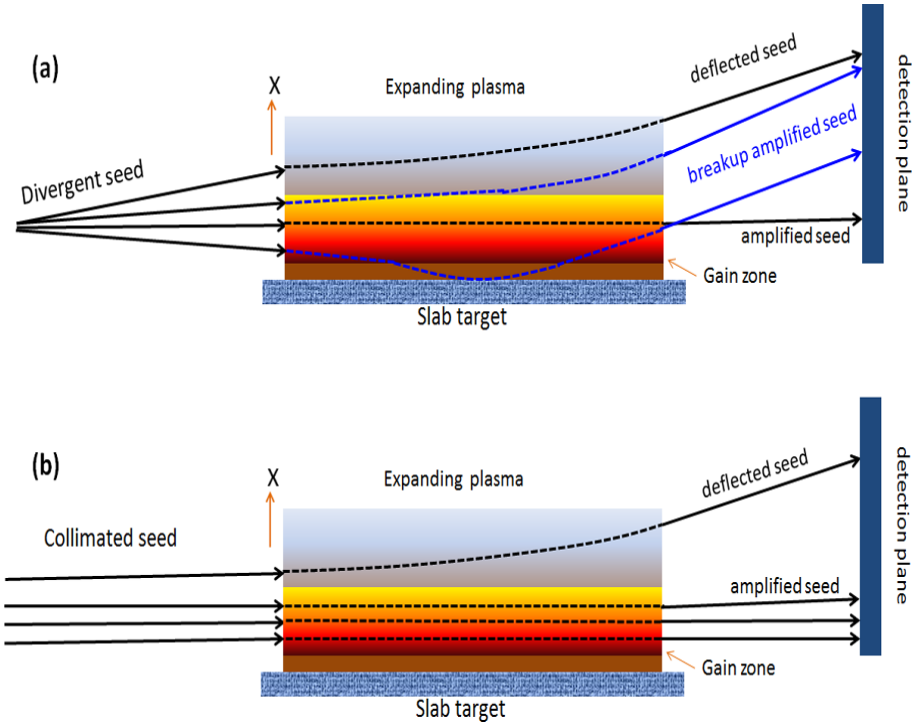

Figure 4.14: (a) Divergent and (b) collimated HH seed beams injected into the x-ray plasma amplifier.

4.4 Simulation of seeding with QSS x-ray lasers

We thus numerically studied the first SXRL seeding experiment demonstrated by Ditmire *et al.* [19]. Three $1054\ nm$ beams, each providing $200\ J$ in an $800\ ps$ pulse, were delivered to the target for pumping the SXRL amplifier. The HH beam with $140\ fs$ pulse duration was then injected into the plasma amplifier with proper time delay. The final amplified seed beam had $0.1\ \mu J$ while the ASE achieved $5\ mJ$, as illustrated in $Fig.\ 4.15(a)$. ASE dominates the x-ray emission from this plasma amplifier after HH injection and the energy amplification observed as ~ 3.5. This is far from the expected signal amplification ≈ 220. Two main effects were taken into account for this observed gain reduction:
1) the spatial overlap between the HH seed beam ($\sim 300\ \mu m$) and gain region ($\sim 80\ \mu m$) of the plasma amplifier,
2) spectral matching of the 21^{st} order harmonic ($\approx 0.01\ nm$) and the $Ga\ XXII,\ J = 2 - 1$ transition line ($\approx 0.005\ nm$) in the plasma amplifier.

Actually, all seeding experiments apart Ditmire's experiment [19] exhibit ASE at negligible level. From our extensive modelling on TCE scheme (discussed later), we observed that ASE starts to have non-negligible contribution for very large plasmas, about $1\ mm$ wide. Even for such plasmas, ASE is not dominant. Since for Ditmire's experiment, the focal width for generating the plasma was about $200\ \mu m$ width, we would expect to observe some ASE but not reaching an energy $1000\ times$ stronger than the amplified seed, as measured in $Fig.\ 4.15(a)$. Also, considering the time-resolved signal, it is striking to observe that the ASE remains at a very strong level of intensity after amplification of the seed. Considering a classical laser, one would expect to have ASE prior amplification of the seed while after, due to gain saturation by the seed, ASE should drop to very low level, as described in $Fig.\ 4.15(b)$. Such behaviour

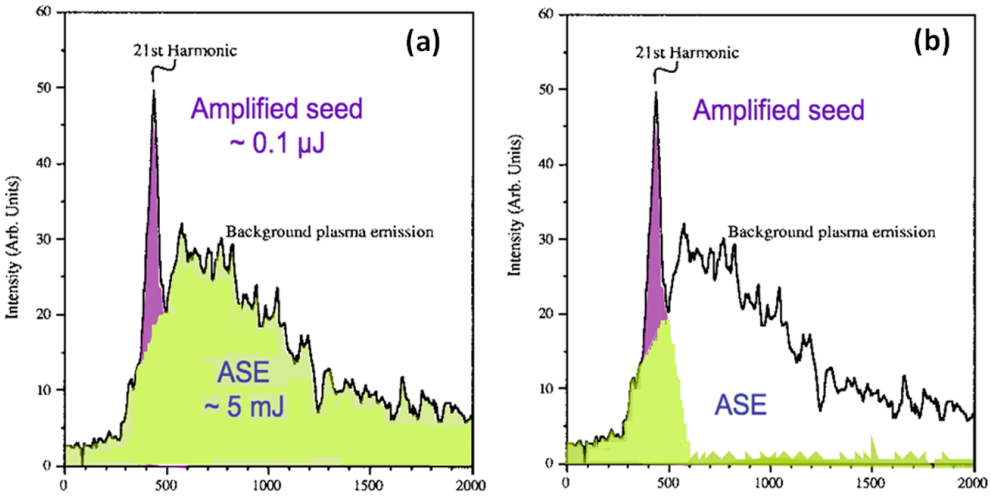

Figure 4.15: Temporal intensity lineout of the seeded SXRL and ASE for (a) Ditmire's experiment and (b) expected result as a classical behaviour of a laser amplifier. from [19]

has been observed on all our previous modelling whatever the plasma size is. This introduction pointed out that the cumulated emission after the seed amplification keeps most of the ASE energy. This peculiar behaviour of QSS plasmas when seeded holds the key to milli-Joule energy. Several issues have to be investigated, within them the most obvious was the seeding intensity. Seeding intensity level plays a crucial role of energy extraction. On Ditmire's experiment, the seeding intensity was rather low (low energy, low geometrical coupling between the seed and the gain region, long pulse duration) with the possible drawback that the saturation was probably not reached.

Therefore, by using the Maxwell-Bloch code (DEEPONE), we modelled exactly Ditmire's experiment as displayed in $Fig.\ 4.16$. Modelling parameters of our Maxwell-Bloch model were adjusted on the basis of Ditmire's experiment with a $200\ fs$, $0.5\ nJ$, $21.2\ nm$ seed, and plasma with an electron density of $4\times10^{20}\ cm^{-3}$ and temperature at $550\ eV$. In the absence of seed, gain peaks at $25\ cm^{-1}$ were in good agreement with the data from previous work [79]. It shows the temporal evolution of the seed and ASE intensities at different locations (z) along the plasma amplifier. Modelling reproduces the experimental data well:

1) the amplified seed ($Fig.\ 4.16$, red lines) is about two times as intense as the ASE ($Fig.\ 4.16$, blue lines);

2) ASE develops strongly before and after the propagation of the seed, its energy ($5\ mJ$) dominates greatly over the energy of amplified seed ($11\ \mu J$);

3) modelled ASE signals presented stochastic characteristics with variable intensities by the presence of much more spikes than the experimental results illustrated in $Fig.\ 4.15$. ASE occurs occasionally from the plasma amplifier due to the plasma polarization density, and the measured temporal profile as well as the seed duration were limited by the temporal resolution $\sim30\ ps$ of the streak CCD;

4) plasma pumped by long pulses lasting hundreds of picoseconds (QSS) has a different intrinsic behaviour in comparison with those of plasmas pumped by picoseconds lasers [12, 13, 36], with the latter exhibiting much lower ASE and very strong seed amplification (~600).

It is interesting to note that increasing the seed intensity by a factor of 1000, changes the ratio between ASE and amplified seed intensities, meaning that during Ditmire's experiment the gain was not

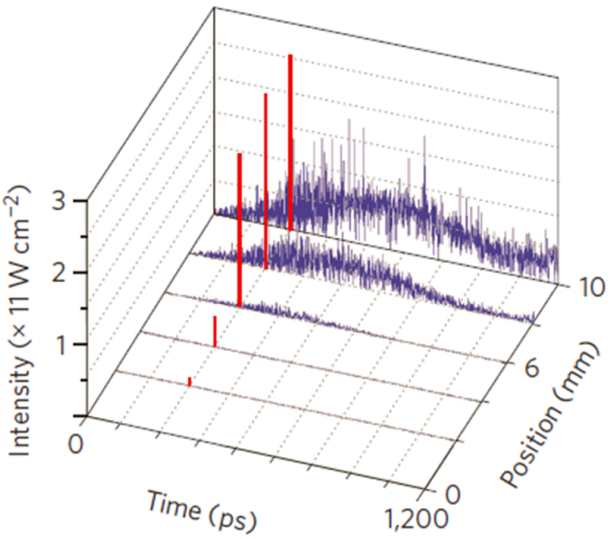

Figure 4.16: Temperal evolution of the amplified seed (red lines) and ASE (blue lines) intensities in the modelling of Ditmire's experiment. from [40, 42]

deeply saturated. However, the seed output energy increases by less than a factor of 2 to reach $20\ \mu J$ while the ASE energy remains unmodified at $5\ mJ$. This result seems contradictory with previous conclusion that the Ditmire's experiment was not running in deep saturation leaving the place for ASE to be amplified after seed propagation. To clarify this peculiar behaviour, temporal response of the lasing ions to seed saturation has to be examined. We thus studied the gain temporal evolution at two locations along the plasma column corresponding to different levels of amplification. At $z = 4\ mm$, as shown in $Fig.\ 4.17(a)$, we observed a strong amplification of the seed ($\sim$900 times) characteristic of unsaturated, exponential gain. ASE was not visible although present at very low intensity. We may observe that seed pulse induces very sharp and strong drop of the gain down to nearly $0\ cm^{-1}$ but only on a very short time. Over most time the gain remains totally unperturbed by the seed, rising. This observation closes the option of using very intense seed for extracting the energy stored in the plasma. Considering the time evolution of the gain for a further position $z = 5\ mm$ along the plasma column ($Fig.\ 4.17(b)$), the amplification of the seed was improved by less than $2\ times$ respected to the previous location. Deep saturation and the rise of ASE prior and after the seed were apparently observed. It is worth nothing that at this location ASE is strong enough to reduce the gain and reaching saturation for strongest spikes. For the first time, we approach an explanation of the presence of strong ASE after seed amplification.

The presence of unperturbed gain after saturated seed was not expected, so we zoom in the gain temporal evolution just around the presence of the seed, for both locations illustrated in $Fig.\ 4.18$. At $z = 4\ mm$ ($Fig.\ 4.18(a)$), a strong drop of gain to nearly $0\ cm^{-1}$ reveals deep saturation. However, gain recovers fully after only $2\ ps$ and then remains at its maximum value for $\sim 2\ ns$. For a position ($Z = 5\ mm$) further along the plasma column ($Fig.\ 4.18(b)$), ASE develops before and after the seed with the effect of reducing the gain. Clearly, it is the very fast regeneration of the gain that enables the ASE to develop. This means over most time the gain remains totally unperturbed by the seed. Seed pulse extracts the energy stored in population inversion during a period od less than 0.1% of the gain lifetime. In the other hand, more than 99.9% of the storage energy is not transferred to the coherent seeded beam, but to the ASE instead. One can also note the development of a weak and short wake after the amplified

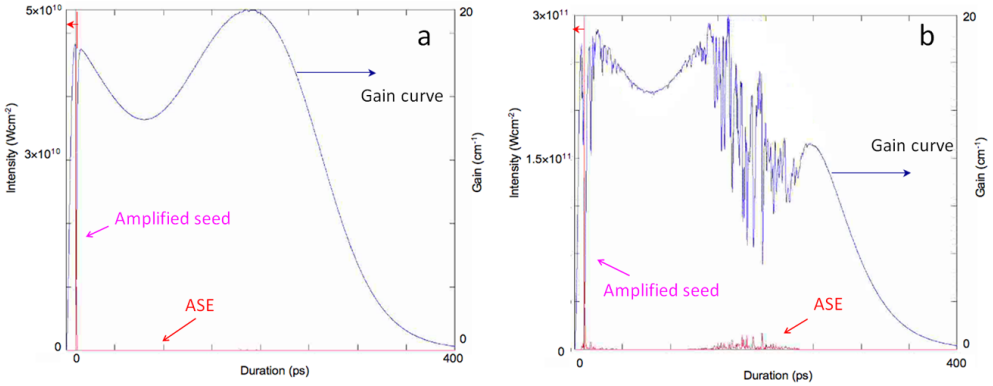

Figure 4.17: Temperal evolution of the gain curve (balck lines) and temporal profile of amplfied seed (red lines) when HH seed beam injected into (a) 4 mm and (b) 5 mm long x-ray plasma amplifier respectively.

seed pulse. ASE is not visible although present at very low intensity. Accordingly, direct seeding with a femtosecond soft x-ray pulse into mJ-class plasma amplifier, which is characterized by gain combining a long lifetime and fast recovery (~ 2 ps), is intrinsically inefficient.

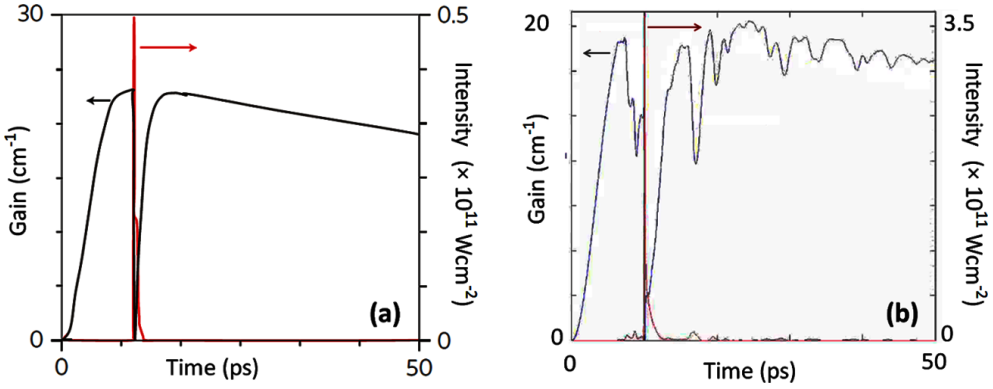

Figure 4.18: Close-up of the emperal profile of the amplfied seed (red lines) and the gain curve (balck lines) when HH seed beam injected into (a) 4 mm and (b) 5 mm long x-ray plasma amplifier, respectively. from [40].

To obtain further information about the gain recovery behaviour, we checked the disturbed gain by femtosecond seeding pulse from different plasma lengths, as displayed in $Fig.\ 4.19(a)$. It is observed that the population inversion is fully depleted after amplification through 2 mm, where the amplified seed becomes strong enough to empty the gain. Another effect is illustrated in $Fig.\ 4.19(b)$, where the effect of the seeding time on the temporal gain is shown. When the HH is seeded before the peak of the unperturbed gain, the gain almost recovers its maximum value afterwards. On the contrary, when the seed arrives after the peak of the gain, the unperturbed gain values are not attained. Pumping conditions are the cause of this behaviour. To better understand this point, we therefore seed the HH pulse into different plasma amplifiers with various electron density after the peak of the gain, as represented in $Fig.\ 4.20(a)$. In the higher n_e plasma, the recovered the gain reaches a higher value. $Fig.\ 4.20(b)$ shows the amplified seed from 1.2 mm long plasma with different electron densities n_e. It is apparent that the "bump" signal (wake) is sensitive to the electron density which directly contributes to the upper level population.

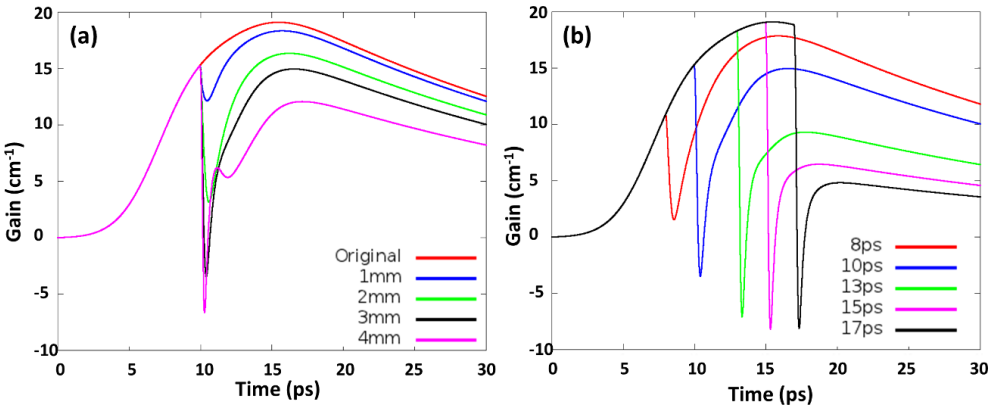

Figure 4.19: Gain recovery behaviours under different seeding conditions: (a) plasma length, (b) seeding time.

Furthermore, this predicted short population inversion recovery time was experimentally measured under various plasma parameters in recent work [80], which will be discussed in Chapter 5.

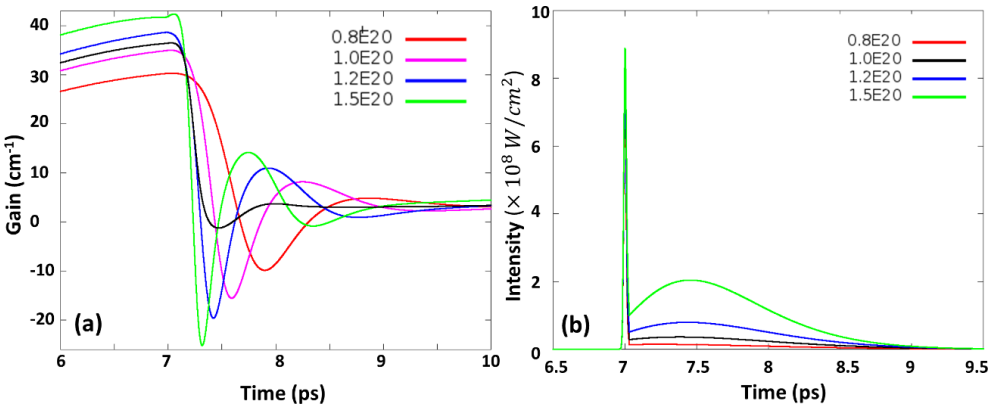

Figure 4.20: (a) Gain dynamics investigation with a variety of plasma density ne: 0.8×10^{20} cm^{-3} (red line), 1×10^{20} cm^{-3} (pink line), 1.2×10^{20} cm^{-3} (blue line), 1.5×10^{20} cm^{-3} (green line). (b) The amplified seed signal from 1.2 mm plasma at various densities.

4.5 Towards GW coherent SXRL

An efficient approach for coherently extracting the stored energy from mJ-class x-ray plasma amplifier by the HH-injection was requested. The first and straightforward way consists of seeding a train of femtosecond coherent pulses separated by 2 ps throughout the entire gain duration. Same parameters as used to obtain $Fig.\ 4.18(a)$ were used for this modelling illustrated in $Fig.\ 4.21(a)$, except that a larger gain cross-sectional area of 4×10^{-4} cm^{-2} was applied. Using 100 seed pulses of 10 nJ each, the total energy at the plasma exit (10 mm) was divided into 7 mJ of amplified coherent seed and nearly 1 mJ of ASE. The ASE is still amplified but not at strong level while amplified seed pulses reach very high intensities up to 1.4×10^{12} Wcm^{-2}. Each pulse has duration of 150 fs equals to the case of single pulse seeding mentioned before. $Fig.\ 4.21(b)$ corresponded to the plasma length of 4 mm, shows that the gain is fully saturated after amplification of each seed pulse, but recovers sufficiently to amplify the next pulse.

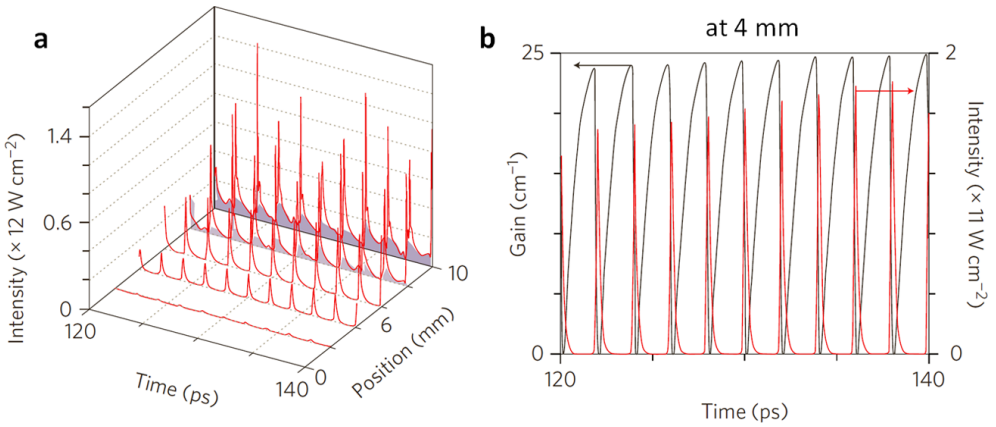

Figure 4.21: (a) Temperal evolution of seeded SXRL (red) and ASE (blue) intensity along the plasma amplifier with multiple seeding approach. (b) Amplified seed pulses temporal profile and the real-time gain curve at at $z = 4$ mm location of plasma amplifier. from [40]

It is interesting to note that the total energy ~ 7 mJ contained in the pulse train is ~ 300 $times$ more than optimized result of Ditmire *et al.*'s experiment [19]. Simultaneously, ASE keeps energy level as low as 1 mJ. However, for extracting these 7 mJ from the plasma, we seed a train of about 100 coherent pulses. Generating such a train pulse will be very challenging. One solution may exist by trapping one or several femtosecond IR pulses in a cavity where a gas jet or a gas cell is placed. HH pulses are emitted at each round-trip by interaction of the intense IR pulse with gas. One may also use an array of birefringent crystals or employ a grating-pair stretcher, a multiple-order wave plate and a linear polariser for the quasi-phase-matching high harmonics generation [81]. However, we could not find any technique able to re-synchronize all the pulses contained in the train in order to generate an unique 150 fs pulse containing a fraction of the 7 mJ. We would like to note that this source would find applications like coherent nano-imprint or coherent imaging of slow varying phenomena like plasmas created by nanosecond lasers.

Owing to the technical challenge of generating and re-synchronizing a train of SXRL pulses, we therefore explored a second scheme, comprising extrapolation from this temporally discrete seed to a temporally continuous seed. This process is based on the use of spatially and temporally coherent beam, but with pulse durations of hundreds of picoseconds, so that the energy can be extracted continuously, as quickly as it is restored. The seed duration in this case is now 200 ps, with 0.1 mJ energy, so that the seeding intensity is maintained far above the self-emission level. The temporal evolution of intensity versus position along the amplifier is presented in $Fig.\ 4.22(a)$, and shows strong coherent seed amplification $(10$ $mJ)$ and very weak ASE spikes $(90$ $\mu J)$. Long seed amplification yields a 1000-fold enhancement of the coherent energy compared to femtosecond seeding and 30% more than when using a pulse train. $Fig.\ 4.22(b)$ shows the temporal gain curve (black line) and amplified seed signal(red line) at $z = 4$ mm. Furthermore, it is important to note that seeding a continuous wave instead of discrete pulse train is very beneficial for limiting ASE. The seed/ASE energy ratio after amplification is 2×10^{-3} for femtosecond seeds, 7 for a pulse train and 110 for this stretched seed, demonstrating the optimized efficiency of this scheme. This significant energy amplification scheme is greatly attractive for the SXRL single-shot diffraction imaging [43, 70].

Considering the implementation of such a long seed pulse, we would like to stress out an important

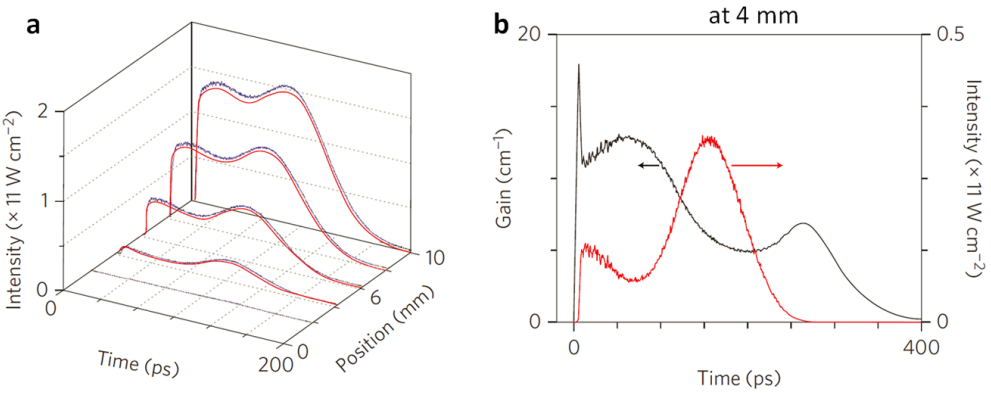

Figure 4.22: (a) Temperal evolution of seeded SXRL (red) and ASE (gap between blue and red) intensity along the plasma amplifier with a long seed pulse ($200\ ps$) instead of discrete pulse train. (b) Amplified seed pulse temporal profile and the real-time gain curve at $z = 4\ mm$ location of plasma amplifier. from [40]

issue. Seeding is interesting only if the output beam has an improved optical quality or shorter duration than ASE. Whatever the pulse duration of the seed, it has to be spatially fully coherent and if possible polarized. To-date only FEL and HH pulses have been demonstrated with full spatial coherence. Although it is possible to seed plasma with FEL, we will not consider this issue for the table-top SXRL source development. HH pulse has never been achieved with pump laser having duration longer than few picoseconds. Indeed, the process of HH generation requires intensities above several $10^{14}\ Wcm^{-2}$ to be efficient. However, at such intensities, gases are ionized deteriorating the phase-matching between HH pulse and the pump laser. A solution has been found by reducing the pump laser duration down to $10's$ and even few femtoseconds. Consequently, we may hardly believe that $200\ ps$ or longer high harmonic pulse might be directly produced by $100's\ ps$ IR laser. Finally, we explored the possibility of generating intense femtosecond HH pulse then stretch them to the nominal duration prior amplification.

Before describing the SXRL stretcher, we would like to consider a key issue. As pointed out before, long pulse ($\sim 200\ ps$), spatial coherent SXRL has some niche of interest. However, our main goal is to generate high energy (mJ-class), fs pulse. This implies that the pulse has to be compressed after amplification. To the best of our knowledge, the only feasible solution we found is an extrapolation of the CPA concept [82] into the soft x-ray range. Within this technique, the different spectral components are separated in time by a grating pair, then amplified and compressed by a similar grating pair. Such system requires the use of temporally coherent and phase-locked seed for the compression stage. Coincidently, HH beam has been demonstrated as fully coherent (in both temporal and spatial) and phase-locked [83].

Consequently, we put forward a proposal of x-ray CPA system, based on table-top plasma amplifier, schematically depicted in $Fig.$ 4.23. It is composed of HH from gas cell/puff, image relay system for the HH seed injection, plasma pre-amplifier, SXRL stretcher, plasma main-amplifier, and the final SXRL compressor. By now, maximum HH pulse energy of soft x-ray range is in nano-Joule level. The intensity of the HH seed pulse will be significantly reduced whilst through the pulse stretcher. Once the seed pulse intensity is below the ASE intensity level, amplification of the seed pulse after the plasma amplifier will hardly be observed, in other words, the energy extraction of the coherent seed from plasma amplifier will be rather inefficient. In addition, seeding with higher intensity will saturate the plasma, destroy the population inversion and prevent the development of ASE and wake, as discussed in Section 4.3.

Therefore, employing a x-ray plasma pre-amplifier is suggested, which can be driven with $1\ J$, $10\ Hz$

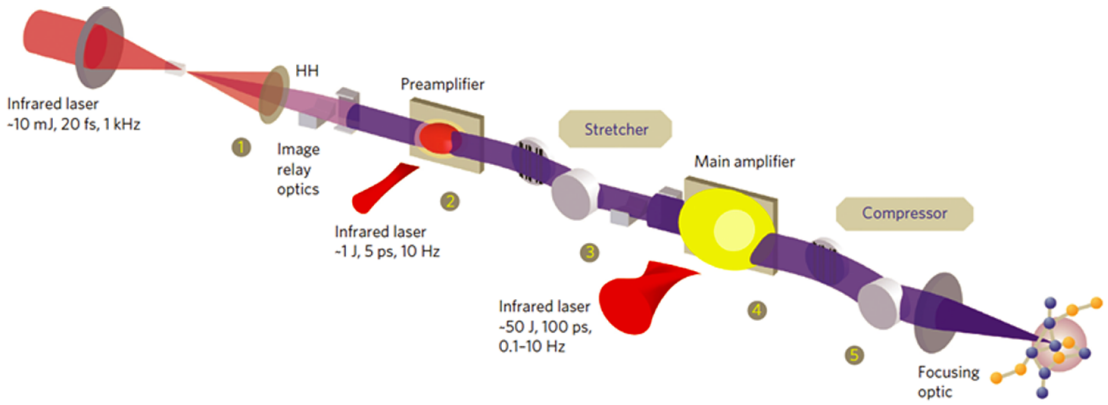

Figure 4.23: Architrcture design of the X-ray CPA sysytem. from [40]

IR laser system as described in Chapter 3, Section 3.4.1. This pre-amplifier should be chosen as similar electron density (n_e) and temperature (T_e) as the main-amplifier. Thus, the line profile of the pre-amplified seed will well match that of the main amplifier. For example, as illustrated in $Fig.\ 3.35$, plasma amplifier created by a combination of long ($200\ ps$) and short ($6\ ps$) laser pulses may achieve the right density and temperature as long as the focal width is larger than $100\ \mu m$. After the pre-amplification, the seed is sent to the stretcher. Stretching the pulse with a grating pair separates in time and spectral components. We thus modified our Maxwell-Bloch model to consider the seed not as a single frequency but as large frequency pulse with spectra-temporal stretch. The different spectral components travelling along paths of different lengths, inducing group velocity dispersion, will separate the spectral components over time. However, in contrary to classical laser amplifiers, plasma conditions evolve over time meaning that every component will not encounter the same gain value. Thus, the gain that the spectral component $\omega = \omega_0 + d\omega$ will find is $G(t, \omega_0 + d\omega)$. As the gain is supposed to have a Lorenzian spectral shape, $G(t, \omega_0 + d\omega)$ can be computed from $G(t, \omega_0)$ the value of the gain at the line centre given by the Bloch-Maxwell equations (Eq. (4.19)-(4.23)) plotted in blue line on $Fig.\ 4.24$. The resulting spectral gain will be the convolution of the Lorenzian shape and the temporal profile of gain ($Fig.\ 4.24$, red line). We may observe a spectral narrowing of the spectrum due to the fast variation of gain near $T = 140\ ps$.

The amplification of the pulse through the plasma induces phase distortion of the seed pulse. For a Lorenzian line shape, the de-phasing is given by

$$\Phi(Z,t) = \frac{-\frac{\omega-\omega_0}{\Delta\omega}}{1+(\frac{\omega-\omega_0}{\Delta\omega})^2} GL, \tag{4.24}$$

where ω_0 is the central frequency, $\Delta\omega$ is the bandwidth and GL is the gain-length product. The exponential of the phase, $e^{-i\phi(z,t)}$, is multiplied to the amplitude of electric field calculated by our modified Maxwell-Bloch model prior computing its Fourier transform and calculating the temporal variation of the intensity.

Moreover, HH pulse exhibits little phase distortion, which is responsible for only a few hundreds of attoseconds of broadening, is negligible compared to the $150\ fs$ Fourier limit of milli-Joule class SXRL. We also calculated the plasma spectral phase deformation considering a $10\ mm$ Zinc plasma amplifier [84], as shown in $Fig.\ 4.25$, the estimated phase deformation is 2 radians. Firstly, assuming a Gaussian profile for the HH seed at the entrance of the pre-amplifier as plotted in $Fig.\ 4.26(a)$. By taking account

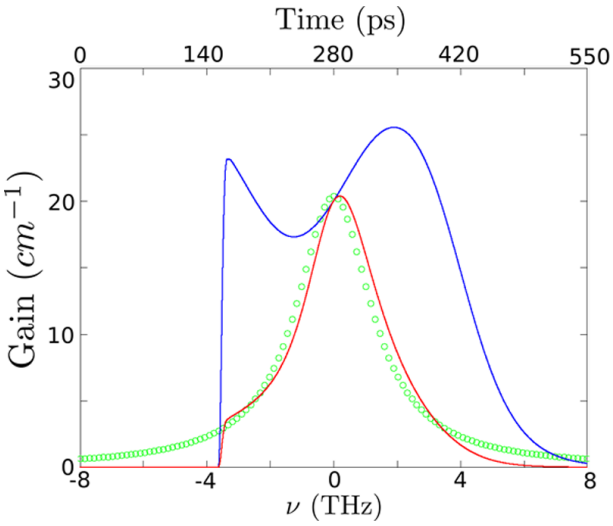

Figure 4.24: Spectral gain for the main amplifier. Gain calculated from our Maxwell-Bloch model (in blue), the spectral components as spread in time by the stretcher (in green) and the convolution of spectral stretch and temporal variation (in red). from [40].

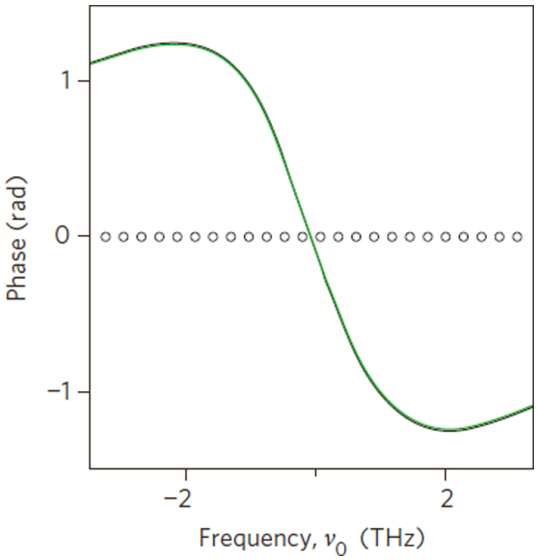

Figure 4.25: Spectral phase of HH seed before (circles) and after (line) the propagation in a $10\ mm$ plasma amplifier. from [40].

of all these effects, we calculated the temporal intensity profile of the output signal which from the pre-amplifier (black line) and after the final amplification and compressor (red line). Note that the HH seed and output signal from the pre-amplifier are normalized for the ease of comparison. It is observed that there is a weak post-pulse containing 3% of the total energy with the final output signal (red line) after the main-amplifier and compressor. The main pulse contains 97% of the full energy and has a pulse duration of $215\ fs$ FWHM. This output temporal profile was obtained computing the Fourier Transform of the electric field of the amplified beam. The small "bump" (post-pulse) can be caused by slight asymmetry in

the spectral gain (see $Fig.\ 4.24$) and by the asymmetries in the phase required during amplification. It is also found as forward shifted comparing to the seed. In addition, the spectral intensity at the entrance (circles) and exit (line) of the main amplifier are illustrated in $Fig.\ 4.26(b)$. It is worth noting that, due to the combination of fast gain regeneration and spectral stretching, the spectral components are amplified quasi-independently. Plasma SXRL, which are normally dominated by homogeneous broadening [39], behave here like quasi-inhomogeneous lasers. Our preliminary calculations show that this characteristic opens the way to achieving $100\ fs$ pulses by means of gain temporal shaping, which will be discussed in next section.

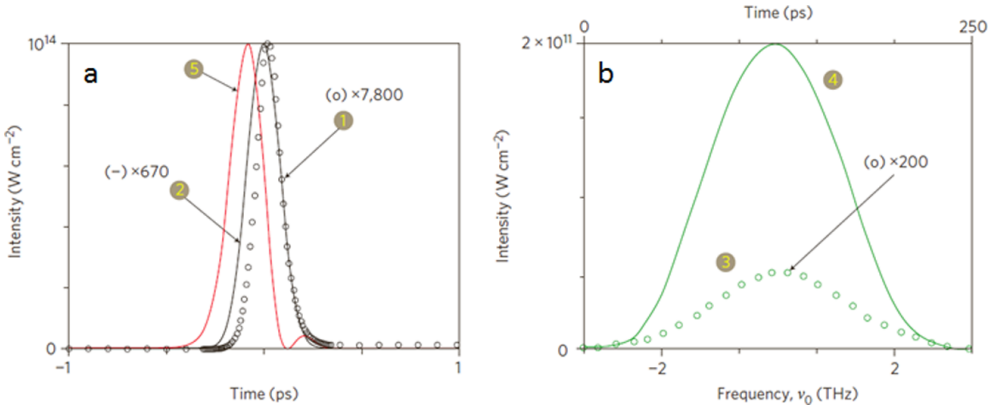

Figure 4.26: Temporal (a) and spectral (b) profile of the SXRL signal at the remarked position related to the marker in $Fig.\ 4.23$. from [40]

Finally, as the bandwidth of a single HH is estimated to be $100\ times$ larger than the linewidth of the SXRL from [84], only 1% of the energy is efficient for seeding to the plasma amplifier. Considering a minimum seeding level of $0.1\ \mu J$ in-band, the HH energy has to be $10\ \mu J$, which is orders of magnitude above the most energetic HH emitted around $20\ nm$. However, plasmas pumped by Joule-class lasers may easily amplify $10\ nJ$ HH up to the required level as demonstrated in black line of $Fig.\ 4.27$. It is important to note that the bandwidth of the amplified seed after the pre-amplifier is well matching the line-width of the SXRL in main-amplifier. Therefore, using the pre-amplified HH seed as the input of the main-amplification, pulse energy requirement is as low as $0.1\ \mu J$ to achieve the final mJ level output. $Fig.\ 4.27$ presents a full spectra-temporal energy calculation including group velocity dispersion, starting from a low-energy HH seed, passing through a plasma pre-amplifier, the stretcher and the main amplifier to produce a $10\ mJ$ pulse. In this calculation,the pre-amplifier was set with $n_e = 2.2\times10^{20}\ cm^{-3}$, $T_e = 531\ eV$, cross-sectional area of the gain zone as $120\times51\ \mu m^2$ and plasma length up to $3\ mm$. Higher electron density and temperature of main-amplifier was chosen to ensure the $1.5-2\ ps$ gain recovery time, and cross-sectional area of the gain zone was set as $4\times10^{-2}\ mm^2$ with plasma length up to $10\ mm$. With the benefit of conical off-axis diffraction gratings, which experimentally demonstrated a diffraction efficiency as high as 70% [75], the final output pulse can thus achieve around $5\ mJ$ (5×10^{14} coherent photons) in $215\ fs$ FWHM. With a power of over $20\ GW$, this new SXRL source is $10,000\ times$ more powerful than previous plasma [76] based SXRL and $100\ times$ higher than the best current x-ray FEL [77, 78].

It is worth noting that using a pre-amplifier and soft X-ray CPA allows a dramatic reduction in the total pumping energy, from previous kJ [19, 84] to $100\ J$. In supplementary, plasma tailoring by shaping the pump laser focal line in space would generate the appropriate conditions [38]. A downscaled version

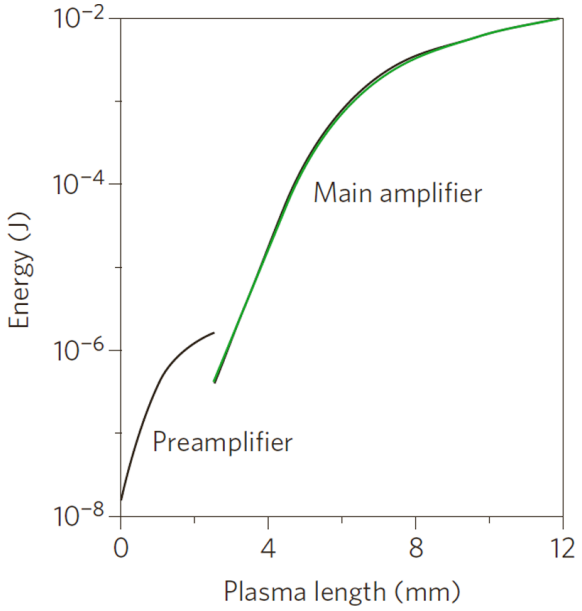

Figure 4.27: Output energy versus plasma length for the pre- and main amplifiers. [40].

could be implemented at small-scale (hundreds of Terawatts, $10\ Hz$) laser facilities to deliver soft X-ray pulses up to $0.5\ mJ$ in $200\ fs$, equivalent to today's best soft X-ray FEL and fully coherent in space and time. Our preliminary design of the SXRL grating-pair single-pass compressor and stretcher is discussed in later in this chapter, Section 4.7. Furthermore, Our preliminary calculations showing the way to achieve $100\ fs$ pulses by means of gain temporal shaping is demonstrated in next section, which brings an attractive prospective of this novel SXRL source.

4.6 Future pulse shortening in SXRL CPA

Basically, a plasma amplifier has a frequency dependent gain and therefore will spectrally modify the pulse during amplification. When the gain is high, the pulse is amplified several orders of magnitude and its bandwidth is narrowed because the relative frequency amplitude within the pulse is modified. We performed this modelling using the Maxwell-Bloch model DEEPONE and defined a frequency dependent gain coefficient with its peak centred near $21.2\ nm$.

As we discussed in above sections, It is interesting to seed longer coherent pulse into the plasma amplifier for higher energy extraction. In the following numerical simulation, the seed beam is considered as the pre-amplified stretched seed pulse (hundreds of picoseconds) sent to the main-amplifier. The temporal gain curve of $21.2\ nm$ for a $100\ ps$-pumped plasma-amplifier is descried as the red line in $Fig.\ 4.28$. In this plasma (up to $20\ mm$ long), cross sectional area of the gain region is $4\times10^{-2}\ mm^2$, $N_e = 4\times10^{20}\ cm^{-3}$, $T_e = 550\ eV$. The coherent seed beam size is set as $2.4\times1.2\ mm^2$ with $10\ \mu J$ pulse energy in $160\ ps$ FWHM. After propagation through $11\ mm$, the seed pulse is amplified with the temporal

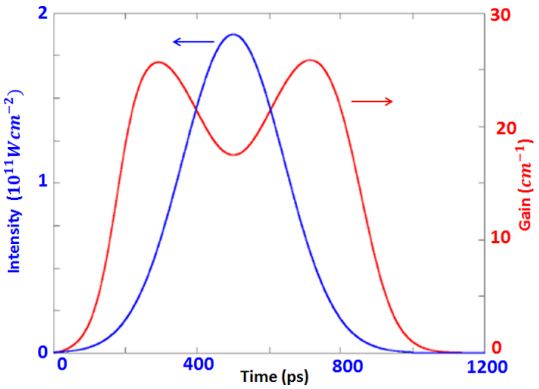

Figure 4.28: Temporal gain curve of $21.2\ nm$ for a $100\ ps$-pumped plasma-amplifier (red line) and pre-amplified stretched seed pulse injected at $T = 500\ ps$ (blue line).

profile (blue line) represented in $Fig.\ 4.29$, while the gain is depleted strongly (red line). The amplified beam is then sent to the x-ray compressor for the pulse compression. It is worth nothing that during the CPA processing, the temporal pulse is always related to the spectra. The final signal was computed through Fourier Transform with pulse duration of $\sim 210\ fs$.

We therefore simulated the final output pulse duration as a function of the propagation distance in plasma amplifier with different seed energy, as illustrated in $Fig.\ 4.30$. The pulse duration is rapidly increasing with the short plasma length ($< 5\ mm$), while from $5\ mm$, the final pulse duration is decreasing as increasing the propagation distance in the plasma. Normally, the collisional pumped plasma is reaching the saturated amplification around $4\ mm$ plasma length. Moreover, as we mentioned before, the temporal gain curve displayed in $Fig.\ 4.28$ is for the specific wavelength $21.2\ nm$, however, the input seed pulse has a finite bandwidth ($\Delta\lambda/\lambda \sim 10^{-4}$) and the relations between gain coefficient and wavelength is as Lorentzian function. This spectral-dependent gain curve with a Lorentzian profile is directly causing the spectral bandwidth of the amplified beam. Therefore, one could understand that the amplification under non-saturated amplifier induces spectral gain narrowing [85] when the plasma length is less than $5\ mm$. This is ultimately broadening the final pulse duration after compressor. However, after $5\ mm$ of the plasma, the gain is saturated for the central wavelength ($21.2\ nm$), as the increasing

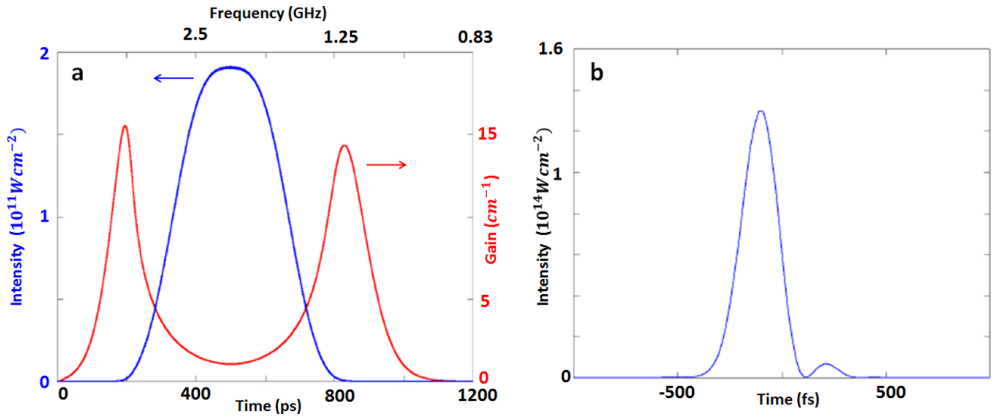

Figure 4.29: (a) Amplified seed (blue line) and depleted gain (red line) of $11\ mm$ *long plasma. (b)Calculated final output SXRL signal after the compressor through Fourier Transform.*

of the plasma length, the spectra-dependent gain are reaching saturation while the rest of the spectral components are still efficiently amplified, broadening the bandwidth of the amplified beam, so that the Fourier Transformed pulse shows the decreasing of the pulse duration.

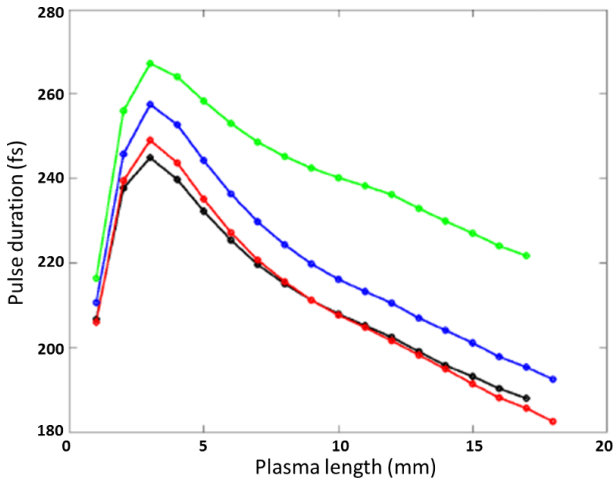

Figure 4.30: Computed final output SXRL pulse duration as a function of the plasma amplifier length with different seed pulse durations: $160\ ps$ *(black line),* $233\ ps$ *(red line),* $300\ ps$ *(green line) and* $333\ ps$ *(blue line).*

This spectral gain saturation behaviour becomes very interesting for the pursuit of Fourier Transform limited SXRL. More temporal gain shaping with different techniques have been attempted. In $Fig.\ 4.31(a)$, temporal gain curve with a "deep hole" in the middle was generated adopting two pump pulses with $50\ ps$ pulse duration. By seeding with a $50\ ps$ FWHM and $10\ \mu J$ pre-amplified seed pulse, pulse duration and energy of final output SXRL after the compressor as a function of plasma length is shown in $Fig.\ 4.31(b)$. Pulse duration below $140\ fs$ was obtained when the plasma length reached 20 mm. Energy amplification indicated a linear amplification curve with the plasma length longer than $5\ mm$ and reached $10\ mJ$ pulse energy. Note that 50% of the energy efficiency through the compressor was taken into account.

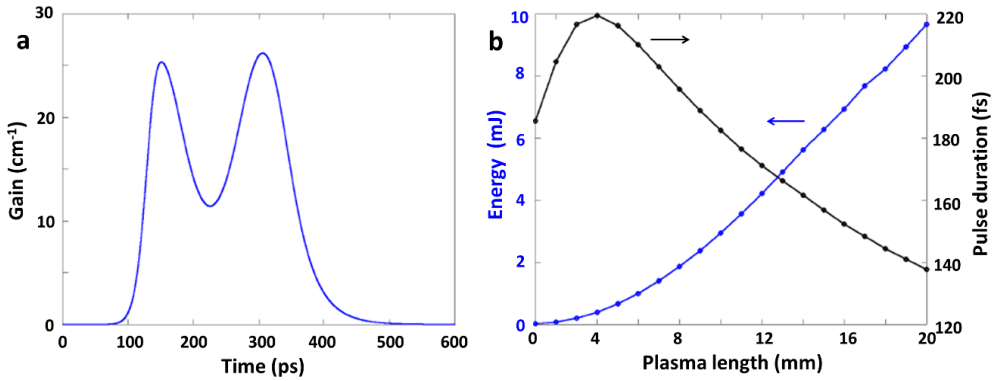

Figure 4.31: (a) "Deep hole" gain shape and (b) the final output pulse energy (blue line) and pulse duration (black) as a function of plasma length.

Another temporal shaping of the gain is displayed in $Fig.\ 4.32(a)$, which is due to two pump pulse with $150\ ps$ pulse duration. It is clear that the shape of the "deep hole" is different from previous case and gain duration is much longer than using $50\ ps$ double pump pulses. In order to extract as much energy as possible from the amplifier, a $300\ ps$ FWHM seed pulse with $10\ \mu J$ energy was seeded at the centre of the gain. Final output over $35\ mJ$ and pulse duration below $150\ fs$ was achieved, as illustrated in $Fig.\ 4.32(b)$. Considering much longer seed pulse $(300\ ps)$ in this case and the seed pulse duration effect demonstrated in $Fig.\ 4.30$, the final output with $20\ mm$ long plasma amplifier could reach Fourier Transform limited ($\sim$100 fs) if one seed with $50\ ps$ pulse. In that case, pulse energy of the final beam would reduced to several milli Joules. Coupled with the $\sim$100 fs, this fully coherent SXRL source is adequate to make diffraction imaging.

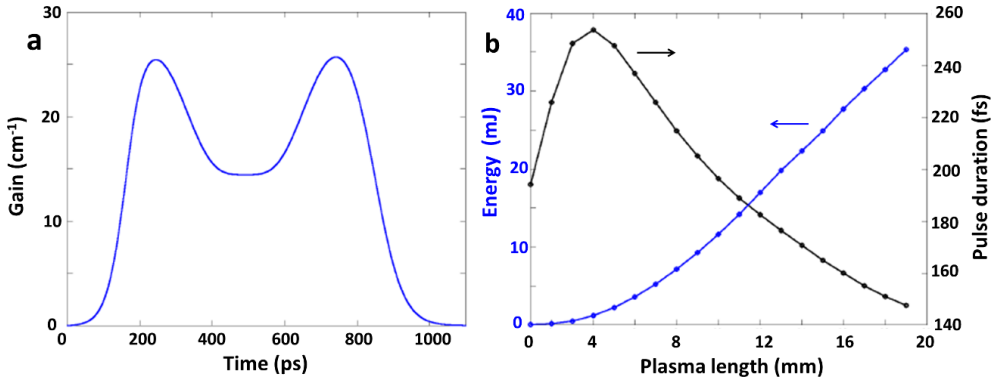

Figure 4.32: (a) "Special hole" gain shape and (b) the final output pulse energy (blue line) and pulse duration (black) as a function of plasma length.

Furthermore, double-main-amplifier configuration was taken into account. $10\ \mu J$, $160\ ps$ seed pulse was injected to the 1^{st} main-amplifier at the first half of the gain curve $(Fig.\ 4.33(a))$, sequentially, the output beam was directly seeded into the 2^{nd} plasma amplifier $((Fig.\ 4.33(b))$. $Fig.\ 4.34$ is showing the output signal from the $10\ mm$ 2^{nd} main-amplifier after compressor. $14\ mJ$ in $150\ fs$ of the final SXRL was eventually achieved.

It is important to point out that the temporal gain shapes we used in this section do not have the

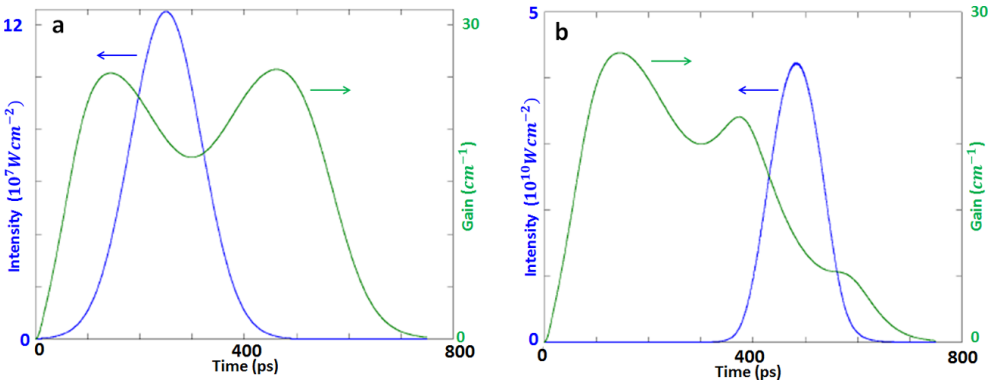

Figure 4.33: Seeding in the fist main-amplifier (a) and its ouput seeded into the second main-amplifier (b).

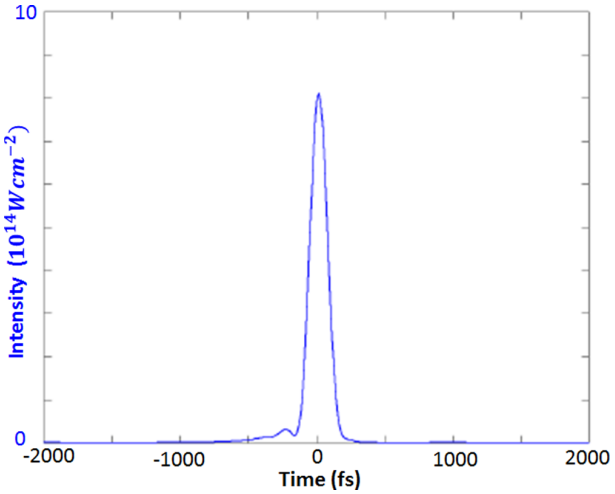

Figure 4.34: Calculated final output SXRL signal from $10\ mm$ *long* 2^{nd} *main-amplifier after the compressor through Fourier Transform.*

practical support, which means all the creation parameters of the special temporal gain shape have not been verified with the experiments. A more practical high-dense plasma simulation code is required to shape the temporal gain curve, such as EHYBRID code [86]. However, this technique by temporal shaping the gain to shorten the final output SXRL pulse from the x-ray CPA system, demonstrated reaching $10\ mJ$ in $100\ fs$, brings an attractive prospective for reaching ultra-high temporal and spatial resolution in the SXRL imaging nowadays [43].

4.7 Technical challenges of SXRL CPA

CPA is a technique for amplifying an ultrashort laser pulse with the laser pulse stretched out temporally and spectrally prior to amplification, as well for compressing the pulse duration with a compressor after amplification to achieve ultrashort laser pulse. Basically, the grating-pair are used for the pulse stretcher and compressor. However, for the short wavelength (below $50\ nm$), the efficiency of the grating is always the most concerning issue.

The groove profile has a significant effect on the light intensity diffracted from the grating. While ruled gratings may have triangular or trapezoidal groove profiles, holographic gratings usually have sinusoidal (or nearly sinusoidal) groove profiles (see $Fig.\ 4.35$). A ruled grating and an holographic grating will have demonstrably different efficiencies (diffraction intensities) for a given wavelength and spectral order. Moreover, ruled gratings are more easily blazed (by choosing the proper shape of the burnishing diamond) than holographic gratings, which are usually blazed by ion bombardment (ion etching). Differences in the intensity diffracted into the order in which the grating is to be used implies differences in the intensities in all other orders as well; excessive energy in other orders usually makes the suppression of stray light more difficult. For the short wavelength laser, blazed grating is preferred.

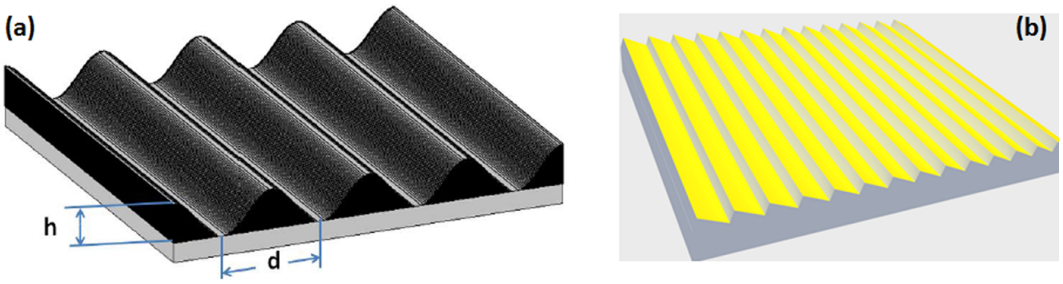

Figure 4.35: Groove profiles for blazed and holographic gratings. (a) Sinusoidal groove profile of an holographic grating. (b) Triangular groove profile of a mechanically ruled grating.

When working with wavelengths below $35\ nm$, grazing-incidence configuration has to be used because of the low reflectivity of conventional coatings at normal incidence. The time compensation in this case is harder because of the intrinsic difficulties that arise from grazing-incidence mountings, which are quite sensitive to aberrations and misalignments. Finally, once the grating's subtended angle is chosen, time compensation is optimum only in a narrow spectral region.It is well known that the grating efficiency at the blaze wavelength in a conical diffraction (off-axis) mounting , in which the direction of incident light belongs to a plane that is parallel to the direction of the grooves, is close to the reflectivity of the coating, as depicted in $Fig.\ 4.36$. The basic equation of off-axis diffraction [75] is:

$$sin\phi(sin\theta + sin\theta') = m\lambda/d, \tag{4.25}$$

where ϕ and θ are the altitude angle and azimuth angle, respectively. The altitude angle is the angle between the direction of incident rays and the direction of grooves. θ' is the azimuth of the diffracted light at wavelength and order m. λ is the operating wavelength and d corresponds to the line spacing of the blazed grating. This can be transformed in classical diffraction formula as

$$sin\theta + sin\theta' = m\lambda/d', \tag{4.26}$$

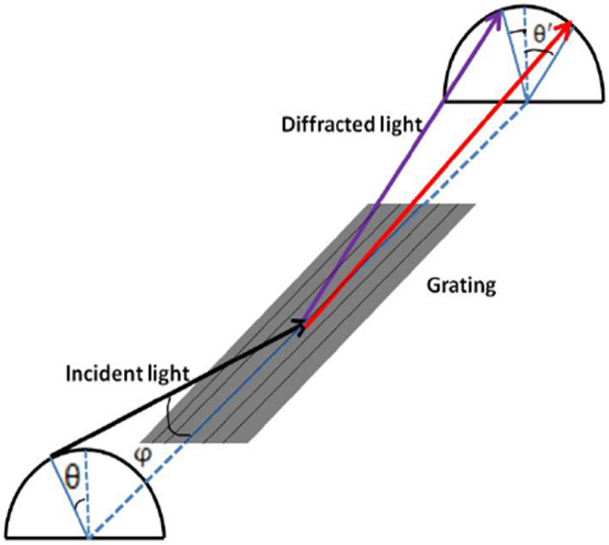

Figure 4.36: Geometry of the conical diffraction.

with

$$d' = dsin\phi. \tag{4.27}$$

The blaze condition of maximum efficiency is described in the classical diffraction geometry: the light has to leave the grating such a way that performs a specular reflection on groove surface, that is $\theta + \theta' = 2\theta_B$m where θ_B is the blaze angle. in addition, when $\theta = \theta_B$, shadowing effects from adjacent grooves would be avoided. So the highest efficiency of a blaze grating in the off-plane mout is achieved when $\theta = \theta' = \theta_B$, which is so called blaze condition. In this case, the grating equation is expressed as

$$2sin\phi sin\theta_B = m\lambda/d, \tag{4.28}$$

efficiency peak occur at

$$\frac{\lambda}{d'} = 2sin\theta_B. \tag{4.29}$$

Moreover, $Fig.\ 4.37$ is showing the conical diffraction in the plane of the groove profile. For a given wavelength λ, we may consider the ratio of the width of a collimated diffracted beam to that of a collimated incident beam to be a measure of the effective magnification of the grating (see $Fig.\ 4.36$). From this figure we see that the ratio between the diffracted beam size b and input beam size (a) is

$$\frac{b}{a} = \frac{cos\theta'}{cos\theta}. \tag{4.30}$$

Since θ and θ' depend on λ through the grating equation, this magnification will vary with wavelength. the ratio $\frac{b}{a}$ is so called anamorphic magnification. For a given wavelength λ, it is only depending on the angular configuration in which the grating is used. Moreover, an Italian group [75] recently demonstrated the high diffraction efficiency at SXRL region (from $18\ nm$ to $45\ nm$) over 50% using the conical diffraction concept in both simulation and experimental results.

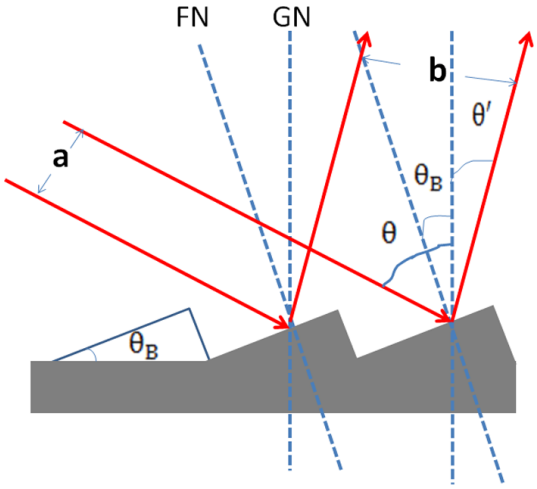

Figure 4.37: Anamorphic magnification of blaze grating.

The stretcher and compressor are designed with similar parameters in order to ensure the best compensation of aberrations generated by the stretcher. Since soft x-rays are highly absorbed in any material, we consider only reflective or diffraction optics. Among all the possible geometries, we consider as the basic design single pass stretcher and compressor in order to maximize the output energy by limiting the number of reflections. It is important to note here that just after the HH source and all along the chain (see $Fig.$ 4.23) the soft x-ray beam is collimated meaning that no extra optic is required to achieve parallel beam at the entrance of the stretcher or compressor. Compressor and stretcher are similar with the only difference of requiring "negative" distance between gratings for the stretcher. This is achieved by imaging the first grating on a position, Z, situated beyond the second grating. Several optical systems have been tested for IR and visible lasers. For the chosen geometry, the system must have a magnification of -1, meaning to reverse the image. Telescopes are the most appropriate. We consider a telescope with minimum reflections composed of two spherical mirrors (one convergent and one divergent) both under grazing incidence. The telescope throughput is assumed to be as high as 64% corresponding to classical single-surface reflectivity of 80%. The compressor is working with the same geometry with a real spacing of $5\ m$ between the two gratings, thus requiring no telescope.

The schematic representation of the stretcher and compressor is shown in $Fig.$ 4.38. The stretcher is composed of a grating working under off-axis incidence, a telescope with magnification of -1 composed of confocal convergent and divergent spherical mirrors and a second grating. The total transmission is evaluated at about 30%. The distances and the angles depend on the wavelengths and the targeted stretch factor. Typically, for achieving $200\ ps$ pulse with a spectral bandwidth of $7\times10^{-3}\ nm$, the distance between gratings is about $5\ m$. The telescope makes an inverted image of the first grating at $5\ m$ on the back of the second grating. The compressor is similar to the stretcher but keeping only the gratings. Their separation equals the distance last grating-image in the stretcher. Note that the beam will be about $2\ mm$ in diameter meaning that between gratings a small tube will be used.

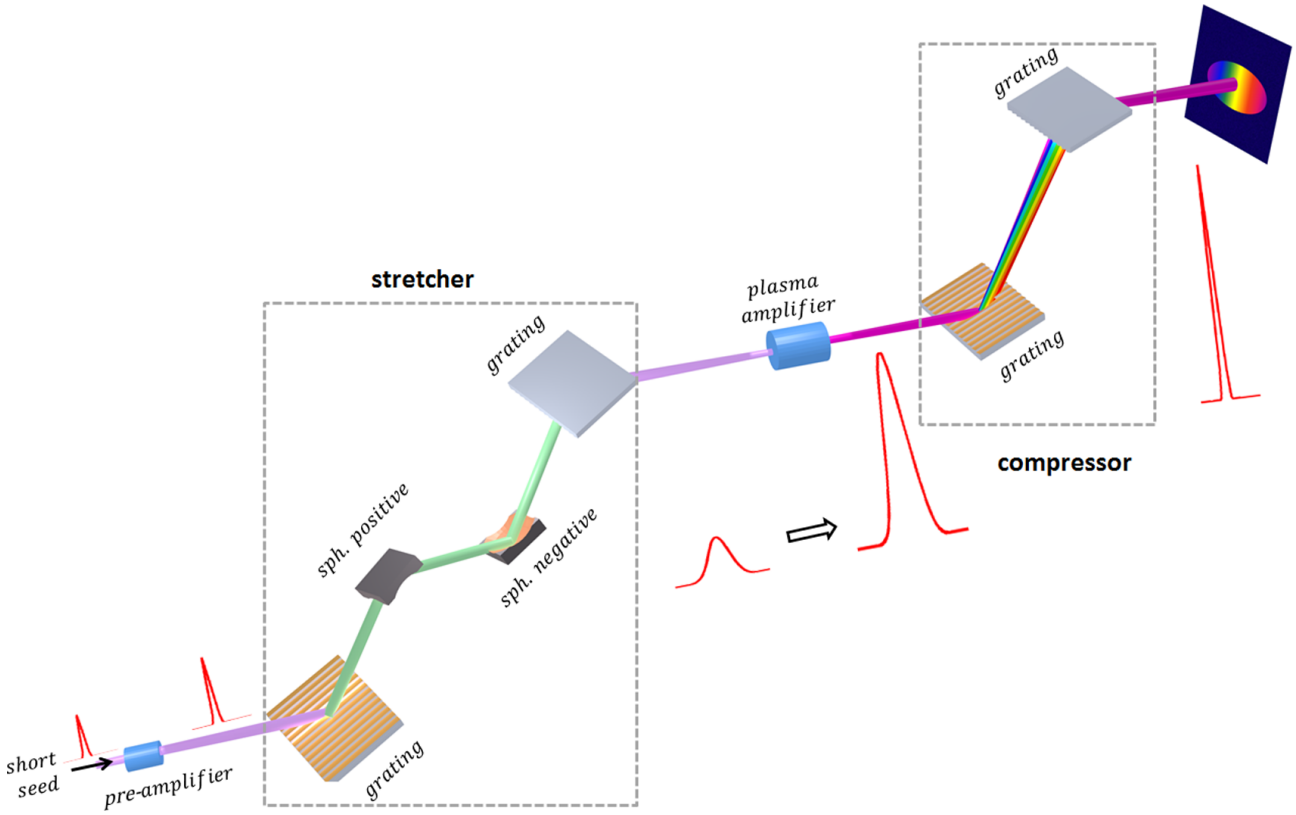

Figure 4.38: Full design of soft x-ray CPA system including the x-ray stretcher and comperessor.

We calculated the geometry of the stretcher and compressor using the classical group velocity dispersion equation:

$$\frac{d^2\phi}{d\omega^2} = \frac{n\lambda^3 Z}{\pi c^2 d^2 cos^3\theta'}, \tag{4.31}$$

and the stretched duration with:

$$\tau = \frac{2}{\tau_0}\frac{d^2\phi}{d\omega^2}, \tag{4.32}$$

where τ_0 is the Fourier-limited incoming pulse duration.

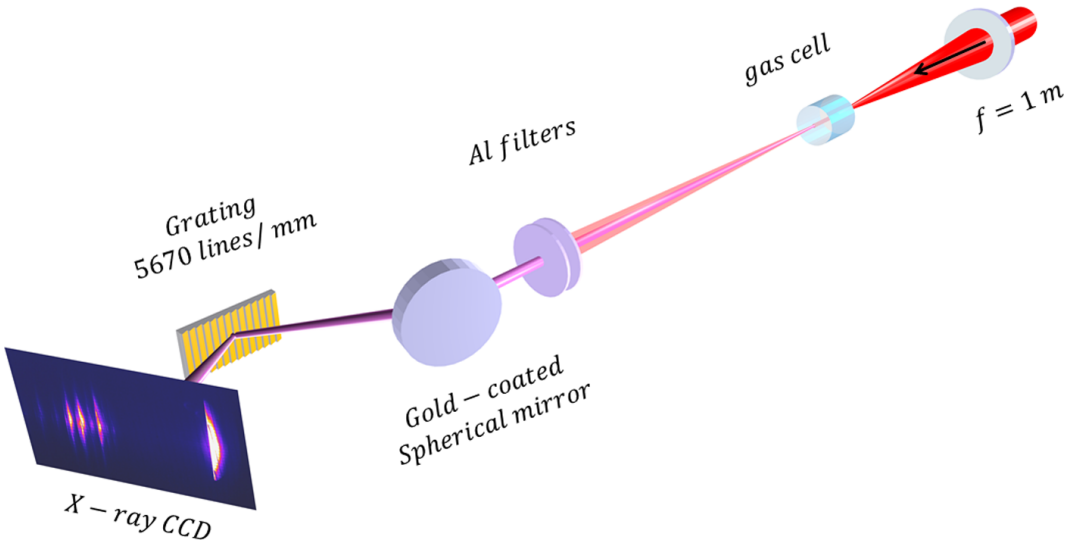

Figure 4.39: Diffraction grating test in classical geometry using HH beam from argon gas cell.

In order to stretch $21.2\ nm$ high harmonic from $200\ fs$ to $200\ ps$, we consider $1000\ lines/mm$ grating with $\phi = 7°$, $\theta = 55.34°$ and $\theta' = -87.72°$. These values are given for central wavelength. Since SXRL bandwidth is much smaller than HH seed, we calculated the stretcher parameters so as to attain $200\ ps$ with narrowest spectrum ($7\times10^{-3}\ nm$). With a distance of $5\ m$ between compressor gratings, the second grating will have an active area of $1\times480\ mm^2$.

As a preliminary test of the conical diffraction, we conducted a grating test experiment at LOA with the HH beam in Salle Orange. Firstly, the classical diffraction grating mounting was performed, as it is schematically showing in *Fig.* 4.39. HH beam was generated by focusing $5\ mJ$, $60\ fs$, $810\ nm$ IR laser into a $15\ mm$ long argon gas cell using a lens $f = 1\ m$. HH driven laser (IR beam) was stopped by the two aluminum filters ($464\ nm$ and $300\ nm$). A gold-coated spherical mirror with $f = 2\ m$ was used to deliver the HH beam to the gold-coated grating, which is with $5760\ lines/mm$. The diffracted HH beam was then detected on the x-ray CCD as it displayed in the detection plane. Within the classical diffraction approach, incident beam was perpendicular to the grooves on the grating. A translating stage was set for the grating, so that the grazing incident angle γ can be varied.

The diffraction patterns of the HH beam from the classical scheme are shown in *Fig.* 4.40. A variety of grazing incident angles were performed: (a) $13.5°$, (b) $20°$, (c) $26.8°$, (d) $31.9°$ and (e) $40°$. The $+1$ order and -1 order are observed apart from the 0 order. Several high harmonics orders have been collected in the $+1$ and -1 diffraction order, as the wavelengths marked in the figure. Optimal grazing incident angles are between $25°$ to $40°$. The separation of the high harmonics orders in the $+1$ and -1 diffraction order are sensitive to the grazing incident angle γ. However, the maximum estimated diffraction efficiency is less than 5%.

Using the same HH beam, the conical diffraction mounting of the grating was sequentially carried out. As it illustrated in *Fig.* 4.41, the grating was set up with groove along the HH beam incident direction, as described in *Fig.* 4.36. In order to study the effect of azimuth angle θ in the conical diffraction configuration, the grazing incident angle (between the HH incidence and grating surface) was fixed at $26.5°$. A rotation stage was employed varying θ.

In the conical diffraction scheme, the diffraction patterns including $+1$, 0 and -1 order are displayed

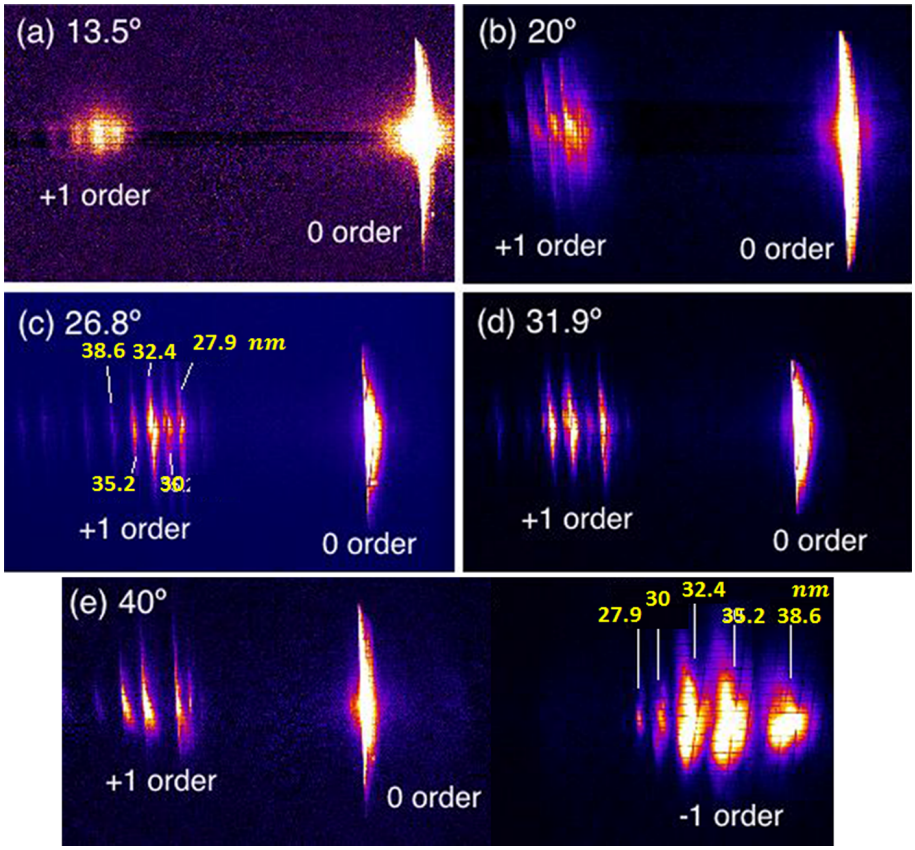

Figure 4.40: The diffracted patterns with different incident angles in the classical diffraction mounting.

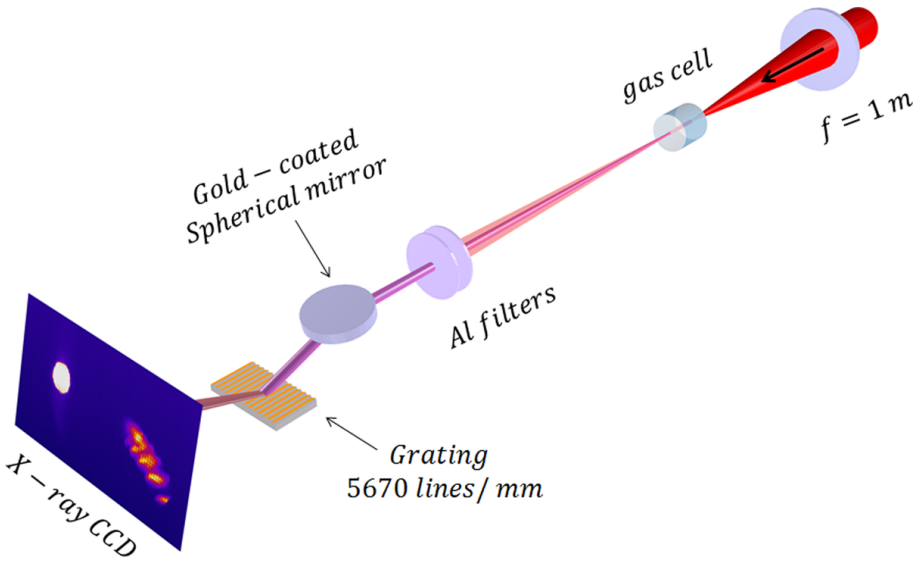

Figure 4.41: Conical diffraction mounting scheme of the blazed grating using HH beam from argon gas cell.

in $Fig.$ 4.42 as a function of incident azimuth angle θ. $\theta = 0^\circ$ corresponded to the incident plane is along the groove direction. Positive value of the angle is indicating a clockwise turning, and vice versa. Due to the experiment condition, one can only detect two diffraction order ($+1$ with 0 orders or -1 with 0 orders), as seen in $Fig.$ 4.41. In the sake of comparison, we combined three diffraction orders in a single image, as illustrated in $Fig.$ 4.42 where the positions of the diffraction patterns have been calibrated. An interesting observation is that the vertical and horizontal separation between the 0 and the other two orders is changing as a function of the azimuth angle θ. At $\theta = -3^\circ$, most part of the $+1$ order diffraction pattern is beyond detection region, while it was full recorded at $\theta = 3^\circ$. However, the full diffraction pattern of -1 order was detected at $\theta = -3^\circ$, and at $\theta = 3^\circ$ it is clipped. Another interesting point is the high harmonics orders at both $+1$ and -1 diffraction order are separated apparently. Further study and efficiency measurement under the conical will be considered in the upcoming experiments. The full calculation, design and experiments on grating-pair SXRL stretcher and compressor would be emerged in the thesis of H. Dacasa.

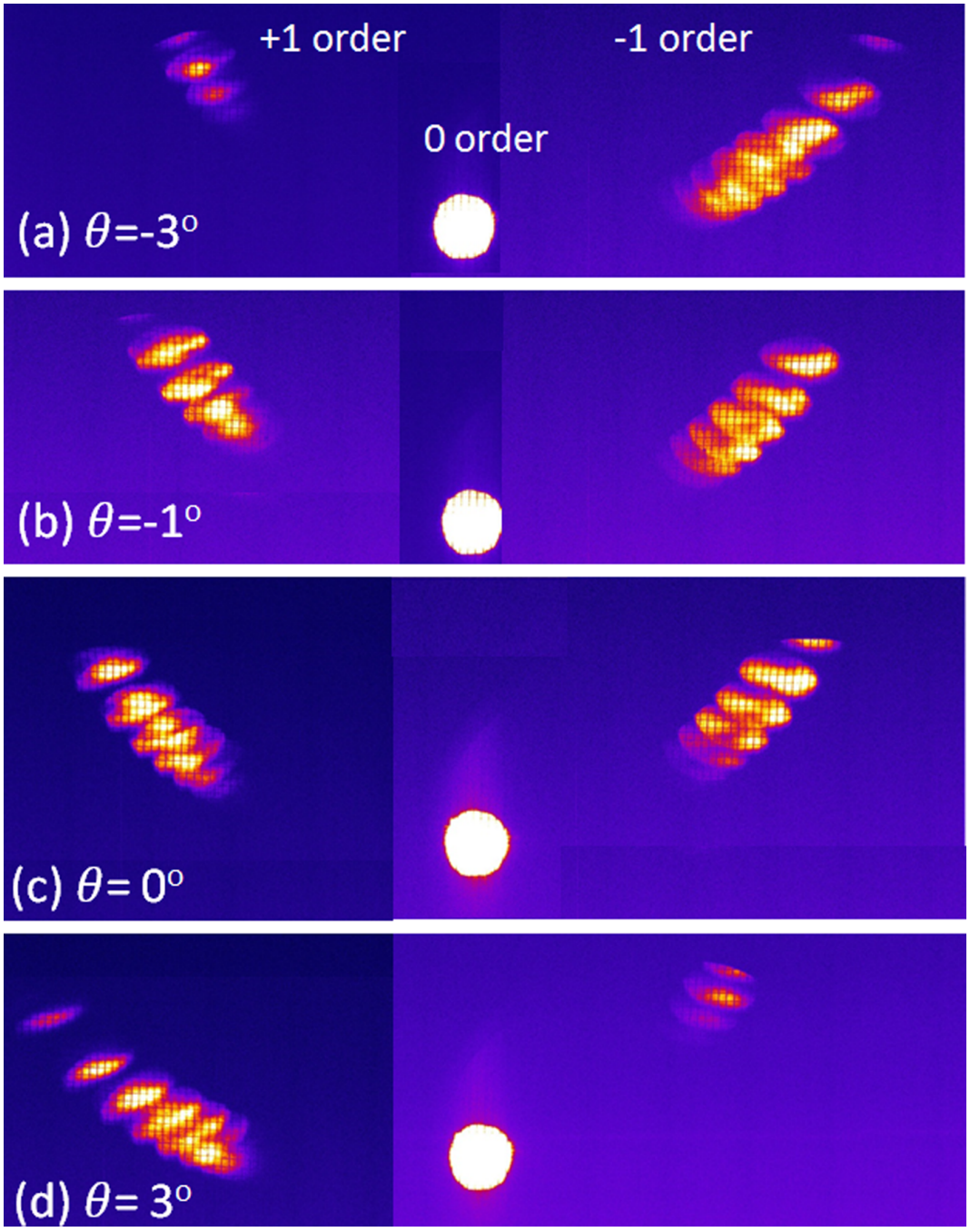

Figure 4.42: HH diffraction patterns from conical mounting with various azimuth angles θ. the "+1", "0" and "-1" order are all displayed.

4.8 Summary

In summary, previous work on 2D Hydrodynamic and 1D time-dependent Maxwell-Bloch modellings on HH-seeded SXRL were firstly mentioned in **Section 4.1-4.3**. Substantial enhancements was obtained in single- and multi-stage plasma amplification schemes. An experiment with double-plasma and wider amplifiers was carried out with some evidence of amplification enhancement. Besides the effort on enlarging plasma cross sectional area, investigation of enlarging time to extract more stored energy in the plasma was performed in **Section 4.4**. As the first time, we successfully explained that the poor seeding efficiency according to Ditmire's experiment [19] is due to the rapid depletion of population inversion. And a fast population inversion recovery behaviour was predicted. Based on this context, in **Section 4.5**, we proposed a soft x-ray CPA scheme. The stretched seed pulse can take the advantage of fast gain recovery after the rapid depletion during the seeding. Further strategy of shortening the pulse duration from x-ray CPA system was discussed in **Section 4.6**. Final output coherent SXRL from the proposed x-ray CPA system could reach several milli-Joule within $150\ fs$. There are two crucial issues in this proposal. One is the x-ray grating efficiency for the stretcher and compressor. Some preliminary results with conical diffraction geometry were demonstrated in **Section 4.7**. The continue work is undergoing and will be done during the thesis of my colleague H. Dacassa. Another important issue is the gain recovery time, the experiment evidence is mandatory to bolster up the x-ray CPA proposal. We therefore conducted a x-ray probe/x-ray pump experiment to diagnostic the gain dynamics of the x-ray plasma amplifier, resolution of $250\ fs$ has been achieved. The detailed experiment is discussed in **Chapter 5**.

Bibliography

[1] D. A. G. Deacon, L. R. Elias, J. M. J. Madey, G. J. Ramian, H. A. Schwettman and T. I. Smith, Phys. Rev. Lett. **38**,892–894 (1977).

[2] S. Jamison, Nat. Photonics **4**,589(2010).

[3] E. Allaria, D. Castronovo, P. Cinquegrana, P. Craievich, M. Dal Forno, M. B. Danailov, G. D'Auria, A. Demidovich, G. De Ninno, S. Di Mitri, B. Diviacco, W. M. Fawley, M. Ferianis, E. Ferrari, L. Froehlich, G. Gaio, D. Gauthier, L. Giannessi, R. Ivanov, B. Mahieu, N. Mahne, I. Nikolov, F. Parmigiani, G. Penco, L. Raimondi, C. Scafuri, C. Serpico, P. Sigalotti, S. Spampinati, C. Spezzani, M. Svandrlik, C. Svetina, M. Trovo, M. Veronese, D. Zangrando and M. Zangrando, Nature Photonics **7**,913 (2013).

[4] D. L. Matthews, P. L. Hagelstein, M. D. Rosen, M. J. Eckart, N. M. Ceglio, A. U. Hazi, H. Medecki, B. J. MacGowan, J. E. Trebes, B. L. Whitten, E. M. Campbell, C. W. Hatcher, A. M. Hawryluk, R. L. Kauffman, L. D. Pleasance, G. Rambach, J. H. Scofield, G. Stone, and T. A. Weaver, Phys. Rev. Lett. **54**,110 (1985).

[5] S. Suckewer, C. H. Skinner, H. Milchberg, C. Keane, and D. Voorhees, Phys. Rev. Lett. **55**, 1753 (1985).

[6] J. Zhang, P. J. Warwick, E. Wolfrum, M. H. Key, C. Danson, A. Demir, S. Healy, D. H. Kalantar, N. S. Kim, C. L. S. Lewis, J. Lin, A. G. MacPhee, D. Neely, J. Nilsen, G. J. Pert, R. Smith, G. J. Tallents, and J. S. Wark, Phys. Rev. A **54**, R4653(1996).

[7] D. Zimmer, B. Zielbauer, V. Bagnoud, U. Eisenbarth, D. Javorkova and T. Kuehl, Optics Exp. **16**, 10398-10403 (2008).

[8] A. L'Huillier, K. J. Schafer and K. C. Kulander, J. Phys. B: At. Mol. Opt. Phys. **24**, 3315-3341 (1991).

[9] B. Dromey, M. Zepf, A. Gopal, K. Lancaster, M. S. Wei, K. Krushelnick, M. Tatarakis, N. Vakakis, S. Moustaizis, R. Kodama, M. Tampo, C. Stoeckl, R. Clarke, H. Habara, D. Neely, S. Karsch and P. Norreys, Nature Physics **2**, 456-459 (2006).

[10] J. J. Rocca, V. Shlyaptsev, F.G. Tomasel, O. D. Cortazar, D. Hartshorn, and J. L. A. Chilla, Phy. Rev. Lett. **73**, 2192 (1994).

[11] M. Benk, K. Bergmann, D. Schäfer, and T. Wilhein, Opt. Lett. **33**, 2359 (2008).

[12] P. Zeitoun, G. Faivre, S. Sebban, T. Mocek, A. Hallou, M. Fajardo, D. Aubert, P. Balcou, F. Burgy, D. Douillet, S. Kazamias, G. De Lacheze-Murel, T. Lefrou, S. Le Pape, P. Mercere, H. Merdji, A. S. Morlens, J. P. Rousseau, and C. Valentin, Nature **431**, 426 (2004).

[13] Y. Wang, E. Granados, F. Pedaci, D. Alessi, B. Luther, M. Berrill, and J. J. Rocca, Nat. Photonics **2**, 94 (2008).

[14] A. Morlens, J. Gautier, G. Rey, Ph. Zeitoun, J. Caumes, M. Kos-Rosset, H. Merdji, S. Kazamias, K. Cassou and M. Fajardo, Optics Lett. **31**, 3095 (2006).

[15] A. Ravasio, D. Gauthier, F. R. N. C. Maia, M. Billon, J-P. Caumes, D. Garzella, M. Géléoc, O. Gobert, J-F. Hergott, A-M. Pena, H. Perez, B. Carré, E. Bourhis, J. Gierak, A. Madouri, D. Mailly, B. Schiedt, M. Fajardo, J. Gautier, P. Zeitoun, P. H. Bucksbaum, J. Hajdu and H. Merdji, Phys. Rev. Lett. **103**, 028104 (2009).

[16] B. Vodungbo, J. Gautier, G. Lambert, A. B. Sardinha, M. Lozano, S. Sebban, M. Ducousso, W. Boutu, K. Li, B. Tudu, M. Tortarolo, R. Hawaldar, R. Delaunay, V. López-Flores, J. Arabski, C. Boeglin, H. Merdji, Ph. Zeitoun and J. Lüning, Nature Communication **3**, 999(2012).

[17] C. D. Macchietto, B. R. Benware, and J. J. Rocca, Opt. Lett. **24**, 1115-1117 (1999).

[18] A. Ritucci, G. Tomassetti, A. Reale, F. Flora, and L. Mezi, Phys. Rev. A **70**, 023818(2004).

[19] T. Ditmire, M. H. R. Hutchinson, M. H. Key, C. L. S. Lewis, A. MacPhee, I. Mercer, D. Neely, M. D. Perry, R. A. Smith, J. S. Wark and M. Zepf, Phys. Rev. A **51**, R4337 (1995).

[20] Y. Wang, E. Granados, M. A. Larotonda, M. Berrill, B. M. Luther, D. Patel, C. S. Menoni, and J. J. Rocca, Phys. Rev. Lett. **97**, 123901 (2006).

[21] J. P. Goddet, S. Sebban, J. Gautier, P. Zeitoun, C. Valentin, F. Tissandier, T. Marchenko, G. Lambert, M. Ribieres, D. Douillet, T. Lefrou, G. Iaquaniello, F. Burgy, G. Maynard, B. Cros, B. Robillard, T. Mocek, J. Nejdl, M. Kozlova, and K. Jakubczak, Opt. Lett. **34**, 2438 (2009).

[22] L.Li, Y. Wang, S. Wang, E. Oliva, L. Yin, T. T. Thuy Le, S. Daboussi, D. Ros, G. Maynard, S. Sebban, B. Hu, J. J. Rocca, and Ph. Zeitoun, Optics Lett. **38**, 4011-4014 (2013).

[23] Y. Wang, M. Berrill, F. Pedaci, M. M. Shakya, S. Gilbertson, Zenghu Chang, E. Granados, B. M. Luther, M. A. Larotonda, and J. J. Rocca, Phys. Rev. A **79**, 023810 (2009).

[24] H. N. Chapman and K. A. Nugent, Nature Photonics **4**, 833-839 (2012).

[25] I. R. Al'miev, O. Larroche, D. Benredjem, J. Dubau, S. Kazamias, C. Moller, and A. Klisnick, Phys. Rev. Lett. **99**, 123902 (2007).

[26] O. Larroche, D. Ros, A. Klisnick, A. Sureau, C. Moller, and H. Guennou, Phys. Rev. A **62**, 043815 (2000).

[27] O. Larroche and A. Klisnick, Phys. Rev. A **88**, 033815 (2013).

[28] A. Klisnicka, L Menga, A Le Mareca and O Larrocheb, Proc. of SPIE, Vol. 8849, 88490L (2013).

[29] C. M. Kim, K. A. Janulewicz, H. Taek Kim, and J. Lee, Phys. Rev. A **80**, 053811 (2009).

[30] C. M. Kim, J. Lee and K. A. Janulewicz, Phys. Rev. Lett. **104**, 053901 (2010).

[31] B. Cros, T. Mocek, I. Bettaibi, G. Vieux, M. Farinet, J. Dubau, S. Sebban, and G. Maynard, Phys. Rev. A **73**, 033801 (2006).

[32] G. Maynard, F. Lambert, N. Andreev, B. Robillar, A. Boudaa, J. Clerouin, B. Cros, A. Lenglet, T. Mocek and S. Sebban, Contrib. Plasma Phys. **47**, 352-359 (2007).

[33] A. Boudaa,G. Maynard and B. Cros,*X-Ray Lasers 2012*, Springer Proceedings in Physics **147**, 45-48 (2012).

[34] Mark Berrill, David Alessi, Yong Wang, Scott R. Domingue, Dale H. Martz, Brad M. Luther, Yanwei Liu, and Jorge J. Rocca, Optics Lett. **35**, 2317-2319 (2010).

[35] S. Magnitskiy, N.Nagorskiy, A. Faenov, T. Pikuz, M. Tanaka, M. Ishino, M. Nishikino, Y. Fukuda, M. Kando, T. Kawachi and Y. Kato, Nature Communications **4**, 1936 (2013).

[36] E. Oliva, Ph. Zeitoun, S. Sebban, M. Fajardo, P. Velarde, K. Cassou, and D. Ros, Optics Lett. **34**, 2640-2642 (2009)

[37] E. Oliva, Ph. Zeitoun, P. Velarde, M. Fajardo, K. Cassou, D. Ros, S. Sebban, D. Portillo, and S. le Pape, Phys. Rev. E **82**, 056408 (2010).

[38] E. Oliva, Ph. Zeitoun, M. Fajardo, G.Lambert, D. Ros, S. Sebban, and P. Velarde. Phys. Rev. A **84**, 013811 (2011).

[39] D. S. Whittaker, M. Fajardo, Ph. Zeitoun, J. Gautier, E. Oliva, S. Sebban, and P. Velarde, Phys. Rev. A **81**, 04286 (2010).

[40] E. Oliva, M. Fajardo, L. Li, M. Pittman, T. T. T. Le, J. Gautier, G. Lambert, P. Velarde, D. Ros, S. Sebban, and P. Zeitoun, Nat. Photonics **6**, 764 (2012).

[41] E. Oliva, M. Fajardo, L. Li, S. Sebban, D. Ros and P. Zeitoun, Opt. Lett. **37**, 4341-4343 (2012).

[42] Ph. Zeitoun, E. Oliva, T. T. T. Le, D.Ros, S. Sebban, L. Li, P. Velarde and M. Fajardo, Applied Sciences **3**, 581-592 (2013).

[43] H. N. Chapman and K. A. Nugent, Nature Photonics **4**, 833-839 (2010).

[44] F. Ogando and P. Velarde, J. Quant. Spectrosc. Radiat. Transf. **71**, 541 (2001).

[45] P. Velarde, F. Ogando, S. Eliezer, J.M. Martinez-Val, J. M. Perlado and M. Murakami, Laser and Particle Beams **23**, 43-46 (2005).

[46] P. Velarde, D. García-Senz, E. Bravo, F. Ogando, A. Relaño, C. García and E. Oliva, Phys. of Plasmas **13**, 092901 (2006)

[47] K. Cassou, P. Zeitoun, P. Velarde, F. Roy, F. Ogando, M. Fajardo, G. Faivre, and D. Ros, Phys. Rev. A **74**, 045802 (2006).

[48] E. Oliva, *Mejora de un código hidrodinámico con transportr de radiación en malla adaptativa refinada (AMR) y su aplicación a los láseres de rayos X*, Universidad Politécnica de Madrid, 2010.

[49] P. Colella and H. M. Glaz, J. Comput. Phys. **59**, 264 (1985).

[50] R. E. Ewing, Multigrid Methods (SIAM, Philadelphis, 1987).

[51] S. Chandrasekhar, *Radiative Transfer* (Dover Publications, New York, 1960).

[52] K. D. Lathrop, Nucl. Sci. Eng. **24**, 381 (1966).

[53] R. M. More, K. H. Warren, D. A. Young, and G. B. Zimmerman, Phys. Fluids **31**, 3059 (1988).

[54] E. Minguez and R. Falquina, Laser Part. Beams **10**, 651 (1992).

[55] M. J. Berger and P. Colella, J. Comput. Phys. **82**, 64 (1989).

[56] C. A. Rendleman, V. E. Beckner, M. Lijewski, W. Crutchfield, and J. B. Bell, Comput. Visualization Sci. **3**, 147 (2000).

[57] C. for Computational Science and Engineering (unpublished).

[58] S. L. Pape and P. Zeitoun, Opt. Commun. **219**, 323 (2003).

[59] Y. Li and G. P. Preztler, Phys. Plasmas **4**, 164 (1997).

[60] B. L. Whitten, A. U. Hazi, M. H. Chen, and P. L. Hagelstein, Phys. Rev. A **33**, 2171 (1986).

[61] W. H. Goldstein, B. L. Whitten, A. U. Hazi, and M. H. Chen, Phys. Rev. A **36**, 3607 (1987).

[62] P. V. Nickles, V. N. Shlyaptsev, M. Kalachnikov, M. Schnurer, I. Will, and W. Sandner, Phys. Rev. Lett. **78**, 2748 (1997).

[63] T. Shirai, Y. Funatake, K. Mori, J. Sugar, W. L. Wiese, and Y. Nakai, J. Phys. Chem. Ref. Data **19**, 127 (1990).

[64] J. A. Koch, B. J. MacGowan, L. B. Da Silva, D. L. Matthews, J. H. Underwood, P. J. Batson, R. W. Lee, R. A. London, and S. Mrowka, Phys. Rev. A **50**, 1877 (1994).

[65] H. V. Regemorter, Astrophys. J. **136**, 906 (1962).

[66] P. Jaegle, Coherent Sources of XUV Radiation, p.114-p.120, Springer (2006).

[67] R. A. London, Phys. Fluids **31**, 184 (1988).

[68] A. Sureau and P. B. Holden, Phys. Rev. A **52**, 3110(1995).

[69] T. Mocek, S. Sebban, G. Maynard, Ph. Zeitoun, G. Faivre, A. Hallou, M. Fajardo, S. Kazamias, B. Cros, D. Aubert, G. de Lacheze-Murel, J. P. Rousseau, and J. Dubau, Phys. Rev. Lett. **95**, 173902 (2005).

[70] A. Sakdinawat and D. Arrwood, Nature Photonics **4**, 840-848 (2010).

[71] A. E. Siegman, *Lasers*, University Science Books: Sausalito, CA, USA, 1986.

[72] L. M. Frantz and J. S. Nodvik, J. Appl. Phys. **34**, 2346 (1963).

[73] A. Calisti, S. Ferri, C. Mossé, B. Talin, A. Klisnick, L. Meng, D. Benredjem and O. Guilbaud, High Energy Density Physics **9**, 516-522 (2013).

[74] B. Ecker, E. Oliva, B. Aurand, D. C. Hochhaus, P. Neumayer, H. Zhao, B.Zielbauer, K. Cassou, S. Daboussi, O. Guilbaud, S. Kazamias, T. T. T. Le, D. Ros, P. Zeitoun, and T. Kuehl, Optics Express **20**, 25391-25399 (2012).

[75] M. Pascolini, S. Bonora, A. Giglia, N. Mahne, S. Nannarone and L. Poletto, Appl. Opt. **45**, 3253–3262 (2006).

[76] H. Daido, Rep. Prog. Phys. **65**, 1513-1576 (2002).

[77] W. Ackermann, G. Asova, V. Ayvazyan, A. Azima, N. Baboi, J. Bähr, V. Balandin, B. Beutner, A. Brandt, A. Bolzmann, R. Brinkmann, O. I. Brovko, M. Castellano, P. Castro, L. Catani, E. Chiadroni, S. Choroba, A. Cianchi, J. T. Costello, D. Cubaynes, J. Dardis, W. Decking, H. Delsim-Hashemi, A. Delserieys, G. Di Pirro, M. Dohlus, S. Düsterer, A. Eckhardt, H. T. Edwards, B. Faatz, J. Feldhaus, K. Flöttmann, J. Frisch, L. Fröhlich, T. Garvey, U. Gensch2, Ch. Gerth, M. Görler, N. Golubeva, H.-J. Grabosch, M. Grecki, O. Grimm, K. Hacker3, U. Hahn, J. H. Han, K. Honkavaara, T. Hott, M. Hüning, Y. Ivanisenko, E. Jaeschke, W. Jalmuzna, T. Jezynski, R. Kammering, V. Katalev, K. Kavanagh, E. T. Kennedy, S. Khodyachykh, K. Klose, V. Kocharyan, M. Körfer, M. Kollewe, W. Koprek, S. Korepanov, D. Kostin, M. Krassilnikov, G. Kube, M. Kuhlmann, C. L. S. Lewis, L. Lilje, T. Limberg, D. Lipka, F. Löh, H. Luna, M. Luong, M. Martins, M. Meyer, P. Michelato, V. Miltchev, W. D. Möller, L. Monaco, W. F. O. Müller, O. Napieralski, O. Napoly, P. Nicolosi, D. Nölle, T. Nuñez, A. Oppelt, C. Pagani, R. Paparella, N. Pchalek, J. Pedregosa-Gutierrez, B. Petersen, B. Petrosyan, G. Petrosyan, L. Petrosyan, J. Pflüger, E. Plönjes, L. Poletto, K. Pozniak, E. Prat, D. Proch, P. Pucyk, P. Radcliffe, H. Redlin, K. Rehlich, M. Richter, M. Roehrs, J. Roensch, R. Romaniuk, M. Ross, J. Rossbach, V. Rybnikov, M. Sachwitz, E. L. Saldin, W. Sandner, H. Schlarb, B. Schmidt, M. Schmitz, P. Schmüser, J. R. Schneider, E. A. Schneidmiller, S. Schnepp, S. Schreiber, M. Seidel, D. Sertore, A. V. Shabunov, C. Simon, S. Simrock, E. Sombrowski, A. A. Sorokin, P. Spanknebel, R. Spesyvtsev, L. Staykov, B. Steffen, F. Stephan, F. Stulle, H. Thom, K. Tiedtke, M. Tischer, S. Toleikis, R. Treusch, D. Trines, I. Tsakov, E. Vogel, T. Weiland, H. Weise, M. Wellhöfer, M. Wendt, I. Will, A. Winter, K. Wittenburg, W. Wurth, P. Yeates, M. V. Yurkov, I. Zagorodnov and K. Zapfe, Nature Photon. **1**, 336–342 (2007).

[78] B. W. J. McNeil and N. R. Thompson, Nature Photon. **4**, 814-821 (2010).

[79] P. B. Holden, S. B. Healy, M. T. M. Lightbody, G. J. Pert, J. A. Plowes, A. E. Kingston, E. Robertson, C. L. S. Lewis and D. Neely, J. Phys. B: At. Mol. Opt. Phys. **27**, 341–367 (1994).

[80] Y. Wang, S. Wang, E. Oliva, L. Li, M. Berril, L. Yin, J. Nejdl, B. M. Luther, C. Proux, T. T. T. Le,J. Dunn, D. Ros, Ph. Zeitoun and J. J. Rocca, Nature Photonics **8**, 381-384 (2014).

[81] T. Robinson, K. O'keeffe, M. Zepf, B. Dromey and S. M. Hooker, J. Opt. Soc. Am. B **27**, 763-772 (2010).

[82] D. Strickland and G. Mourou, , Opt. Comm. **56**, 219 (1985).

[83] P. M. Paul, E. S. Toma, P. Breger, G. Mullot, F. Augé, Ph. Balcou, H. G. Muller, and P. Agostini, Science **292**, 1689 (2001).

[84] B. Rus, T. Mocek, A. R. Präg, M. Kozlová, G. Jamelot, A. Carillon, D. Ros, D. Joyeux, and D. Phalippou, Phys. Rev. A **66**, 063806 (2002).

[85] F. Tissandier, S. Sebban, M. Ribi'ere, J. Gautier, Ph. Zeitoun, G. Lambert, A. Barszczak Sardinha, J.-Ph. Goddet, F. Burgy, T. Lefrou, C. Valentin, and A. Rousse, Phys. Rev. A **81**, 063833 (2010).

[86] G. J. Tallents, J. Phys. D: Appl. Phys. **36**, R259-R276 (2003).

CHAPTER 5

Dynamics of SXRL Solid-Plasma Amplifier

The main pursuit of working with x-ray plasma amplifier is to reach saturated amplification, which allows maximum energy extraction from the plasma. As described in $Eq.\ 2.10$ (see **Chapter 2**), saturation intensity of the x-ray plasma amplifier is corresponding to the recovery time of the population inversion between the lasing levels, so called gain recovery time τ_r. There is no experimental value of the gain recovery time in the past 40 years. Moreover, the gain recovery time of the x-ray plasma amplifier predicted by our Maxwell-Bloch modelling (described in Chapter 4) opened an attractive prospect of achieving fully coherent mJ-class SXRL with the seeding concept in table-top facility. These encouraged us to perform an experiment to measure this crucial parameter of the x-ray plasma amplifier $--$ gain recovery time. Experiment was carried out at Colorado State University in collaboration with Prof. Jorge J. Rocca's team [1].

5.1 Double-independent HH generations

The premier issue for the experiment of gain dynamics diagnostics is to generate two independent and controllable HH seed pulses. HH driven laser was from the femtosecond beam line described in Chapter 3, Section 3.4, $Fig.\ 3.28$. This $60\ fs$ IR laser ($810\ nm$) with beam diameter of $15\ mm$ was divided into two divisions using a beam splitter shown in $Fig.\ 5.1$. Equivalent pulse energy around $17\ mJ$ for both beams were obtained after this beam splitter. A time delay and energy adjustable Mach-Zehnder interferometer was sequentially employed. Delay line was set-up with the reflected beam from the first

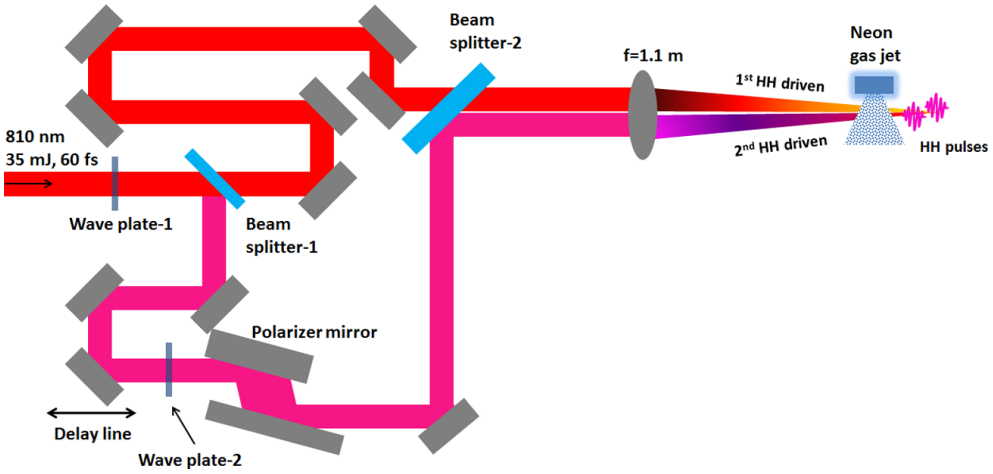

Figure 5.1: Mach-Zehnder interferometer sysytem for double HH-driven IR lasers. The time delay and energy controlling were set up in the refelected beam path from the first beam splitter.

beam splitter. And Brewster polarizer was adopted for energy adjustment. Two HH-driven beams were

separated by $\sim 6\ mm$ in vertical on the second beam splitter. Two temporally and spatially separated HH pulses were generated when focusing these two IR lasers into a single neon gas jet using a $f/44$ focal lens ($f = 1.1\ m$), as illustrated in $Fig.\ 5.2$. According to the vertical separation between two IR lasers before focusing, the estimated angle between the two focused beams is $5.5\ mrad$. The interacted neon gas was spurted from a gas puff with backing pressure ~ 1.5 bar. In the sake of avoiding interference between each other, the two focusing IR lasers were superimposed at $16\ mm$ after the gas centre, as it traced out in the close-up of $Fig.\ 5.2$. Separation between the two HH sources inside the gas puff was observed as $\sim 90\ \mu$m. With the Benefit of the Mach-Zehnder system, displayed in $Fig.\ 5.1$, time delay between the two HH pulses can be adjusted with a step of $250\ fs$.

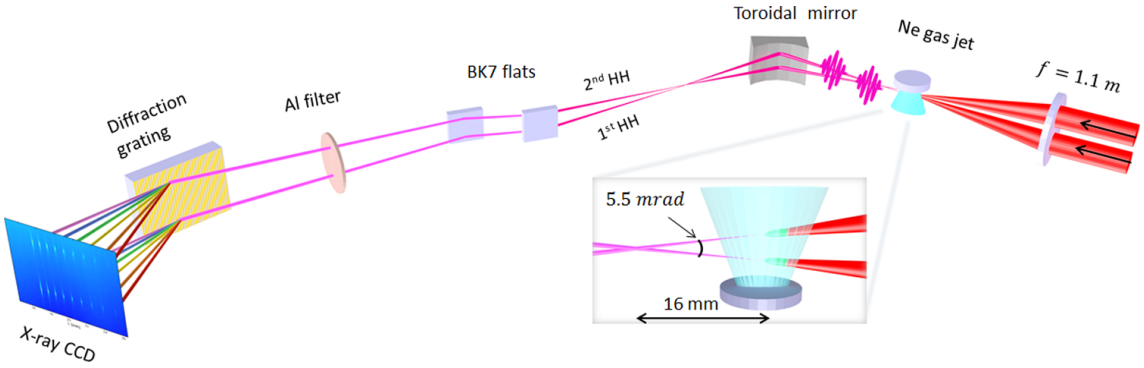

Figure 5.2: Experiment schematic of double HH beams generation with a single neon gas jet.

In order to minimize the refraction effect during the HH seeding into plasma amplifier (see discussion in Chapter 4, Section 4.3.3), a toroidal mirror with focal length of $0.25\ m$ was employed as relay-imaging optics. The overlapped point of the two HH pulse after the gas puff was then relay-imaged with a magnification of one onto the target chamber using a $9.65°$ grazing incident angle. Further details about the SXRL amplifier creation and the synchronization with two HH seed pulses will be discussed in the later section.

A pair of $BK7$ flat mirrors were adopted along the propagation of the two HH pulses with $9°$ grazing incident angle to stop most of the IR lasers. Further filtering was performed using a $300\ nm$ thick aluminium (Al) filter. As illustrated in $Fig.\ 5.3$, the cut-off edge of the transmission curve for this Al filter is at $17\ nm$. Blue line indicates the transmission of purified $300\ nm$ Al filter, and more than 60% over $17\ nm - 26.5\ nm$ is achieved. However, when taking into account the oxidization and coating effect, which induced a configuration of $290\ nm$ Al, $10\ nm\ Al_2O_3$ and $100\ nm$ Parylene-C (C_8H_7Cl), the transmission efficiency is down to below 30% ranging from $17\ nm$ to $26.5\ nm$.Spectrums of the two HH pulses were sequentially detected with a soft x-ray spectrometer comprises a variable-line-spacing diffraction grating (nominally $1200\ lines/mm$) and a x-ray CCD ($Andor\ DO436$). Distance between CCD and grating is $237\ nm$. Owing to the angle ($5.5\ mrad$) between the two HH-driven IR lasers after focusing (see $Fig.\ 5.2$), the two HH pulses were eventually separated in spatial on the CCD detection plane, thus allowing for their simultaneous detection.

Only the odd numbered high harmonics were observed due to the symmetrical reason [3, 4, 5], as marked in the spectral image ($Fig.\ 5.4(a)$). Horizontal coordinate is the lasing wavelength in nm and vertical axis corresponded to the spatial divergence in $mrad$. Two independent HH beams generated with a proper time delay ($6\ ps$ in this sample) are spatially separated on the CCD detection plane. The

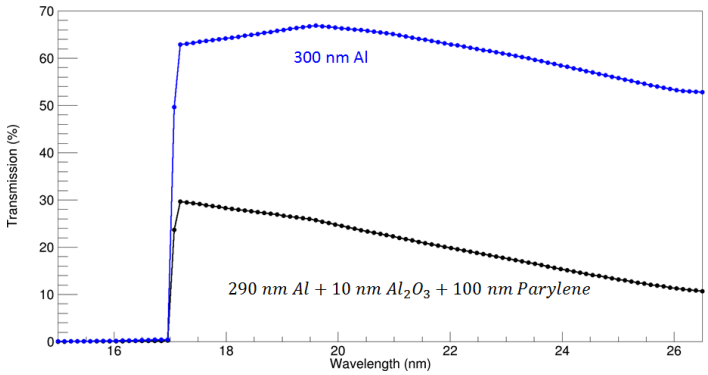

Figure 5.3: Al Filter transmission curve of the SXRL ranging from $15\ nm$ *to* $26.5\ nm$*. The upper blue curve indicates the transmission of* $300\ nm\ Al$ *filter and lower black curve corresponds to a complex Al filter composed of* $290\ nm\ Al$*,* $10\ nm\ Al_2O_3$ *and* $100\ nm\ Parylene - C\ (C_8H_7Cl)$*. data from [2]*

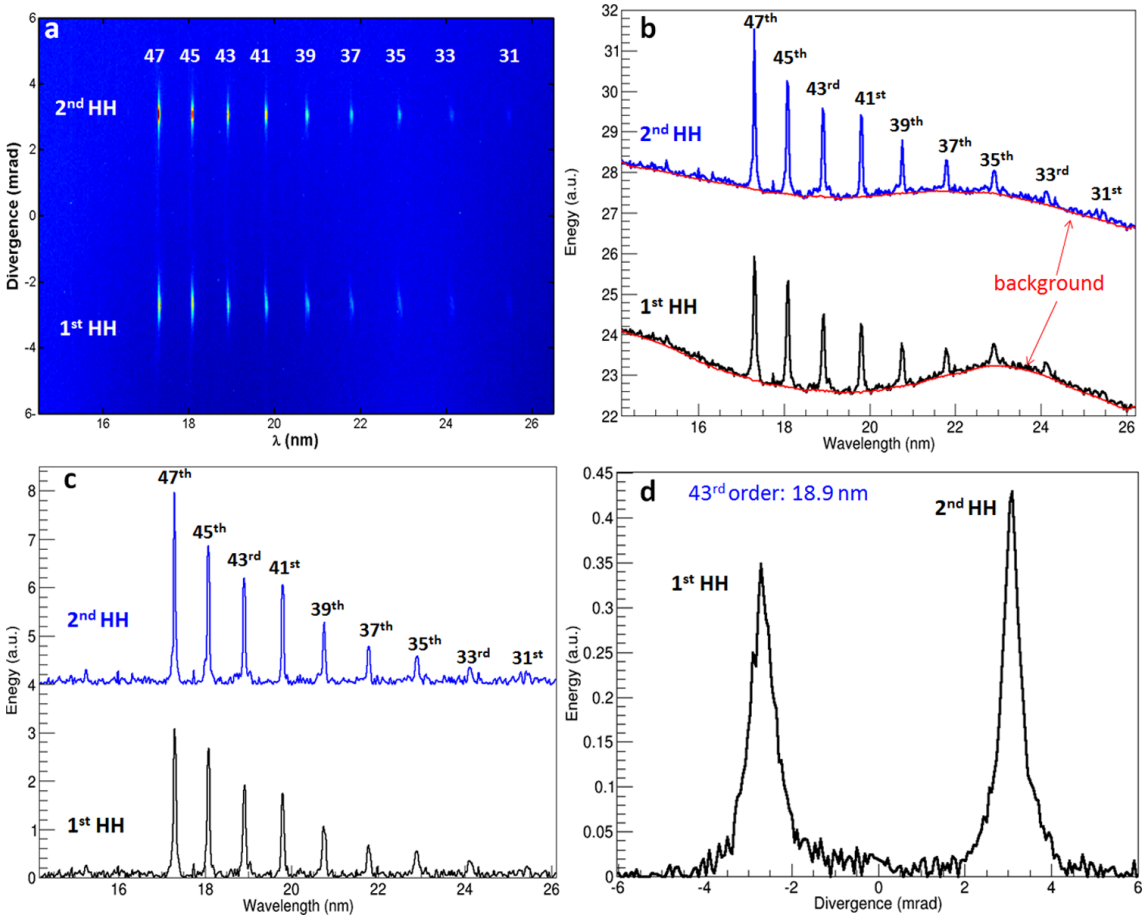

Figure 5.4: Comparison of double-HH pulses detected on x-ray CCD coupled with a diffraction grating. Time delay between the two pulses is $6\ ps$*. The* 2^{nd} *HH spectral line is offset in energy for ease of comparison. (a) Raw image of double-HH pulses, (b) integral spectral line-out of the double HH pulses, (c) line-out without background of double-HH spectrums, (d) spatial integral line-out of the* 43^{rd} *order* $(18.9\ nm)$ *for both HH pulses.*

lower beam is the 1^{st} generated HH, so called HH-pump, and the upper beam is the 2^{nd} HH which is used as HH-probe during the gain dynamics diagnostics in following Sections. HH orders from the 31^{st} to the 47^{th} were observed in this detection with respect of the $810\ nm$ driven lasers. Integral line-out of both spectra including full beam information are plotted in $Fig.\ 5.4(b)$. Vertical axis is corresponding to the line energy with arbitrary units (a.u.). The 2^{nd} HH spectral line-out is offset in energy for ease of comparison. Red fitting lines are indicating the general background,which might be caused by dark current noise of CCD and the scattering lights in the vacuum chamber. It is therefore removed out in the sequential data processing, as it shown in $Fig.\ 5.4(c)$. Due to population inversion mechanism of the molybdenum-plasma amplifier (see **Chapter 2, Section 2.6.1**), which will be used in the upcoming seeding experiments, only the 43^{rd} harmonics $(18.9\ nm)$ can be amplified after seeding. We therefore plotted the most interested line for both HH beams as a function of divergence in $Fig.\ 5.4(d)$. Divergence of the two HH beams are observed as less than $1\ mrad$.

To calibrate the HH beam energy, several compensation factors have to be taken into account. The photo-electron pair curve and the quantum efficiency over broad energy range of the $Andor\ DO436$ x-ray CCD used in this experiment are represented in $Fig.\ 5.5(a)$ and $Fig.\ 5.5(b)$, respectively. The diffraction efficiency of the grating is considered as $\sim 10\%$ and the reflection rate of the $BK-7$ flats within 9° grazing incident angle is estimated as 75% for wavelength at $18.9\ nm$. Finally, coupled

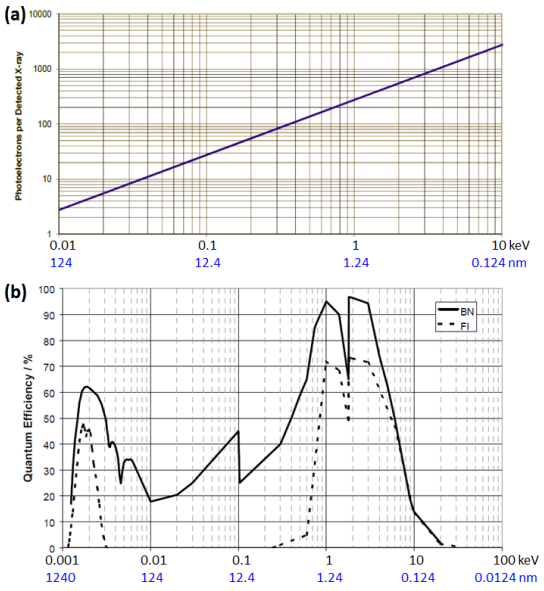

Figure 5.5: Andor DO436 x-ray CCD photo-electron pair (a) and quantum efficiency (b) over broad energy range. from [6]

with the contribution of the Al filter described in $Fig.\ 5.3$, one could calibrate the energy of the 43^{rd} harmonics $(18.9\ nm)$ by energy integration, as displayed in $Fig.\ 5.4(d)$, confirming $5.8\ pJ$ for the 1^{st} HH pulse and $6.2\ pJ$ for the 2^{nd} HH pulse, respectively. This is weaker comparing with the optimized HH using this beam line [7]. A main effect of this lower energy is considered that the laser-gas reaction region to generate HH is $16\ mm$ before the focal spot according to the experimental setup, which could substantially reduce the intensity of the HH-driven filed. For better understanding of this behaviour, a sketch of the two HH-driven beams focusing in the gas puff was art-worked in $Fig.\ 5.6$. Only 5% of

the peak intensity was achieved at the centre of the gas puff respected to the focal spot. Fortunately, the high energy of the HH seed pulse is not the essentially required in the gain dynamics diagnostics. Instead of that, independence of the two HH is the crucial point.

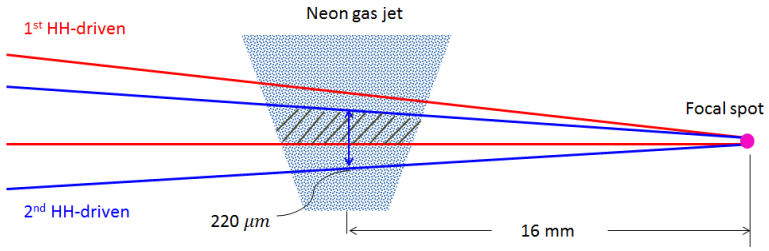

Figure 5.6: Geometrical sketch of the driven IR lasers for double-HH generation in the gas puff. Same beam parameters of both HH pulses were assumed. Estimated focusing beam size at the centre of the gas is $220\ \mu m$*, while the separation between each other is* $90\ \mu m$*.*

Therefore, in order to study the independence between the two HH beams, time evolution investigation of the HH pulses was carried out by varying the time delay between the two HH-driven IR lasers. The 1^{st} HH pulse was retained at constant time, while the 2^{nd} HH pulse was generated with a variety of time delays after it. Typical spectral image and its integral line-out of both HH beams for time delay from $0.25\ ps$ to $7\ ps$ were demonstrated in $Fig.\ 5.7$, where the 2^{nd} HH spectral line-out are offset in energy for ease of comparison. Throughout the $7\ ps$ time range, the 1^{st} HH beam remained the same characteristics. At delay of $0.25\ ps$, apparent bandwidth broadening was observed in the 2^{nd} HH pulse. From delay $0.5\ ps$ to $1\ ps$, the spectral profile was improving, only slight distortion can be observed. Fortunately, after $1\ ps$ time delay, the two HH signals became totally independent and stable.

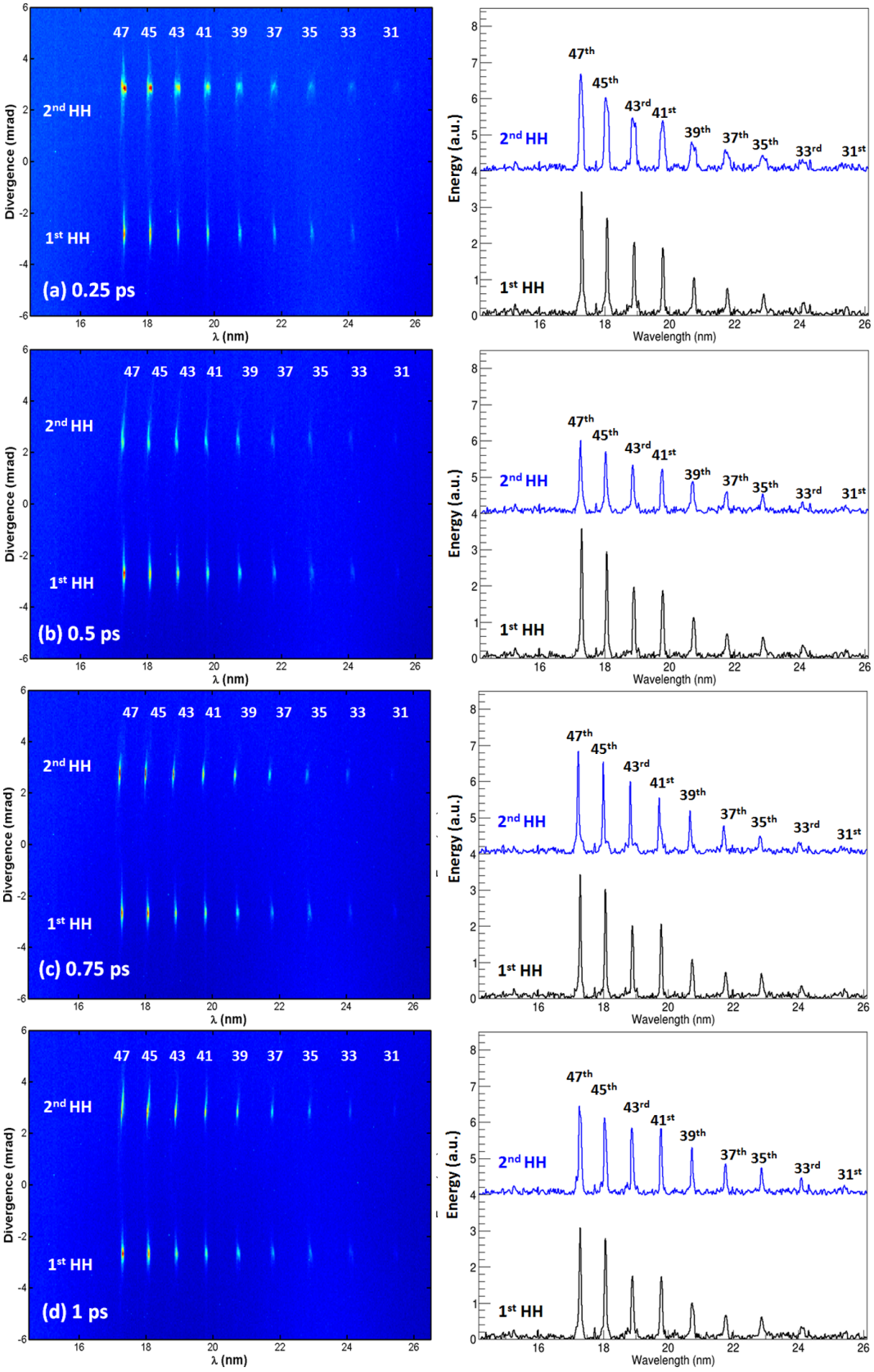
47 45 43 41 39 37 35 33 31
2nd HH
1st HH
(a) 0.25 ps
(b) 0.5 ps
(c) 0.75 ps
(d) 1 ps
Divergence (mrad)
λ (nm)
Energy (a.u.)
Wavelength (nm)
47th 45th 43rd 41st 39th 37th 35th 33rd 31st

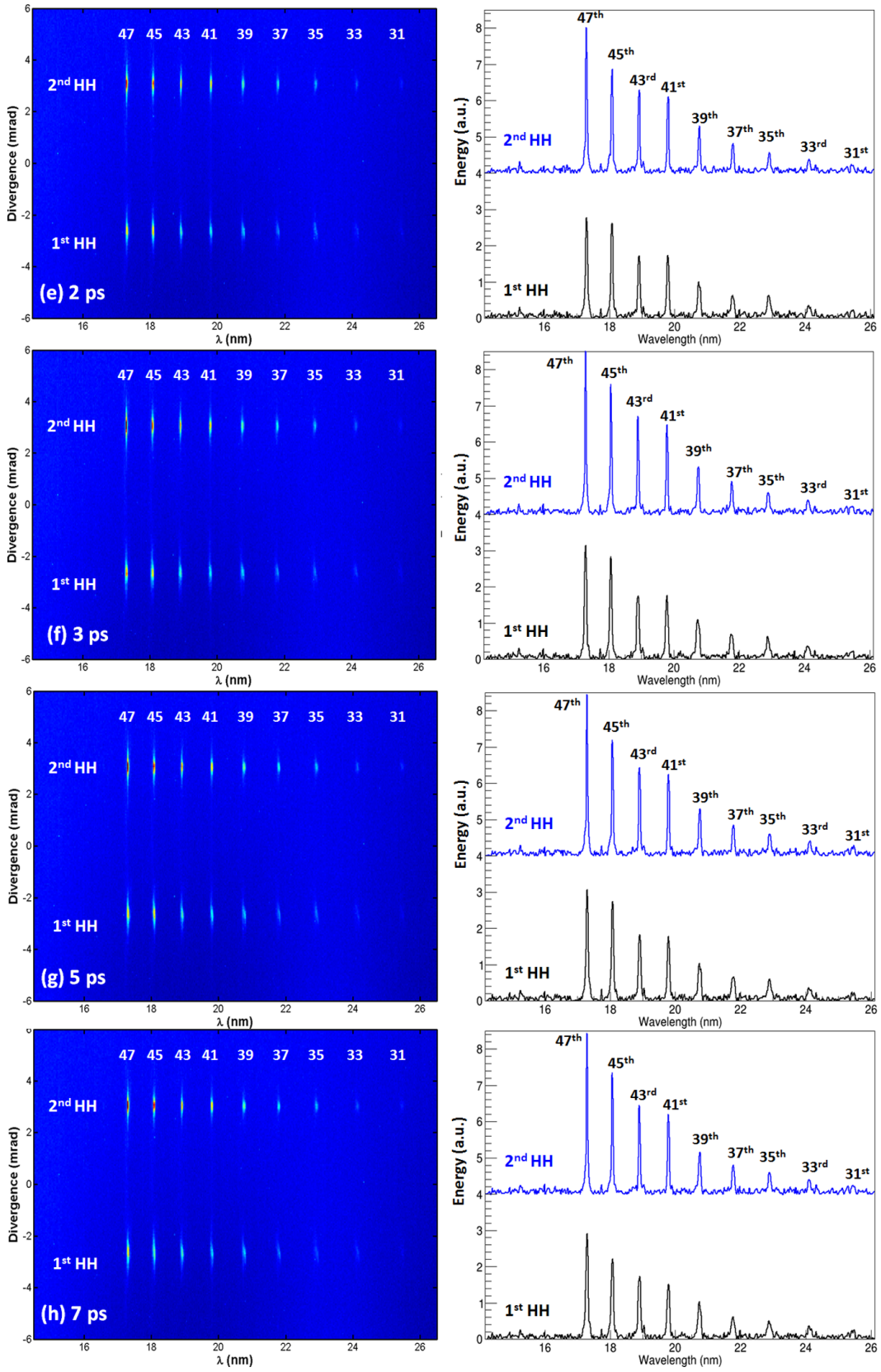

Figure 5.7: Raw image (left) and spectral line-out (right) of double HH pulses with a variety of time delays between each other: (a) 0.25 ps, (b) 0.5 ps, (c) 0.75 ps, (d) 1 ps, (e) 2 ps, (f) 3 ps, (g) 5 ps and (h) 7 ps. The 2^{nd} HH spectral line-out are offset in energy for ease of comparison.

More detailed study of the energy stability for both HH pulses are demonstrated in $Fig.\ 5.8$, where only the 43^{rd} order of HH was taken into account. Energy stability of the 1^{st} HH beam represented in black line is fixed in time. Blue line is indicating the 2^{nd} HH beam energy stability as a function of time delay respected to the 1^{st} HH generation. In the sake of comparison, the result of 1^{st} HH was divided into ten data groups, each group is corresponded to $20\ shots$ and related to the different times of the 2^{nd} HH generations because of the milli-second level time resolution during the CCD acquisition. All the error bars are corresponding to $20\ shots$. Average pulse energy of both-HH is about $6\ pJ$. There is small energy fluctuation of the 2^{nd} HH when time delay between the two HH is less than $1\ ps$, while the 1^{st} HH is as stable as expected. It is interesting to note the measured beam energy of the 2^{nd} HH pulse at $0.25\ ps$ time delay is beyond the average HH beam energy by $\sim 1\ pJ$. However, when one checks out the spectral profile displayed in $Fig.\ 5.7(a)$. Spectral broadening was obvious for the 2^{nd} HH pulse at this closing time delay ($0.25\ ps$). Due to the narrow lasing linewidth of the amplified seed, injecting this HH pulse into the plasma amplifier, the seeding efficiency would be depressed [8, 9]. According to the spectral shape, the effective seed energy of the 2^{nd} HH pulse at $0.25\ ps$ times delay is estimated as the similar value as at $0.5\ ps$ and $0.75\ ps$ time delays.

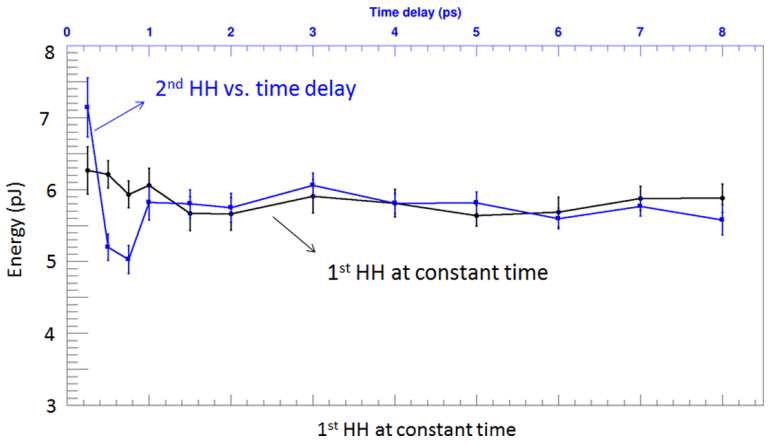

Figure 5.8: Pulse energy stability of the 1^{st} (black line) HH at constant time and the 2^{nd} (blue line) HH with time delay over $8\ ps$ respected to the constant time of 1^{st} HH. The error bars are corresponding to $20\ shots$. It is noted that only the 43^{rd} order of both HH was taken into account.

This energy fluctuation of the 2^{nd} HH pulse could be caused by the quantum path [10] effect during the generation. As illustrated in $Fig.\ 5.6$, separation of the two beams is $\sim 90\ \mu m$ at the gas centre where the focusing beam size is $\sim 220\ \mu m$. That caused a overlap in space between the two IR driven lasers, as depicted in the shade area. When time delay between the two driven lasers is small (such as $0.25\ ps$), the second HH generation is possible to be influenced by the ionization caused by the 1^{st} HH-driven laser around the overlap region (shade area). Consequently, atomic dispersion and electronic dispersion contributed to the quantum path will have to be taken into account [10, 11, 12]. Further understanding of this influence, a 2D hydrodynamic simulation of the gas-based double-HH generation is required. One should be noted that this energy fluctuation behaviour of the 2^{nd} HH pulse is sensitive to the experiment conditions. However, the energy fluctuation less than 10% of the 2^{nd} HH pulse when delay is less than $1\ ps$ is the common observation. In the upcoming gain dynamics diagnostics experiments in the following Sections, the double-HH pulses are studied separately in each case.

In general, the advantage of this double-HH generation technique is allowing to inject two convergent HH-seed into the exactly same region of plasma amplifier using an imaging optics. As comparison, it would be a challenge to meet this point by setting two separated focal spots in the gas as demonstrated recently [13]. It is interesting to note that the 2^{nd} HH seed pulse energy fluctuation less than 10% when time delay is less than 1 ps. Further improvements to generate two independent HH beams can be developed by using two separated gas cells/puffs or by employing a phase plate [14]. Nevertheless, both HH-pulse shot-to-shot energy stabilities in current approach are adequate to perform gain dynamics diagnostic of the x-ray plasma amplifier.

5.2 Gain dynamics of 3 mm plasma with 5 ps IR pump pulse

After the preparation of the double HH-seed beams, we conducted injection seeding experiment with coherent HH pulses. Collisionally excited SXRL amplifier operating in the $4d^1S_0 \rightarrow 4p^1P_1$ transition of Ni-like molybdenum at 18.9 nm was dedicated to this gain dynamics diagnostics. The GRIP scheme (see **Chapter 2, Section 2.6**) composed of two long pre-pulses (200 ps) and one short pump pulse (5 ps) was adopted to create the transient large population inversion x-ray plasma amplifier [15, 7, 16]. The plasma creation is similar to it performed in the seeded SXRL (SSXRL) wave front measurement experiment described in Chapter 3, Section 3.4. The two long pulses and the short pump pulse are from $\lambda = 810$ nm Ti:sapphire CPA laser system introduced in Chapter 3 ($Fig.$ 3.28). Early precursor pulse (30 mJ, 200 ps) and the pre-pulse (250 mJ, 200 ps), separated by 5 ns time delay, were irradiated with line-focusing on the molybdenum slab target surface by normal incident angle. A combination of spherical lens and cylindrical lens were adopted to make the line foci with 40 μm width [15], which allows to create a plasma approaching the Ni-like ionization stage. The expanding plasma was subsequently heated by a short pump pulse (500 mJ, 5 ps) arriving at 600 ps after the pre-pulse. A similar focusing line as pre-pulse obtained by the same approach was delivered to the plasma with grazing incident angle of 23°. By this rapid heating into the plasma region, electron density can achieve $\sim 2.6\times10^{20}$ cm^{-3} and electron

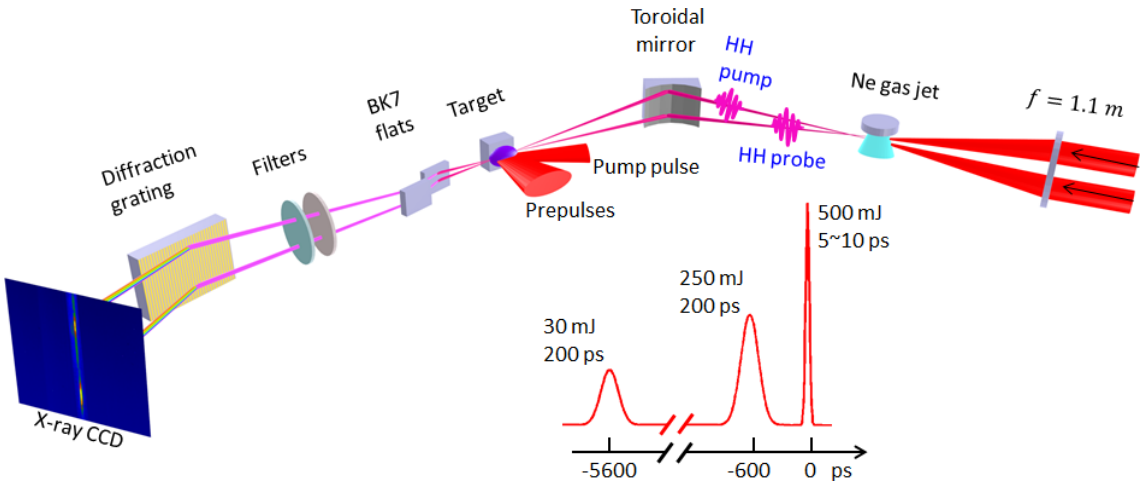

Figure 5.9: Experiment schematic of double HH seeded into plasma amplifier with a variety of delays to measure the gain recover time of x-ray plasma amplifier.

temperature could reach $\sim 500\ eV$ [20], where a large transient population inversion was formed.

In subsequent, as represented in $Fig.\ 5.9$, the two independently controllable HH-seed pulses, hereafter called HH pump (in the sense that it strongly perturbs the lasing ion excited level populations)) and HH probe (used to analyse the temporal evolution of the perturbed population), respectively, were overlapped at $16\ mm$ after the centre of gas puff as explained in Section 5.1. This overlap point was relay-imaged with a magnification of one into the middle of the plasma amplifier using a 9.65° grazing incidence toroidal mirror with $0.25\ m$ focal length. Time matching between the two HH-seed pulses and the short pump pulse was performed using a double-frequency crystal. The time at $T = 0\ ps$ was defined as the arrival time of the peak of the plasma heating IR short pump pulse. Moreover, a photograph showing the layout of target chamber in this experiment is illustrated in $Fig.\ 5.10$.

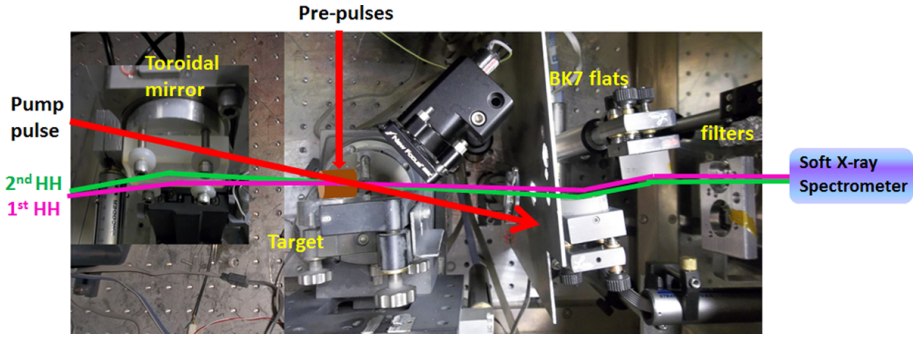

Figure 5.10: Photograph of the target chamber layout in the seeding experiment.

The diagnostic system is similar to it described in Section 5.1 ($Fig.\ 5.2$). An extra $200\ nm$ zirconium (Z_r) filter was added to avoid the CCD saturation due to the energy amplification. Analogously, oxidization and coating effect to the transmission of the filter was taken into account, as it shown in $Fig.\ 5.11(a)$. This Z_r filter was consider as a combination of $190\ nm\ Z_r$, $10\ nm\ Z_rO$ and $100\ nm\ Parylene - C$ (C_8H_7Cl). The transmission curve as a function of wavelength for the Z_r filter coupled with Al filter is plotted in $Fig.\ 5.11(b)$. With respect to the data processing of double-HH pulses in the previous section, this calculated transmission efficiency of the two filters is taken into account in the following energy calibration.

The main idea to diagnostic the gain dynamics of the x-ray plasma amplifier is that the 1^{st} HH seed to pump and the 2^{nd} HH seed to probe. $Fig.\ 5.12(a)$ shows the raw image of the detected double seeded SXRL (SSXRL) by x-ray CCD coupled with a diffraction grating. Time delay between the two seeding is $2\ ps$. Only a single wavelength at $18.9\ nm$ was observed due to x-ray plasma population inversion mechanism described in Chapter 2. Normally, ASE is the self-emission from the plasma amplifier with large divergence and incoherent in spatial. Owing to the diffraction grating coupled with x-ray CCD detection configuration, the full ASE information was collected by compressing into a narrow line in the spectral image, which is indicated in the bright line shape at $18.9\ nm$ in this figure. There are two bright spots at this specific wavelength, the left one is corresponding to the amplified 1^{st} HH-seed and the right one is the amplified 2^{nd} HH pulse. Due to the cross angle ($5.5\ mrad$) between the two HH-seed mentioned in Section 5.2, the two amplified seed beams are eventually separated in spatial on the detection plane.

Moreover, lifetime of ASE depended on the de-exciting process is considered as $\sim 10\ ps$, while the pulse duration of the SSXRL was measured as $\sim 1\ ps$ [17]. However, exposure time of the x-ray

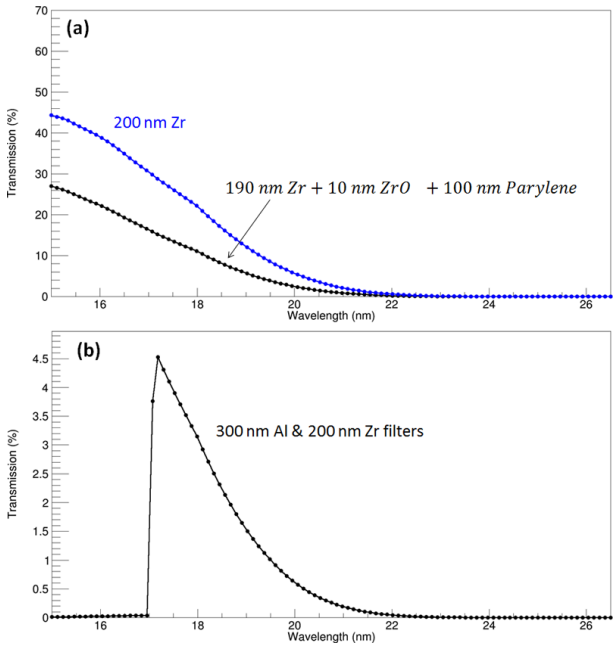

Figure 5.11: (a) Zr filter transmission curve of the SXRL range from 15 nm *to* 26.5 nm. *The upper blue curve indicated the transmission of* 200 nm *Zr filter and lower black curve corresponded to a complex Zr filter composed of* 190 nm Z_r, 10 nm ZrO *and* 100 nm $Parylene - C$ (C_8H_7Cl). *(b) Combinable* 300 nm *Al filter with* 200 nm Zr *filter transmission for the soft x-rays, the oxidation and* $Parylene - C$ *film were taken into account. data from [2]*

CCD ($\sim$100 ms) is much longer than all those lasing processing time. Therefore, the detected signal is composed of amplified seed and ASE. As the best of our knowledge, the device of the x-ray detection within picoseconds temporal resolution does not exist.

Integral line-out around 18.9 nm is displayed in $Fig.$ 5.12(b) as a function of spatial divergence, which consists of ASE, the 1^{st} SSXRL and the 2^{nd} SSXRL. The red fitting curve is implying ASE distribution which was known as large divergence and homogeneous in spatial due to the stochastic nature. One can assume the general shape of ASE is circular, the collected ASE spatially compressed by the spectrometer inducing more intensity contribution at the centre as the distribution shape illustrated in the red curve. Nevertheless, large divergence as $\sim$25 $mrad$ of the ASE signal was observed. In comparison, the divergence of fully coherent SSXRL beams were significantly improved to $\sim$1 $mrad$ at FWHM. In addition, the total energy of ASE is 5 times more than each SSXRL beam. For ease of understanding the data, ASE as the background signal was removed during the SSXRL data processing.

Seeding SXRL by injection of HH seed into plasma amplifier is dependent on the seed energy and stability. $Fig.$ 5.13 shows the energy stability of HH pump and HH probe as a function of time. HH pump (black line) was fixed at a constant time ($T = 3$ ps after the arrival of the peak of short pump pulse ($T = 0$ ps). The detected data was then divided into seven shot groups. Each shot-group is relative to the time step of the HH probe due to the milli seconds low time resolution during the CCD acquisition. HH probe (blue line) was injected into the plasma amplifier with a variety of time from $T = 3$ ps to $T = 8$ ps. The energy of HH pump ($\sim$3 pJ) is slightly weaker than the HH probe beam (($\sim$3.7 pJ).

In subsequent, the two independent HH pulses were used for gain dynamic diagnostics. HH pump was firstly sent to plasma amplifier at $T = 3$ ps after the arrival of the peak of short pump pulse

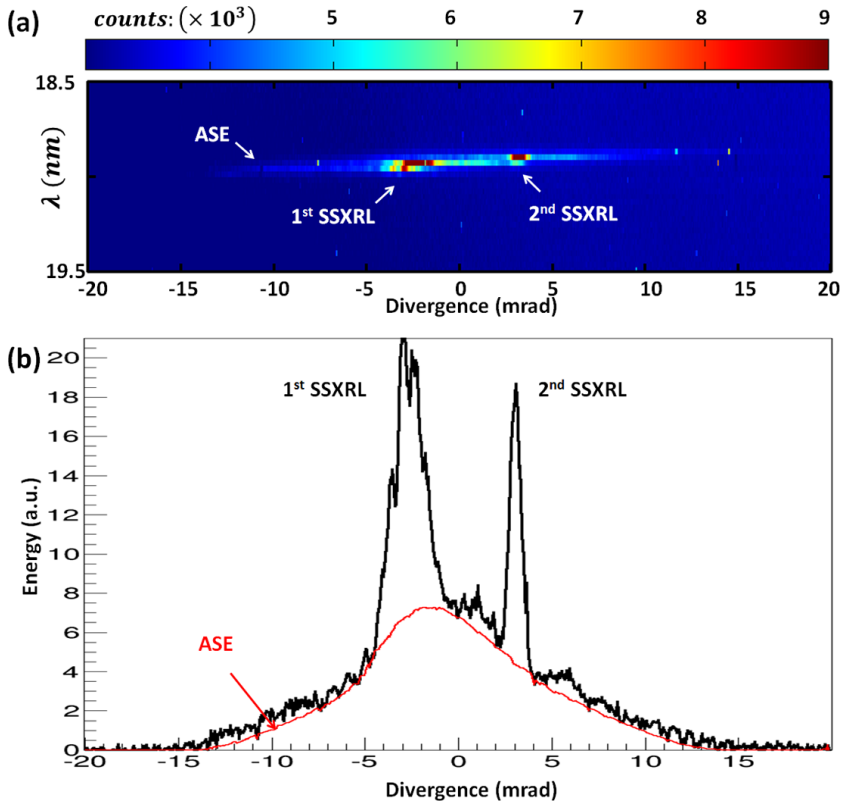

Figure 5.12: (a) Raw image of the detected double seeded SXRL, which consists of ASE signal, seeding at $T = 3$ ps (1^{st} $SSXRL$) and seeding at $T = 5$ ps (2^{nd} $SSXRL$). The bright line is the ASE background lasing from the plasma amplifier. $T = 0$ ps is corresponding to the arrival time of the peak of short pump IR laser. (b) Spatial integral line-out around 18.9 nm of the final output signal. Red fitting curve is indicating the ASE signal.

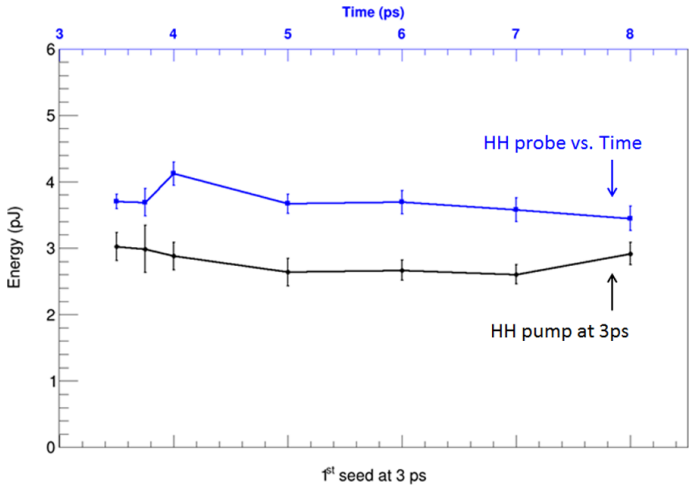

Figure 5.13: HH pump (balck line) energy stability with seeding at $T = 3$ ps and HH probe (blue line) seeded at varying time from $T = 3$ ps to $T = 8$ ps. $T = 0$ ps indicated the arrival time of the peak of short pump pulse. Error bars are corresponding 20 $shots$ of fluctuations.

($T = 0\ ps$). According to our prediction of the depletion of population inversion and its subsequent recovery behaviour [18], the HH probe beam was sequentially injected to the plasma with a variety of time delays. Typical images of the measured amplified HH probe and HH pump ranging from $T = 3\ ps$ to $T = 11\ ps$ are illustrated in $Fig.\ 5.14$. Left figures are the raw spectrum CCD images, and the right figures are the integral line-out around $18.9\ nm$ as a function of spatial divergence, in which the ASE background was removed out. $Fig.\ 5.14(a)$ shows the amplified HH probe without HH pump at $T = 3\ ps$. From $Fig.\ 5.14(b)$ to $Fig.\ 5.14(l)$, HH pump was seeded at $T = 3\ ps$ while HH probe was sent into the plasma at different time from $T = 3.25\ ps$ to $T = 11\ ps$. Slightly energy fluctuation of the 1^{st} SSXRL was observed, which could be caused by the HH seed stability (see $Fig.\ 5.13$), spatial matching between seed beam and gain zone and the evolution of plasma amplifier leading the complex refraction as mentioned in previous chapters. At $T = 3.25\ ps$ ($Fig.\ 5.14(b)$), the amplified 2^{nd} HH seed was extremely low closing to or below the detection limit. It is apparent that the time-dependent amplification of the 2^{nd} HH seed was increasing from $T = 3.5\ ps$ ($0.5\ ps$ after the first seeding) and reaching its maximum around $T = 5\ ps$, after that it was declined till $T = 11\ ps$. This rapid dropping ($T = 3\ ps\ to\ T = 3.25\ ps$), quick recovering ($T = 3.25\ ps\ to\ T = 5\ ps$) and gentle declining behaviour ($T = 5\ ps\ to\ T = 11\ ps$) of the amplified 2^{nd} HH seed is interesting in respect of our simulation results (see **Chapter 4, Section 4.4**).

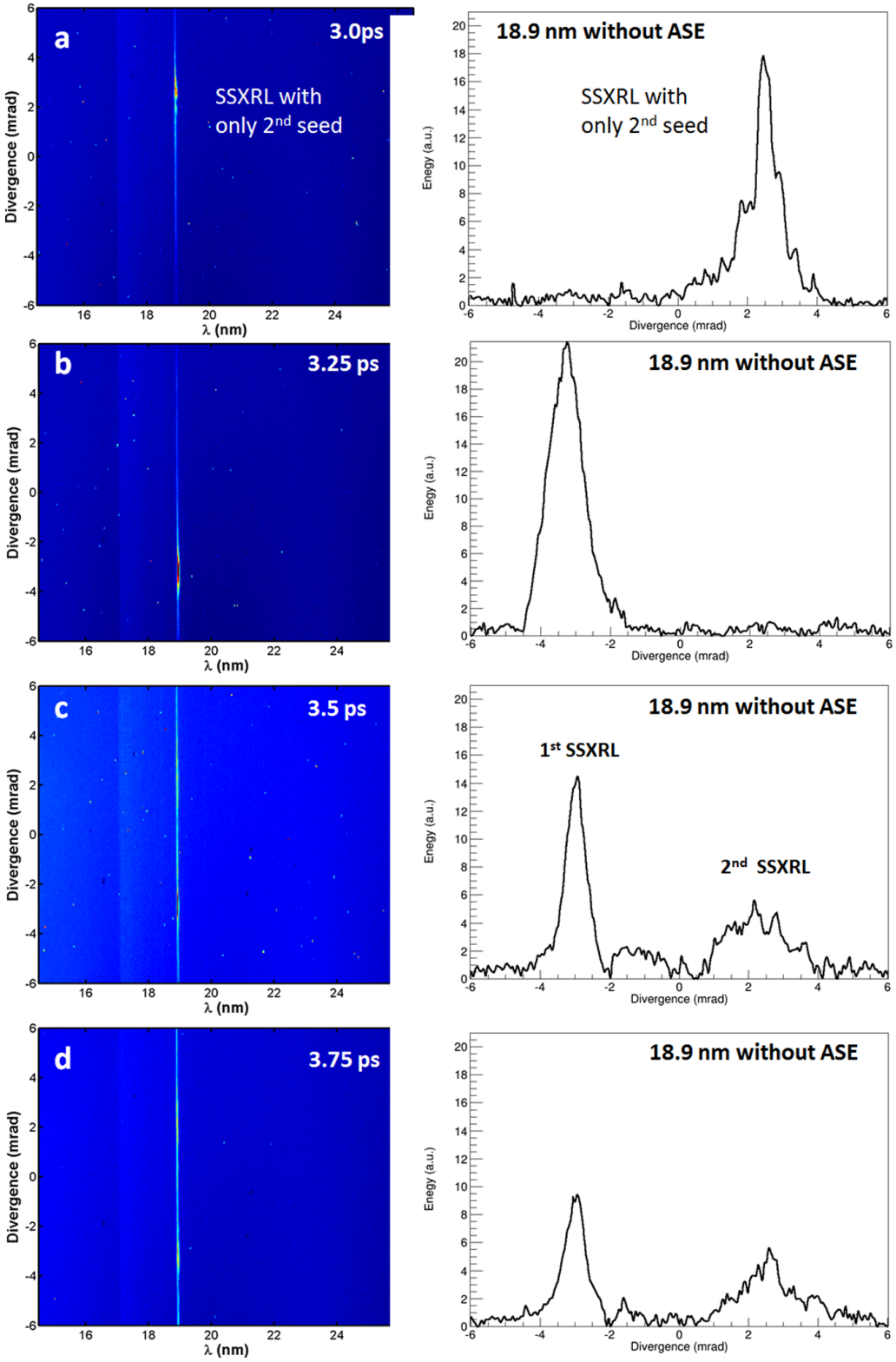
a
3.0ps
SSXRL with
only 2nd seed
Divergence (mrad)
λ (nm)
18.9 nm without ASE
SSXRL with
only 2nd seed
Enegy (a.u.)
Divergence (mrad)
b
3.25 ps
18.9 nm without ASE
c
3.5 ps
18.9 nm without ASE
1st SSXRL
2nd SSXRL
d
3.75 ps
18.9 nm without ASE

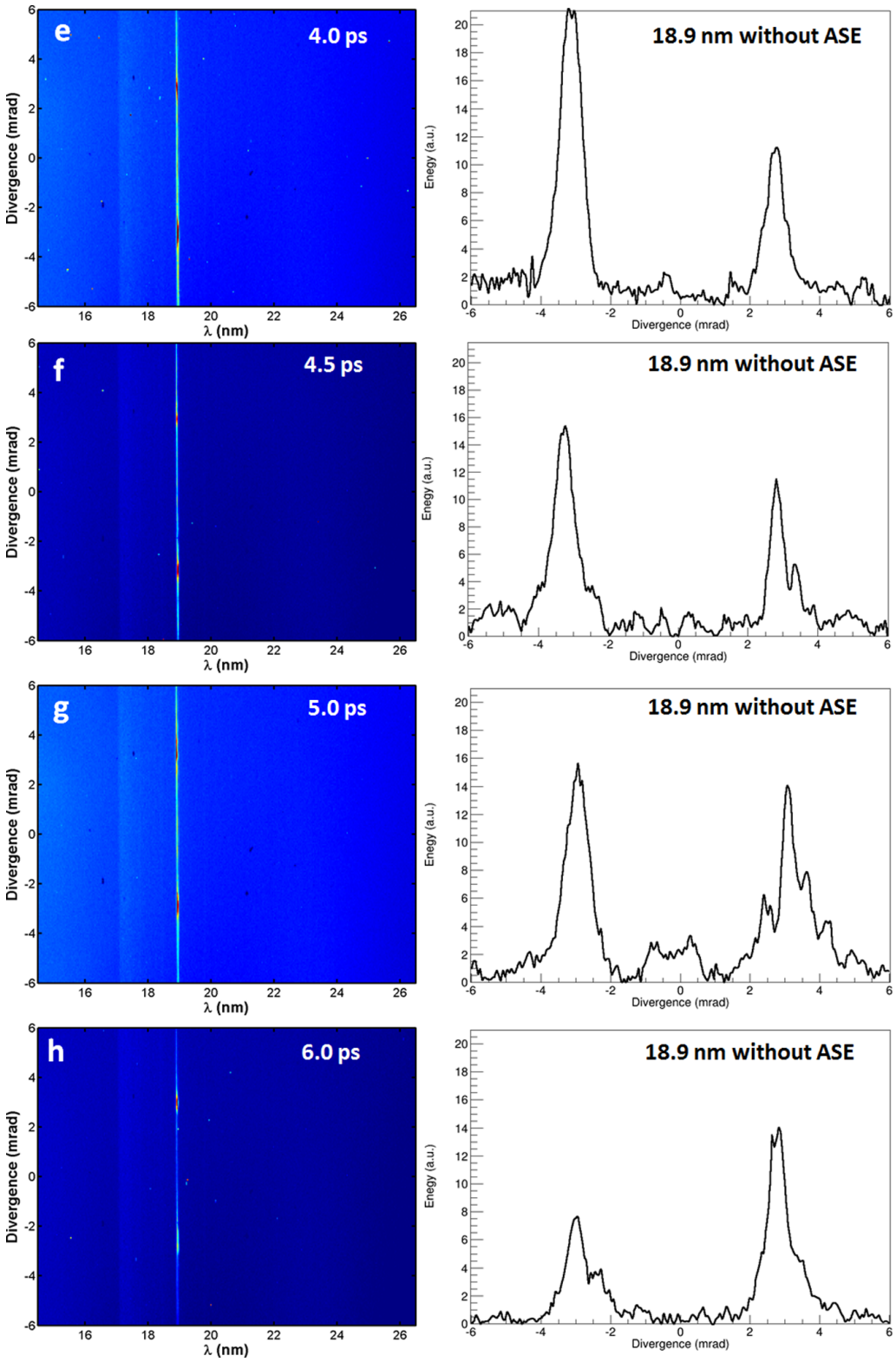
e
4.0 ps
18.9 nm without ASE
f
4.5 ps
18.9 nm without ASE
g
5.0 ps
18.9 nm without ASE
h
6.0 ps
18.9 nm without ASE
Divergence (mrad)
λ (nm)
Enegy (a.u.)
Divergence (mrad)

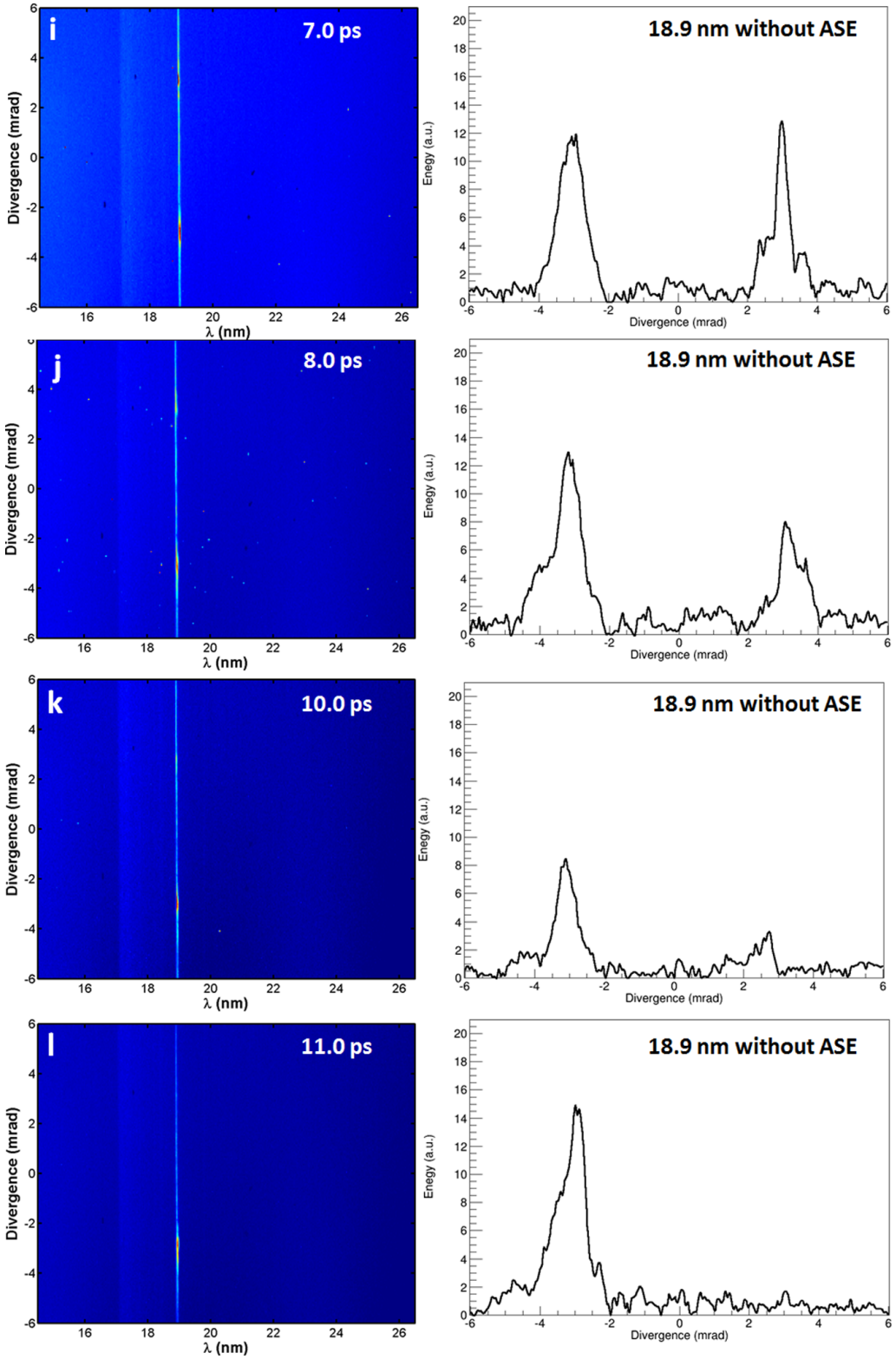

Figure 5.14: Samples of spectral image (left) and integral spatial line-out around $18.9\ nm$ *of the double seeded SXRL. The HH pump was seeded at* $T = 3\ ps$ *and the HH probe was injected to the plasma amplifier at series of time after the HH pump : (a)* $T = 3.25\ ps$*, (b)* $T = 3.5\ ps$*, (c)* $T = 3.75\ ps$*, (d)* $T = 4\ ps$*, (e)* $T = 4.5\ ps$*, (f)* $T = 5\ ps$*, (g)* $T = 6\ ps$*, (h)* $T = 7\ ps$*, (i)* $T = 8\ ps$*,(j)* $T = 9\ ps$*,(k)* $T = 10\ ps$ *and (l)* $T = 11\ ps$*. ASE background signal was removed in the line-out curves.*

In order to further understand the double-seeding behaviour, 10 consecutive shots at each time delay were carried out. ASE (blue line) and the 1^{st} SSXRL (black line) energy stability are showing in $Fig.$ 5.15. All the data are divided into 12 groups for ease of comparison with the energy temporal evolution of the

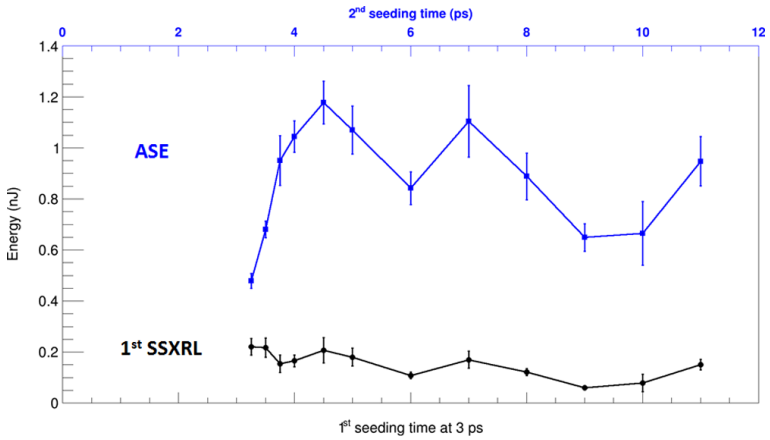

Figure 5.15: Temporal evolution of ASE (blue line) and the energy curve (black line) of the amplified HH pump (1^{st} SSXRL) seeded at $T = 3$ ps.

2^{nd} SSXRL (see $Fig.$ 5.16). One should be noted that the 1^{st} seed was injected at $T = 3$ ps. Throughout the whole curves in $Fig.$ 5.15, energy of ASE was observed as 0.85 $nJ \pm 0.11$ nJ and the 1^{st} SSXRL was obtained as 0.15 $nJ \pm 0.03$ nJ. More than 60 $times$ energy amplification was achieved when comparing the 1^{st} SSXRL and the HH pump (see $Fig.$ 5.13). The incoherent ASE takes 5 $times$ more energy than the fully coherent amplified seed, while ASE energy fluctuation is $\sim 27\%$ due to its stochastic nature. However, after seeding, the amplified seed beam energy stability is much improved, the remained slight instability mainly dependent on the refraction effect due to the plasma evolution. An evidence of the refraction effect under similar experiment condition was provided in Chapter 3, Section 3.4, $Fig.$ 3.50, where a spatial shifting on the detection plane was demonstrated.

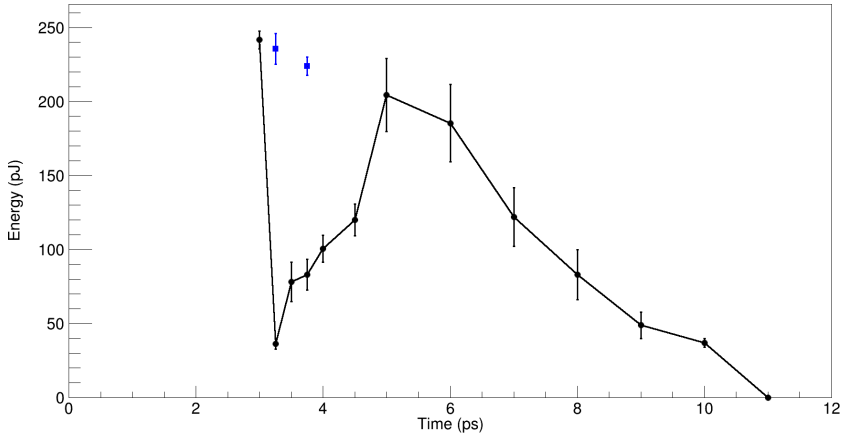

Figure 5.16: Observed gain recovery curve (black line) by seeding HH pump at 3 ps and HH probe with virious delay over 8 ps into the plasma amplifier. The two blue spots are the measured seeded SXRL with only the HH probe signal at 3.25 ps and 3.75 ps, receptively. All the error bars are corresponding to more than ten shots.

As a consequence, the energy curve of the HH probe after amplification through the plasma previously perturbed by the HH pump, as a function of time after the peak of the plasma heating IR short pulse, was displayed as the black line in $Fig.\ 5.16$. In this case, the HH pump was seeded at $T = 3\ ps$ relative to the short IR plasma heating pulse, and HH probe was varied from $T = 3.25\ ps$ to $T = 11\ ps$. At $T = 3.25\ ps$, the output energy of the HH probe was near or below the detection limit, which is the signature of negligible amplification and thus of partially complete depletion of population inversion by HH pump. At a HH pump-HH probe delay of $\Delta t = 0.5\ ps$ ($T = 3.5\ ps$) amplification is already observable, but not yet a full recovered gain. However, at $T = 5\ ps$, the energy of the amplified HH probe is equal to its value without the HH pump and then following the single seeding amplification curve. The rapid gain dropping ($\sim$250 fs) was caused by the depletion of the population inversion when seeding a 60 fs FWHM HH pulse in to the plasma amplifier. It is more interesting to note that the gain was soon fully recovered after 1.75 ps. And the following amplification of the HH probe from $T = 6\ ps$ to $T = 11\ ps$ was indicating an unperturbed plasma amplifier during that period. The decreasing trend after was due to the electron collisional pumping corresponded to the 5 ps FWHM short pump pulse. At the optimal time delay (3 ps) between the HH seed and peak of short pump pulse, amplification of $\sim$68 $times$ was achieved.

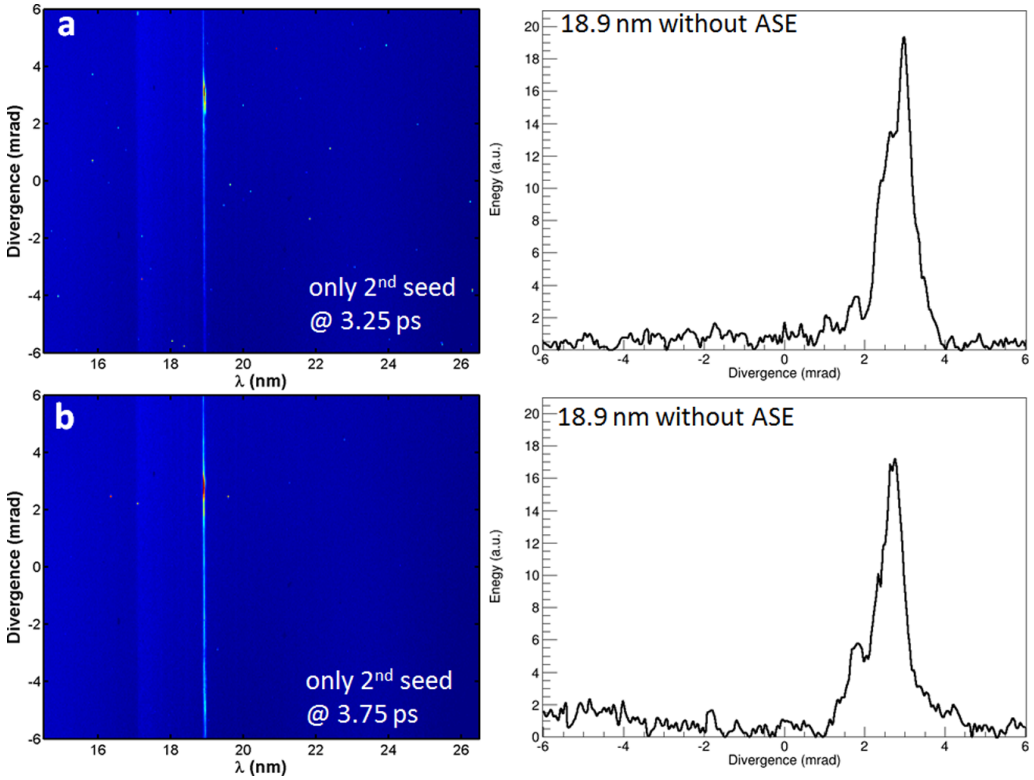

Figure 5.17: Sample images of the seeded SXRL by only injecting HH probe pulse into plamsa amplifier at (a) 3.25 ps *and (b)* 3.75 ps*, respectively.*

It is important to note that, in $Fig.\ 5.16$, the data of amplified HH probe at $T = 3\ ps$ was taken without HH pump to avoid the interference between the two HH pulses. In comparison, only the amplified HH probe without HH pump were measured at $T = 3.25\ ps$ and $T = 3.75\ ps$, receptively, which are described as the blue spots in $Fig.\ 5.16$. Two sample images of $T = 3.25\ ps$ and $T = 3.75\ ps$ with only the HH

probe seed are displayed in $Fig.\ 5.17(a)$ and $Fig.\ 5.17(b)$, respectively. When one compares this case with the double-seeded case at $T = 3.25\ ps$ and $T = 3.75\ ps$, it shows an apparent evidence of the gain depletion due to the HH pump.

Furthermore, double HH pulses with higher energy respected to $Fig.\ 5.13$ were employed to measure the gain dynamics, as represented in $Fig.\ 5.8$. Both HH-seed pulses were at same energy level of $\sim 6.1\ pJ$, which is about 2 $times$ of the previous seed pulses in $Fig.\ 5.13$. Using only the HH pump pulse, the single amplified HH-seed energy curve, as a function of time delay between the HH seed and peak of short pump pulse, was obtained as plotted in black line in $Fig.\ 5.18$. This curve is also relative to the gain curve of the plasma amplifier. Owing to the saturation effect of this dense plasma, the gain coefficient is not given. However, the maximum gain was indicated at $T = 3\ ps$, which is in good agreement with our previous results with lower seed energy showed in $Fig.\ 5.16$. Over $600\ pJ$ of the SSXRL was achieved at this optimum seeding time implying ~ 100 times amplification compared to the HH seed ($6.1\ pJ$). With the double seeding technique coupled with scanning of time delay, similar energy recovery curve was obtained (blue line) when HH pump was seeded at $T = 3\ ps$, as illustrated in $Fig.\ 5.18$. Rapid gain dropping $\sim 250\ fs$ and subsequent recovery time of $\sim 1.75\ ps$ were confirmed.

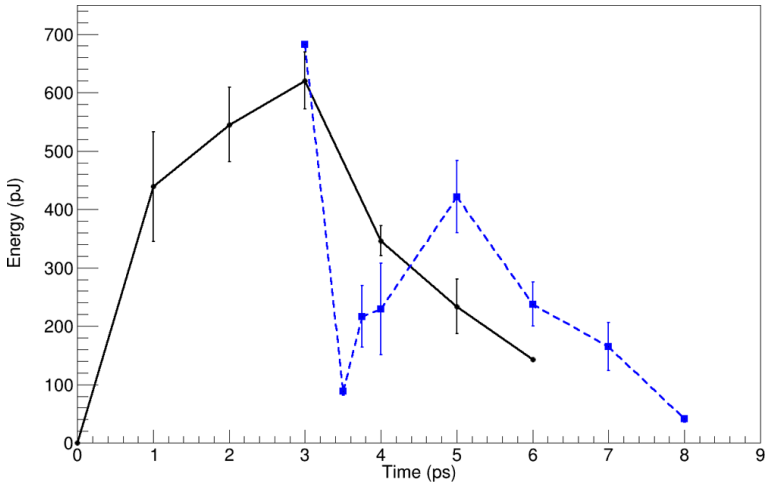

Figure 5.18: Amplified seeding curve (balck line) and recovery curve (blue line) measure by HH pump seeded at 3 ps and HH probe with series of time delays. The two HH-seed beams are represented in $Fig.\ 5.8$ which are about 2 $times$ stronger than that in $Fig.\ 5.13$.

5.3 Gain dynamics of $2.5\ mm$ plasma with $5\ ps$ IR pump pulse

Plasma column length plays an important role in the x-ray plasma amplifiers. The variation of the seed intensity and pulse shape as it propagates along the amplifier is initially governed by a narrowing of its bandwidth, which is not supported by the narrower amplifier linewidth, but by saturation of the gain [7, 19]. Previous work [15, 7] demonstrated that saturated amplification of the x-ray plasma amplifier could be achieved at an amplifier length of about $3\ mm$. It motivated us to seed the HH pulses into a shorter plasma amplifier for the gain dynamics diagnostics. Therefore, we performed this gain recovery time measurement with $2.5\ mm$ molybdenum slab target. All the other conditions were remained the same as previous diagnostics described in Section 5.2.

First of all, a single coherent HH pulse amplified in population inversion created in dense plasma was studied. In $Fig.\ 5.19$, spectrum image and integral line-out of the 43^{rd} HH order are displayed in $Fig.\ 5.19(a)$) and $Fig.\ 5.19(b)$ respectively. The estimated energy of this specific HH order was ~ 4.0 pJ. After seeding, significantly amplified seed was observed in $Fig.\ 5.19(c)$. Integral line-out around 18.9 nm is represented in $Fig.\ 5.19(d)$. It is interesting to note that black line is comprised of ASE and the amplified seed signals from the plasma amplifier. Basically, due to the stochastic nature of self-emission, ASE is considered as with large spatial divergence estimated as 25 $mrad$ in Section 5.2. Interestingly, ASE from this short plasma amplifier $(2.5$ $mm)$ was observed at negligible level. Black line in this figure indicated most of the energy from amplified seed, which was estimated as 195 pJ. So that, an amplification factor of ~ 50 at wavelength of 18.9 nm was achieved after the coherent HH beam propagating in the 2.5 mm long plasma column. In comparison with the HH pulse seeded into the 3 mm long plasma amplifier, amplification of this plasma is slightly weaker, while the ASE signal is dramatically depressed. This would be interesting for the phase imaging applications of coherent SXRL. It is also the curiosity of the gain dynamics within this lower self-emission in this plasma amplifier.

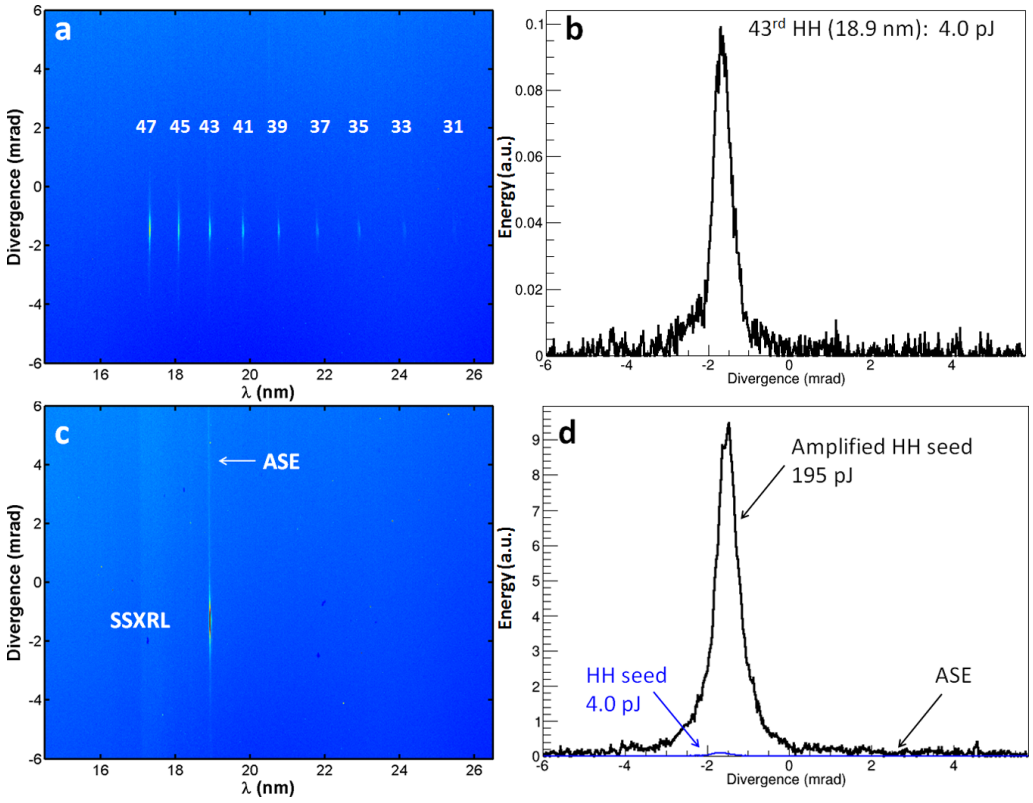

Figure 5.19: Comparison of HH seed (a, b) and amplified seed (SSXRL) at $T = 3$ ps (c, d). The 43^{rd} order of HH was amplified by ~ 50 $times$ with the injection to 2.5 mm long Mo x-ray plasma amplifier. $T = 0$ ps is corresponding to the arrival time of the peak of short pump pulse.

To study the dynamics of this short plasma amplifier $(2.5$ $mm)$, the time-dependent amplification curve is primarily required. A single HH seed pulse seeding into the plasma with various time delay to the arrival of short pump pulse is often the way to obtain time-dependent amplification curve. Shot-to-shot energy stability over 10 $shots$ of the HH seed pulse contributed to the amplification curve is illustrated

in $Fig.\ 5.20$. Obtained HH seed pulse energy value is $4.2\pm0.3\ pJ$, which is adequate to perform gain dynamics diagnostics of the plasma amplifier.

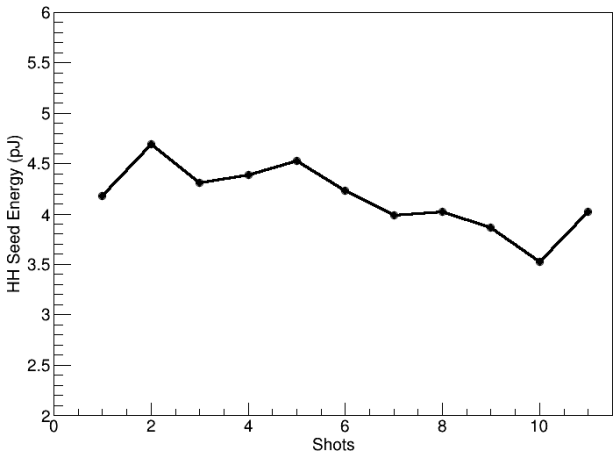

Figure 5.20: HH seed shot-to-shot energy stability for amplification curve measurement using $2.5\ mm$ Mo plasma column and $5\ ps$ (FWHM) short pump pulse.

$T = 0\ ps$ is corresponding to the arrival time of the peak of short pump pulse. Due to the ultrashort pulse duration ($\sim 60\ fs$) of the HH pulse, when scanning the HH seed pulse injection time to the plasma amplifier respected to $T = 0\ ps$, one could get the temporal evolution of the population inversion in the plasma amplifier. Within this context, a series of typical output signals at different time to seed HH pulse into plasma are illustrated from $Fig.\ 5.21(a)$ to $Fig.\ 5.21(j)$ with time step of $1\ ps$. The left images are the spectral raw images from the CCD coupled with diffraction grating detection system. Integral line-out around $18.9\ nm$ are displayed in the right figures. It is important to point out that the line-out figures are including the ASE signal, which implying ASE is at negligible energy level. At $T = 0\ ps$, amplified seed (SSXRL) was near or below the detection limit. It was then increasing due to the injection time delaying and rapidly reaching its maximum amplification at $T = 3\ ps$. However, the declining of this amplified seed lasted for $8\ ps$.

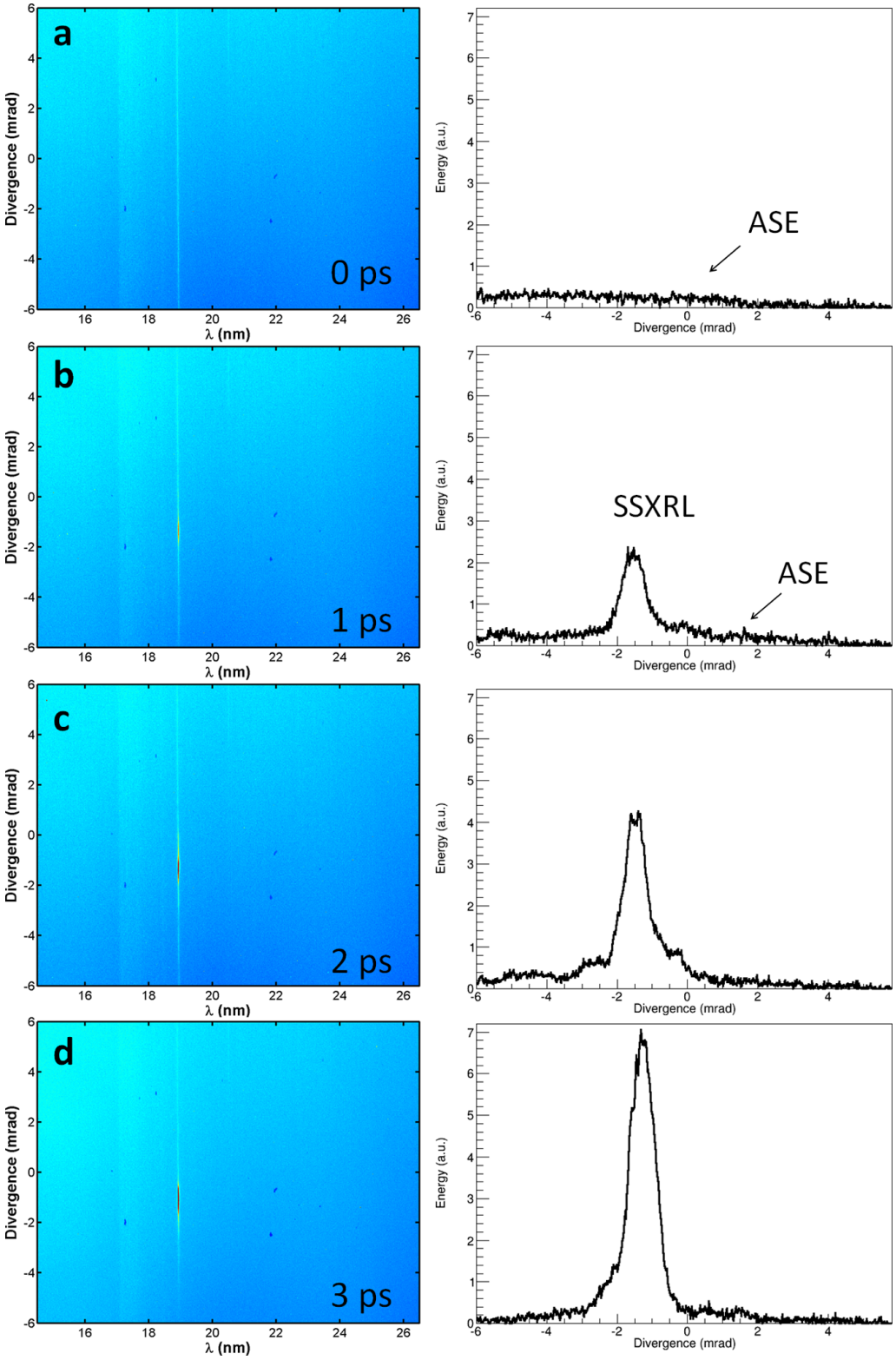
a
0 ps
b
1 ps
c
2 ps
d
3 ps
Divergence (mrad)
λ (nm)
Energy (a.u.)
Divergence (mrad)
ASE
SSXRL
ASE

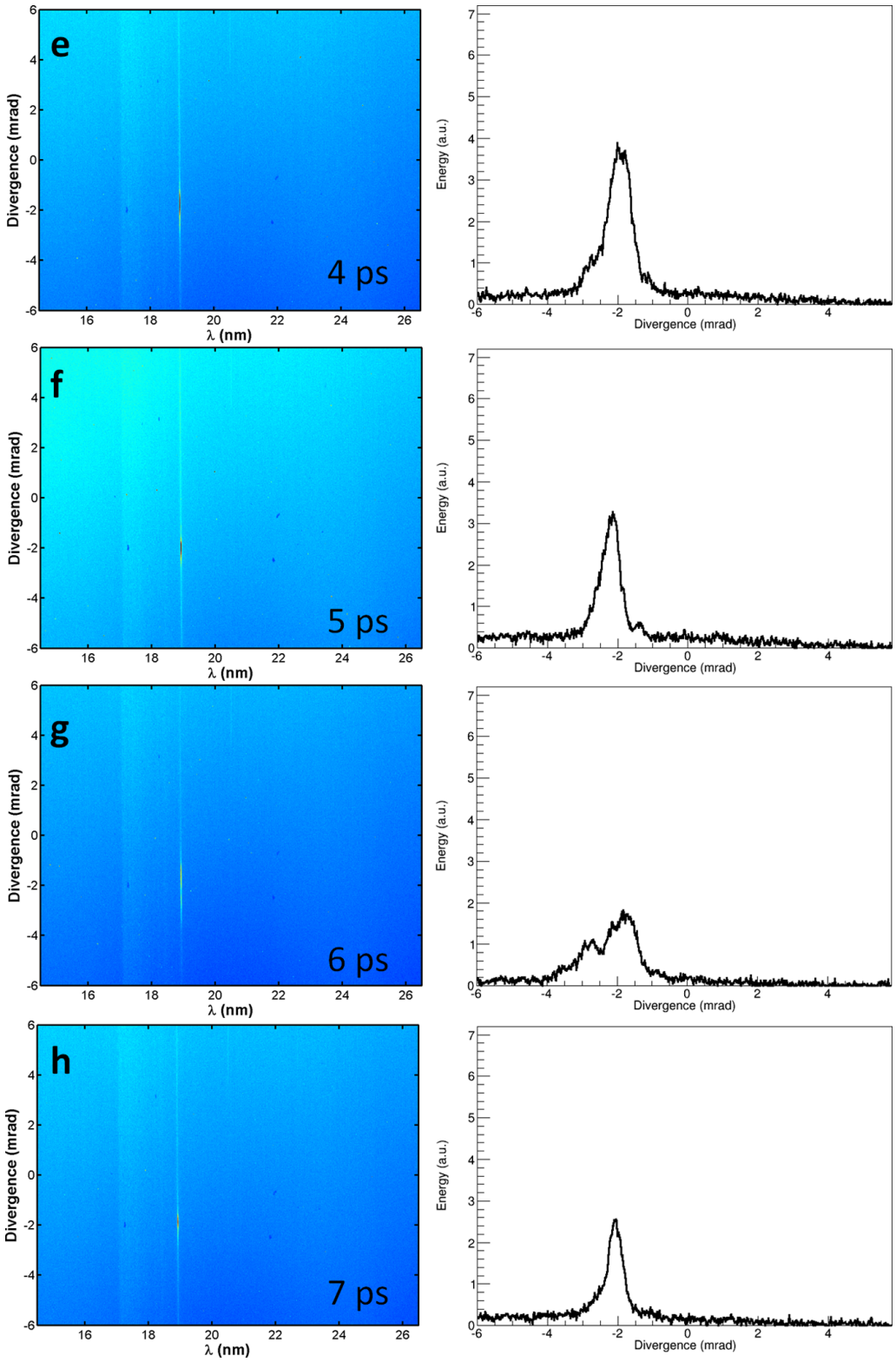
e
4 ps
f
5 ps
g
6 ps
h
7 ps
Divergence (mrad)
λ (nm)
Energy (a.u.)
Divergence (mrad)

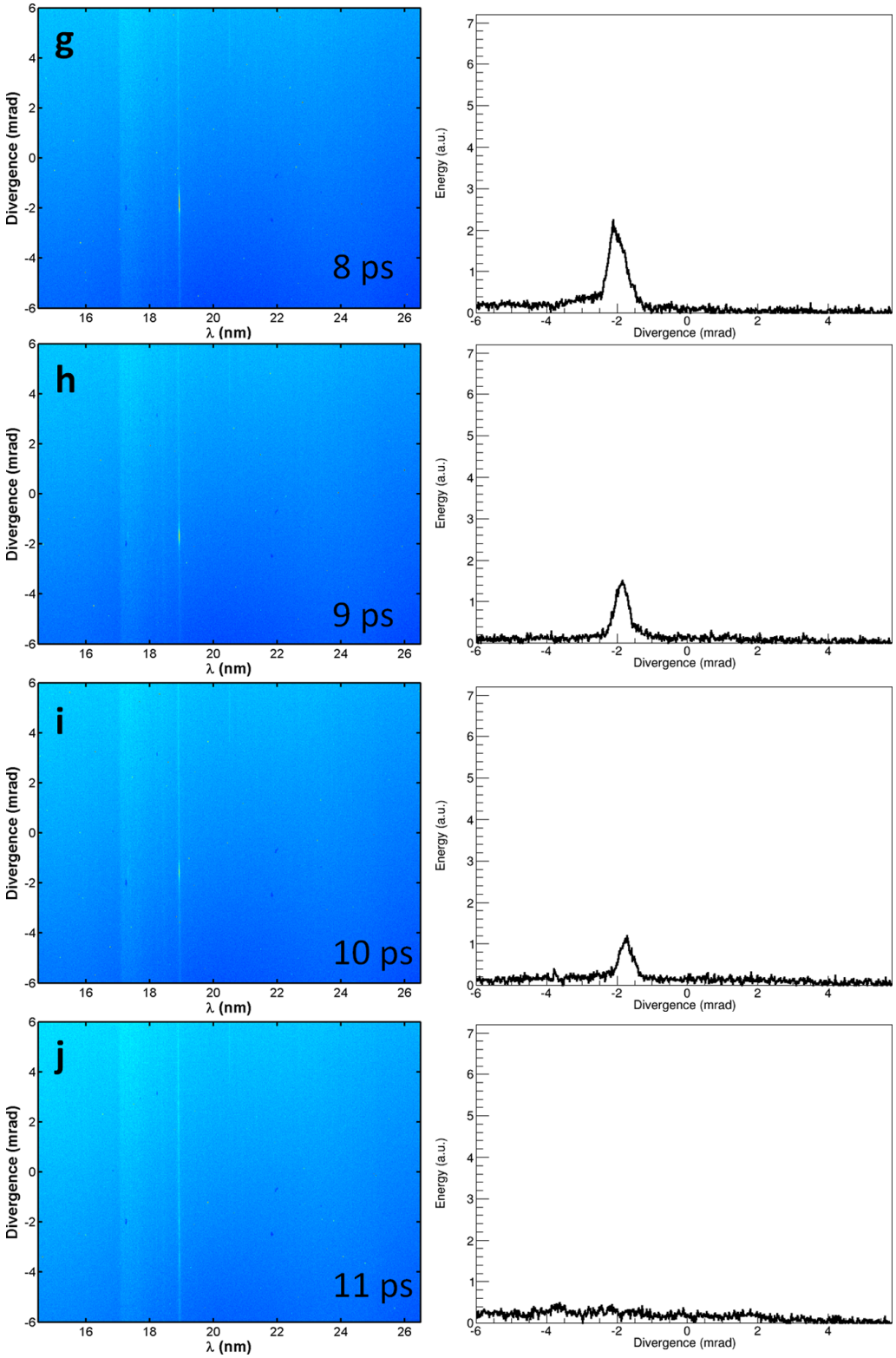

Figure 5.21: Typical seeded SXRL imeges from different HH-injection time respected to the peak of short pump pulse. Left images are spectrum detected by x-ray CCD coupled with diffraction grating, the right images are the spatial line-out of the amplified seed at $18.9\ nm$.

Considering an investigation of 10 consecutive shots at each time delay, the amplification curve was sequentially obtained and displayed in $Fig.$ 5.22 (black line). The grey shade is indicating to the error bar over 10 $shots$. The population inversion life time $\sim$11 ps was then obtained which is in consistence with our previous observation in 3 mm long plasma amplifier (see $Fig.$ 5.16). Based on this knowledge, the HH-pump/HH-probe technique described in above seeding two HH-seed pules into plasma was then demonstrated for the gain dynamics diagnostic.

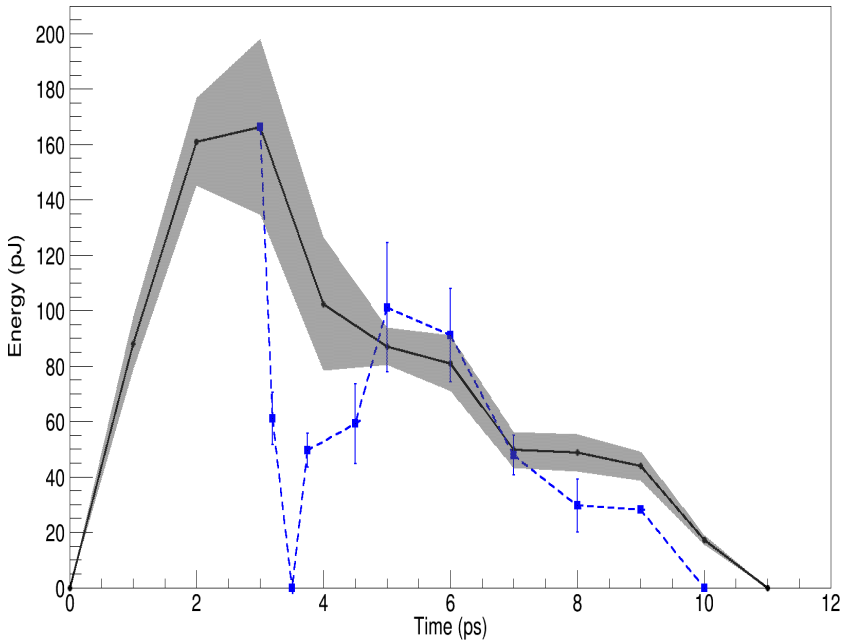

Figure 5.22: Energy amplification curve (black line) and gain recovery curve (blue line) for 2.5 mm *Mo plasma amplifier of* 18.9 nm *SXRL pumped by short pulse with* 5 ps *FWHM temporal duration. Each error bar is corresponding to* 10 *different shots.*

Finally, the gain recovery curve was measured seeding HH pump at peak of the gain ($T = 3$ ps) and delaying the HH probe with variety of time delays in respect to the HH pump, as demonstrated with blue line in $Fig.$ 5.22. The gain was totally depleted at 500 fs after the seeding, which is slightly slower than the previous case (250 fs) in 3 mm plasma amplifier described in $Fig.$ 5.16. However the recovery time from the valley to the equivalent value of single-seeding was observed as 1.5 ps, which is mildly shorter than seeding at the longer plasma amplifier (3 mm). Seeded SXRL has been reported that the pulse duration is predominately determined by the Lorentzian component of amplifier linewidth, operation at a higher plasma density would result in a nearly inversely proportional pulse width [7]. The plasma density and SXRL propagation in the amplifier play an important role in the gain dynamics which could cause the mild difference of the gain depletion time and recovery time between the two different plasma amplifiers. However, the detection limit of this measurement is 250 fs due to the time step when scanning the HH probe. Another effect should be also taken into account is the quality of the two HH seed pulses along the time delay. As displayed in $Fig.$ 5.23, generally, energy fluctuation of both HH pump and HH probe within around 1 ps and average energy of each is $\sim$4 pJ. However, when the delay between HH pump and HH probe is less than 1 ps, the second HH pulse (HH probe) got energy reduction by the influence due to the ionization of the gas cause by the HH-pump driven laser field, as explained in Section 5.1. The seed

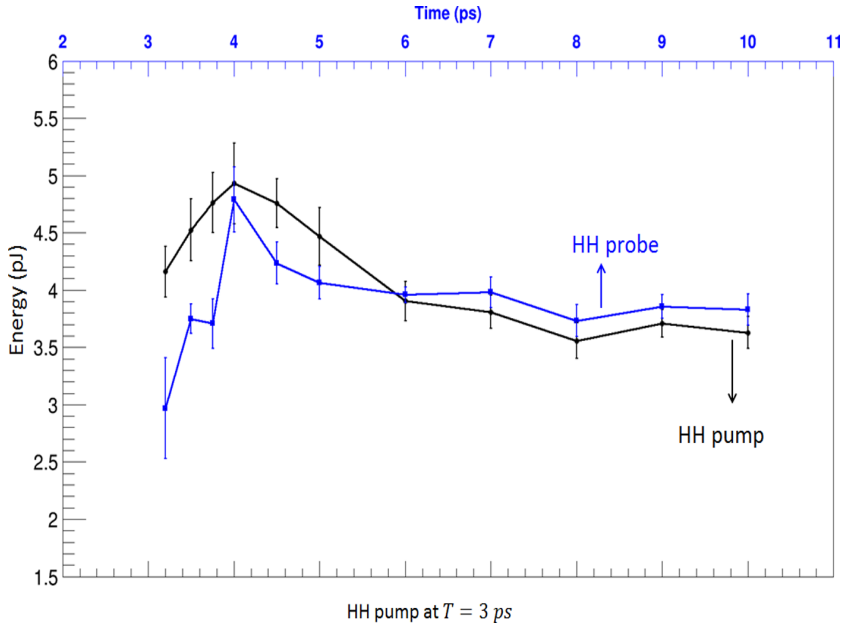

Figure 5.23: HH seed energy stability of HH pump (black line) and HH probe (blue line). All the error bars are corresponding to $10\ shots$.

energy difference within $2-3\ pJ$ only showed the amplified energy gap when one compares $Fig.\ 5.16$ and $Fig.\ 5.18$, the behaviour of the gain dynamic remains the same. Further understanding these points, a series of the recovery curves calculated at various seeding conditions, based on Maxwell-Bloch model (DeepOne Code), are demonstrated in Chapter 4, Section 4.4. In addition to that, further discussion according to this experiment results are included in Section 5.5.

5.4 Gain dynamics of $3\ mm$ plasma with $10\ ps$ IR pump pulse

Dynamics of the x-ray plasma amplifier is dependent on the electron and ions conditions which are due to the pumping field for the population inversion. Changing the parameters of the short pump laser is the interest of understanding plasma hydrodynamics. In addition, the plasma parameters (density, temperature, ionization) are not constant over the amplification period due to the hydrodynamic evolution. It is interesting to seed the HH pump at different time respected to the peak of short pump pulse. We therefore conducted this experiment seeding double HH-seed into $3\ mm$ long plasma amplifier with large transient population inversion created by $10\ ps$ FWHM short pump pulse. The non-linear dynamics of ionic levels in plasma after being perturbed by an intense external soft x-ray seed at different time respected to the peak of short pump pulse are studied in this section.

To conventionally study this x-ray plasma amplifier, the time-dependent amplification curve (indicated to gain curve) was firstly figured out. Single HH seed with pulse energy around $6\ mJ$ was seeded into plasma amplifier with a variety of injection times from $T = 0\ ps$ to $T = 10\ ps$. Here, $T = 0\ ps$ is corresponding to the arrival time of the peak of short pump pulse. Typical spectral images from each injection time are illustrated by the left of $Fig.\ 5.24$. The right figures are indicating to the integral

line-out around $18.9\ nm$, which consist of amplified seed and ASE signal. It is worth nothing that the ASE energy level is apparently lower than observed in $Fig.\ 5.12$, where the $3\ mm$ long plasma amplifier was created by two pre-pulses (see $Fig.\ 5.9$) coupled with $5\ ps$ short pump pulse. Owing to the short pump IR laser pulse energy ($\sim 500\ mJ$) from the second arm described in $Fig.\ 3.28$, the longer pulse duration ($10\ ps$) in current experiment induced lower irradiate intensity to create the plasma amplifier in respect of the previous experiment demonstrated in Section 5.2 ($Fig.\ 5.12$). This could explain the obtained less ASE energy in $Fig.\ 5.24$ when comparing to it in $Fig.\ 5.12$. However, the ASE level is still stronger than that comes from the $2.5\ mm$ long plasma amplifier represented in $Fig.\ 5.19$.

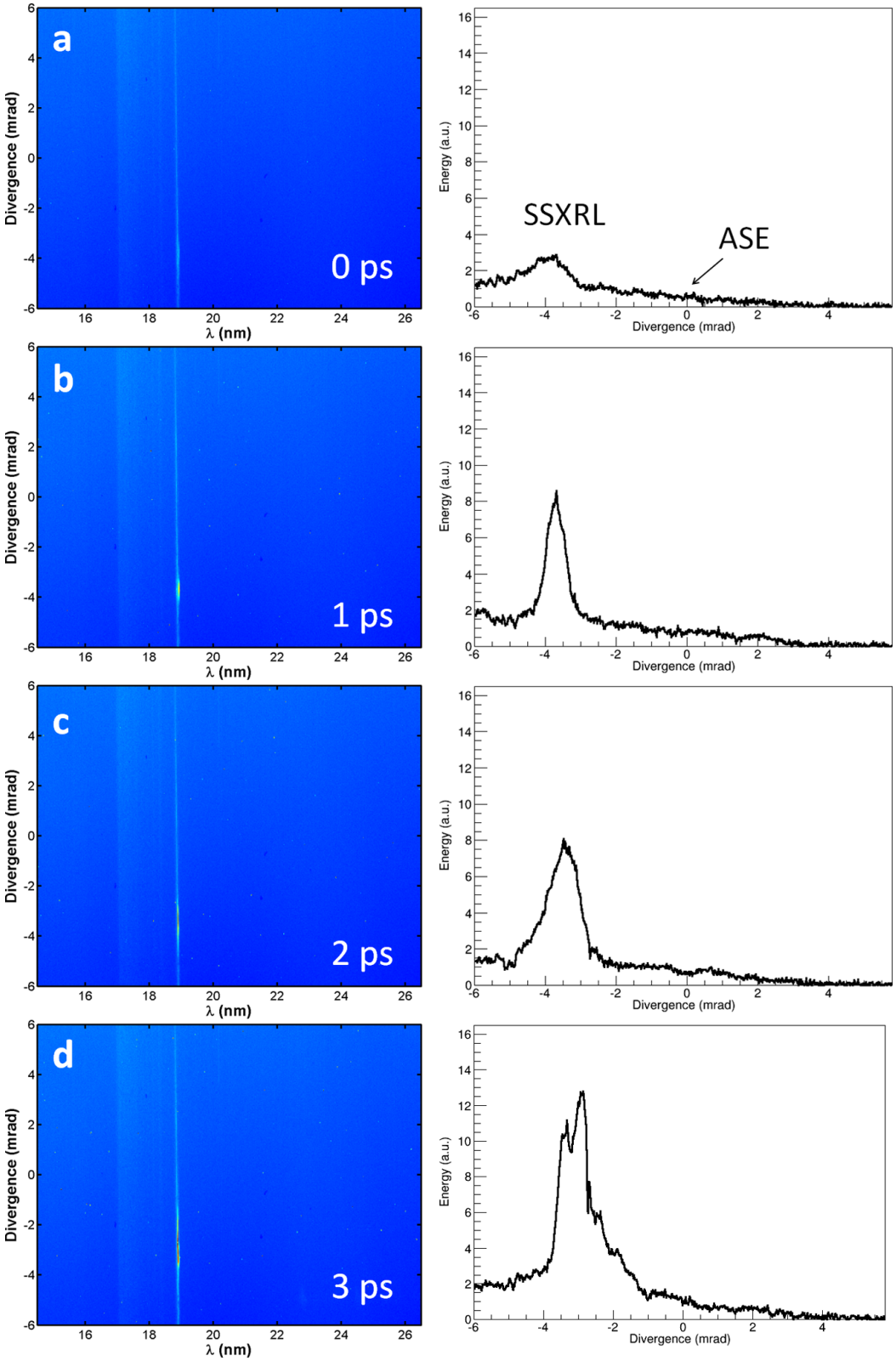
a
0 ps
b
1 ps
c
2 ps
d
3 ps
Divergence (mrad)
λ (nm)
Energy (a.u.)
Divergence (mrad)
SSXRL
ASE

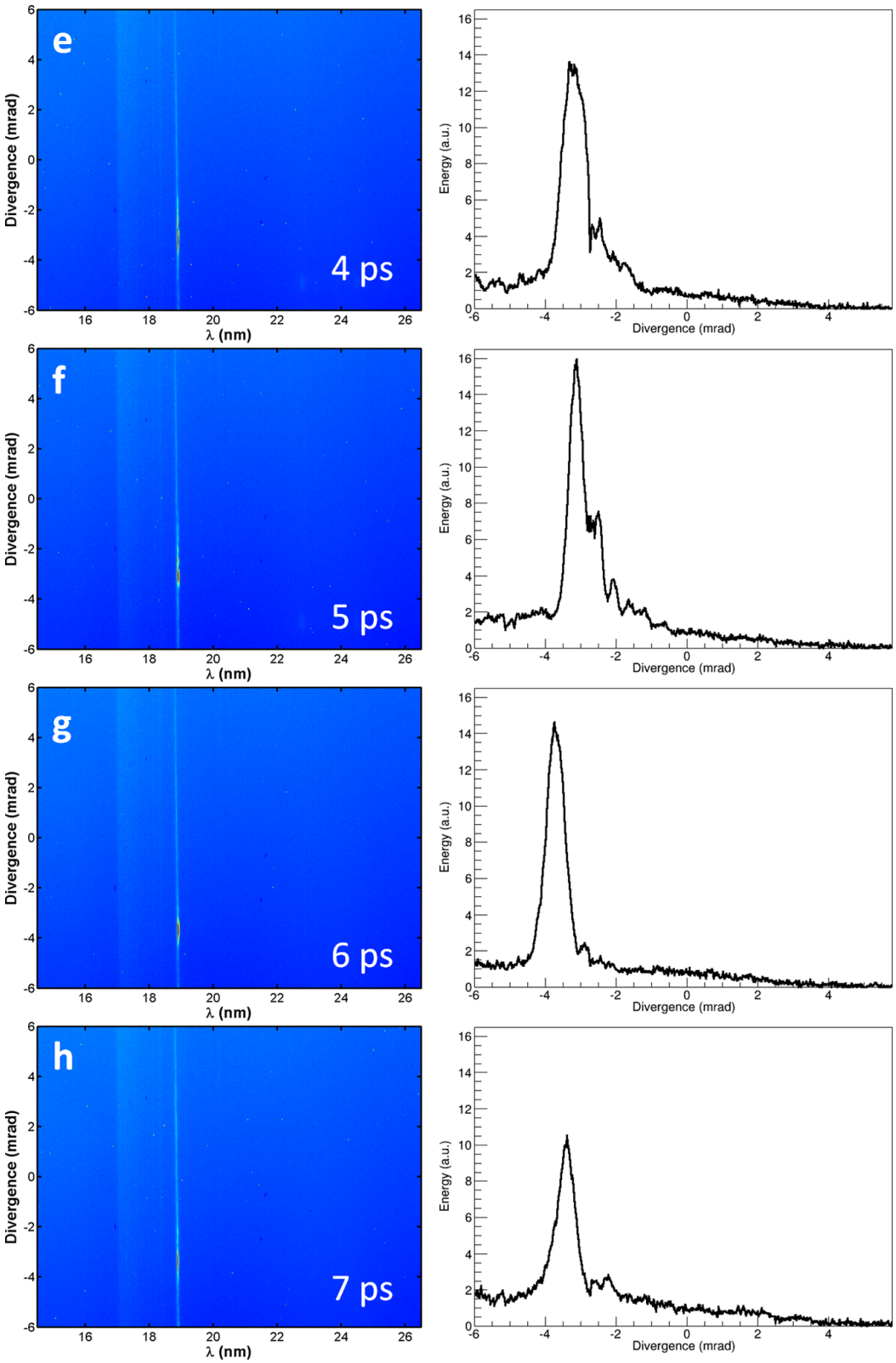
e
4 ps
f
5 ps
g
6 ps
h
7 ps
Divergence (mrad)
λ (nm)
Energy (a.u.)
Divergence (mrad)

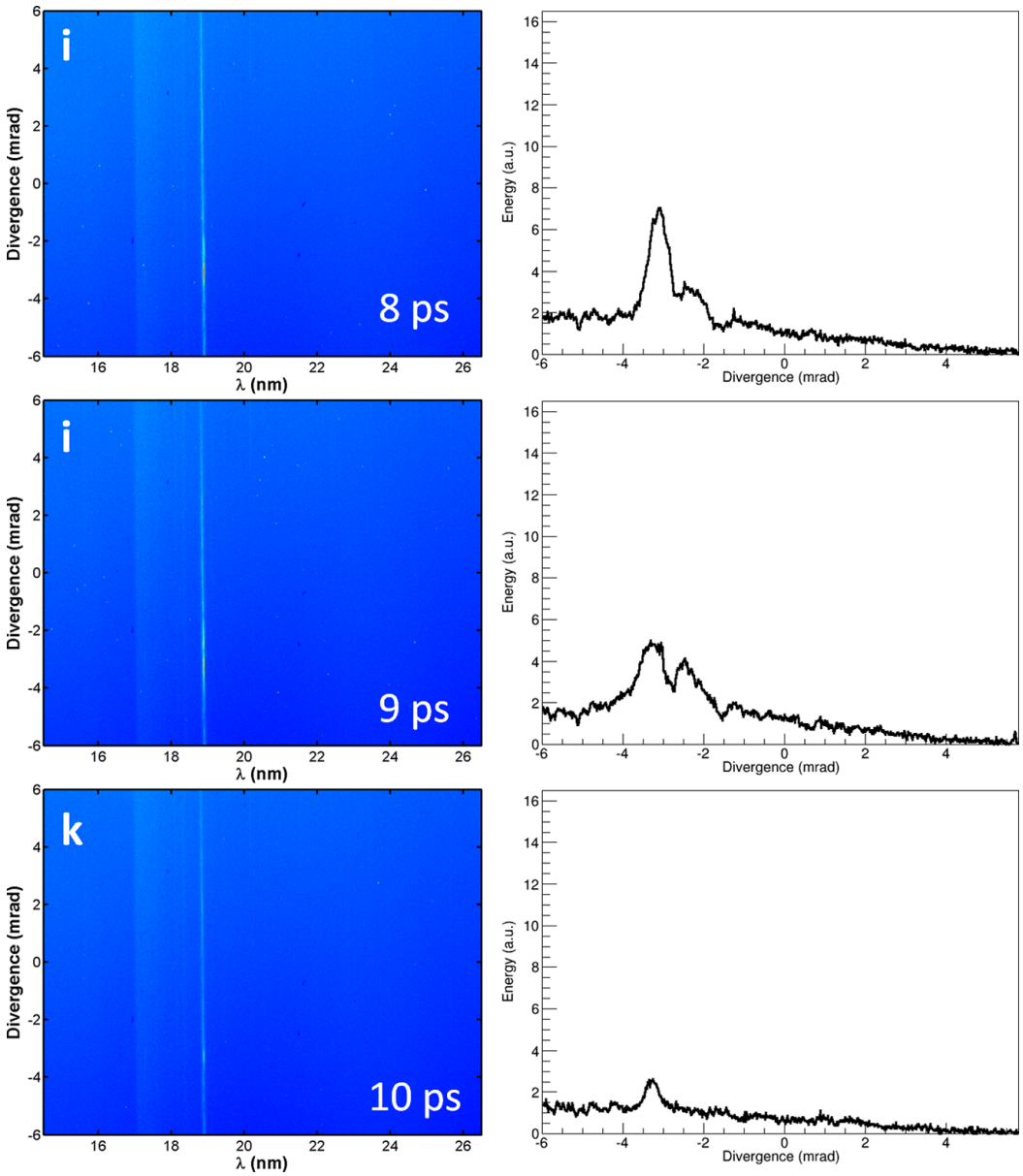

Figure 5.24: Sample evolution of seeded SXRL by injecting the HH seed at different time delays respected to the arrival time of short pump pulse (peak-to-peak). The x-ray plasma amplifier is $3\ mm$ *long, generated by two pre-pulses and* $10\ ps$ *short pump pulse with grazing incident angle of* $23°$.

Interestingly, slight amplification of the seed pulse was observed at $T = 0\ ps$, while it was not apparent in the case of pumping plasma with $5\ ps$ IR laser pulse as mentioned in Section 5.2 and Section 5.3. The amplified seed beam was becoming stronger when increasing time delay between the seeding and short pump pulse. It was then reaching its maximum value at $T = 5\ ps$, and the amplification decaying took similar time as increasing. As displayed in $Fig.\ 5.24(k)$, the amplified seed beam was closing to the detection limit. For the further step $T = 11\ ps$, the amplified seed was below the detection limit. Sequentially, ten consecutive shots at each time delay were carried out to measure the amplification curve of this $3\ mm$ long plasma amplifier pumped by $10\ ps$ IR laser pulse. Due to the $10\ ps$ IR pump pulse, a symmetrical shape of amplification curve was obtained in $Fig.\ 5.25$. A lifetime over $11\ ps$ of the population inversion was implied. At $T = 5\ ps$, the maximum amplified seed pulse energy at $360\ pJ$ was achieved which indicating an amplification factor $\sim 60\ times$ respected to the HH seed pulse energy $\sim 6\ pJ$.

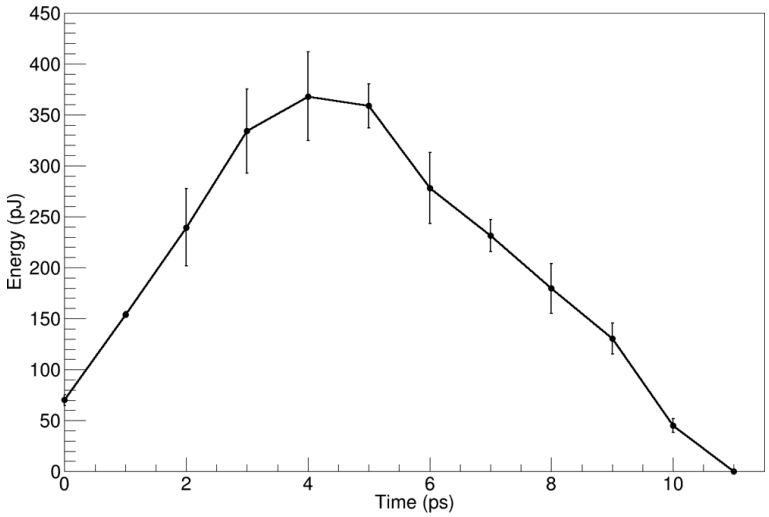

Figure 5.25: Amplification curve of 2.5 mm long x-ray plasma amplifier length generated by two pre-pulses and grazing incident short pump pulse with duration of 5 ps at FWHM.

In subsequent, the double HH-seed pulses were adopted to diagnostic the seeding gain behaviour of the x-ray plasma amplifier. It is interesting to note that, in the previous two experiments described in Section 5.2 and Section 5.3, the HH-pump was seeded at the peak of amplification curve. According to our simulation results om gain dynamics, the recovered amplification value is dependent on the HH-pump seeding time as illustrated in $Fig.\ 4.19(b)$. We therefore performed two experiments in this section with HH-pump seeding before ($T = 3\ ps$) and after ($T = 6\ ps$) the maximum amplification, respectively.

At first, the HH-pump seeded at $T = 3\ ps$ was studied. Energy stability of both HH pump (black line) and HH probe (blue line) beams are represented in $Fig.\ 5.26$. Black lines is indicating the HH pump generated at constant time $T = 3\ ps$, and the data was divided into 10 groups. Each group including 10 consecutive shots is corresponding to the time steps of HH probe beam as explained in Section 5.2 and Section 5.3. Blue line is the HH probe energy stability with the delayed generation time from $T = 3.25\ ps$ to $T = 10\ ps$. Pulse energy of HH pump was measured as $6.1\ pJ \pm 0.2\ pJ$ and HH probe was observed to be $4.8\ pJ \pm 0.2\ pJ$. HH probe beam energy fluctuation around 10% was observed with delay less than $1\ ps$ respected to the HH pump beam.

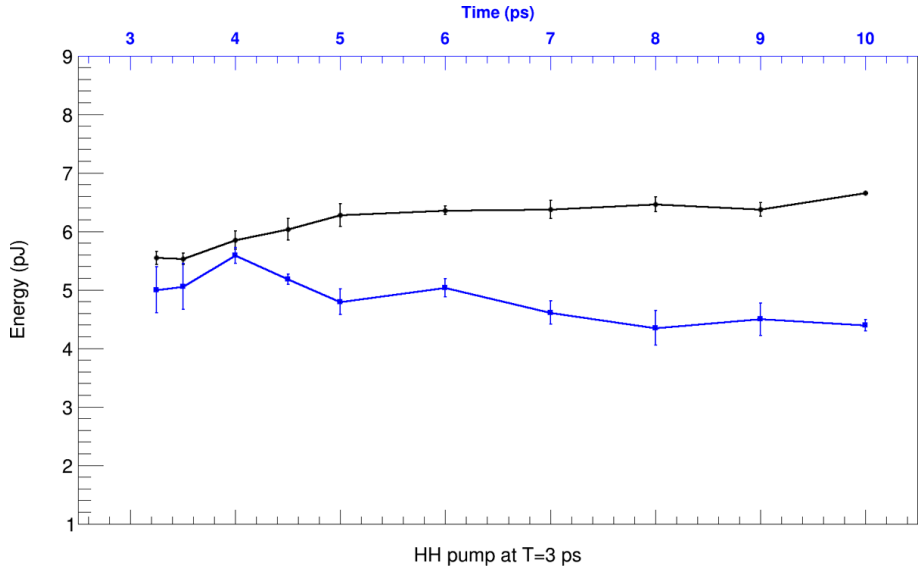

Figure 5.26: Energy stability of HH pump (black lines) and HH probe (blue lines) for HH pump seeded at $T = 3$ ps. Each error bar is corresponding to over 10 $shots$.

A series of typical spectral images (at left) and integral spatial line-out around 18.9 nm (at right) from $T = 3$ ps to $T = 10$ ps are illustrated in $Fig.$ 5.27. For ease of comparison, the ASE signal was removed out in the line-out figures according to the approach described in $Fig.$ 5.12. In order to avoid the interference between the HH pump and HH probe pulses at $T = 3$ ps, which is the seeding time of HH pump pulse, the HH pump pulse driven IR laser was blocked. So that only the HH probe was used to injection into the plasma amplifier as shown in $Fig.$ 5.27(a). From $Fig.$ 5.27(b) to $Fig.$ 5.27(k), the HH pump beam was firstly seeded at $T = 3$ ps while HH probe was seeded with different time delays respected to the HH pump seeding. At $T = 3.25$ ps, the amplified HH probe pulse was near or below the detection limit, which is not obvious to be seen. It is caused by the population inversion depletion due to the plasma previously perturbed by the HH pump pulse as explained in Section 5.2 and Section 5.3. Then an increasing of the amplified HH probe pulse was observed as delaying the injection time. The achieved maximum amplification of the HH probe was at $T = 5$ ps, which is 2 ps after the HH pump seeding. This recovered signal was then decreased slowly following the decaying of the gain till $T = 10$ ps.

Over 10 consecutive shots at each time step described above were conducted. After full time scanning of HH probe pulse from $T = 3$ ps to $T = 10$ ps, an energy recovery curve, which is implying to the gain recovery curve, was obtained in $Fig.$ 5.28. It is apparent that the full gain depletion is within 250 fs in the plasma amplifier perturbed by an intense HH pump beam. However, one could also note that the gain recovery time was obtained as 1.75 ps (from $T = 3.25$ ps to $T = 5$ ps). This result is in good agreement with the observation demonstrated in Section 5.2 and Section 5.3 with different plasma parameter. One should be noted that the full recovered amplification appeared at $T = 5$ ps achieved higher energy than the original single HH probe seeding at $T = 3$ ps. This is because of the temporal gain evolution as implied in $Fig.$ 5.25. The amplification at $T = 5$ ps is higher than it was in $T = 3$ ps. This behaviour shows that the perturbed x-ray plasma amplifier has the potential to be recovered to follow its normal temporal evolution.The duration between this perturbation and full recovery is ~ 2 ps. Moreover, one can also find that the amplification of the recovery curve ($Fig.$ 5.28) is lower than the

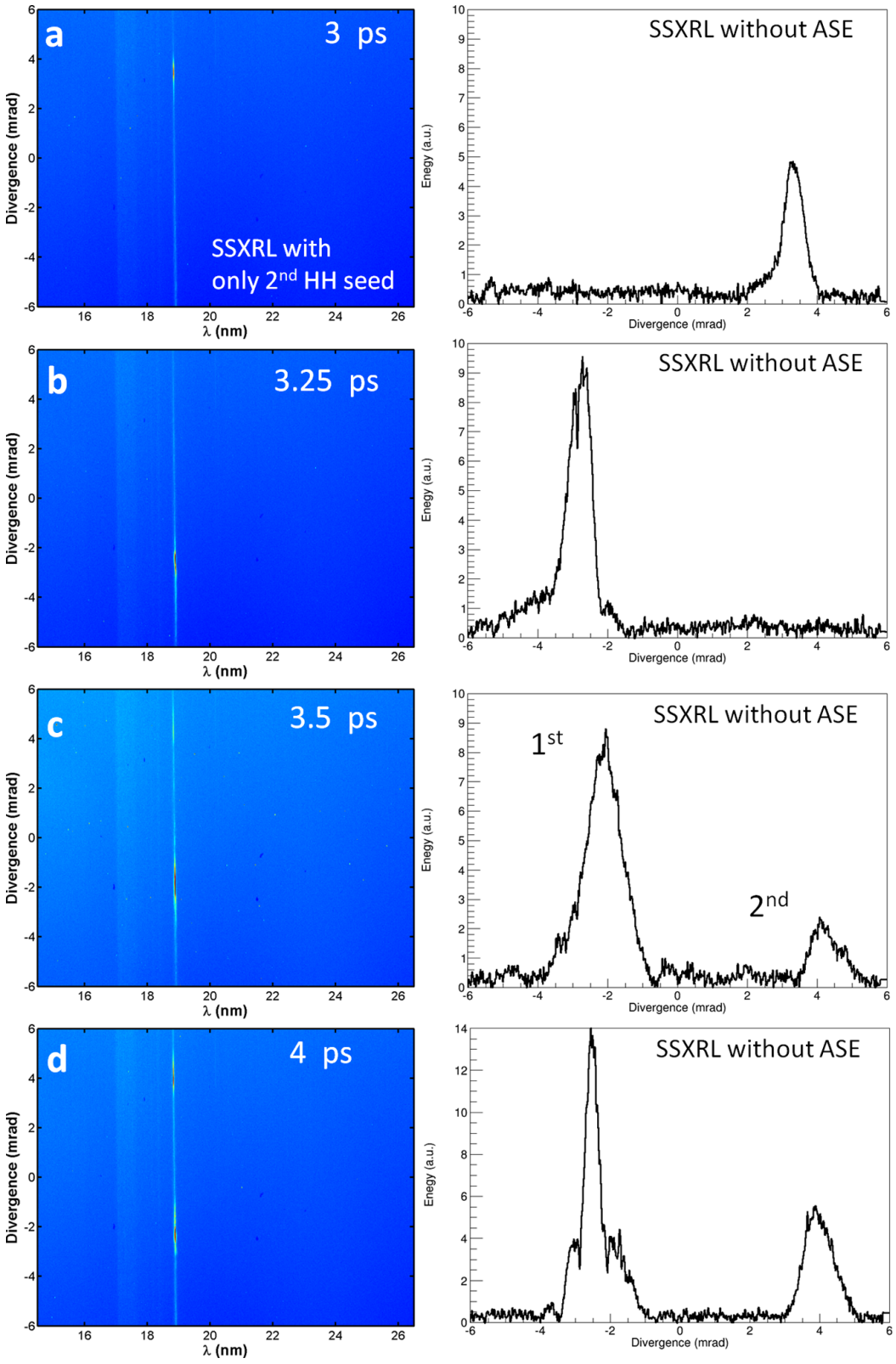
a
3 ps
SSXRL with
only 2nd HH seed
SSXRL without ASE
b
3.25 ps
SSXRL without ASE
c
3.5 ps
1st
2nd
SSXRL without ASE
d
4 ps
SSXRL without ASE
Divergence (mrad)
λ (nm)
Enegy (a.u.)
Divergence (mrad)

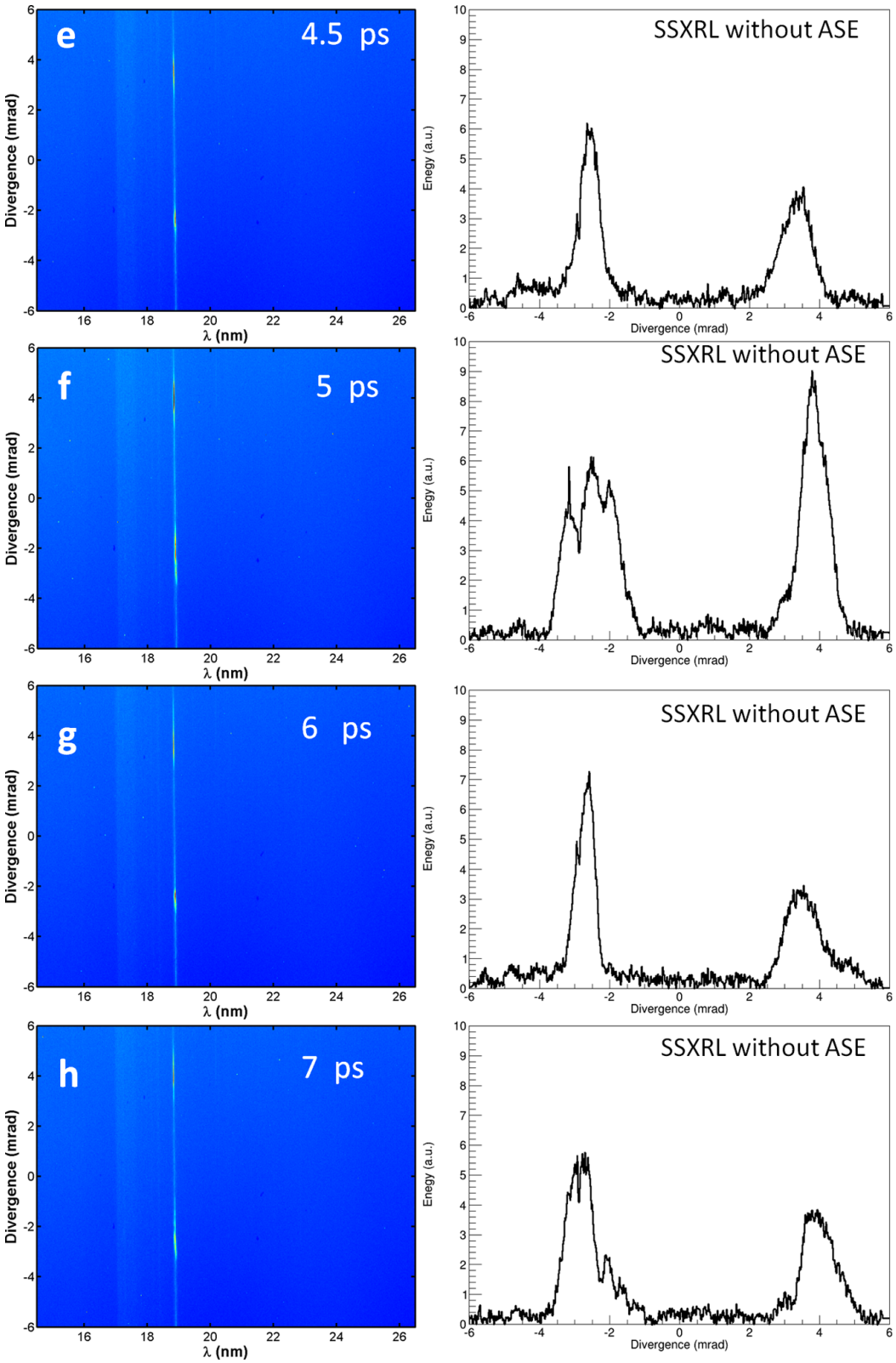
e
4.5 ps
f
5 ps
g
6 ps
h
7 ps
Divergence (mrad)
λ (nm)
Enegy (a.u.)
Divergence (mrad)
SSXRL without ASE

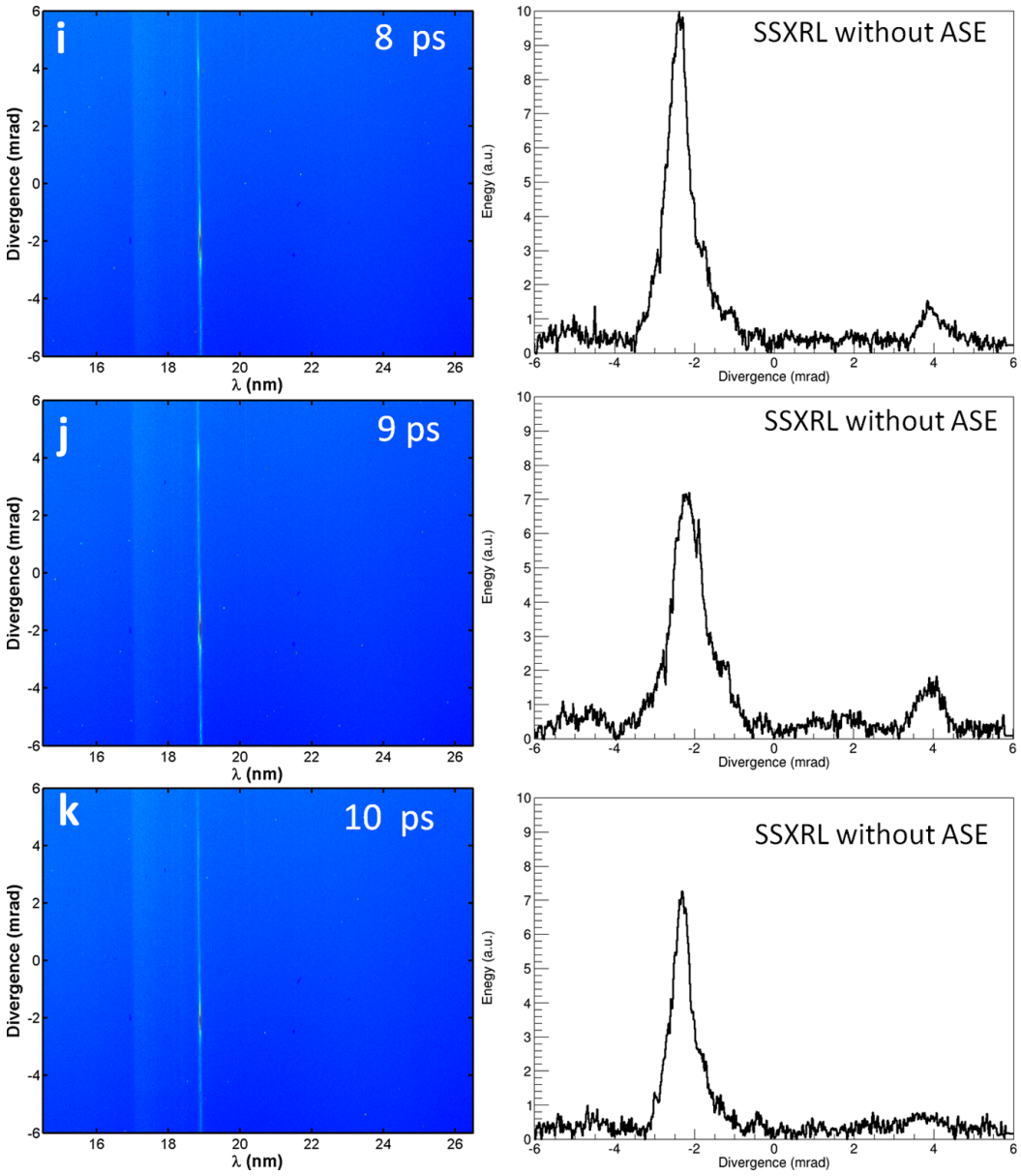

Figure 5.27: Double-HH seeding evolution with a variety of time delays between each other. HH pump was fixed at 3 ps *respected to the short pump pulse.* $T = 0$ ps *is corresponding to the arrival time of the peak of short pump pulse. The Mo-plasma is* 3 mm *long with short pump pulse duration at* 10 ps *FWHM.*

original measured amplification curve ($Fig.$ 5.25). HH seed pulse energy difference should be taken into account. HH seed beam energy for to measure the original amplification curve is $\sim 6\ mJ$, however the HH probe beam energy is $\sim 4\ mJ$ as displayed in $Fig.$ 5.26. Further analysis on the seed energy influence is discussed in Section 5.5.

Secondly, the HH-pump seeded at $T = 6$ ps was investigated. Energy stability of both HH pump (black line) and HH probe (blue line) beams are displayed in $Fig.$ 5.29. Black lines is the HH pump generated at constant time ($T = 6$ ps), while the data were divided into seven groups to ease comparing

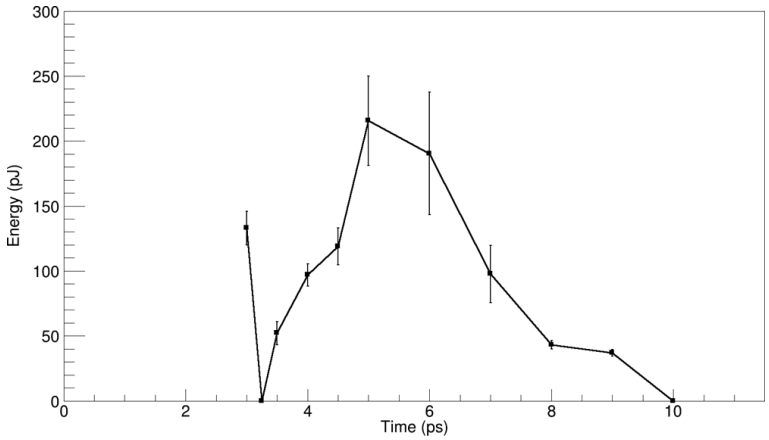

Figure 5.28: Gain recovery curve for HH pump injected at $3\ ps$ *into the plasma amplifier.*

with the HH probe beam as explained in Section 5.2 and Section 5.3. Blue line is corresponding to the HH probe energy stability with the various generation time from $T = 6.25\ ps$ to $T = 10\ ps$. HH pump pulse energy was measured as $6.2\ pJ \pm 0.1\ pJ$ and HH probe pulse was observed to be $5.2\ pJ \pm 0.1\ pJ$. One could see slight energy fluctuation around 10% of HH probe beam when the generation time is closing to (from $T = 6.25\ ps$ to $T = 7\ ps$) the HH pump pulse generation. This interference was explained in the Section 5.1. Nevertheless, the slight energy fluctuation has no essential impact to the gain dynamics diagnostics.

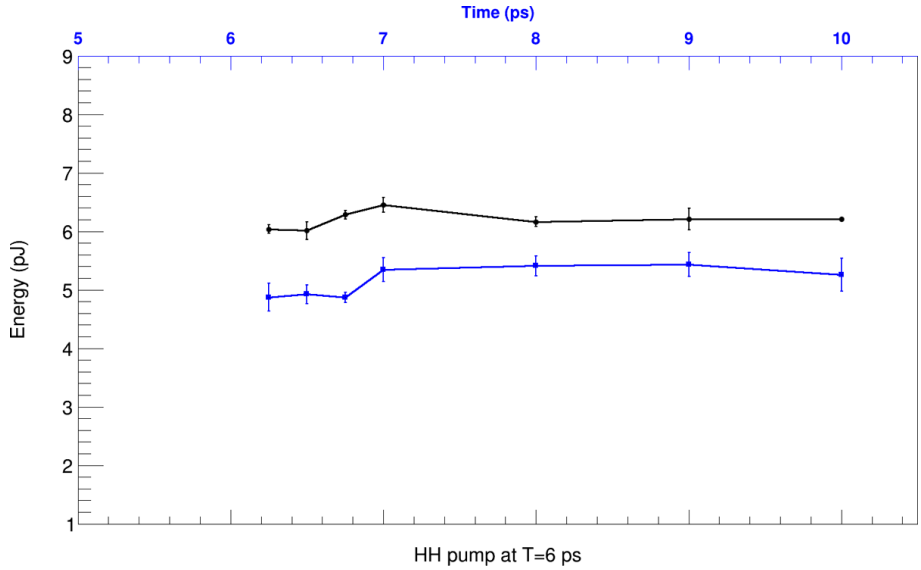

Figure 5.29: Energy stability of HH pump (black lines) and HH probe (blue lines) for HH pump seeded at $T = 6$ ps*. Each error bar is corresponding to over* $10\ shots$*.*

Within the same idea as before, the two HH seed pulses were eventually used to measure the gain recovery time. In $Fig.\ 5.30(a)$, only the HH probe pulse was seeded at $T = 6\ ps$ to avoid the interference between HH pump beam and HH probe beam. From $Fig.\ 5.30(b)$ to $Fig.\ 5.30(g)$, HH pump was seeded

at $T = 6\ ps$ and HH probe was following with a series of time delays from $T = 6.25\ ps$ to $T = 10\ ps$. The amplified HH pump beam was observed as energy fluctuation less than 10%. A slight amplification of the HH probe pulse was recognized at $T = 6.25\ ps$. No amplification of the HH probe pulse was detected at $T = 6.5\ ps$, however, it was then recovered to a certain level at $T = 8\ ps$. It was soon decreased near to the detection limit at $T = 10\ ps$ as displayed in $Fig.\ 5.30(g)$.

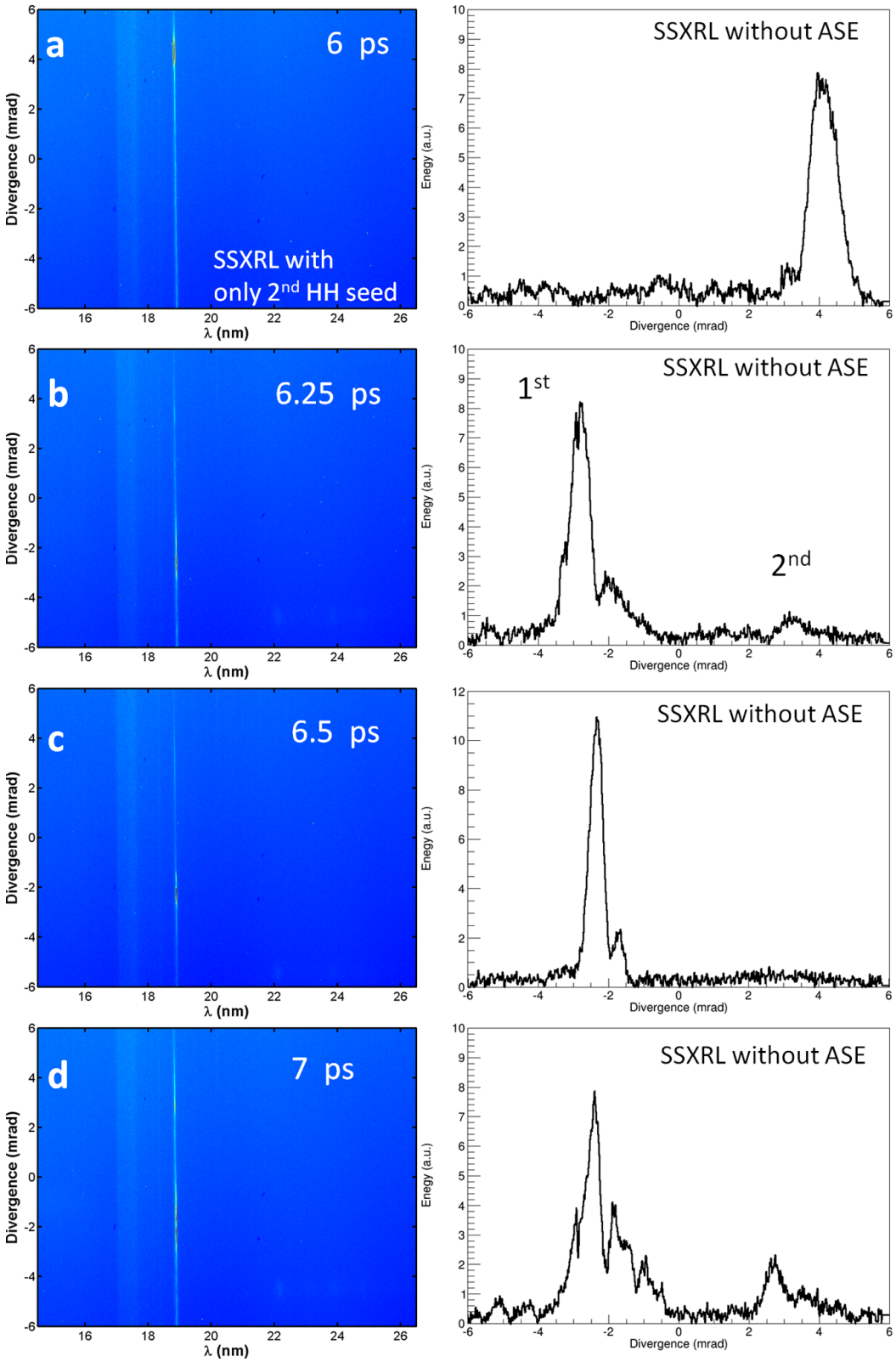

Ten consecutive shots at each injection time of the HH probe beam was conducted. Throughout the

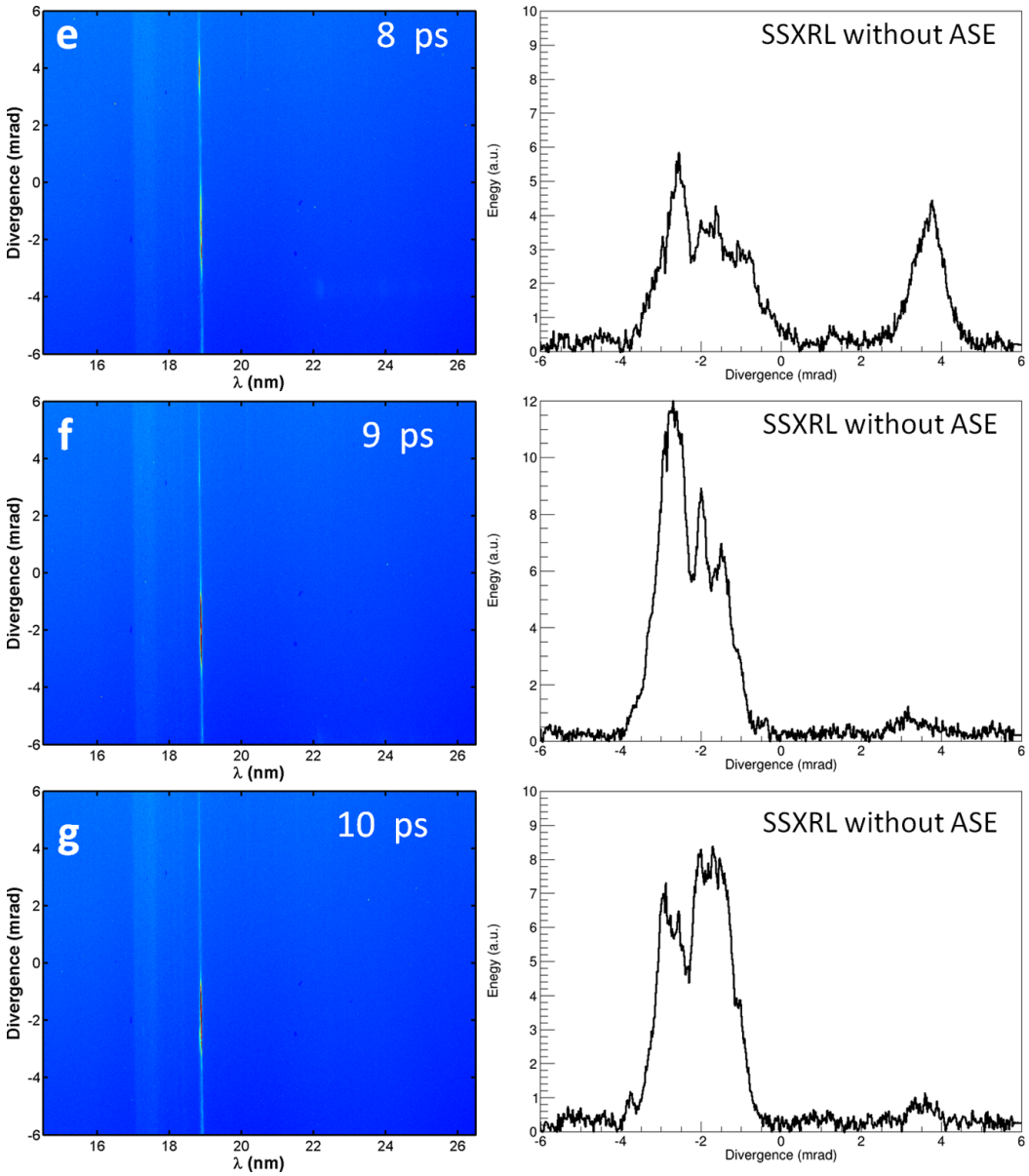

Figure 5.30: Double-HH seeding with a variety of time delays between each other. HH pump was seeded at $T = 6$ ps while HH probe was followed with a series of time delays from $T = 6.25$ ps to $T = 10$ ps.

seeding time from $T = 6$ ps to $T = 10$ ps, one could get the population inversion recovery curve for HH pump seeded at $T = 6$ ps at current plasma amplifier, as represented in $Fig.$ 5.31. It is implying that the depletion of the population inversion was from $T = 6$ ps to $T = 6.5$ ps and the recovery time took 1.5 ps (from $T = 6.5$ ps to $T = 8$ ps). One should pay attention to that the full recovered population inversion never reaches the same level attained at $T = 6$ ps without the HH pump, because at this time the gain is rapidly dropping as it shown $Fig.$ 5.25.

Consequently, we have observed that, in the x-ray plasma amplifier, the population inversion depletion after ultrashort intense seeding ($\sim$60 fs) is fully depleted in $250 - 500$ fs. However, the gain is then

rapidly recovered in $1.5 - 1.75\ ps$ due to the pumping supporting of the collisional excitation from ground sate to upper lasing level (see **Chapter 2**, $Fig.\ 2.14$). The recovered value is following the amplification of the plasma amplifier represented in $Fig.\ 5.25$, which is dependent on the time respected to the peak of short pump IR laser. It is important to point out the original amplification curve was measured using only the HH-pump beam. Therefore, energy gap between the recovery curves ($Fig.\ 5.31$, $Fig.\ 5.28$) and original amplification curve ($Fig.\ 5.25$) is depending on the seed energy difference between the HH pump and HH probe beams. This seed energy effect will be discussed in Section 5.5. Moreover, HH pump seeded at various time, in respect of the plasma short pump IR laser pulse, inducing different recovered gain value which is dependent on the temporal gain evolution, as described in both experimental ($Fig.\ 5.28$ and $Fig.\ 5.31$) and simulation ($Fig.\ 4.19$).

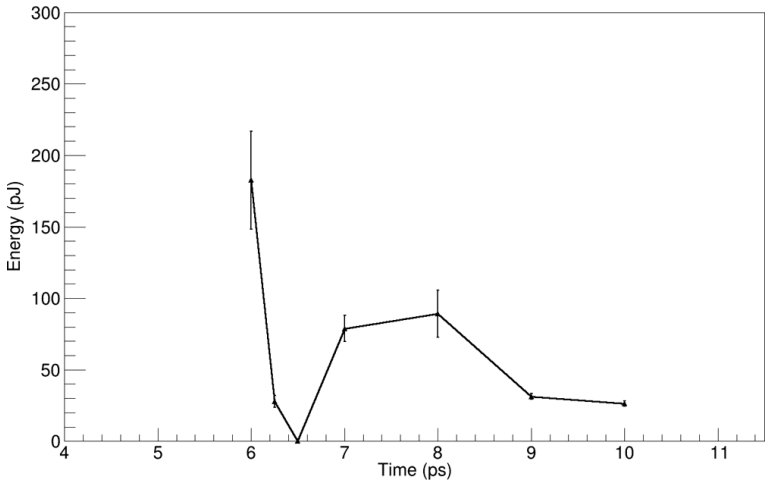

Figure 5.31: Gain recovery curve obtained by seeding HH pump at $T = 6\ ps$ and HH probe at a variety time delays after it.

5.5 Supplementary discussion and Modelling of double-pulse amplification

There are several typical issues are observed during the gain dynamics diagnostic experiment. Such as the effect of HH seed pulse energy and the interference between the two amplified seed are discussed in Section 5.5.1. Furthermore, in Section 5.5.2 and Section 5.5.3, the gain recovery experiment achieved at Colorado State University has been compared with Maxwell-Bloch modelling performed in our group. This numerical study initially aimed at benchmarking our Maxwell-Bloch model onto the experiment with specifically the question of confirming the gain recovery time that is at the heart of soft X-ray Chirped Pulse amplification technique. As we will see, the modelling showed several interesting features about the dynamic of amplified ultra-fast harmonic seed. We will display here only the key results since the full study encompasses hundreds of cases.

5.5.1 Supplementary discussion

Firstly, it is interesting to point out the importance of the HH pump pulse energy during this gain dynamics diagnostics. For instance, in Section 5.2, we demonstrated a case with HH pump seeded at $T = 3\ ps$ and HH probe injected at $T = 3.25\ ps$. As described in $Fig.\ 5.32(a)$, the 1^{st} SSXRL (amplified HH pump) was well amplified at $T = 3\ ps$ and the 2^{nd} SSXRL (amplified HH probe) was below or near the detection limit. This is explained as the population inversion depletion after seeding. However, when the HH pump was not sufficiently amplified at $T = 3.0\ ps$, the amplification of the followed HH probe at $T = 3.25\ ps$ can be apparently observed, as displayed in $Fig.\ 5.32(b)$. According to the measured amplification curved illustrated in $Fig.\ 5.25$, the maximum gain was achieved at $T = 3\ ps$, meaning that an intense HH pump seeded at $T = 3\ ps$ could reach maximum amplification. Simultaneously, the population inversion would be totally depleted. However, once the amplified HH pump was not strong due to the spatial mismatching, refraction in the plasma column or HH-pump seed pulse energy, the population inversion of the plasma amplifier still remains at some level which allows to amply the followed HH probe beam at $T = 3.25\ ps$.

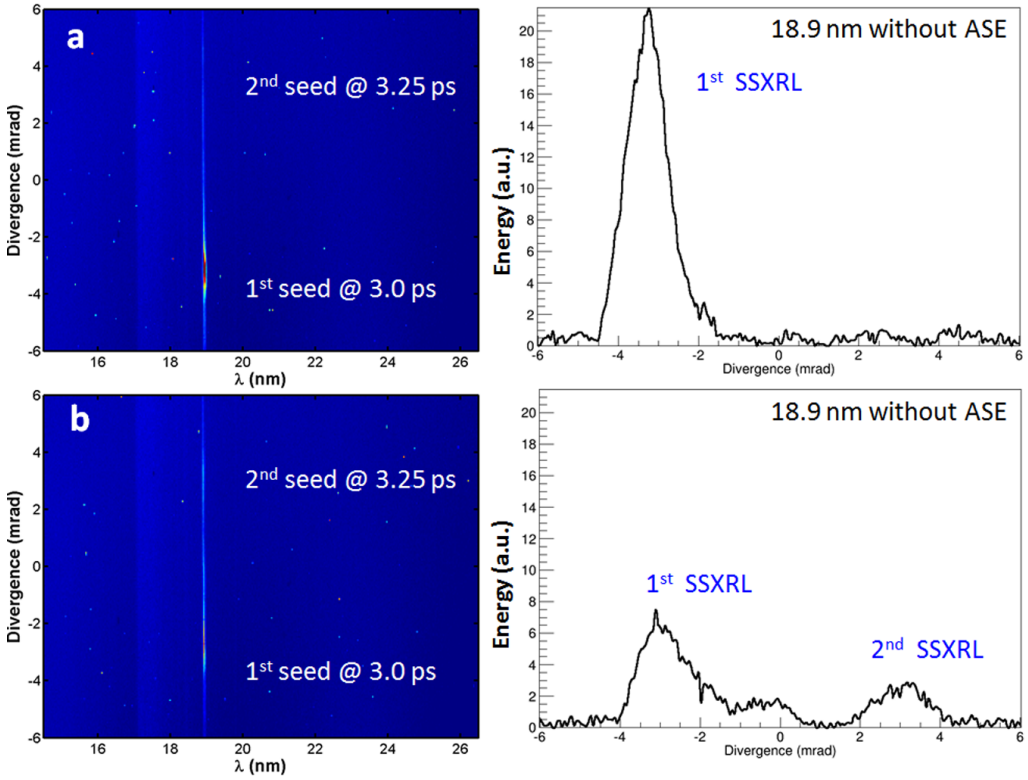

Figure 5.32: Spectral images (left) and integral line-out around $18.9\ nm$ (right) of double-seeded SXRL with the 1^{st} seeding (HH pump) at $T = 3\ ps$ and the 2^{nd} seeding (HH probe) at $T = 3.25\ ps$. (a) The 1^{st} seed was amplified sufficiently, the 2^{nd} seeding was below or near the detection limit. (b) The 1^{st} seed was not reaching saturated amplification, the 2^{nd} seed was apparently observed. ASE signal was removed out in the line-out figure for ease of comparison.

Secondly, output seeded SXRL pulse energy is proportional to the input seed pulse energy as described in $Eq.\ 2.1$. In this gain dynamics diagnostics experiment, different pulse energies of the HH

probe beam were used. As it shown in $Fig.\ 5.33$, the $3\ mm$ long plasma amplifier was pumped by $5\ ps$ short IR pump pulse. HH pump was seeded at $T = 3\ ps$ and HH probe pulses with various energies were seeded at $T = 5\ ps$, when the gain is fully recovered. Integral spectral line-out of double HH pulses are displayed in $Fig.\ 5.33(a1)$, $Fig.\ 5.33(b1)$ and $Fig.\ 5.33(c1)$. The lower one is the HH pump pulse and the upper one is the HH probe pulse. Integral spatial line-out of the 43^{rd} order HH pulse around $18.9\ nm$ are depicted in $Fig.\ 5.33(a2)$, $Fig.\ 5.33(b2)$ and $Fig.\ 5.33(c2)$ with different pulse energies of the HH probe beam. After seeding to the $3\ mm$ plasma amplifier, the amplified seeds at $18.9\ nm$ are illustrated in $Fig.\ 5.33(a3)$, $Fig.\ 5.33(b3)$ and $Fig.\ 5.33(c3)$. Amplification around $60\ times$ was observed on the HH pump pules. Comparing these three cases with different seeding energies of HH probe pulse, one could conclude that the output amplified seed energy is partially dependent on the seed pulse energy with non-linear relation.

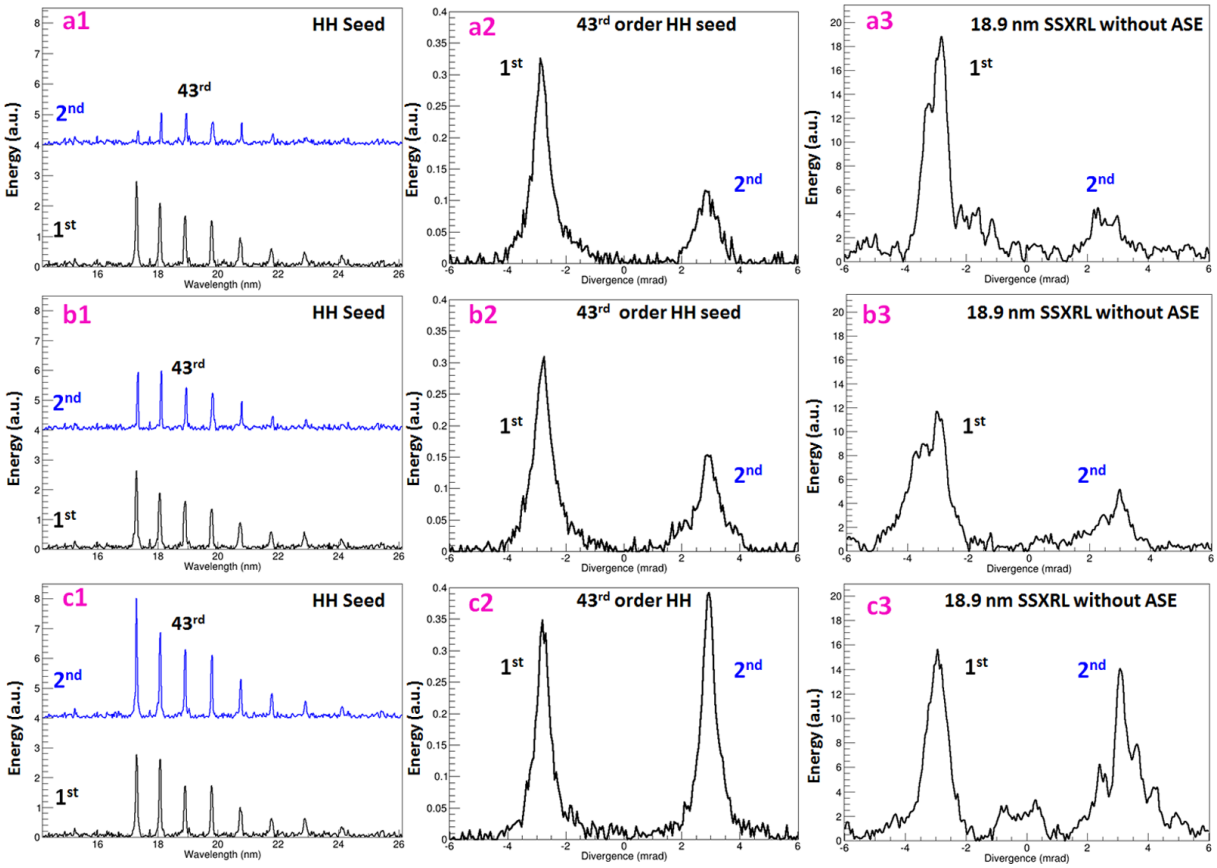

Figure 5.33: Comparison of SSXRL output with various of the 2^{nd} HH seed energies. (a1)-(a3): Integral spectral line-out of the HH seed with same energy of 1^{st} and different energies of 2^{nd} HH seed. (b1)-(b3): Spatial line-out of the double HH seed around $18.9\ nm$ (43^{rd} HH order). (c1)-(c3): Spatial line-out of the double seeded SXRL (SSXRL) with the 1^{st} seeding at $T = 3\ ps$ with same energy and the 2^{nd} seeding at $5\ ps$ with a variety of energies. ASE signal was removed out.

Thirdly, some interference was observed between the double-seeding outputs. Further analysis of $Fig.\ 5.14(g)$ is done in $Fig.\ 5.34$, where the $3\ mm$ plasma amplifier was pumped with $5\ ps$ short IR laser. The HH pump beam was seeded at $T = 3\ ps$ and HH probe was sent at $T = 5\ ps$, when the population

inversion was fully recovered. Spectral image and integral line-out around $18.9\ nm$ of the double-seeded SXRL are displayed in $Fig.\ 5.34(a)$ and $Fig.\ 5.34(b)$, respectively. It consists of ASE and double amplified seed pulses as marked in $Fig.\ 5.34(b)$. The red line indicates ASE fitting curve. Interestingly, a third beam was clearly observed between the two amplified beam. The wake of each amplified beam must be taken into account to explain this phenomena. Normally, after HH pulse seeded into the plasma amplifier, the amplified seed signal is followed by a long wake signal (several picoseconds) as illustrated in $Fig.\ 4.4$. Considering that the time delay between HH pump and HH probe pulses is $2\ ps$, the HH probe can be superposed to the wake of the HH pump. Interference between the wake caused by HH pump seeding and the amplified HH probe could occur. Furthermore, the two output amplified seed signals are simulated using a time-dependent Maxwell-Bloch modelling coupled with two-dimensional hydrodynamic modelling [20]. More discussion will be given in Section 5.5.3. Nevertheless, this experiment was not designed for the detection of wake signal. Further investigation requires a particular seeding experiment.

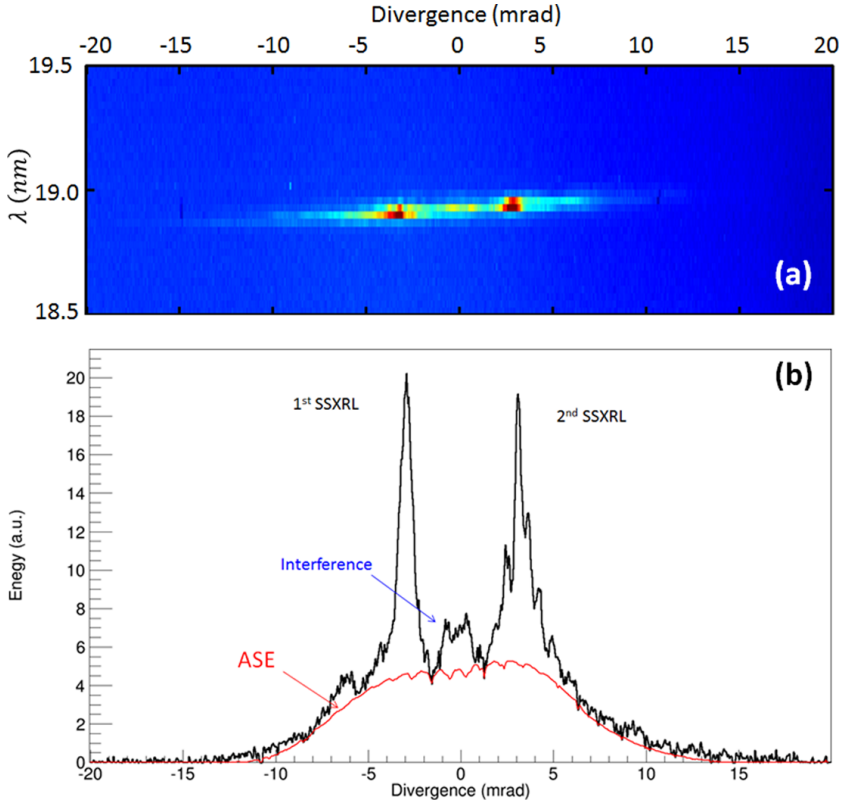

Figure 5.34: Spectral image (a) and integral line-out (b) around $18.9\ nm$ of the double-seeded SXRL from $3\ mm$ long plasma amplifier pumped with $5\ ps$ short IR laser pulse . HH pump was seeded at $T = 3\ ps$ and HH probe was injected at $T = 5\ ps$.

5.5.2 Gain and gain recovery dynamics versus seeding conditions

It is noticed that experimental results could not be precisely reproduced unless the spatio-temporal dynamics of the lasing ion is fully taken into account. $Fig.\ 5.35$ shows the simulated spatio-temporal evolu-

tion of the lasing ion relative abundance ($Fig.\ 5.35(a)$) and the mean degree of ionization ($Fig.\ 5.35(b)$) used in the Maxwell-Bloch model later. As the HH probe beam covers regions of different ionization and Nickel-like ion density, the modelling has to spatially average the plasma parameters for comparison with the experimental data. This method using averaged valued gave very good modelling-experiment agreement. In contrast, considering local plasma parameters for HH probe or HH pump amplification lead to clear disagreement with experimental data. Thus, this pump-probe experiment not only uncovers the gain recovery dynamics due to electron collisions but also serves as a diagnostic of the ionization mechanisms in the hot dense plasma amplifier with $100s$ femtosecond resolution.

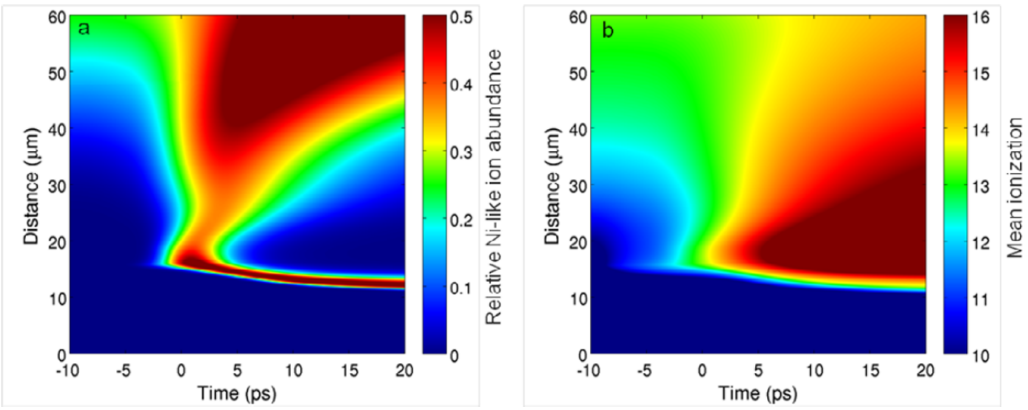

Figure 5.35: Hydrodynamic simulation of the lasing ion abundance. In figure (a), false color map of the spatio-temporal variation of Ni-like Molybdenum relative abundance as calculated by the hydrodynamic code. Figure (b) displays in false color the mean plasma ionization. For both figures, the temporal scales are set in a way that $t = 0\ ps$ is the time when the short IR heating pulse hits the plasma. The target surface lies at "$0\ \mu m$" position with positive distances corresponding to vacuum. from [1]

The first part has been to directly reproduce the experimental data by adjusting the seeding conditions. The plasma density was extracted from the results of a 2D hydrodynamic modelling performed by Mark Berrill from Colorado State University, USA (see $Fig.\ 5.35$). Although this kind of code gives realistic values of the plasma parameters in general, the peculiar grazing incidence geometry for the IR pump laser cannot be fully treated with a 2D code. This implies that the plasma conditions as seen by the high harmonic seed might be slightly different from those given by the code. Also, despite a lot of efforts to know precisely the high harmonic parameters, some errors may exist. The most evident is the energy injected in the gain region that is lower than the energy measured directly at the exit of the gas puff used to generate the high harmonics. The reflections of the different optical elements are relatively well known, however the exact geometrical coupling (ratio between the surface of the gain zone to the high harmonic cross-sectional surface) and bandwidth of the HH seed and amplified seed [8] are very difficult to access experimentally. Finally, we also explored the influence of the high harmonic pulse duration as a general test.

On $Fig.\ 5.36$, we compare the influence of the energy of the HH pump pulse, when seeded at $3\ ps$ onto the depletion of the gain. When its energy is doubled from (a) $5\ pJ$ to (b) $10\ pJ$ and then doubled again up to (c) $20\ pJ$, we may observe that the gain depletion is not stronger. However, the gain does not fully recover. For the case when the pump is seeded at $6\ ps$, the gain is already rather low and no difference is visible.

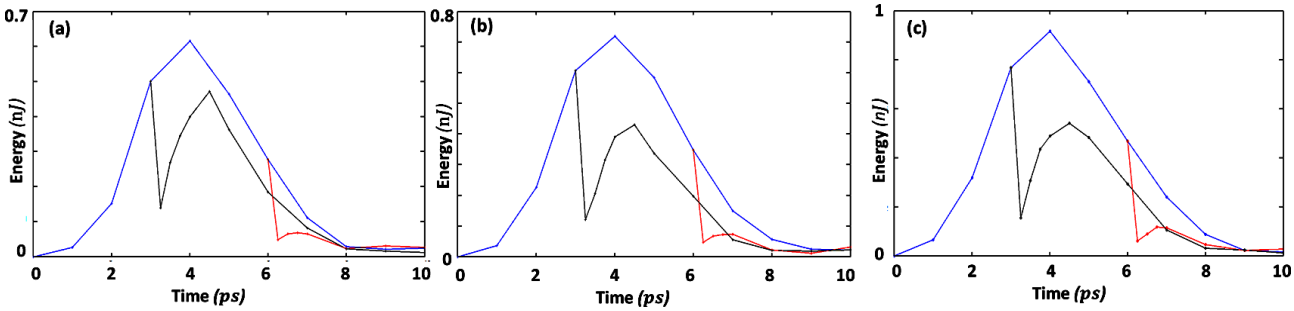

Figure 5.36: Blue, black and red curves stand for the amplified energy of HH pump alone, the HH probe when the HH pump is seeded at $3\ ps$ *and* $6\ ps$ *respectively. HH pump energy at the plasma entrance is (a)* $5\ pJ$*, (b)* $10\ pJ$ *and (c)* $20\ pJ$*.*

For a given HH pump energy, the influence of the HH probe energy can be noticed on the maximum amplification level. Indeed when doubling the energy of the HH probe from $2\ pJ$ (see $Fig.\ 5.37(a)$) to $4\ pJ$ (see $Fig.\ 5.37(b)$), the output energy at maximum amplification raises from $42\ pJ$ to $52\ pJ$. This small change is due to the saturation of the amplification.

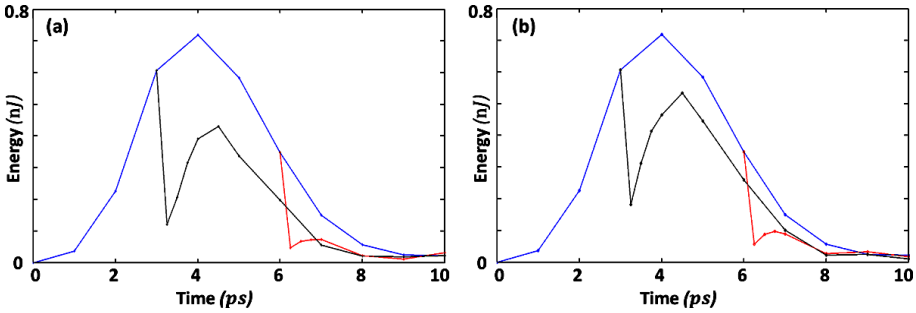

Figure 5.37: Same colour selection as $Fig.\ 5.36$*. The HH probe energy is* $2\ pJ$ *for case (a) and* $4\ pJ$ *for case (b).*

We thus varied the plasma conditions in $Fig.\ 5.38$. The most sensitive parameter in the simulation is the electron density. We thus concentrated our work on that parameter. We modified the electron density from the initial value by dividing it by a factor of 2 and multiplying it by a factor of 1.5. The gain of the HH pump alone is very much modified with density. At lowest density (case $1, 0.5\ times$ the density given by the code), the amplification rises much faster to peak at $3\ ps$, while for the highest density the peak is shifted to $4\ ps$. Also the amplification of the HH probe pulse is strongly modified. We may observe that when the density is very low (0.5 and $0.8\ times$ the nominal value) and the HH pump is seeded at $6\ ps$, the amplification is negligible showing a very weak gain recovery. On the contrary for the HH pump at $3\ ps$, the lowest densities give relatively high amplification.

As a conclusion, we observed that the gain recovery experiment is very sensitive to electron density. This is an excellent probe. The very good agreement between our experiment and the modelling for the electron density calculated by the 2D hydrodynamic code gives a wonderful benchmark of the code. It is interesting to note also that the high harmonic energy is not critical on the gain recovery dynamic.

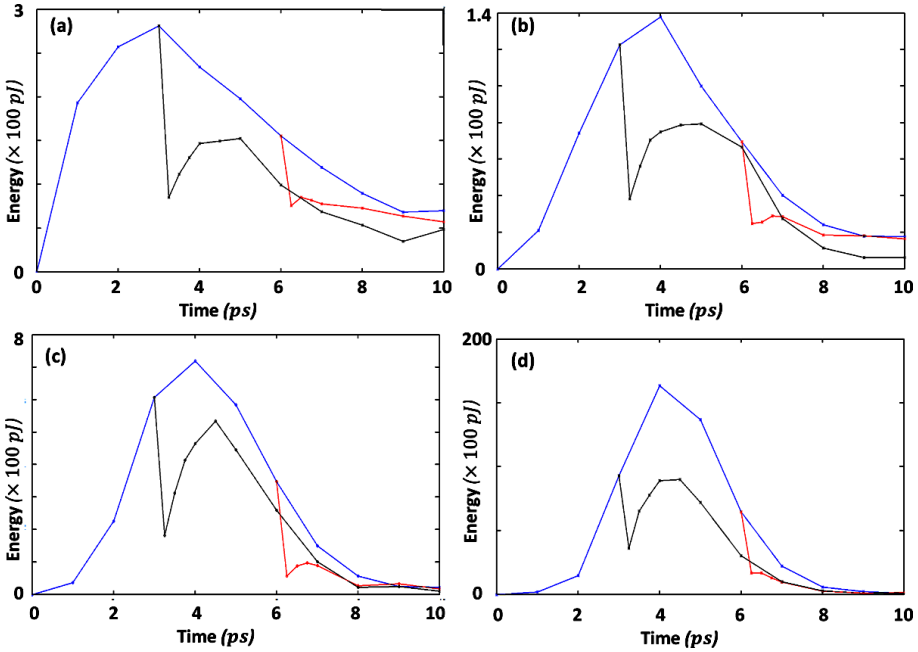

Figure 5.38: Same colour selection as $Fig.$ 5.36. The electron density raises from (a) 0.5, to (b) 0.8, (c) 1 and (d) 1.5 the nominal value given by the $2D$ hydrodynamic code with respect to the plasma parameters described in $Fig.$ 5.35.

5.5.3 Temporal evolution of the amplified HH pump and probe intensities versus seeding conditions

The above modelling being in good agreement with the experiment, which give high confidence on the other results of the simulations. A key result is the temporal evolution of the output intensities for both the HH pump and HH seed pulses. Indeed, although the HH seed (both pump and probe) are $30\ fs$ in duration, it is well known that with the seeding conditions, the harmonic pulse itself is barely amplified while creating a wake field that contains most of the output energy [21, 22, 23]. Since for a single pulse, the wake field might be as long as $5\ ps$, at the time of the experiment and early data treatment it was unclear how this long wake may impact the gain recovery measurement. The images in $Fig.$ 5.39 show the temporal evolution of the two HH pulses when the pump is seeded at $T = 3\ ps$ and the probe is varied from $T = 3.25\ ps$ to $T = 5\ ps$.

Although the above images have been displayed from the shortest delay $(250\ fs)$ between the pump and the probe, we invite the reader to look at the images from the $Fig.\ 5.39(f)$ to $Fig.\ 5.39(a)$ for having a better understanding of the interaction between the two amplified seed pulses. On $Fig.\ 5.39(f)$, the HH pump and HH probe exhibits nearly the same shape with the peak of the amplified HH followed by a wake field lasting about $2\ ps$. Although the peak intensity of the HH pulse is higher than the intensity of the wake, the total energy is much higher for the wake than for the HH pulse. As one may expect, where there is the highest the density, there is the shortest wake. Also, it is interesting to note that for the case at $n_e = 1.6\times10^{20}\ cm^{-3}$, ASE appears prior the HH probe.

When the probe is seeded closer and closer to the pump, three phenomena appeared:
1) the amplified HH pulse intensity decreases to be quickly negligible (for a delay around $0.75\ ps$ to $1\ ps$),

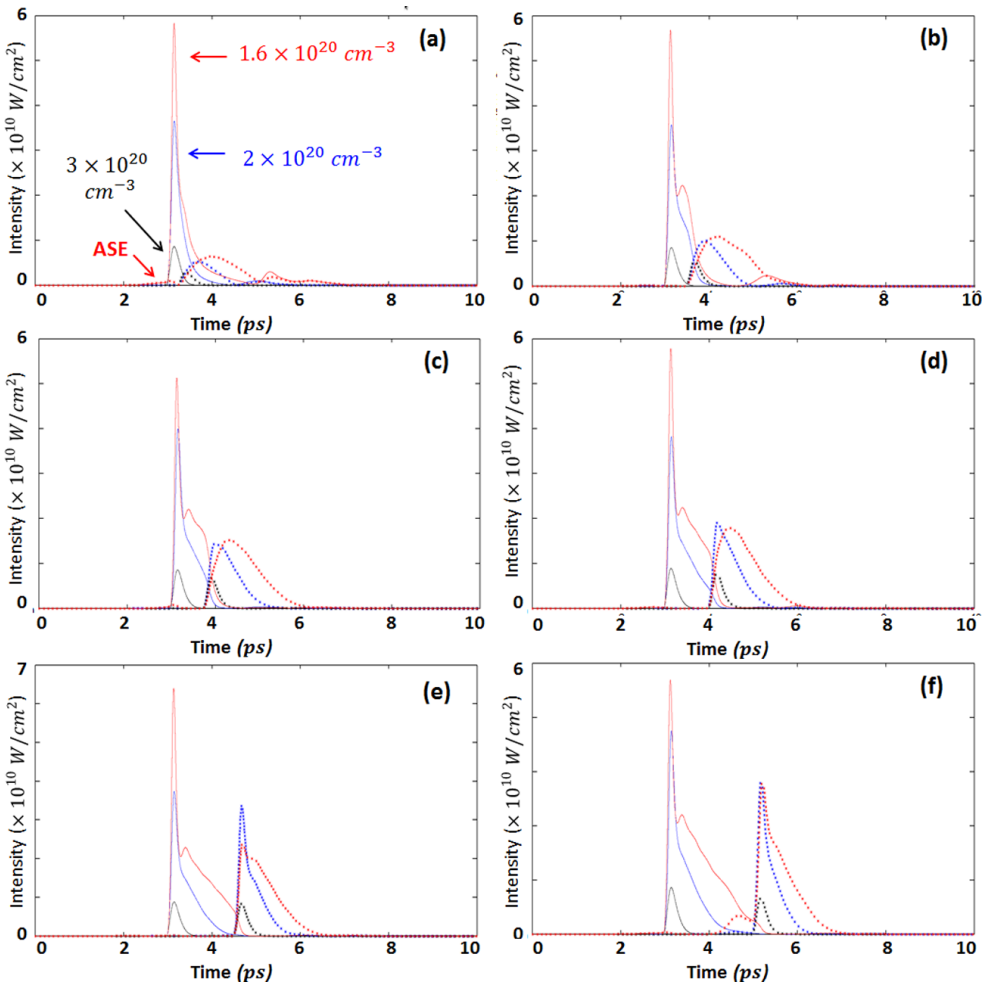

Figure 5.39: Temporal evolution of the intensity of the HH pump (plain lines) and HH probe (dotted lines) for different densities: $1.6\times10^{20}\ cm^{-3}$ *(red lines),* $2.0\times10^{20}\ cm^{-3}$ *(blue lines) and* $3.0\times10^{20}\ cm^{-3}$ *(black lines). From (a) to (f), the seeding time of the HH pump is kept constant at* $3\ ps$ *while the seeding time of the probe is varying: (a)* $3.25\ ps$*, (b)* $3.5\ ps$*, (c)* $3.75\ ps$*,(d)* $4\ ps$*, (e)* $4.5\ ps$ *and (f)* $5\ ps$*.*

2) the intensity of the wake field decreases also from $3\times10^{10}\ Wcm^{-2}$ to $0.8\times10^{10}\ Wcm^{-2}$,
3) the wake field of the amplified HH pump is clipped, to leave place for amplifying the HH probe only when the delay is more than $350\ fs$,
The strong change on the temporal shape of the amplified HH probe is due to the polarization of the plasma by the HH pump, that prevents it to react sufficiently fast for keeping the temporal structure of the HH probe. However, the reductions of the HH probe intensity (and thus energy) and the clipping of the wake initiated by the HH pump is clearly an effect of the saturation.

We performed the same modelling when seeding the HH pump at $T = 6\ ps$ and thus the HH probe from $T = 6.25\ ps$ up to $T = 8\ ps$ (see $Fig.\ 5.40$). We observed the same cross-talk between the two pulses with nearly the same effects. However, it is interesting to note that for a delay of $2\ ps$ ($Fig.\ 5.40(e)$), the amplified HH probe does not exhibit the peak characteristic of the harmonic as one can see on$Fig.\ 5.39(2)$. It is very likely due to the low population inversion achieved at this time

($T = 8\ ps$), that is thus more strongly modified by the wake field of the HH probe that in the case of the HH pump is seeded at $3\ ps$ and HH probe at $5\ ps$. We observe also a strong ASE ahead of the HH probe.

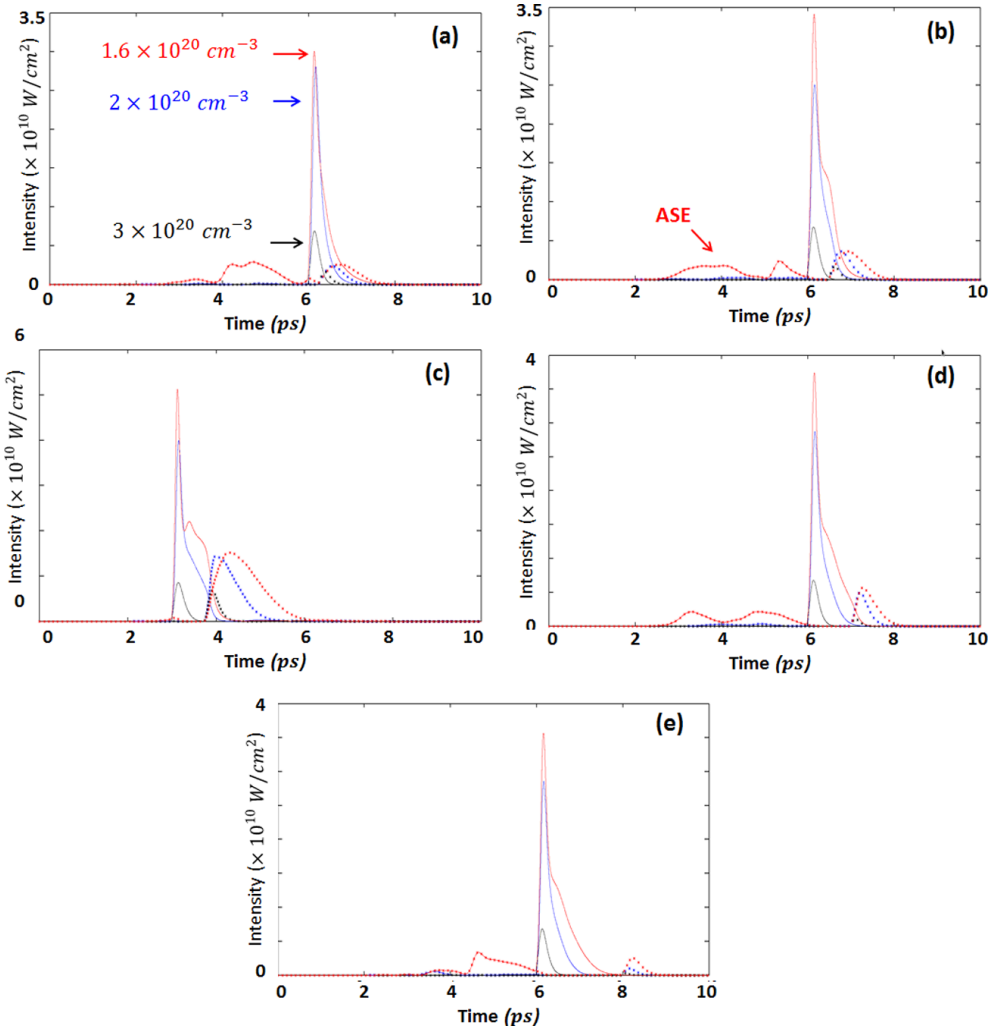

Figure 5.40: Temporal evolution of the intensity of the HH pump (plain lines) seeded at $T = 6\ ps$ and HH probe (dotted lines) seeded at (a) $T = 6.25\ ps$, (b) $T = 6.5\ ps$, (c) $T = 7\ ps$,(d) $T = 7.5\ ps$ and (e) $T = 8\ ps$ and for different densities: $1.6\times10^{20}\ cm^{-3}$ (red lines), $2.0\times10^{20}\ cm^{-3}$ (blue lines) and $3.0\times10^{20}\ cm^{-3}$ (black lines).

In conclusion, the detailed modelling showed a quite complex interaction between the two amplified pulses due to the plasma polarization and the saturation. We may imagine two slightly delayed HH pulses for shortening the first pulse duration when using low-density amplifier. We would like to stress out that these modelling are one dimension only. However, Sophie Kazamias, Sameh Daboussi and the colleagues [24] have shown that two tilted IR pump lasers may produce, due to constructive interference, an enhancement of the on-axis field generating a HH beam at the bisectrix of the two pump pulses. On very few measurements, we observed a weak pulse at the middle of the two amplified HH pulses, as it shown in $Fig.\ 5.34$. We have the strong feeling that such beam is generated from a mechanism similar to that observed by S. Kazamias, S. Daboussi *et al.* [24] and due to the interference of the two amplified

HH pulses. The very interesting point here is that such on-axis beam appeared for HH pump-probe delays up to $2\ ps$ that are much larger than the HH pulse duration ($30\ fs$). If confirmed it is a clear evidence that the HH wake fields kept the spatial coherence of the HH pulse due to plasma polarization. Obviously, $3D$ Maxwell-Bloch modelling is necessary to model this case. In collaboration with Alfonso Barbas from Prof. Pedro Velarde's group, we are setting up the required $3D$ Maxwell-Bloch code.

Bibliography

[1] Y. Wang, S.Wang, E. Oliva, L. Li, M. Berril, L. Yin, J. Nejdl, B. M. Luther, C. Proux, T. T. T. Le,J. Dunn, D. Ros, Ph. Zeitoun and J. J. Rocca, Nature Photonics **8**, 381-384 (2014).

[2] X-ray data base from http://www.cxro.lbl.gov/

[3] A. McPherson, G. Gibson, H. Jara, U. Johann, T. S. Luk, I. A. McIntyre, K. Boyer and C. K. Rhodes, J. Opt. Soc. Am. B **4**, 595 (1987).

[4] M. Ferray, A. L'Huillier, X. F. Li, L. A. Lompre, G. Mainfray and C. Manus, J. Phys. B: At. Mol. Opt. Phys. **21**, L31 (1988).

[5] A. L'Huillier, K. J. Schafer and K. C. Kulander, J. Phys. B: At. Mol. Opt. Phys. **24**, 3315-3341 (1991).

[6] http://www.andor.com/

[7] Y. Wang, E. Granados, F. Pedaci, D. Alessi, B. Luther, M. Berrill, and J. J. Rocca, Nat. Photonics **2**, 94 (2008).

[8] L. M. Meng, D. Alessi, O. Guilbaud, Y. Wang, M. Berrill, B.M. Luther, S. R. Domingue, D. H. Martz, D. Joyeux, S. De Rossi, J. J. Rocca, and A. Klisnick, Optics Express **19**,12087-12092 (2011).

[9] A. Calisti , S. Ferri , C. Mossé, B. Talin, A. Klisnick, L. Meng, D. Benredjem and O. Guilbaud, High Energy Density Physics **9**, 516-522 (2013).

[10] D.H. Reitze, S. Kazamias, F. Weihe, G. Mullot, D. Douillet, F. Aug, O. Albert, V. Ramanathan, J.P. Chambaret, D. Hulin, P. Balcou, Opt. Lett. **29**, 86–88 (2004).

[11] T. Kanai, S. Minemoto and H. Sakai, Nature **430**, 470-474 (2005).

[12] C. Figueira de Morisson Fariam Phys. Rev. A **76**, 043407 (2007).

[13] S. Daboussi, S. Kazamias, K. Cassou, O. Guilbaud, M. Pittman, O. Delmas, O. Neveu, B. Cros, G. Maynard and D. Ros, Appl. Phys. B **111**, 7-14 (2013).

[14] A. Camper, T. Ruchon, D. Gauthier, O. Gobert, P. Salieres, B. Carre, and T. Auguste, Phys. Rev. A **89**, 043843 (2014).

[15] Y. Wang, E. Granados, M. A. Larotonda, M. Berrill, B. M. Luther, D. Patel, C. S. Menoni, and J. J. Rocca, Phys. Rev. Lett. **97**, 123901 (2006).

[16] L. Li, Y. Wang, S. Wang, E. Oliva, L. Yin, T. T. Thuy Le, S. Daboussi, D. Ros, G. Maynard, S. Sebban, B. Hu, J. J. Rocca, and Ph. Zeitoun, Optics Lett. **38**, 4011-4014 (2013).

[17] Y. Wang, M. Berrill, F. Pedaci, M. M. Shakya, S. Gilbertson, Zenghu Chang, E. Granados, B. M. Luther, M. A. Larotonda, and J. J. Rocca, Phys. Rev. A **79**, 023810 (2009).

[18] E. Oliva, M. Fajardo, L. Li, M. Pittman, T. T. T. Le, J. Gautier, G. Lambert, P. Velarde, D. Ros, S. Sebban, and P. Zeitoun, Nat. Photonics **6**, 764 (2012).

[19] F. Tissandier, S. Sebban, M. Ribi'ere, J. Gautier, Ph. Zeitoun, G. Lambert, A. Barszczak Sardinha, J.-Ph. Goddet, F. Burgy, T. Lefrou, C. Valentin, and A. Rousse, Phys. Rev. A **81**, 063833 (2010).

[20] M. Berrill, D. Alessi, Y. Wang, S. R. Domingue, D. H. Martz, B. M. Luther, Y. Liu, and J. J. Rocca, Optics Lett. **35**, 2317-2319 (2010).

[21] I. R. Al'miev, O. Larroche, D. Benredjem, J. Dubau, S. Kazamias, C. Moller, and A. Klisnick, Phys. Rev. Lett. **99**, 123902 (2007).

[22] C. M. Kim, J. Lee and K. A. Janulewicz, Phys. Rev. Lett. **104**, 053901 (2010).

[23] E. Oliva, Ph. Zeitoun, M. Fajardo, G. Lambert, D. Ros, S. Sebban, and P. Velarde. Phys. Rev. A **84**, 013811 (2011).

[24] S. Daboussi, *Accord de phase et quasi accord de phase en génération d'harmoniques d'ordres élevés: effect de la pression et du guidage laser*, February 2013.

CHAPTER 6

Conclusions and Perspectives

Soft x-ray lasers (SXRL) have become essential research tools across several disciplines, from biology, chemistry, nonlinear optics, nanostructure to atomic physics. However, most of the table-top SXRL are based on the process of amplified spontaneous emission (ASE). The long pulse duration ($\sim ps$) and low spatial coherence due to the stochastic nature of ASE are limiting factors for applications. ASE self seeding with oscillator-amplifier configuration was firstly attempted at GSI (Germany), which showed poor energy amplification and limited improvement on the coherence (**Chapter 3, Section 3.1**). Seeding highly ionized x-ray plasma amplifiers with fully coherent and ultra-short high order harmonics (HH) pulses have shown great potential. Therefore this thesis aimed at progressing further on understanding and improving this scheme thanks to numerical and experimental studies.

HH-seeded SXRL was tested using neon-like titanium plasma ($32.6\ nm$) at LASERIX facility, which was discussed in **Chapter 3, Section 3.2**. Amplification of the seed was evident but limited by refraction experienced in the plasma. A second SXRL seeding experiment was then carried out in Colorado State University with nickel-like molybdenum plasma amplifier ($18.9\ nm$). High energy amplification ($\sim 100\ times$) has been measured. The use of toroidal mirror to image relay the HH source onto the entrance of plasma amplifier may account for this. Meanwhile, an x-ray Hartmann wave front sensor was employed to measure the wave front of both HH seed and amplified seed beams (**Chapter 3, Section 3.3**). Due to the spatial filtering of the HH seed during the amplification process, HH-seeded SXRL showed a good wave front with distortions reaching $\lambda/5$ root-mean-square. The wave front was improved by $2.5\ times$ as compared to the HH seed while at the same time the stability was increased $4\ times$. Wave front was also studied versus the injection time. Finally, back-propagation of this seeding x-ray source was performed indicating a tiny source size $\sim 20\ \mu m$, which confirms its high brightness of $\sim 1\times 10^{26}\ photons{\cdot}s^{-1}{\cdot}mm^{-2}mrad^{-2}$. This seeded SXRL source showed the capability of reaching diffraction-limited ($\lambda/14$) beam by optimizing the input HH seed beam quality.

Based on a $2D$ hydrodynamic code (ARWEN) and $1D$ time-dependent Maxwell-Bloch model (Deep-One) developed by our colleagues from Universidad Politecnica de Madrid and collaborators, full time-dependent calculation of the amplification of HH seed in SXRL amplifier was worked out in **Chapter 4**. Seeding a single plasma-amplifier was firstly simulated. Seeding an elongated HH pulse ($200\ fs$) into a $1\ mm$ wide plasma amplifier showed energy up to $1.4\ \mu J$ in $80\ fs$ duration. Modelling of multi-stage plasma amplifier gave output SXRL pulse achieving $25\ \mu J$ in $80\ fs$.

Further exploring the capacity of extracting higher energy from plasma, here pumped by ns infrared lasers, while keeping the pulse duration short showed a surprising drop of efficiency. Detailed study of the amplification process revealed a rapid depletion ($< 300\ fs$) of the gain followed by a full recovery after about $1.5\ ps$, strongly limiting direct amplification of the short pulse while leaving ASE reaching $mJ\ level$.

At last, in **Chapter 5**, gain recovery time was measured for the first time in a soft x-ray pump/soft x-ray probe experiment conducted at Colorado State University in USA. Two HH pulses were seeded in plasma with variable time delays. The relative amplification of both pulses allow to directly measuring

the gain recovery time ($\sim 1.7\ ps$). It was found in very good agreement with our modelling. Moreover, in **Chapter 4**, we numerically explored the possibility to amplify at pulse train ($100\ pulses$) or a single long pulse with duration fitting the gain lifetime. In the sake of practical reality, we concentrated our study on amplification of long HH pulse by transposing the so-called Chirped Pulse Amplification (CPA) to the soft x-rays. Modelling showed that pulses with energy of several mJ with duration around $200\ fs$ could be generated with soft x-ray CPA. Compressor is here a key element, some first studies are presented. Further CPA SXRL pulse shortening was discussed by temporal shaping the gain profile, which provides a capability of reaching Fourier-limited beam ($\sim 100\ fs$).

A brief summary of the SXRL source development, illustrated in the following figure ($Fig.\ 6.1$), shows the progress on peak intensity and pulse duration. Experimental achievements and numerical predictions of the HH sources, ASE from laser-induced plasma, seeded SXRL (SSXRL) from both gas- and solid-based plasma amplifiers, soft x-ray CPA system and x-ray free-electron lasers (XFEL at FLASH) have been taken into account. The partially achievements need to be verified (such as optimized focusing with the diffraction-limited beam and final decision of the submitted article). All the prospected results are, so far, only done as the simulation work.

In context of current thesis work, one could have a near future outlook:
1) soft x-ray gratings are capable to reach high diffraction efficiency ($\sim 50\%$) under the conical diffraction configuration;
2) the nowadays PW Ti:sapphire laser facilities are adequate to built a soft x-ray CPA system;
3) soft x-ray CPA has a potential of reaching mJ-level SXRL pulse within $140\ fs$ time duration;
4 once the first soft x-ray CPA system successfully established, it can be extended to the "water window";
5) long HH pulse (tens of ps) generation may be interesting in injection to the plasma amplifier;
6) generation of ultra-fast pulse trains for quasi-phase-matching HH generation need to be worked out to reach a train of seed pulses for the amplification in x-ray plasma amplifier;
7) the relevant detection techniques of the ultrashort SXRL pulse need to be widely studied, such as pulse duration measurement and observation of Rabi-oscillation;
8) SXRL probing technique will become to be a preferred diagnosis approach in many scientific areas, for example, plasma diagnosis;
9) many important applications that demand high spatial (nanometer) and high temporal (hundreds of femtoseconds) resolutions will be benefited with this SXRL source.

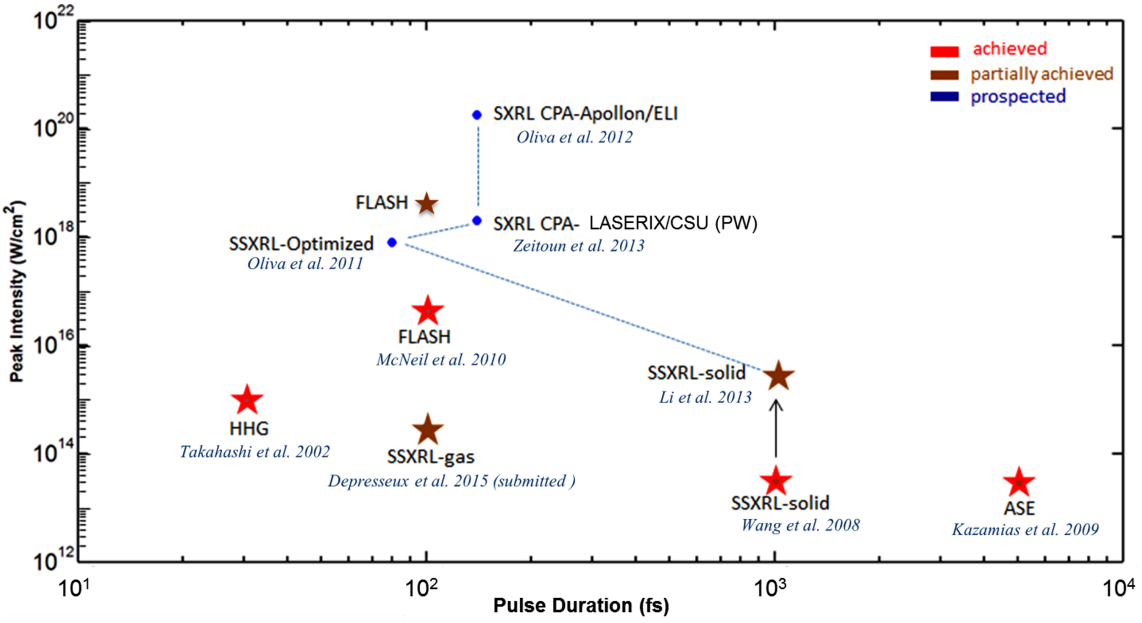

Figure 6.1: State-of-the-art development of plasma-based soft x-ray lasers.

Appendices

APPENDIX A

Wave Front Aberrations

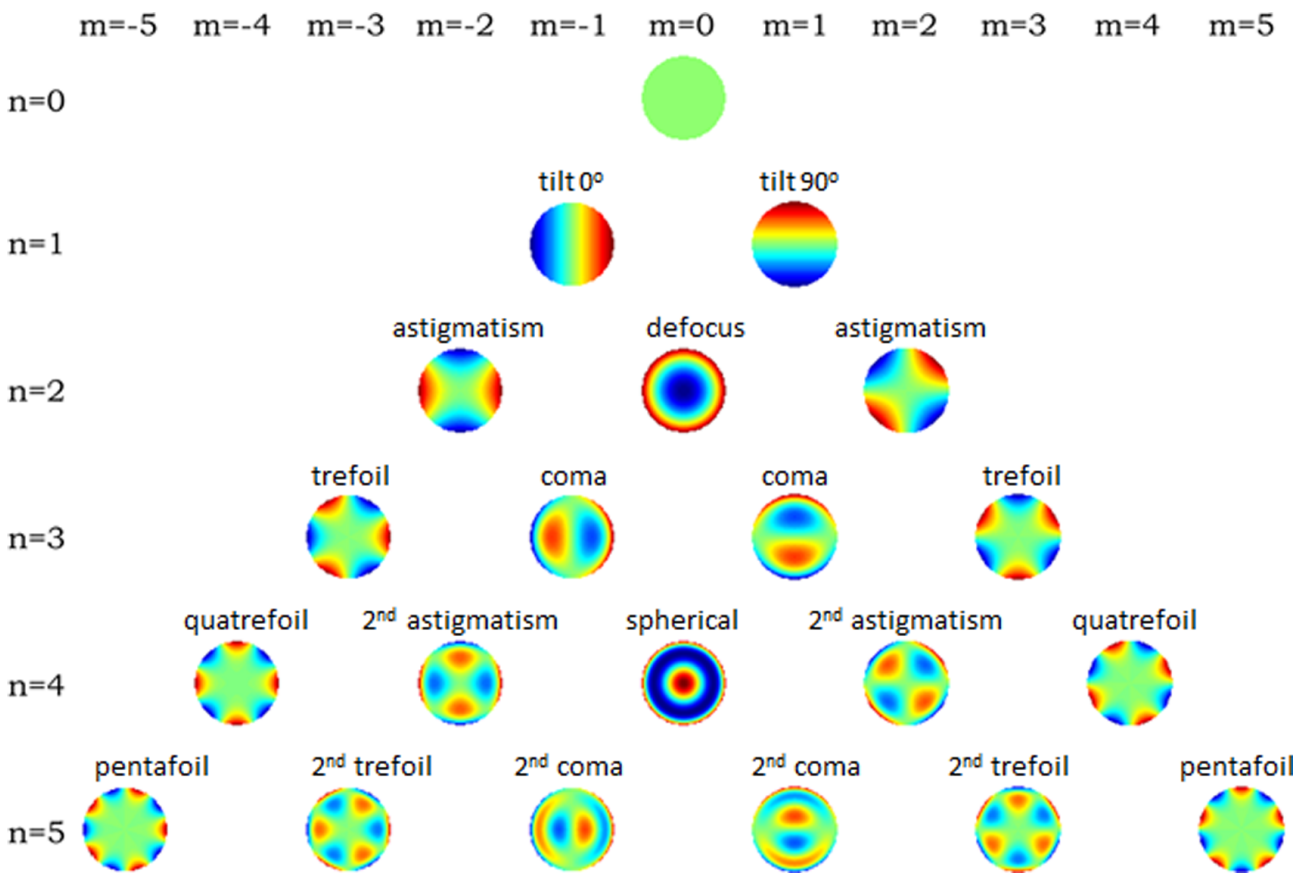

Figure A.1: Aberrations expressed by Zernike Polynomials.

Table A.1: Expression for Zernike RMS Polynomials

N^o	n	m	Polynomial	Classical name
1	1	1	$2\rho\cos\theta$	Tilt at 0^o
2	1	-1	$2\rho\sin\theta$	Tilt at 90^o
3	2	0	$\sqrt{3}(2\rho^2\text{-}1)$	Focus
4	2	2	$\sqrt{6}\rho^2\cos2\theta$	Astigmatism at 0^o
5	2	-2	$\sqrt{6}\rho^2\sin2\theta$	Astigmatism at 90^o
6	3	1	$\sqrt{8}(3\rho^2\text{-}2)\rho\cos\theta$	Coma at 0^o
7	3	-1	$\sqrt{8}(3\rho^2\text{-}2)\rho\sin\theta$	Coma at 90^o
8	4	0	$\sqrt{5}(6\rho^4\text{-}6\rho^2\text{+}1)$	3^{rd} order spherical
9	3	3	$\sqrt{8}\rho^3\cos3\theta$	Trefoil at 0^o
10	3	-3	$\sqrt{8}\rho^3\sin3\theta$	Trefoil at 90^o
11	4	2	$\sqrt{10}(4\rho^2\text{-}3)\rho^2\cos2\theta$	5^{th} order astigmatism at 0^o
12	4	-2	$\sqrt{10}(4\rho^2\text{-}3)\rho^2\sin2\theta$	5^{th} order astigmatism at 45^o
13	5	1	$\sqrt{12}(10\rho^5\text{-}12\rho^3\text{+}3\rho)\cos\theta$	5^{th} order coma at 0^o
14	5	-1	$\sqrt{12}(10\rho^5\text{-}12\rho^3\text{+}3\rho)\sin\theta$	5^{th} order coma at 90^o
15	6	0	$\sqrt{7}(20\rho^6\text{-}30\rho^4\text{+}12\rho^2\text{-}1)$	5^{th} order spherical
16	4	4	$\sqrt{10}\rho^4\cos4\theta$	Tetrafoil at 0^o
17	4	-4	$\sqrt{10}\rho^4\sin4\theta$	Tetrafoil at 45^o
18	5	3	$\sqrt{12}(5\rho^5\text{-}4\rho^3)\cos3\theta$	7^{th} order trefoil at 0^o
19	5	-3	$\sqrt{12}(5\rho^5\text{-}4\rho^3)\sin3\theta$	7^{th} order trefoil at 90^o
20	6	2	$\sqrt{14}(15\rho^6\text{-}20\rho^4\text{+}6\rho^2)\cos2\theta$	7^{th} order astigmatism at 0^o
21	6	-2	$\sqrt{14}(15\rho^6\text{-}20\rho^4\text{+}6\rho^2)\sin2\theta$	7^{th} order astigmatism at 45^o
22	7	1	$\sqrt{16}(35\rho^7\text{-}60\rho^5\text{+}30\rho^3\text{-}4\rho)\cos\theta$	7^{th} order coma at 0^o
23	7	-1	$\sqrt{16}(35\rho^7\text{-}60\rho^5\text{+}30\rho^3\text{-}4\rho)\sin\theta$	7^{th} order coma at 90^o
24	8	0	$3(70\rho^8\text{-}140\rho^6\text{+}90\rho^4\text{-}20\rho^2\text{+}1)$	7^{th} order spherical
25	5	5	$\sqrt{12}\rho^5\cos5\theta$	Pentafoil at 0^o
26	5	-5	$\sqrt{12}\rho^5\sin5\theta$	Pentafoil at 90^o
27	6	4	$\sqrt{14}(6\rho^6\text{-}5\rho^4)\cos4\theta$	9^{th} order tetrafoil at 0^o
28	6	-4	$\sqrt{14}(6\rho^6\text{-}5\rho^4)\sin4\theta$	9^{th} order tetrafoil at 45^o
29	7	3	$4(21\rho^7\text{-}30\rho^5\text{+}10\rho^3)\cos3\theta$	9^{th} order trefoil at 0^o
30	7	-3	$4(21\rho^7\text{-}30\rho^5\text{+}10\rho^3)\sin3\theta$	9^{th} order trefoil at 90^o
31	8	2	$\sqrt{18}(56\rho^8\text{-}105\rho^6\text{+}60\rho^4\text{-}10\rho^2)\cos2\theta$	9^{th} order astigmatism at 0^o
32	8	-2	$\sqrt{18}(56\rho^8\text{-}105\rho^6\text{+}60\rho^4\text{-}10\rho^2)\sin2\theta$	9^{th} order astigmatism at 45^o
33	9	1	$\sqrt{20}(126\rho^9\text{-}280\rho^7\text{+}210\rho^5\text{-}60\rho^3\text{+}5\rho)\cos\theta$	9^{th} order coma at 0^o
34	9	-1	$\sqrt{20}(126\rho^9\text{-}280\rho^7\text{+}210\rho^5\text{-}60\rho^3\text{+}5\rho)\sin\theta$	9^{th} order coma at 90^o
35	10	0	$\sqrt{11}(252\rho^10\text{-}630\rho^8\text{+}560\rho^6\text{-}210\rho^4\text{+}30\rho^2\text{-}1)$	9^{th} order spherical

Table A.2: Expression for Legendre Polynomials

N^o	Polynomial	Classical name
1	x	Tilt at 0^o
2	y	Tilt at 90^o
3	$\frac{1}{2}$(3x^2-1)	Cylinder at 0^o
4	xy	Astigmatism at 45^o
5	$\frac{1}{2}$(3y^2-1)	Cylinder at 90^o
6	$\frac{1}{2}$(5x^3-3x)	Linear coma at 0^o
7	$\frac{1}{2}$(3x^2-1)y	–
8	$\frac{1}{2}$(3y^2-1)x	–
9	$\frac{1}{2}$(5y^3-3y)	Linear coma at 90^o
10	$\frac{1}{8}$(35x^4-30x^2+3)	–
11	$\frac{1}{2}$(5x^3-3x)y	–
12	$\frac{1}{4}$(3x^2-1)(3y^2-1)	–
13	$\frac{1}{2}$(5y^3-3y)x	–
14	$\frac{1}{8}$(35y^4-30y^2+3)	–
15	$\frac{1}{8}$(63x^5-70x^3+15x)	–
16	$\frac{1}{8}$(35x^4-30x^2+3)y	–
17	$\frac{1}{4}$(5x^3-3x)(3y^2-1)	–
18	$\frac{1}{4}$(3x^2-1)(5y^3-3y)	–
19	$\frac{1}{8}$(35y^4-30y^2+3)	–
20	$\frac{1}{8}$(63y^5-70y^3+15y)	–
21	$\frac{1}{16}$(231x^6-315x^4+105x^2-5)	–
22	$\frac{1}{8}$(63x^5-70x^3+15x)y	–
23	$\frac{1}{16}$(35x^4-30x^2+3)(3y^2-1)	–
24	$\frac{1}{4}$(5x^3-3x)(5y^3-3y)	–
25	$\frac{1}{16}$(3x^2-1)(35y^4-30y^2+3)	–
26	$\frac{1}{8}$(63y^5-70y^3+15y)x	–
27	$\frac{1}{16}$(231y^6-315y^4+105y^2-5)	–
28	$\frac{1}{16}$(429x^7-693x^5+315x^3-35x)	–
29	$\frac{1}{16}$(231x^6-315x^4+105x^2-5)y	–
30	$\frac{1}{16}$(63x^5-70x^3+15x)(3y^2-1)	–
31	$\frac{1}{16}$(35x^4-30x^2+3)(5y^3-3y)	–
32	$\frac{1}{16}$(5x^3-3x)(35y^4-30y^2+3)	–
33	$\frac{1}{16}$(3x^2-1)(63y^5-70y^3+15y)	–
34	$\frac{1}{16}$(231y^6-315y^4+105y^2-5)	–

APPENDIX B

Scientific Publications

---

1) G. O. Williams, A. I. Gonzalez, S. Kunzel, **L. Li**, M. Lozano, E. Oliva, B. Iwan, S. Daboussi, W. Boutu, H. Merdji, M. Fajardo, and Ph. Zeitoun, *Fourier transform holography with high harmonic spectra for attosecond imaging applications*, Optics Letters,*In Press*, (2015).

2) B. Ecker, B. Aurand, D. C. Hochhaus, P. Neumayer, B. Zielbauer, E. Oliva, **L. Li**, T. T. T. Le, Q. Jin, H. Zhao, K. Cassou, S. Daboussi, O. Guilbaud, S. Kazamias, D. Ros, P. Zeitoun and T. Kuehl, *Double-stage soft x-ray laser pumped by multiple pulses applied in grazing incidence*, Journal of Physics B: Atomic, Molecular and Optical Physics **48**, 144009 (2015).

3) Yong Wang, Shoujun Wang, Eduardo Oliva, **Lu Li**, Mark Berrill, Liang Yin, Jaroslav Nejdl, Bradley M. Luther, C. Proux, T. T. Thuy Le, Jim Dunn, David Ros, Phlippe Zeitoun and Jorge J. Rocca, *Gain dynamics in a soft x-ray laser amplifier perturbed by a strong injected x-ray field*, Nature Photonics, **8**, 381-384 (2014).

4) **Lu Li**, Yong Wang, Shoujun Wang, Eduardo Oliva, Liang Yin, T. T. Thuy Le, Sameh Daboussi, David Ros, Gilles Maynard, Stephane Sebban, Bitao Hu, Jorge J. Rocca, and Philippe Zeitoun, *Wavefront improvement in an injection-seeded soft x-ray laser based on a solid-target plasma amplifier*, Optics Letters, **38**, 4011-4014 (2013).

5) Phlippe Zeitoun, Eduardo Oliva, T. T. Thuy Le, David Ros, Stephane Sebban, **Lu Li**, Pedro Velarde and Marta Fajardo, *X-ray Chirped Pulse Amplification: towards GW Soft X-ray Lasers*, Applied Sciences, **3**, 581-592 (2013).

6) Eduardo Oliva, Marta Fajardo, **Lu Li**, Moana Pittman, T. T. T. Le, Julien Gautier, Guillaume Lambert, Pedro Velarde, David Ros, Stephane Sebban and Philippe Zeitoun, *A proposal for multi-tens of GW fully coherent femtosecond soft x-ay lasers*, Nature Photonics, **6**, 764-767 (2012).

7) Eduardo Oliva, Marta Fajardo, **Lu Li**, Stephane Sebban,David Ros, and Philippe Zeitoun, *Soft x-ray plasma-based seeded multistage amplification chain*, Optics Letters, **37**, 4341-4343 (2012).

8) **Lu Li**, Yong Wang, Shoujun Wang, Eduardo Oliva, Liang Yin, T. T. Thuy Le, David Ros, Gilles Maynard, Stephane Sebban, Jorge J. Rocca, and Philippe Zeitoun, *Wave Front Study of Fully Coherent Soft X-ray Laser using Hartmann Sensor*, Proceeding in International Conference of Soft X-ray Lasers (ICXRL2014), *In Press* (2015).

9) **Lu Li**, Yong Wang, Shoujun Wang, Eduardo Oliva, Liang Yin, T. T. Thuy Le, Sameh Daboussi, David

Ros, Gilles Maynard, Stephane Sebban, Bitao Hu, Jorge J. Rocca, and Philippe Zeitoun, *Wavefront of a seeded soft x-ray laser based on a solid-target plasma amplifier*, Proceedings of the SPIE, Volume **8849** (2013).

10) **Lu Li**, Yong Wang, Shoujun Wang, Eduardo Oliva, Mark Berrill, Liang Yin, Jaroslav Nejdl, Bradley M. Luther, C. Proux, T. T. Thuy Le, Jim Dunn, David Ros, Jorge J. Rocca and Phlippe Zeitoun, *High harmonics pump-probe study on gain dynamics of soft x-ray laser plasma amplifier*, *In Preparation*, (2015).

APPENDIX C

Acknowledgements

This thesis presents not only my work in the past three years, it is a milestone in a decade of group work on high harmonics seeded soft x-ray lasers at Laboratoire d'Optique Appliquée (LOA), France. My experience was based on the previous achievements of this subject. Since September 2011, I have been given unique opportunities and taken advantages of them. I wish to thank dozens of the researchers for the remarkable contribution prior to this work.

First and foremost, I would like to thank my supervisor, **Dr Philippe Zeitoun**, vice-director of LOA, whom has been supporting me over three years. He firstly helped me to get the scholarship for this PhD program and carefully arranged everything before my first arrival at France. As the first time living abroad from China, I could feel the huge social and cultural difference from what I had experienced. Philippe and his whole family did a great job to help me integrate into the local life. He assiduously inspired me from every little bit with the completely new subject to me. Even with hard work everyday, he kept discussion with me at any available time for divergent physics. I greatly appreciate all the experiments, conferences and training schools that he provided to me, which improved my professional skills, opened my scientific minds and enriched my horizontal knowledge. He snatched at every chance to improve my experimental expertises and scientific life skills. I wouldn't finish this thesis manuscript without his guiding, correction, encouragement and moral support during some difficult times. A special thanks to him for his help of my post-doc position at Queen's University Belfast and his support of the thesis defence in all the ways. Finally, the most important thanks to him for becoming a lifelong friend.

It has been a great pleasure working with **Prof. Jorge J. Rocca** for two major experiments at Colorado State University, US. Many thanks for his personal and professional guidance of the experiments. I can always benefit from his rich experience and breadth of knowledge. I've been very glad to work with his team (**Yong Wang, Shoujun Wang, Liang Yin** and **Mark Berrill** and grateful for the two successful experiments and the following publications. I would also like to thank both his wife **Carmen Menoni** and him for their hospitality and good care at Fort Collins, which made me feel at home. Some other lovely people (such as **Kaarin Goncz**) from Colorado State University helped me a lot during my staying there. I do appreciate all the favours and kindness.

Many experiments have been done together at LOA and GSI (Germany) with **Prof. Marta Fajardo** from IST, Portugal. I have learnt a lot from her and from the excellent team (**Gareth Willams** and **Swen Künzel**). Thanks to them for spending so much time together. It has been wonderful experience working on different experiments. I would also like to give my gratitude to **Prof. Thomas Küehl** for the two collaborated experiments at GSI, Darmstadt. His kindness and considerate arrangement are greatly appreciated. It was very nice to work with his soft x-ray laser team (**Boris Ecker, Bastian Aurand** and **Bernhard Zielbauer**). I am indebted to **Prof. Bitao Hu** (Lanzhou University), who awoke me from ignorance. I will never forget all his efforts to guide and inspire me. He is always behind of me and encouraging me to move forward. I had wonderful and life-enhancing four years experience working with him at Lanzhou University, China. More working groups I'm grateful to: **Olivier Guilbaud, Moana**

Pittman, Olivier Delmas, Julien Demailly, Sophie Kazamias, and David Ros from LASERIX); **Andrea Le-Marec, T. T. Thuy Le, Gilles Maynard, Annie Klisnick** from LPGP, France; **Daniel Ursescu, Gabriel V. Cojocaru** from INFLPR, Romania; **Aura-ines Gonzalez and Willem Boutu** from Saclay CEA, France; **Guillaume Dovillaire** from Imagine Optic, France.

A special thanks to **Dr Eduardo Oliva** (LOA, LPGP and Universidad Politécnica de Madrid (Spain)). He helped me from the first day when I arrived at Paris. He was a patient life guide for my living in Paris. Furthermore, his excellent simulation work on this subject positively inspired and encouraged all the experiments in the current thesis work. I'm very grateful for his rich discussion of physical understanding. He turned me up in this project and raised me up by continuous help over three years. Thank you to him for being one of my best friends.

There are many important people from LOA who helped me in all the ways. Lovely people from FLEX group – **Stéphane Sebban, Julien Gautier, Guillaume Lambert, Fabien Tissandier, Boris Vodungbo,** and **Antoine Rousse**, are never tired of answering my various questions. I can't remember how many troubles I have brought to them, but they never complained, always offer help in thick and fast. I benefit a lot from all the kind discussion with them. There are no perfect words to express my gratitude to my team members **Benoît Mahieu and Hugo Dacasa**. I'm indebted all their accompaniments of the late lunches, late experiments and complicated paperworks. It was my great pleasure to stay in the same office with them. I would say to the kind-heart newcomer – **Thai-Hoa Chung** that she is lucky to have all the lovely people around. The mechanical fabrication is very important to the experiment. I'm grateful to **Charles Jean-Loup**, whom I can always count on for working out any design. Thank **Magali Lozano** for her looking after the laser system of Salle Orange. Her hard work ensuring the good output laser beam is greatly appreciated for all of our experiments done there. She is also a good companion for the coffee breaks and hanging out. I would like to give a big hug to all the people in LOA secretary group – **Carole Gratpanche, Lucie Huguet, Patricia Toullier, Sandrine Tricaud,** and **Octavie Verdun**. I quite appreciate their dealing with the hardest paperworks for me over the three years. They are always doing their best to make my life and work easier, and I do feel their kind intentions each time. Office life is always involved with the computers, software and internet. I can't imagine how I would suffer from that without the professional assistance from **Maxence Le Sourd** over ages. Life is much simpler to have this kind of genius around. I'm very grateful to **Yi Liu** for the brotherhood in both life and work. Every discussion stimulated me in a forward way. I would like to also give my gratitude to all the support from his family. Many other people from LOA have helped me continuously, I sincerely thank you to them: **Davide Boschetto, Yohann Brelet, Adrien Depresseux, Gauillaume Point, Aurelien Houard, Yves-Bernard Andre, Pengji Ding, Zacaria Essaidi, Sergey Mitryukovskiy** and **Amelie Jarnac** and so on.

My thesis jury members guided me through all the manuscript. Thank you to **Dr Hamed Merdji, Prof. Gregory J. Tallents, Dr Sameh Daboussi, Prof. Victor Malka, Prof. Jorge J. Rocca,** and **Dr David Ros** for their hard work and valuable time on my thesis manuscript and the final defence. I'm honoured to have all of them in the panel and I enjoyed the great benefits from their comments and corrections.

Many thanks to **Zheng Lin, Yongjun He** and his family for the great favour of organizing the following party after defence. I'm delighted to have such warm friends. There are dozens of good friends I would like to give my gratitude: **Carlier family, Haozhe Deng and Arnaud, Hongmei Sun, Stephane Vouillaume, Lang Lieu, Ximeng Zeng, Jijin Wang, Limin Meng, Jin Huang, Ning Chu, Yi Huang, Yan Ren, Yan Zhu, Qingshan Tang, Chengjun Li, Wenxin Huang, Xianwen Luo, Juanjuan Jia, Yang Xiang, Zhesheng Chen, Shiguang Li, Jie Yang, James Lambert, Jie Xu, Meihui Zheng, Martin**

Reguerraz, Xiaojun Wang, Xiao Xu, Lili Lu, Feng Liu, Chunliang Liu with his family, Salim Perchy, Alonso Celis, Louis Dumont, Arevik Gevorgyan, Freshteh Asgari, Fatima Jardali, Olimpiu Roib, Sai Ma, Yuhua Li, Dorra Mlouhi, Maimouna Bocoum, Oana-Zenaida Pascan, Xinwei Wu, Xiaoping Yuan, Xue Cheng, Wenhua Zhang with his family, Xuefeng Wang, Juan Liu, Lulu Chen, Runmin Zou, Jingjie Ding, Zuoye Liu, Jun Su, Siqi Wang, etc. for all the good times in the past three years.

This thesis is dedicated to my family, especially to my grandmother **Qingmei Wang**, my parents **Zhaolan Li and Junde Li**, my uncle **Junhua Li**, my brother **Qiang Li**, sister in law **Ting Liu** and lovely niece **Kexuan Li**. Uncle **Junhua Li** passed away with a pancreatic cancer during my thesis writing. My father **Junde Li** was diagnosed with a lung cancer one month ago. I'm very grateful to **Dr Brendan Dromey**, **Dr Matt Zepf** and **Dr Philippe Zeitoun** for their hearty support and enlightenment. I wish x-ray laser source can finally contribute to address the human cancer.

List of Figures

List of Tables

Photograph

From left to right: *Victor Malka, Gregory Tallents, Jorge Rocca, Sameh Daboussi, Hamed Merdji, David Ros, Philippe Zeitoun (with Lu LI* at front).
November 21st, 2014 , Palaiseau, France

Figure C.1: Photograph of the thesis defense.

Résumé:
Les lasers émettant des rayons X-mous sous forme d'impulsions cohérentes ultracourtes (SXRL pour soft X-ray laser en anglais) sont des outils appropriés à l'étude de la dynamique ultrarapide des atomes, molécules, surfaces et matériaux. Le présent manuscrit expose des travaux numériques et expérimentaux sur l'injection par harmonique élevée d'un amplificateur SXRL compact.

Des essais sur l'installation LASERIX montrèrent une amplification limitée dans un plasma d'ions néonoïdes du titane ($32.6\ nm$), due à la réfraction du faisceau harmonique injecté. Le front d'onde d'un SXRL à $18.9\ nm$ fut ensuite mesuré au Colorado State University (CSU), en fonction de différents paramètres d'amplification. L'étude numérique d'un plasma à grande section efficace démontra la génération d'impulsion SXRL de plusieurs dizaines de μJ et d'une durée $80\ fs$. Une modélisation plus poussée du processus d'amplification a révélé une déplétion rapide ($< 300\ fs$) du gain suivie par une reprise après environ $1.5\ ps$, vérifiée expérimentalement durant une expérience pompe-sonde (rayons X / rayons X) effectuée au CSU. Ceci a inspiré le concept d'amplification à dérive de fréquence dans les rayons X. Une modélisation complète annonce une émission SXRL totalement cohérente de l'ordre du GW ($200\ fs$, plusieurs mJ).

Metrology of High Harmonics Seeded Soft X-ray Laser Based on Solid-Plasma Amplifier

Abstract:
Ultrashort coherent soft x-ray lasers (SXRL) are adequate to capture dynamics in atoms, molecules, surfaces and materials at the ultrashort time-scales. In current dissertation, we numerically and experimentally studied on a table-top fully coherent SXRL source. The main idea is to seed high harmonic pulse into laser-induced plasma achieving significant energy amplification.

The first attempt was tested using neon-like titanium plasma ($32.6\ nm$) at LASERIX facility. Then wave front of this seeded SXRL beam ($18.9\ nm$) was measured approaching diffraction-limited ($\lambda/14$) using Hartmann wave front sensor at Colorado State University. Numerical studying on short plasma with large cross-sectional area demonstrated $10's$ of μJ and $\sim 80\ fs$ SXRL pulse. Further modelling of the amplification process revealed a rapid depletion ($< 300\ fs$) of the gain followed by a full recovery after about $1.5\ ps$. A novel x-ray pump/x-ray probe experiment was successfully conducted to verify it. This inspired the X-ray chirped pulse amplification (CPA) concept. It promises GW fully coherent SXRL (several mJ) with a capability of reaching Fourier-limited beam ($\sim 100\ fs$).

Key Words: soft X-ray laser; plasma amplifier; Hartmann sensor; wave front; high harmonics; seeding; gain recovery; population inversion ...

Discipline: Physics

Ecole Polytechnique
Route de Saclay, 91128 Palaiseau, France